PREPARATION AND CHARACTERIZATION OF NEW OXIDE ION CONDUCTING AND DIELECTRIC MATERIALS WITH FLUORITE AND PEROVSKITE RELATED STRUCTURES

By

KATARI VASUNDHARA

CHEM01200904021

Bhabha Atomic Research Centre, Mumbai

A thesis submitted to the Board of Studies in Chemical Sciences

In partial fulfillment of requirements for the Degree of

DOCTOR OF PHILOSOPHY

OF

HOMI BHABHA NATIONAL INSTITUTE

March 2015

Homi Bhabha National Institute

Recommendations of the Viva Voce Board

As members of the Viva Voce Board, we certify that we have read the dissertation prepared by **Ms. Katari Vasundhara** entitled **"Preparation and characterization of new oxide ion conducting and dielectric materials with fluorite and perovskite related structures"** and recommend that it may be accepted as fulfilling the dissertation requirement for the Degree of Doctor of Philosophy.

Chairman: Prof. R. K. Vatsa — Date: 6.11.2015

Guide/Convener: Prof. A. K. Tyagi — Date: 6.11.2015

Member: Prof. V. Sudarsan — Date: 6.11.2015

Member: Prof. S. N. Achary — Date: 6.11.2015

External Examiner: Prof. Nand Kishore — Date: 6.11.2015

Final approval and acceptance of this thesis is contingent upon the candidate's submission of the final copies of the thesis to HBNI.

I hereby certify that I have read this thesis prepared under my direction and recommend that it may be accepted as fulfilling the thesis requirement.

Date: 6.11.2015
Place: Mumbai

Guide

Dr. A. K. TYAGI
Head, Solid State Chemistry Section
Chemistry Division
Bhabha Atomic Research Centre
Mumbai - 400 085, India

STATEMENT BY AUTHOR

This dissertation has been submitted in partial fulfilment of requirements for an advanced degree at Homi Bhabha National Institute (HBNI) and is deposited in the library to be made available to borrowers under rules of the HBNI.

Brief quotations from this dissertation are allowable without special permission, provided that accurate acknowledgement of source is made. Requests for permission for extended quotation from or reproduction of this manuscript in whole or in part may be granted by the Competent Authority of HBNI when in his or her judgment the proposed use of the material is in the interests of scholarship. In all other instances, however, permission must be obtained from the author.

Katari Vasundhara

DECLARATION

I, hereby declare that the investigation presented in the thesis has been carried out by me. The work is original and has not been submitted earlier as a whole or in part for a degree / diploma at this or any other Institution / University.

Katari Vasundhara

List of publications arising from the thesis

1. Size dependent magnetic and dielectric properties of nano $CoFe_2O_4$ prepared by a salt assisted gel-combustion method.
K. Vasundhara, S. N. Achary, S. K. Deshpande, P. D. Babu, S. S. Meena and A. K. Tyagi.
*J. Appl. Phys.*113 (2013) 194101-194107.

2. Phase evolution and oxide ion conduction behaviour of $Dy_{1-x}Bi_xO_{1.5}$ ($0.0 \leq x \leq 0.5$) composite systems.
K. Vasundhara, S. J. Patwe, A. K. Sahu, S. N. Achary and A. K. Tyagi.
RSC. Adv. 3 (2013) 236-244.

3. Structural and oxide ion conductivity studies on $Yb_{1-x}Bi_xO_{1.5}$ ($0.0 \leq x \leq 0.5$) composites.
K. Vasundhara, S. N. Achary, S. J. Patwe, A. K. Sahu, N. Manoj and A. K. Tyagi.
J. Alloy. Compd. 596 (2013) 151-157.

4. High temperature structural, dielectric and ion conduction properties of orthorhombic $InVO_4$.
K. Vasundhara, S. J. Patwe, S. N. Achary and A. K. Tyagi.
J. Am. Ceram. Soc. 96 (2013) 166-173.

5. Effect of annealing environment on low temperature magnetic and dielectric properties of $EuCo_{0.5}Mn_{0.5}O_3$.
K. Vasundhara, S. N. Achary, S. K. Deshpande, P. D. Babu, H. G. Salunke, N. Gupta and A. K. Tyagi.
J. Phys. Chem. C. 118 (2014) 17900-17913.

6. Improvement of magnetodielectric coupling by surface functionalization of nickel nanoparticle in Ni and PVDF (polyvinylidene fluoride) nano-hybrids.
B. P. Mandal, **K. Vasundhara,** E. Abdelhamid, G. Lawes, H. G. Salunke and A. K. Tyagi.
J. Phys. Chem. C. 118 (2014) 20819-20825.

7. Enhancement of dielectric permittivity and ferroelectricity of modified cobalt nanoparticle and Polyvinylidene fluoride based composite.
K. Vasundhara, B. P. Mandal and A. K. Tyagi.
RSC. Adv. 5 (2015) 8591-8597.

8. Structure, thermal and electrical properties of calcium doped pyrochlore type praseodymium zirconate.
K. Vasundhara, S. N. Achary and A. K. Tyagi.
Int. J. Hydrogen. Energy. 40 (2015) 4252-4262.

9. Structure and electrical properties of layered perovskite type $Pr_2Ti_2O_7$: Experimental and theoretical investigations.
S. J. Patwe, **K. Vasundhara** , N. P. Salke, S. K. Deshpande, R. Rao, M. K. Gupta, R. Mittal, S. N. Achary and A. K. Tyagi.
J. Mater. Chem. C. 3 (2015) 4570-4584

10. Magnetic and dielectric properties of Y_2MMnO_6 (M = Co, Ni): effect of annealing environment.
K. Vasundhara, P. D. Babu, S. K. Mishra, R. Mittal, S. N. Achary, S. K. Deshpande and A. K. Tyagi
J. Appl. Phys. **(Communicated)**.

Conferences

1. Structure and ionic conductivities of $Dy_{1-x}Bi_xO_{1.5}$ compositions ($0.00 \leq x \leq 0.50$).
Vasundhara, S. J. Patwe, S. N. Achary and A. K. Tyagi.
International conference on material science and technology (ICMST 2012), June 2012, Pala, Kottayam, Kerala, India.

2. Magnetic and dielectric properties of nano $CoFe_2O_4$ prepared by a salt assisted gel-combustion method.
K. Vasundhara, S. N. Achary, S. K Deshpande, P. D. Babu, S. S. Meena and A. K. Tyagi.
Interdisciplinary symposium for material chemistry (ISMC-2012), Dec, 2012, BARC, Mumbai, India.

3. Polyvinylidene fluoride and cobalt based composite with high dielectric constant.
K. Vasundhara, B. P. Mandal and A. K. Tyagi.
Asian conference on solid state ionic (ACSSI-2014), June, 2014, NUS, Singapore.

Others

1. Preparation and characterization of new oxide ion conducting and dielectric materials with fluorite and perovskite related structures.
Researchers Scholars Meet 2014, Mumbai, India. (Oral Presentation)

Katari Vasundhara

Dedicated to.....

My Beloved Family and

My Teachers

ACKNOWLEDGEMENTS

As there is a famous saying which says that the “Guru” be prayed even before God, so I would first like to thank my guide Dr. A. K. Tyagi, Head, Solid State Chemistry Section, Chemistry Division. Nothing is possible without his proper guidance and timely help. I am ever thankful to him for accepting me as one of his research student. It is my immense pleasure to acknowledge Dr. A. K. Tyagi for his support and constant encouragement throughout the course of my doctoral work. I owe my deep sense of gratitude towards him for introducing me to the area of fascinating world of ionic conductor and dielectric materials. Thank you very much Sir for everything!!!

I wish to express my special thanks to Dr. S. N. Achary for keeping me hooked and interested in my research work. This thesis would not have been complete without his valuable suggestions and discussions throughout the Ph.D. period. It has been a great privilege and honour to be associated with Dr. S. N. Achary.

I am much grateful to Dr. T. Mukherjee (Ex. Director, Chemistry Group, BARC) who encouraged me to join to Solid State Chemistry Section, where I have truly enjoyed being an active member of the group. Sincere thanks are due to Dr. B. N. Jagatap, Director, Chemistry Group, BARC and V. K. Jain, Head, Chemistry Division, BARC for their wholehearted support and encouragement. Doing any research work requires lots of technical and scientific inputs from the renowned and experienced individuals in respective field. During my research, I have collaborated with many such individuals. I would like to thank Dr. A. K. Sahu (Glass & Advanced materials Division), Dr. R. Mishra, Dr. N. Manoj (Chemistry Division), Dr. S. K. Deshpande, Dr. P. D. Babu (UGC-DAE Consortium for Scientific Research, Mumbai), Dr. H. G. Salunke, Dr. N. Gupta (Technical Physics Division), Dr. S. K. Mishra, Dr. R. Mittal, Dr. RekhaRao, Dr. M. K.

Gupta (Solid State Physics Division) for allowing me to use instruments available with them and for sharing of their knowledge.

I would like express my very gratefulness to Dr. S. J. Patwe for care and affection and also for teaching me solid state chemistry. A lot of thanks to Dr. B. P. Mandal, Dr. Vinita Gupta, and Mr. R. K. Shukla for their timely suggestions, motivations and scientific discussion. Also, I would like to extend my thanks to Dr. O. D. Jayakumar, Dr. M. Roy, Dr. A. Singhal and Dr. Dimple Dutta for their useful suggestions.

I would like to thank all my doctoral committee members who have taken time from their busy schedule to give valuable comments on my research progress and for their fruitful and positive recommendations.

I would like to thank my childhood friends, with whom I can share the moments of joy as well as sorrows, especially Varija and her family, for their care and affection. I would also thank to my friends Teja, Saroja, Kalpana, D. Lakshmi and Shreelekha who have always encouraged me in all aspects. I am deeply thankful to my friends who made my Ph.D. journey so attainable by sharing their advices and experiences. Especially, I thank Jerina and Farheen for all time cooperation and constant help. I thank both of them for their endless patience for answering my queries and clarifying silliest doubts. I wish to thank my dear friends and lab members Mohsin, Pooja, Anita and Samatha for providing friendly environment and lots of help.

It is my pleasant duty to thank technical staff, especially, Mrs. Aruna who taught me proper pellet-making. I would also like to thank Ms. Mani, Mrs. Vishaka, Mrs. Nisha and all office staff of Chemistry Division, for their timely help whenever required.

I thank my batch-mates for their suggestions and encouragement during my stay in the Institute. No words to express my gratitude to my friends and well-wishers, who made my stay a pleasant, memorable and enjoyable in the campus. I thank all of them, whose names might have not appeared but whose assistance has helped in the progress of my research work.

Last but not the least, the most important persons of my life, I thank my parents who brought me up and supported me throughout my educational life. I am pleased to acknowledge my brother Naresh who gave me countless encouragement during my studies. Specially, I am indebted to my husband Madhu for his care, understanding and endless patience. Words cannot express how grateful I am to my parents- in-law for their moral support.

Finally, I would like acknowledge the financial support from the DAE-SRC-ORI Grant of Dr. A.K. Tyagi.

Katari Vasundhara

ABSTRACT

The ionic conducting and dielectric materials are important classes of the electro-ceramics which have significant relevance in the fuel cell and sensor technologies. In the class of ionic conductors, fluorite-type Bi_2O_3 and cation substituted Bi_2O_3 / ZrO_2 based ceramics exhibit high oxide ion conductivity and thus, they have attracted wide research attention. However, zirconia based materials exhibit high oxide ion conductivity only at higher temperature. Though Bi_2O_3 based materials show appreciable conductivity at moderate temperature they are highly reactive to other components used in devices and have limited stability. In order to obtain appreciably ionic conductivity and higher stability, series of compositions as $Ln_{1-x}Bi_xO_{1.5}$ ($0.00 \leq x \leq 0.50$), where Ln = Dy and Yb, were prepared and their electrical properties were measured. Similarly, pyrochlore-type oxides also form a potential class of oxide ion conductors as they exhibit appreciable conduction at moderate temperature. Thus, such materials can be electrolytes for fuel cell, especially for moderate or intermediate temperature fuel cells. In this regard, several compositions, as $Pr_{2-x}Ca_xZr_2O_7$ ($0.00 \leq x \leq 0.20$) were prepared and investigated in detail. Recently, double perovskite-type materials have drawn significant attention due to their fascinating magnetic and electrical properties as well as multiferroic or magnetodielectric properties. The cation ordering and magnetic properties of such materials depend upon the preparation conditions. Several perovskite-type materials like Eu_2CoMnO_6, Y_2CoMnO_6 and Y_2NiMnO_6 were synthesized by gel-combustion method and their dielectric properties were investigated after annealing in various conditions. Polymer nano-composites are of great importance because of their high energy density and high breakdown voltage. Co and Ni loaded PVDF composites were prepared and their electrical properties were investigated. In both the cases enhancement in dielectric

constant was observed whereas the composites with the surface modified Ni showed higher magnetodielectric coupling. Additionally, electrical properties of $InVO_4$ and $CoFe_2O_4$ have also been investigated. Finally the relations between structure and ionic conductivity / dielectric properties between different classes of materials are discussed.

CONTENTS

Synopsis

Last century witnessed extensive use of natural resources throughout the world. The rate of usage of natural resources necessitates efforts to find alternative energy resources, which must be efficient and eco-friendly as well as cost effective. Thus, to find and develop alternatives to natural sources is a challenge to contemporary research. Also, the future solution for energy crisis will be a judicious combination of various developed technologies to get maximum benefits. This combination of technologies is for both production and storage of energy. There are different types of energy conversion (fuel cell, solar cell, batteries) and storage technologies (capacitor and super-capacitors). Fuel cell is an electrochemical device which converts the energy of chemical reaction to electrical energy. Similarly, battery is an energy storage material. There are three basic components in the fuel cell and battery viz. cathode, anode and electrolyte. Due to technological feasibility, Intermediate Temperature Solid Oxide Fuel Cell (IT-SOFC) (general operation temperature ~ 500-700^{o}C) have received great attention as potential power generation systems. In addition, the lowering the operating temperature of SOFC improves cell durability and reduces the system cost. The performance of IT-SOFCs is strongly dependent on the cathode and electrolyte interface. Since fuel cell resistance depends upon the electrolyte resistance, considerable amount of research efforts are being carried out to decrease the electrolyte resistance. Even though fuel cells are used for many applications, they are still not efficient and cost effective to meet high power demand at reasonable cost. Thus, research efforts are also being carried out for better energy storage device viz. battery. Though batteries have capability of storing large amount of energy in small volume, the fast discharge rate and degradation on long run operation are their limitations. To overcome these limitations, capacitor technology is considered as an alternative important technology in the power storage system. In addition, the

miniaturization of electronic devices requires capacitors with good dielectric properties and high energy density. In this thesis work, preparation and properties of some oxide ion conductors and dielectrics have been investigated.

Among the oxide ion conducting solid electrolytes, yttria stabilized zirconia (YSZ) is the most widely investigated material for SOFC. However, YSZ exhibits high conductivity only at high temperature and thus is not suitable for the fuel cells operated at lower or intermediate temperatures. Therefore, lots of research efforts have been carried out worldwide for the development of ionic conductors having higher conductivity at lower temperature. Among these systems, Bi_2O_3 is considered as a promising alternative material. Depending upon the temperature, Bi_2O_3 exists in several polymorphs, named as α, β, γ, δ and ε [1]. Among these various polymorphs of Bi_2O_3, the δ-phase has highest ionic conductivity (σ_0 = 2.3 S/cm at 800 °C) and thus has considerable importance. The high ionic conductivity of δ-Bi_2O_3 is due to its fluorite-type structure with high concentration of oxygen vacancies and high polarizability of Bi^{3+}. On the other hand, δ-phase is stable only in a narrow temperature range i.e. from 730 °C to its melting point 804 °C. Stabilization of this high temperature δ-phase at lower temperature can be achieved by doping with trivalent rare-earth ions such as Y^{3+}, Dy^{3+}, Er^{3+} etc. [1-2]. Though, several studies have been devoted to the development of electrolytes based on δ-Bi_2O_3, the lower stability and higher reactivity still remained as limitations for its practical usage in SOFC. Concepts have also been used to employ a thin interlayer of stable oxide ion conductors like YSZ over the surface of Bi_2O_3 facing the fuel. This prevents direct contact of fuel and electrolyte and hence reduces the reduction induced degradation of Bi_2O_3. However, such approach cannot prevent the degradation of the electrolytes as reaction of Bi_2O_3 and ZrO_2 leads to precipitation of several ternary stable phases of Bi_2O_3-ZrO_2 system[3]. In order to reduce the contribution of the reactive

Bi_2O_3in electrolyte, Bi-deficient phases in Bi_2O_3-Ln_2O_3 system may be envisaged as potential candidates for the electrolyte application. In an optimum concentration of Bi_2O_3, a significant improvement on the thermal-stability at the expense of partial loss of conductivity can be achieved. In the aim of obtaining stable electrolyte, phase evolution and conductivity in $Ln_xBi_{1-x}O_{1.5}$ (Ln= Dy^{3+} and Yb^{3+}; $0.0 \leq x \leq 0.5$) compositions were investigated in the present thesis work.

A few ordered compounds having fluorite related structures are also known to exhibit appreciable ionic conduction. Pyrochlore-type $A_2B_2O_7$ compounds form a class of materials in this category. Formation and stability of the pyrochlore structure depend on the ionic radii of the A and B site cations. The pyrochlore-type structure is observed when the ionic radius of A and B site cations satisfies the limiting condition as $1.48 < r_A/r_B < 1.78$. If radius ratio exceeds 1.78, the perovskite-type structure is preferred [4]. Pyrochlore structure can be viewed as a defect-fluorite structure. Due to presence of one unoccupied anion position, the anions (oxygen ion) can easily migrate through vacancy sites resulting in high oxygen ionic conductivity of about 10^{-2} S/cm at 1000 °C, thus pyrochlore type materials are also considered as promising candidates for SOFC application. Cations exhibiting multiple valences can be of importance to introduce electronic conduction. Being mixed valence states, zirconates of Pr are likely to be important candidates for such properties. The details of the structural and electrical properties of Ca^{2+} substituted pyrochlore-type $Pr_2Zr_2O_7$ have been investigated in this thesis work. The $A_2B_2O_7$ type rare-earth (RE) titanates with Ti^{4+} as B-site cation form monoclinic perovskite type structure for RE = La, Nd and Pr. The detailed structural and electrical properties of perovskite type $Pr_2Ti_2O_7$ are studied in this work.

In recent years, double perovskite $A_2BB'O_6$ (R = rare-earth; B and B′ are *3d* transition metal ions) are being investigated for their application as magnetoelectric and multiferroic materials [5]. In view of this, series of compositions as Ln_2MMnO_6 (Ln=Eu and Y; M=Ni and Co) were prepared and characterized. The need of energy storage systems with high energy density has led to the development of polymer composite systems [6]. Polymers have the high breakdown strength but the dielectric constants of these materials are very low. Among the different types of polymer, PVDF (polyvinylidene fluoride) is a promising material due to its ferroelectric nature. PVDF has different types of polymorphs and only the β-phase of PVDF has the high dielectric constant. In the aim to increase the amount of β phase, [7] systematic studies on polymer composites have been carried out in this thesis. It was found that the dielectric constant of the polymers can be increased by introducing ceramic fillers and metal nanoparticles into the matrix. Preparations of the PVDF-Co and PVDF-Ni composites and dielectric properties have been investigated in this thesis.

The introduction and detailed studies of subject matter of this thesis are explained in different chapters. The layout and content of these chapters are briefly explained below.

Chapter 1: General introduction

This chapter gives a general background on energy crisis and the importance of fuel cells and energy storage materials. Oxygen ion conductivity mechanism in fluorite, pyrochlore and perovskite structured materials and brief literature survey on these materials are presented in this chapter. Practical importance of the ionic conductors in fuel cells, oxygen sensors and oxygen pumps are discussed in this chapter. The general background of the dielectric materials and their classifications are discussed in second part of this chapter. Literature survey on the different types of dielectric materials is also briefly

discussed. The importance of polymer nano-composites in energy storage is also explained.

Chapter 2: Experimental techniques

This chapter contains the fundamental aspects of general preparation procedures and characterization techniques. Various chemical methods used to synthesize the multi-component oxides, in particular, gel combustion technique, solid state reaction method and polyol assisted synthesis are briefly discussed in this chapter. Different characterization techniques like spectroscopic, microscopic and diffraction methods used in the thesis work are also discussed. Phase analyses of the samples were carried out by using X-ray diffraction technique. Scanning Electron Microscopy (SEM) was used for the investigation of microstructure of prepared samples. Raman spectroscopy has been employed to study the short range order in mixed oxides. X-ray photo-electron spectroscopy (XPS) technique was used to study the oxidation states of the ions involved. Various other techniques used in this study, such as Thermogravimetry (TG), measurement of ionic conductivity have also been explained.

Chapter 3: Preparation and characterization of oxide ion conductor in Bi_2O_3-Ln_2O_3 (Ln= Dy and Yb) systems

In this chapter, phase evolution and electrical properties of compositions in Bi deficient region of Bi_2O_3-Ln_2O_3 (Ln = Dy and Yb) systems are presented. A series of compositions as $Ln_{1-x}Bi_xO_{1.5}$ (Ln^{3+}= Dy^{3+} and Yb^{3+}; $0.0 \leq x \leq 0.5$) were prepared by solid state reaction of Dy_2O_3 or Yb_2O_3 and Bi_2O_3.X-ray diffraction, Raman spectroscopy, Scanning electron microscopy and *ac*-impedance spectroscopy were used to characterize the prepared samples. In case of $Dy_{1-x}Bi_xO_{1.5}$ ($0.0 \leq x \leq 0.5$) samples, all the compositions except for x = 0.40 show composite phases either as rhombohedral and C-type rare-earth oxide phases or rhombohedral and fluorite-type phases. A single phase with rhombohedral lattice was

observed at the composition with x = 0.40 in the Dy_2O_3-Bi_2O_3 system. In case of $Yb_{1-x}Bi_xO_{1.5}$ ($0.0 \leq x \leq 0.5$) system, except x = 0.00, all other compositions have composite structure of a feebly Bi^{3+} doped Yb_2O_3 and about 35 % Yb^{3+} doped Bi_2O_3.With increasing concentration Bi^{3+}, the fraction of F-type phase systematically increases. Electrical properties of these samples have been investigated from impedance measurements. To interpret the Cole-Cole plot various impedance models comprising of resistor, capacitor and constant phase element have been used. All the studied $Ln_{1-x}Bi_xO_{1.5}$ (Ln = Dy and Yb; $0.0 \leq x \leq 0.5$) compositions showed oxide ionic conductivity, which increases with the concentration of Bi^{3+}. Typical activation energies (E_a) for the studied compositions were in the range of 1.1 to 1.4 eV. The pre-exponential factor increases with Bi^{3+} concentration. Temperature dependent conductivities have been explained on the basis of increased contributions of grain boundaries and the formation of fluorite-type δ-Bi_2O_3phase.

Chapter 4: Studies on structural and electrical properties of $Pr_2B_2O_7$ type compounds (B= Zr^{4+}andTi^{4+})

In this chapter preparation and electrical properties of two $A_2B_2O_7$ type compositions, namely $Pr_2Zr_2O_7$ (pyrochlore) and $Pr_2Ti_2O_7$ (perovskite) are presented. Series of compositions as $Pr_{2-x}Ca_xZr_2O_7$ (x = 0.00, 0.10 and 0.20) were prepared by gel-combustion method followed by heating at higher temperature in reducing Ar-H_2 atmosphere. These samples were characterized by XRD, Raman spectroscopy and ac-impedance studies. Single phase samples with pyrochlore-type structure were observed for compositions with x = 0.00 and 0.10 while the composition with x=0.20 showed pyrochlore-type phase along with a small amount of perovskite $CaZrO_3$ phase. From HT-XRD studies, the retention of cubic pyrochlore structures was observed. TG curves shows maximum of about 1 % weight gain attributed to oxidation of Pr^{3+} in all the samples. The electrical

conductivity of $Pr_{2-x}Ca_xZr_2O_7$ceramics was investigated by complex impedance spectroscopy over a frequency range of 0.1 Hz to 10MHz in the temperature range of 0 to 700 °C. The temperature dependent conductivities of the studied samples show Arrhenius type behaviour. The electrical conductivity of the $Pr_{2-x}Ca_xZr_2O_7$ decreases and electronic conductivity increases with the increase of Ca^{2+}. The activation energy (*Ea)* for electronic conduction of pyrochlore-type $Pr_{2-x}Ca_xZr_2O_7$ were 0.42, 0.63 and 0.91 eV for x=0.00, 0.1 and 0.2, respectively. The electrical properties of the studied samples have been correlated with structural parameters and explained by the coexisting electronic and ionic conductivities.

Second part of this chapter deals with the structure, thermal and dielectric properties of layered perovskite type $Pr_2Ti_2O_7$. It is well known that with increase in the radius ratio in $A_2B_2O_7$, the structure changes from pyrochlore to layered perovskite. $Pr_2Ti_2O_7$ was prepared by solid state reaction method involving constituent oxide. The monoclinic ($P2_1$) structure was found to be stable compared to the orthorhombic $Pna2_1$ or $Cmc2_1$ structures. The variable temperature XRD studies and differential thermal analyses studies revealed absence of structural transition to $Cmc2_1$ up to 1000 °C. A partial decomposition of $Pr_2Ti_2O_7$ to cubic perovskite-type structure was observed at around 1400 °C. Electric field polarization studies confirm the ferroelectric nature of $Pr_2Ti_2O_7$. The electrical properties of $Pr_2Ti_2O_7$ were investigated from 100 to 800 °C by *ac*-impedance spectroscopic studies.The low temperature dielectric data indicate two different types of relaxations, one at lower frequency side due to thermally activated polarization process arising from the grain boundaries and other one a temperature independent relaxation due to dipolar reorientation. The activation energy for thermally activated relaxation process was 0.38 eV and it can be attributed to interfacial polarization due to the ionic movements. $Pr_2Ti_2O_7$ exhibits ionic conductivity at still higher temperature. The temperature

dependent ionic conductivity shows a deviation around 427 °C where the activation energy decreases from 0.83 to 0.59 eV.

Chapter 5: Tunable magnetic and dielectric properties of Ln_2MnMO_6 (Ln = Eu and Y, M=Co and Ni)

In this chapter, structure, dielectric and magnetic properties of perovskite type Y_2CoMnO_6 (YCMO) and Y_2NiMnO_6 (YNMO) and Eu_2CoMnO_6 (ECMO) compounds are presented. All the compositions were prepared by gel combustion method followed by high temperature sintering. All the products were characterized by powder XRD, which revealed a monoclinic cation ordered structure for YCMO and YNMO while ECMO sample was found to adopt cation disordered orthorhombic structure. The variations of structure, magnetic and dielectric properties of all these materials have been investigated after annealing in different atmospheres. Limited stabilities of these materials on annealing in inert atmosphere were observed. Magnetization measurements show the paramagnetic to ferromagnetic transition in all the samples and they were found to depend on the preparation conditions. Both ECMO and YCMO samples show metamagnetic transition and this behaviour depends on nature of rare-earth ion and conditions of annealing. The presence of randomly distributed clusters of ferromagnetically and antiferromagnetically paired magnetic ions and their relative proportions was reflected in their magnetic properties. The dielectric measurements on these samples show distinct frequency and temperature dependent features in YCMO and ECMO compared to YNMO samples. A large relative permittivity with ε' of about 10^4 was observed in these samples under both O_2 and air annealed conditions. Multiple dielectric relaxations were observed in all the samples which were annealed in inert atmosphere. The analyses of temperature and frequency dependent dielectric data were also explained in this chapter.

Chapter 6: Magnetic and dielectric properties of M: PVDF ferroelectric composite films (M=Co and Ni)

The continuous increase of energy demands and consumption of natural resources causes the demand of increasing attention on high efficiency energy storage materials. This has been a great motivation for the development of dielectric materials with superior energy density. In view of this, cobalt and nickel nanoparticles loaded polyvinylidene fluoride (PVDF) composites have been prepared. Cobalt and nickel nanoparticles were prepared by polyol method using sodium borohydride and hydrazine hydrate as reducing agents. The surface of the Ni nanoparticle was modified by the hydroxyl groups. Flexible polymer films were prepared by solution-cast method with dimethyl formamide as (DMF) polar solvent. The films have been characterized by X-ray diffraction, infrared spectroscopy, electrical polarization measurement and dielectric relaxation spectroscopy. In both the cases remarkable increase in the amount of polar β phase of PVDF has been observed. Dielectric constant of the both the composite (Co-PVDF and Ni-PVDF) increases with the increase in the concentration of the Co and Ni nanoparticles. The high dielectric constant of the composites was attributed to the space charge polarization at the interfaces between cobalt nanoparticle and PVDF and the development of several micro-capacitor structures. The electrical field dependent polarization also increases with the concentration of Co and Ni nanoparticles. In case of surface modified Ni, the leakage current is drastically reduced. However, the magnetic moment of the modified composite was found to be little lower than that for unmodified one. Most importantly, composites with surface modified nickel exhibit significantly higher magneto-dielectric coupling than the unmodified one. The details of the results of strcture and property investgations on Co-PVDF and Ni-PVDF composites were explained in this chapter.

Chapter 7: Preparation, structure and physical properties of some transition metal based complex oxides

In this chapter, preparation and electrical properties of two complex oxides, namely, $InVO_4$ and $CoFe_2O_4$ were explained. The salient details of these studies are as follows:

The frequency dependent conductivity and dielectric properties of the orthorhombic $InVO_4$ were studied. The structural analyses using high temperature XRD reveal that orthorhombic lattice was retained up to 750 °C. Significantly increased conductivity was observed at higher temperature due to appreciable grain boundary conductivity contribution. From the dielectric property measurements, permittivity values were found to be maximum at high temperature and low frequency. The frequency dispersion studies indicate thermally activated hopping process in electrical and dielectric properties.

Nanoparticles of $CoFe_2O_4$ were prepared by gel-combustion method in presence of KCl. The as-prepared sample and sample heated at 900 °C for 24 h were investigated in details by XRD, Infrared spectroscopy, Mössbauer Spectroscopy and Scanning Electron Microscopy. The average particle sizes for the as-prepared and heated products were about 6 and 50 nm, respectively. X-ray diffraction and Mossbauer spectroscopy results showed spinel type structure with all Fe in 3+ oxidation states for both the samples. The low temperature dielectric and magnetic properties of sample were studied by ac-impedance spectroscopy and SQUID magnetometry. The field and temperature dependent magnetization studies indicate ferromagnetic nature for 50 nm particles while super paramagnetic nature for 6 nm sized sample. Increase in the dielectric permittivity was observed with the decrease in the particle size. Both the samples exhibited variable range polaron hopping conduction.

Chapter 8: Summary and future scope

In this chapter the results of various studies in different types of materials were explained and compared in brief. The final conclusions of these studies were also summarized in this chapter. The future scope of thesis work has been elaborated. In particular, further insights on the preparation dependent properties on conducting and dielectric materials are desirable and they form the future scope. Also the possible applications of the prepared material in SOFC and capacitors need to be further investigated in future.

References

1. M. J. Verkerk and A. J. Burggraaf, J. Electrochem. Soc. 128 (1981)75-82.
2. V. V. Kharton, E. V. Naumovich, A. A. Yaremchenko and F. M. B. Marques, J. Solid State. Electrochem. 5 (2001) 160-187.
3. (a)I. Abrahams, A. J. Bush, S. C. MChan, F. Krok and W. Wrobel, J. Mater. Chem.11(2001) 1715-1721;(b)C. Michel, V. Caignaert and B. Raveau, J. Solid State Chem. 90 (1991) 296-301.
4. M. A. Subramanian, G. Aravamudan and G. V. S Rao, Prog. Solid State Chem.15 (1983) 55-143.
5. (a) M. Fiebig, T. Lottermoser, D. Fröhlich, A. V. Goltsev and R. V. Pisarev, Nature 419 (2002) 818-820; (b)S. W. Cheong and M. Mostovoy, Nat. Mater. 6(2007) 13-20.
6. (a) Q .Wang and L. Zhu, J. Polym. Sci., Part B: Polym. Phys. 49 (2011) 1421-1429;(b)A. J. Lovinger, Science 220 (1983) 1115-1121.
7. (a) M. G. Broadhurst, G. T. Davis and J. E. McKinney, J. Appl. Phys. 49(1978)4992-4997;(b)H. Kawai, Jpn. J. Appl. Phys8 (1969) 975-976.

LIST OF FIGURES

LIST OF TABLES

LIST OF ABBREVATIONS

BOPP	Bioxially Orientated Polypropylene
BSE	Back Scattered Electrons
BTO	$BaTiO_3$
CPE	Constant Phase Element
CSZ	Calcia Stabilized Zirconia
DTA	Differential Thermal Analyses
ECMO	Eu_2CoMnO_6
EFG	Electric Field Gradient
EIS	Electrochemical Impedance Spectroscopy
EXAFS	Extended X-Ray Absorption Of Fine Structure
FC	Field Cooled
FT-IR	Fourier Transform Infrared
HT-XRD	High Temperature X Ray Diffraction
IT-SOFC	Intermediate-Temperature Solid Oxide Fuel Cell
KNN	$(K,Na)NbO_3$
LFD	Linear Frequency Dispersion
LSCF	$La_{0.6}Sr_{0.2}Co_{0.2}Fe_{0.8}O_3$
LSGM	$La_{0.8}Sr_{0.2}Ga_{0.85}Mg_{0.15}O_{3-ö}$
LSM	$La_{0.8}Sr_{0.2}MnO_3$
MIEC	Mixed Ionic Electronic Conduction
MW	Maxwell Wagner
PANI	Poly aniline

PEN	Polyethylene Naphlate
PP	Polypropylene
PPS	Polyphenylene sulfide
PTO	$Pr_2Ti_2O_7$
PVDF	Polyvinylidene Fluoride
RE	Rare-Earth
RP	Ruddlesden-Popper
SE	Secondary Electrons
SEM	Scanning Electron Microscopy
SOFC	Solid Oxide Fuel Cell
SQUID	Superconducting Quantum Interference Device
TEC	Thermal Expansion Coefficient
TGA	Thermo-gravimetric Analysis
XPS	X-Ray Photoelectron Spectroscopy
XRD	X Ray Diffraction
YCMO	Y_2CoMnO_6
YNMO	Y_2NiMnO_6
YSZ	Yttria Stabilized Zirconia
ZFC	Zero Field Cooled

CHAPTER 1
GENERAL INTRODUCTION

Chapter 1

1.1. Introduction

Natural resources including water, energy and fertile land are the basis of our life on earth and these resources are back bone of every economy. Current usage rate of these available resources in both developed and developing countries poses a concern for future generations due to their limited availability and non-renewable nature. Global consumption of these natural resources will be almost triple of the current consumption in future. In order to set a limit on the use of natural and non-renewable resources, alternate renewable energy sources have been of huge demand. The usage of alternate energy sources has two aspects, first being production of energy from non fossil sources and second being storage of the produced energy in some viable mean. Thus, the alternate energies sources like solar energy, wind power, fuel cells, geothermal and hydro-electric etc. will be the future energy sources, while energy storage can be in the form of chemical, biological, electrochemical, electrical, mechanical, thermal and electrical etc. In case of electrical energy, the batteries, capacitor, super capacitor, superconductor etc. are the optimum and viable storage media. The usage and performance of such devices rely on the involved active materials like ionic conductors, dielectric or magnetic materials, having appropriate properties. Thus, research on suitable ionic conductors or dielectric or magnetic materials is desired for development of useful devices or media for future generations. In view of this, the current material research has been focused on good ionic conductors or dielectric materials. For practical applications, an ionic conductor should have high ionic conductivity at moderate temperature or room temperature,

high chemical stability and high compatibility with other components of the devices, while the good dielectric materials should exhibit high dielectric constant, high charge density, low leakage and high breakdown strength. In the present thesis, efforts were made to develop new oxide ion conductors and to study fundamental properties of some dielectric materials, and magneto-dielectric materials.

In this chapter, a brief introduction to the ionic conductor, in particular solid oxide ion conductor and dielectric materials including single phase or composites have been discussed. Also, the present status of the research on oxide ion conductors and dielectric materials is also mentioned. The properties and mechanism of these materials are explained on the basis of their structural features.

1.2. Solid state ionic conductors

Solid state ionic conductors are class of materials which exhibit higher ionic conductivity like liquid electrolyte and form an important part of fuel cell. After the discovery of large electrical conductivities in PbF_2 and AgF_2 by Faraday in 1938, the study on ionic conduction in solids became a blooming research area in materials science. Generally solid electrolytes are characterized by high ionic conductivity with negligible electronic conductivity. Ionic conduction in solid electrolytes originates from the motion of cations or anions in the bulk solid and they are referred as cationic conductors or anionic conductors, respectively. Such solid electrolytes have many advantages than analogous liquid electrolytes in devices, viz. as electrode materials in electrochemical devices like mobile telephones, laptops and pace makers etc. Ionic conductivity strongly depends on the temperature. At high temperature, conductivity of about 0.1 S/cm (1273 K) can be approached in certain solid electrolytes like yttria

stabilized zirconia (YSZ) and scandia-stabilized-zirconia (ScSZr) etc. [1]. However, certainly there is a need to develop improved electrolyte in terms of high conductivity and chemical stability for versatile application. In order to achieve these properties in a solid ionic conductor, two general research approaches have been followed and they are as follow.

1. Search for new compounds and structures for high levels of ionic conductivity.

2. Modification of existing materials by homogenous or heterogeneous substitution of isovalent or aliovalent ions.

A number of research efforts on ionic conductor show that ionic conduction in solid materials depends on their structural and micro-structural features. Most of the materials studied for oxide ion conduction contain oxygen vacancies and in all of them hopping of O^{2-} ions mediated by oxygen vacancies is the major conduction mechanism. Systematic investigations on conduction mechanism of crystalline materials suggest that the structures with following features show high ion conduction.

- Structures having larger unoccupied (vacant) sites equivalent to those occupied sites.
- The energy involved for migration of ions from one occupied site to the unoccupied sites must be small, i.e. site energy of the ions in occupied and unoccupied sites should be close.

Oxide ion conductivity has been observed predominantly in different class of structural materials with either intrinsic oxygen ion vacancies or amenable for the

formation of oxygen ion vacancies. Typical structures with potential to exhibits oxygen ion conductors are explained below.

1.3. Materials exhibiting oxide ion conductivity

As mentioned above, the structural features of crystalline materials have prime importance for exhibiting oxide ion conductivity. There are a number of structure types which has intrinsic structural arrangements or flexibility of the structure for sustaining anion defects and exhibit ion conduction.

1.3.1. Fluorite-type materials

Most extensively studied oxide ion conductors belong to the class of materials having fluorite-type structure. The term "fluorite" originates from the name of the mineral fluorite, CaF_2. Oxide ion conductors with the fluorite structure type are an exciting class of materials and are involved in many technological applications. The general formula of fluorite structure is AO_2 (where A is tetravalent cation and occupies face centered position of a cubic unit cell with anions (oxygens) in the eight tetrahedral sites) as shown in the **Fig.1.1**. One important feature of fluorite structure is its ability to sustain a high degree of substitution and large anion non-stoichiometry. Thus, the structure can form a highly disordered anion sublattice leading to fast oxide ion conduction **[**1b,2].

Thorium dioxide (ThO_2), uranium dioxide (UO_2) and ceria (CeO_2) etc. readily form fluorite-type crystal structure. Since the ionic radius of Zr^{4+} is small to form eight coordinated polyhedra with O^{2-}, the zirconia (ZrO_2) form fluorite-type structure only at high temperature or by partial substitution with another (usually larger) cations or by creation of anion disorder. Cubic zirconia, a widely studied oxide ion conductor

is an example of fluorite-type oxide ion conductor. A common procedure to get oxide ion conductivity in fluorite structure of ZrO_2 is substitution of cation sites with aliovalent rare-earth ion, Y^{3+}, Sc^{3+} etc. In order to maintain the electrical neutrality, such doping leads to anion vacancies and oxide ion conduction then proceeds through oxide ion jump via anion vacancies [1b,2]. Y^{3+} is the most common dopant used for stabilizing the cubic fluorite-type phase of zirconia.

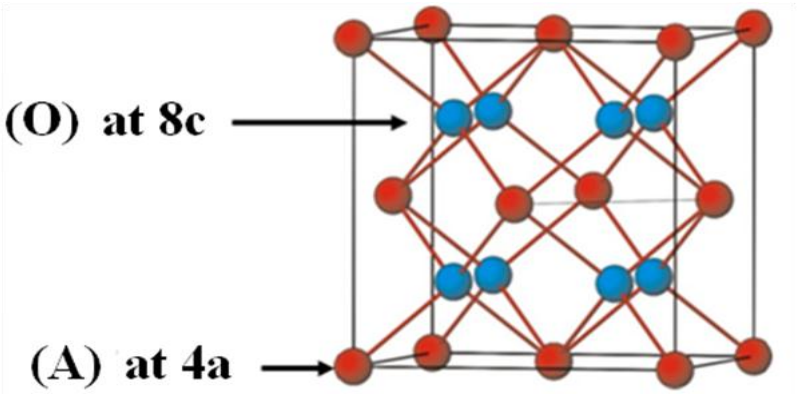

Fig.1.1: Fluorite structure (cubic, Fm3m).

The ionic conduction in fluorite-type structure is related to the intrinsic or extrinsic vacant sites for anions. Under the influence of an external electric field, the motion of oxygen ions through the oxygen vacancies creates a net current in oxide ion conductors. The easiest jump is along the edge of the cube formed by eight oxygen ions or vacancies. Hence, ionic conductivity of fluorite structure also depends on the size of the dopant ion and it tends to be highest for the cation with ionic radius close to host cation radius, e.g. $Zr_{1-x}Sc_xO_{2-x/2}$ and $Ce_{1-x}Gd_xO_{2-x/2}$ (CGO), etc. In such cases the dopants introduce vacancies in the lattice without significant alteration in structure and thus, the clustering or association of defects remains to minimum [2]. Similar to stabilized ZrO_2, fluorite-type Bi_2O_3 (i.e. δ-Bi_2O_3) is also a known oxide ion conductor. The highest oxide ionic conductivity among the known oxide conductors is observed

in δ-Bi_2O_3. However, the δ-Bi_2O_3 phase is stable only at high temperature, i.e. above 1002 K [3]. In order to stabilize the δ-Bi_2O_3 at room temperature, a number of substituents have been reported in literature [4]. At higher dopant concentrations, such solid solutions based ionic conductors often show a decreasing trend in conductivity. The interaction between the substituted ions and anions or vacancies resulting into defect cluster is the dominating reason for the decreasing trend in conductivity.

1.3.2. Pyrochlore-type materials

The second largest class of material exhibiting oxide ion conduction has pyrochlore-type structure. Pyrochlore oxides are named after the mineral pyrochlore, (NaCa)(NbTa)O_6F/(OH). The general formula of the pyrochlore structure is $A_2B_2O_6O'$, where A can be cations with 3+ or 2+ oxidation states and B can be cations with 4+ or 5+ oxidation states. The pyrochlore structure can be considered as an ordered variant of defective fluorite solid solution. In the defect fluorite structure, A and B cations are randomly distributed at face centered positions, whereas oxygen ions are occupied at the tetrahedral sites. The ordered pyrochlore has five different crystallographic sites for ions. The larger (A) cations are located at (*16c*) with coordinates (0 0 0) and have 8 fold coordination while the smaller (B) cations are occupied at *16d* site with (½ ½ ½) coordinate and have six fold coordination. Two distinct types of anions (O and O′) occupy *48f* (x 1/8 1/8) and *8a* (1/8 1/8 1/8) sites, respectively. An additional position, *8b* (3/8 3/8 3/8) is also available for anions in pyrochlore structure. Normally, this site is vacant in $A_2B_2O_7$ type pyrochlore. The 8*a* sites are surrounded by four A cations and 8b vacancy sites are surrounded by four B cations as shown in **Fig.1.2**. [5]. The nature of the polyhedra changes with the oxygen parameter x. The value of x ranges

between the theoretical values of 0.3125 and 0.375. At x = 0.375, the A cations are located in a perfect cube and there is no displacement of oxygen ions from a perfect cubic array whereas, B cations are in the center of highly distorted octahedral. At x = 0.3125, the B cations are in perfect octahedral coordination. Both polyhedra are distorted when the value of x lies between these two values.

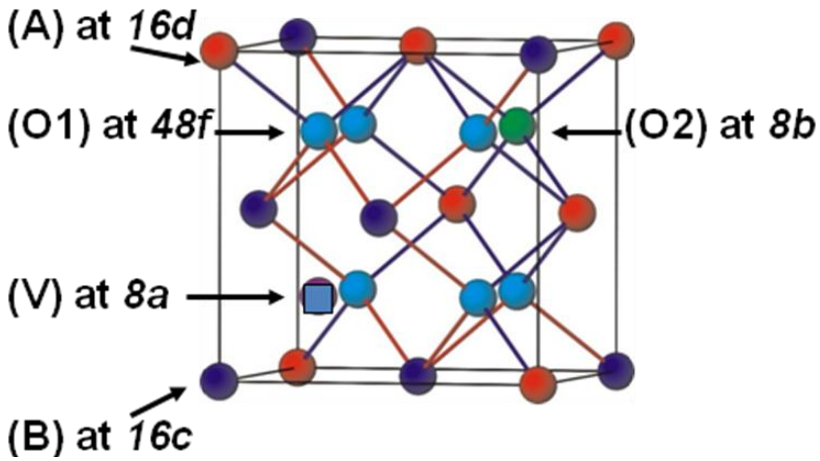

Fig.1.2: Pyrochlore structure (cubic, Fd3m).

Existence and stability of the pyrochlore is governed by the relative cationic radius and oxygen parameter "x". The $A_2B_2O_6O'$ pyrochlore structure is found to be stable within radius ratio limit $1.40 \leq r_A/r_B \leq 1.71$, whereas the $A_2^{2+}B_2^{5+}O_6O_1$ pyrochlore structure, this limit is extended to wider range, viz. $1.4 < r_A/r_B < 2.2$. The cation pairs with r_A/r_B smaller than 1.40 prefer to form defect fluorite structure due to the easy swapping of two cations [5a,6]. Apart from these structural aspects, the stability of pyrochlore also depends upon the temperature, pressure and procedures adopted for preparation. At higher temperature often materials can transform from perfect pyrochlore to defect fluorite structures.

As mentioned, the presence of intrinsic vacant oxygen sites makes them potential oxide ion conductor, due to easy migration of anion (oxygen ion) from occupied sites to vacant sites. Such anion migration can result in high oxygen ionic conductivity at higher temperature, viz. ~10^{-2} S/cm at 1273 K and thus, makes them promising candidates for SOFC (Solid Oxide Fuel Cell) application. Also, the wide tolerance range of composition and nonstoichiometry of pyrochlore compounds makes them favorable for varieties of applications like sensors, catalysts, dielectrics and in nuclear waste management.

In this thesis, two compositions as $A_2B_2O_7$, with A = Pr^{3+} and B = Zr^{4+} and Ti^{4+}) have been prepared and characterized in details. Among these, the composition $Pr_2Zr_2O_7$ has pyrochlore-type structure due to the satisfying ionic radius criteria. Also, the details of structures and electrical properties of Ca^{2+} substituted pyrochlore-type $Pr_2Zr_2O_7$ have been explained. The $A_2B_2O_7$ type rare-earth (RE) titanates with Ti^{4+} as B-site cation form monoclinic perovskite-type structure for RE = La, Nd and Pr. The detailed structural and electrical properties of perovskite-type $Pr_2Ti_2O_7$ are studied in this work.

1.3.3. Perovskite-type materials

Similar to fluorite and pyrochlore, materials with perovskite-type structure have also been reported to exhibit higher ionic conductivity with suitable composition. The perovskite-type ABO_3 materials can give rise to anion vacancy upon substitution of suitable cations either at A or B sites. Several anion deficient perovskite-type materials are considered as promising materials for IT-SOFC (intermediate-temperature solid oxide fuel cell). In such structural materials oxygen ion conduction

occurs when oxygen ion jumps from one vacant site to adjacent vacant sites. **Fig.1.3** depicts the structure of an ideal cubic ABO_3 perovskite lattice, where A cation are occupied at the corner of the cube and B cations occupy the center of the cube while the oxygen ions are at the face centered positions. In such arrangement, the smaller B cations are octahedrally coordinated by oxygen ions while the larger A cations are coordinated to twelve oxygen ions.

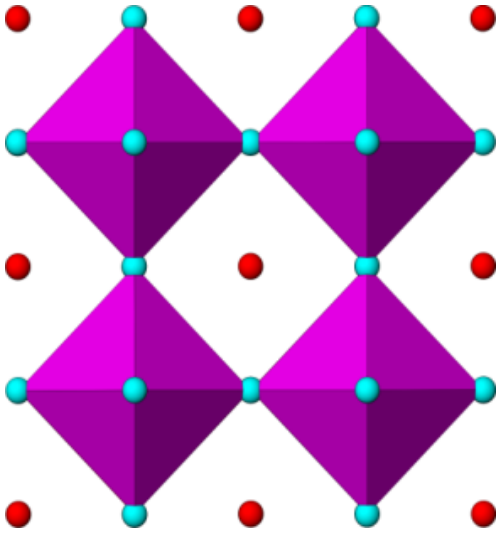

Fig.1.3: Perovskite structure.

In the ideal cubic perovskite structure each cations (A and B) in the perfect size to be in contact with an oxygen anion, where the B-O distance is equal to a/2 and the A-O distance is a/√2, where a is the cubic unit cell parameter. The ratio of these expressions for the cell length is known as Goldschmidt Tolerance Factor and is denoted as *t*, which is applicable at room temperature. Thus, the ions can be assumed as rigid sphere following the relation given below is considered as formation criteria of perovskite structure.

$$r_A + r_O = t\sqrt{2}(r_B + r_O) \qquad [1.1]$$

Where, r_A, r_B and r_O are ionic radii of the A and B site cation and oxygen ion, respectively.

The ideal cubic perovskite is formed when *t* is close to 1 e.g. $SrTiO_3$ and it remains in cubic structure within the limit $0.89 \leq t \leq 1$ [7]. If the A ion is smaller than the ideal case, the *t* value becomes less than one and it results in lower symmetric structure e.g. orthorhombic $GdFeO_3$ (t = 0.81) [8]. If t is in the range of 1.00 to 1.13, the hexagonal symmetry of the perovskite structure is stable e.g. $LaAlO_3$, $BaNiO_3$ etc. Thus, the deviation from the limit of tolerance factor can be used to measure the degree of distortion in a perovskite structure.

The compositional and structural diversity of perovskites arise from the high flexibility of the structure with respect to cationic and anionic substitution, tolerance to distortion and cation order. Cation ordering either at A site or B site gives ordered superlattices for perovskites. The composition $A_2BB'O_6$ show the commonest type of cation ordered structure where the B-sites are ordered and the unit cell shows lower symmetry and larger unit cell parameters. The structural diversity in perovskites also arises from another aspect, which is the stacking of alternate AO and BO_2 layers. Ruddlesden-Popper (RP), Jacobson-Dion, Aurivillius-types layered perovskite structures are formed due to such stacking variations and differences in the layer structures. The third aspect of the structural diversity of perovskite is nonstoichiometry. The nonstoichiometry in perovskite structure is usually considered with respect to A site or anion deficiencies. In the anion deficiency, the compounds with the general formula $A_2B_2O_5$ exhibit ordered or disordered anion deficiency. The

Brownmillerite structure and $Ca_2Mn_2O_5$ structure are two examples of these ordered structures which are also of importance for solid state ionic conduction.

1.4. Effect of temperature on ionic conduction

With increasing temperature, the oxide ions become more labile due to their increasing vibrational amplitude and thus, they easily hop from occupied sites to vacancies. Additionally, the more defects are formed and defect clusters are collapsed with the increase in temperature. Hence, ionic conductivity always shows an increasing trend with increasing temperature. The variation of ionic conductivity, σ, with temperature is generally described by Arrhenius equation

$$\sigma = \frac{A}{KT} \exp\left(-\frac{E_a}{KT}\right) \qquad [1.2]$$

Where E_a = activation energy for ion migration, k = Boltzmann constant, and T= temperature.

The activation energy, E_a, can be calculated easily from the slope of the ln (σT) versus T^{-1} plot. The pre-exponential factor, A, is given by Eq (1.3)

$$A = \frac{1}{3}(Ze)^2 n\, d^2\, w_o \qquad [1.3]$$

Where, Ze is the charge of the carrier ion, n is the vacancy concentration, d is the unit jump distance of the ion (usually the closest pair distance), and w_0 is the attempt frequency.

From the above equations, it is clear that the conductivity increases with the dopant concentration. But this is valid only at lower concentration of dopant. At higher level

of dopant concentration the defect association arises, which adversely affects the ionic conductivity.

The ionic conductivity is related to the diffusion coefficient, *D*, through the Nernst-Einstein equation

$$\sigma = nq^2D/k_BT \qquad [1.4]$$

Where, q = ionic charge, n = number of ions per unit volume, and D = self-diffusion coefficient of ions.

The diffusion coefficient, D is given as

$$D = zNc(1 - c)a_l{}^2\nu/k_BT, \qquad [1.5]$$

Where, Nc = concentration of ions, a_l = distance between the sites, z = number of nearest neighbour sites and ν = jump frequency.

The jump frequency is related to temperature as below

$$\nu = \nu_0 \exp(-E_a/k_BT) \qquad [1.6]$$

Where E_a = free energy barrier between two sites, ν_0 = site frequency of the ion.

1.5. Practical importance of ionic conductors

Solid state ionic conductors have wide range of practical applications some of them are explained below.

1.5.1. Solid Oxide Fuel Cell (SOFC)

Fuel cell is an electrochemical device which converts the energy of chemical reaction into electrical energy without involving combustion (heat) as an intermediate step. In a solid oxide fuel cell (SOFC) layout, as shown in the **Fig.1.4**, the anode and cathode are separated by an electrolyte that is an oxygen ion conducting material. Oxidant gas (usually the air) is supplied to the cathode, and the fuel is supplied to the

anode. Oxidant is reduced at the cathode side and fuel is oxidized at the anode. In general, on the cathode side, oxygen catalytically reacts with a supply of electrons to become oxygen ions, which diffuse through the electrolyte to the anode side. On the anode side, the oxygen ions react with hydrogen to form water and free electrons.

The basic components of a ceramic fuel cell stack are the electrolyte, the anode, the cathode and inter-connect. A load connected externally between the anode and cathode completes the electrical circuit. In this configuration, the difference of the chemical potential between oxidant gas and fuel is converted to the electrostatic potential difference of the anode and the cathode. Thus, the electromotive force can be obtained.

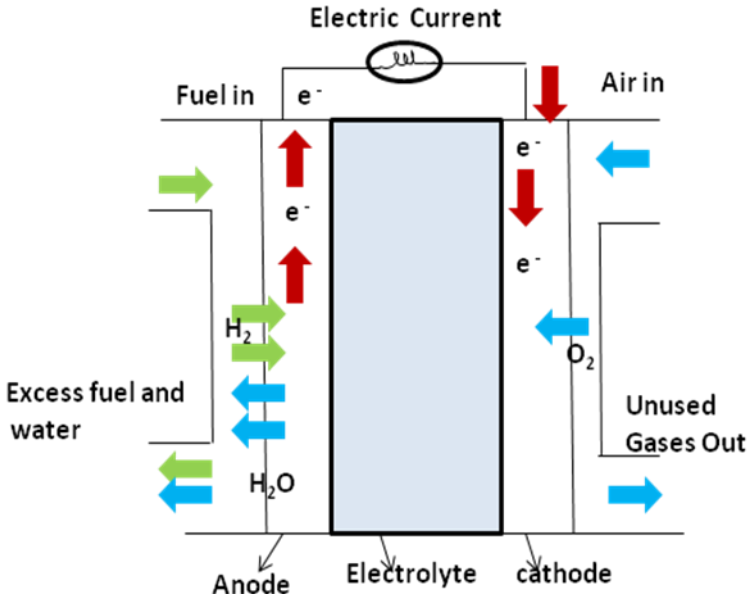

Fig.1.4: Solid Oxide Fuel Cell (SOFC) layout [9].

The electrolyte is the prime component in SOFC and it should have several important properties, like (i) high ionic conductivity with negligible or no electronic conductivity (ii) enough mechanical strength (iii) chemical compatibility between

electrode materials (iv) matching of the thermal expansion coefficient (TEC) with electrode material. Yttria-stabilized zirconia [$(Y_2O_3)_{0.08}$-$(ZrO_2)_{0.92}$) or (8-YSZ)] is the most common electrolyte in SOFCs. Concerning to the electrodes, they must have a high electronic conductivity, sufficient porosity to allow transport of products of fuel oxidation from electrolyte/fuel electrode interface, should have high catalytic activity to quickly exchange charges, chemical and dimensional stability, matched thermal expansion coefficient with the electrolyte and interconnect materials. Currently, porous Ni is the most common anode material for SOFC application. Lanthanum manganite, suitably doped with alkaline earth elements $La_{0.8}Sr_{0.2}MnO_3$ (LSM) and $La_{0.6}Sr_{0.2}Co_{0.2}Fe_{0.8}O_3$ (LSCF) are also used as cathode material in standard SOFC.

1.5.2. Oxygen sensors

Oxygen sensors play an important role in pollution control from cement industries, automobile engine management, biological and food processing plants etc. [6]. Oxygen ion conductors can be used in these solid state potentiometric oxygen sensors. When sensor is exposed to gas environment, oxygen molecules gets adsorbed on the porous Pt electrode and dissociates into atomic oxygen, then these oxygen atoms diffuse in to the boundary of electrolyte and to other electrode as O^{2-} ions. The overall reaction can be represented as

$$\frac{1}{2}O_{2(g)} + 2e'_{pt} + V_{O(YSZ)} \rightarrow O^{x}_{YSZ} \qquad [1.7]$$

The concentration of the oxygen in the environment is measured by equilibrium potential measurement on solid electrode–electrolyte cell using Nernst equation. The electrode used in oxygen sensor should possess the good catalytic activity for oxidation, reduction of oxygen and it should have porous microstructure to manifest

enough triple phase boundaries. Concerning to the electrolytes, they need to be a good oxygen ion conductor. YSZ is the most commonly used electrolyte in sensors with air as the reference electrode [10].

1.5.3. Oxygen pump

One of the important applications of oxygen ion conductor is in electrochemical pump to control the oxygen content in a flowing inert gas. It requires the application of external voltage across the wall of the solid electrolyte tube, through which the gases or liquids flow [11]. This technique has been followed for the removal of oxygen from liquid metals [12].

1.6. Literature survey on ionic conductors

Since the discovery of ionic conduction in solid state, research efforts have been made to find new materials and evaluation of the ionic conduction mechanism. Also, in last few decades the research got an impetus for the development of oxide ion conductors for practical application, like fuel cell. For better ionic conduction at lower temperature, electrical properties of wide varieties of materials have been investigated. In the aim of the present thesis work on oxide ion conductors, literatures on various types of potential electrolytes have been surveyed and they are summarized below.

1.6.1. Stabilized zirconia electrolytes

In the aim of solid electrolytes for SOFC, stabilized zirconia is the most widely explored electolyte. The stabilized zirconia has fluorite type structure which is high temperature polymorph of pure monoclinic zirconia (ZrO_2). The cubic form of ZrO_2 has the good ionic conductivity but this polymorph cannot be retained below 2573 K [11b,13]. A common procedure to get oxide ion conductivity in zirconia is to stabilize

the high temperature polymorph at ambient temperature by doping of cation with lower valence [Y^{3+}, Sc^{3+}, Ca^{2+} etc.]. YSZ is one of the best electrolytes considered for SOFC, but shows desired conductivity only at high temperature and thus, not suitable for low temperature applications [14]. Scandium stabilized zirconia ($Zr_{1-x}Sc_xO_{2-x/2}$, ScSZ) at the 8% doping level of Sc^{3+} can be a potential replacement for YSZ. But high cost of Sc limits its application [1a,15]. Another drawback with ScSZ is that at higher scandia contents (*e.g.*10–12 mole %), the cubic phase transforms to a rhombohedral phase. Cubic phase of zirconia can also be stabilized by other dopants Ca^{2+}, Yb^{3+}, In^{3+}, Sm^{3+}, Mg^{2+} etc. [16]. The Yb^{3+} substituted zirconia shows comparable conductivity with the YSZ and ScSZ, while Mg^{2+} is the least efficient to improve ionic conduction. In both (YSZ, ScSZ) samples, the conductivity decreases with increasing the dopant concentration due to the association of point defects. The tendency of defect association increases with the increase in mismatch of the ionic radii of dopant and host ions. The effect of ionic radii of dopant ions on ionic conductivity, defect association and oxygen migration enthalpy has been investigated in large number of reports [17]. An alternate strategy to improve ionic conduction and to minimize the defect association in stabilized ZrO_2 is by codoping with alkaline earth-cations and other ions [18]. However, no significant improvement has been observed. Another research area of zirconia is focused on improving the density by appropriate sintering procedures, like using sintering aids [19] or using nano sized YSZ prepared by different methods [20].

1.6.2. Ceria based systems

Ceria (CeO_2) has the fluorite structure at ambient condition and has also been explored extensively for electrolyte application. Doping of CeO_2 with other oxides

such as rare-earth or alkaline-earth cations increases the oxygen ion vacancy and these materials exhibit high conductivity at lower temperatures. This makes them superior alternative electrolyte for decreasing operating temperature of SOFC. Like the case of zirconia, the highest conductivity is obtained for the lower size mismatch of the dopant and host radii. Codoping of Gd^{3+} and Sm^{3+} (in concentration of 10 to 20%) in CeO_2 shows higher conductivity than the YSZ at low temperature (773 -973 K) [1b]. However, the problems associated with ceria electrolytes is the ease of reduction at low oxygen partial pressure. Partial reduction of the Ce^{4+} to the Ce^{3+} leads to electronic conduction, nonstoichiometric and lattice expansion, which causes internal short-circuiting in the cell and associated mechanical stresses [21]. A number of attempts by the codoping with rare-earth ions have been made to increase the redox stability of these electrolytes [22]. However, this procedure had shown limited success. $Ce_{0.9}Gd_{0.1}O_{1.95}$ (CGO) codoped with Sm^{3+} and Nd^{3+} does not show improved results [23]. The sintering temperature of doped ceria can be decreased by addition of small amount of divalent transition metal ion (e.g Co^{2+}) [24]. CGO has the good chemical stability with the commonly used cathode material including LSM, LSC ($La_{1-x}Mn_xO_3$, $La_{1-x}Co_xO_3$) etc. which lead to its use it in composite cathode with LSM [25].The interface interaction between the YSZ and cathode material can be minimized by using CGO as interlayer in between them [26].

1.6.3. δ-Bi_2O_3

In the aspect of solid electrolytes, δ-Bi_2O_3 has drawn considerable interest due to its higher ionic conductivity (σ_0 = 2.3 S/cm at 1073 K) compared to other solid electrolytes. On the other hand, δ-phase is stable only in the narrow temperature interval i.e. from 1003 K to its melting point 1073 K. The high ionic conductivity of δ-

Bi_2O_3 is due to its fluorite structure with intrinsic defects in oxygen sublattice. Stabilization of this high-temperature δ-Bi_2O_3 phase at lower temperature has been achieved by doping with rare-earth ions such as Y^{3+}, Dy^{3+}, Er^{3+} etc. [27] or combination of such ions with higher valent cations such as W^{6+} or Nb^{5+} [28]. However, substitution of Bi with other cations decreases the ionic conductivity. Minimum concentration of dopant is essential to stabilize the high temperature fluorite phase. Further increasing dopant concentration, the oxygen ion mobility again decreases due to decrease in the unit cell volume and increase in the average strength of the cation-anion bond. Thus, optimization of dopant concentration is desired for high ionic conductivity. First ionic conductivity increases with the ionic radius and another one is X_{min} (X_{min} = minimum concentration of dopant required for stabilization of the fluorite structure) increase with the ionic radius. However, the influence of ionic radius on conductivity is smaller than the concentration of rare-earth dopant. Maximum ionic conductivity is observed for the Er and Y containing phases namely $Bi_{0.80}Er_{0.2}O_{1.5}$ and $Bi_{1-x}Y_xO_{1.5}$ (x=0.23–0.25) [27b]. These binary and ternary phases have higher ionic conductivity but with time they slowly transforms to vacancy ordered rhombohedral phase, which has the lower ionic conductivity. This phase transformation can be minimized by the incorporation of higher valent cations such as Zr^{4+}, Ce^{4+}, $Nb^{5+}$and W^{6+} [28-29]. Alternate problems associated with Bi_2O_3 electrolytes are due to the reduction in reducing atmosphere at the anode of SOFC. Such problems can be avoided by using thin layer of Sm^{3+} incorporated ceria electrolyte on the anode side [30].

1.6.4. $La_{0.8}Sr_{0.2}Ga_{0.85}Mg_{0.15}O_{3-\delta}$ (LSGM) electrolytes

The high conductivity of doped lanthanum gallate ($LaGaO_3$) with Mg and Sr of general formula $La_{1-x}Sr_xGa_{1-y}Mg_yO_{3-\delta}$ was reported by Ishihara et al. in 1994 [31]. At same temperature, the conductivity of the composition $La_{0.9}Sr_{0.1}Ga_{0.8}Mg_{0.2}O_{3-\delta}$ (LSGM) is higher (0.12 S/Cm at 1273 K) than the YSZ (0.034 S/Cm at 1273 K) and ScSZ [32]. LSGM not only have the comparable ionic conductivity with ceria at low temperature but also is superior to CGO in terms of higher chemical stability in low oxygen partial pressure. Simultaneous doping of Mg^{2+} and Sr^{2+} leads to the reduction in the GaO_6 octahedra tilt and hence increasing the symmetry, which is the responsible for the high oxide ion conductivity. Also, the negligible binding energy for Sr^{2+} dopant cluster favors the high conductivity. In contrast, the Mg^{2+} doping has significant vacancy trapping which increase activation energy for migration. Thus, the conductivity shows two distinct behavior with variation of temperature [33]. The ionic conductivity of LSGM can be improved by doping with the transition metals such as Co and Fe. In low concentration of Co (<0.1%) improved electrical conductivity is observed. Among all the transition metal dopants (Co, Ni, Fe etc.), the one with similar size to that of Mg^{2+} is can be effective for stabilizing high-temperature cubic form [29,34]. Even though this material has high conductivity at low temperature, the formation of phase pure gallate is difficult due to segregation of secondary phases such as $LaSrGa_3O_7$ and $LaSrGaO_4$ during synthesis [46]. Also the high reactivity of LSGM with Ni, commonly used anode in SOFC, is also a limiting factor. In addition, it forms the ionically insulating phase between the LSGM and Ni containing anode due to chemical reaction at higher temperature [35]. Volatilization of Ga observed in reducing atmosphere, is another limitation of LSGM materials.

1.6.5. $Ba_2In_2O_5$

Electrical conductivity of $Ba_2In_2O_5$ is purely oxygen ionic in dry atmosphere whereas it shows mixed ionic and p-type electronic conducting under oxidizing condition, and protonic in H_2O containing medium. At the order-disorder temperature (1198 K) the crystal of $Ba_2In_2O_5$ changes from orthorhombic to tetragonal lattice and the later shows the fast ionic conduction. On further increase in the temperature to 1313 K, oxygen vacancies becomes fully disordered and exhibits pure ionic conduction with ionic transport number unity [36]. The high temperature cubic perovskite can be stabilized at lower temperature by cation substitution on either Ba or In site. Substitution of In^{3+} with dopants such as Zr^{4+}, Ce^{4+}, Sn^{4+} or Hf $^{4+}$, Ga^{3+}, Al^{3+}, Sc^{3+}, Y^{3+}, Yb^{3+}, W^{6+}, Cu^{2+}, Si^{4+}, Ti^{4+}, Ta^{5+}, Nb^{5+}) or Ba by La^{3+}, Sr^{2+} and Pb^{2+} have been used to stabilize the disordered cubic perovskite phase [37]. The ideal cathode material for this material is $(La_{0.6}Sr_{0.4})(Mn_{1-x}Fe_x)O_{3-\delta}$. However, the high reactivity of $Ba_2In_2O_5$ with CO_2, and instability in reducing atmosphere etc. limit its usage in practical fuel cells [38].

1.7. Dielectric materials

Dielectric materials have the large technological applications and have increasing demand in the world of electronic devices. The degree of miniaturization in memory devices based on capacitive components, such a static and dynamic random access memories, depends on the dielectric constant of the material. Hence, a lot of research work is going on the dielectric materials. Dielectric materials are poor conductor of electricity and their main function are (1) to keep away the conducting plates from coming in contact, allowing for smaller plate separations and therefore higher capacitances, (2) to increase the effective capacitance by reducing the electric

field strength, (3) to reduce the possibility of shorting out by sparking (more formally known as dielectric breakdown) during operation at high voltage [39]. The capacitance is related to other factors as follows**:**

$$C = \varepsilon_0 \varepsilon_r A/d \qquad [1.8]$$

Where, ε_0 is the dielectric constant of the free space (8.854×10^{-12} F/m), d is distance between the plate, A is area of the dielectric materials and ε_r is the dielectric constant of the dielectric layer.

The energy stored in the capacitor may be considered to be the same as the work done in moving a charge from low to high potential and it can be written as

$$W = U = Q^2/2C \quad (Q = CV)$$

$$= C^2V^2/2C$$

$$U = \tfrac{1}{2} CV^2 \qquad [1.9]$$

Where, Q is charge on the metallic foils and V is the potential difference between the plates.

The dielectric constant is one of the fundamental electrical properties of solids [40]. Dielectric measurements give the ability of polarizability of ions in a solid. Variation of the dielectric properties with frequency and temperature have the advantages in understanding the polarization mechanism [55-58], the process of electrical conduction [41], defect concentration [42] and nature of bonding [43].

1.7.1. Dielectric polarization

When a dielectric sample is placed in an electric field E, the opposite electric charges are displaced and acquire a permanent dipole moment. Thus, the dielectric material is polarized under the electric field. The polarization P or dipole density can be represented by**:**

$$P=\frac{p}{v} \qquad [1.10]$$

Where, p = permanent dipole momentum v = volume of the sample

Different types of polarizations, viz. electronic, ionic, dipolar, and spontaneous polarization as shown in the **Fig.1.5** occur in dielectric materials when placed inside an electric field. Electronic polarization (Pe) occurs due to displacement of the center of negatively charged electron cloud relative to positive nucleus of atom by the applied electric field. Ionic polarization (Pi) occurs in ionic materials. In an ionic lattice, the positive ions are displaced in the direction of applied field whereas negative ions get displaced opposite direction to the applied electric field, giving rise to net dipole moment. If the molecules possess permanent dipole moment, such as H_2O molecules, the rotation of these dipoles under an electric field will produce the dipolar polarization (Pd). Therefore, the dipolar polarization is strongly dependent on the frequency of the applied electric field and on the temperature. Space charge or interfacial polarization occurs in heterogeneous systems such as multi-component materials or incompatible chemical substance containing materials. The charge carriers are accelerated by an applied field until they are opposed by and/ or trapped at the physical barriers in such these heterogeneous systems. This buildup of charges

causes the polarization of the material. Space charge polarization (Ps) is governing factor of dielectric properties. Electronic, ionic and orientation polarization arises when charges are locally bound in atoms, molecules, or structures of solids or liquids. By the application of low frequency field some of these bound charge carriers migrate over a distance. In case of space charge polarization, the motion of these charge carriers is reduced due to trapping of charges within the materials. Accumulation of these charges increases the overall capacitance of a material.

The total contribution of polarization to the dielectric constant is therefore a summation of the above mentioned individual polarization.

$$Pt = Pe+Pi+Pd+Ps \qquad [1.11]$$

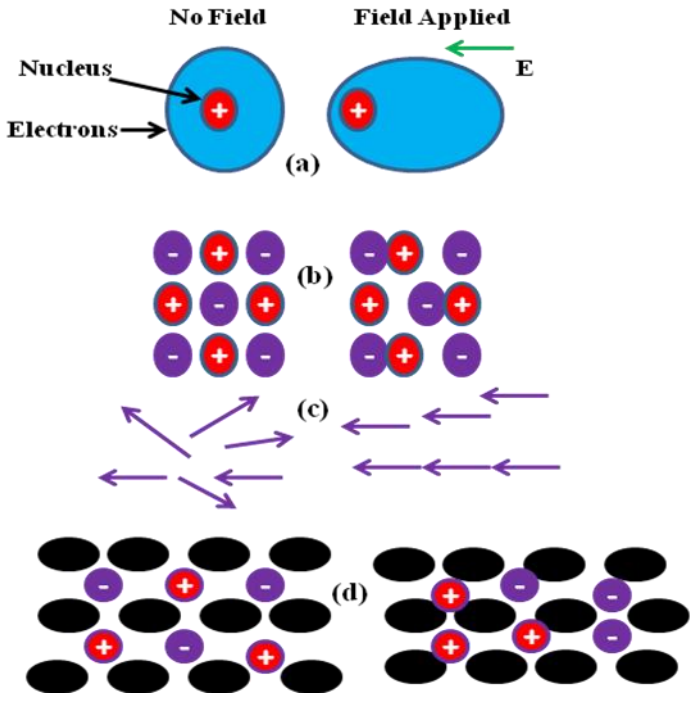

Fig.1.5: Schematics major polarization mechanisms Electronic polarization (b) ionic polarization (c) orientation polarization (d) space charge polarization [44].

1.7.2. Frequency response of dielectric mechanisms

Different types of polarizations respond in different way to the frequency. When the frequency of the applied field is sufficiently low, all types of polarization can be observed. Electronic displacement responds rapidly to the field reversals, and therefore no lag of the polarization contribution occurs up to 10^{17} Hz. Since ions are larger in size and are bound in the crystal structure, have less mobility. The polarization effect of ionic displacement decreases at 10^{13} Hz. At this frequency, the ionic displacement begins to lag the field reversals. Orientation polarization takes a time of the order of 10^{-12} to 10^{-10} sec to reach equilibrium value in liquid and solids. When the applied field has a frequency of 10^{10} to 10^{12} Hz, orientation polarization fails to reach its equilibrium value and contribute less to the total polarization as frequency increases. The space charge polarization in general is observed at lower frequency region where the ionic mobility does not follow the ac frequency. This is usually observed in Hz- to kHz range. Each dielectric mechanism has a characteristic "cutoff frequency." As frequency increases, the slow mechanisms drop out in turn, leaving the faster one contributing to ε_r, as expected, capacitance value, i.e. dielectric constant, always decreases with increasing frequency.

1.7.3. Dielectric loss

Dielectric loss occurs when dielectric material interacts with alternating electric field. Due to different types of polarization there is a phase lag between the phase of the input field and output field which causes the energy loss. It can be represented as

$$\tan\delta = \varepsilon''/\varepsilon \qquad [1.12]$$

Where ε′ is the relative permittivity or dielectric constant ε″ is the energy loss in the dielectric medium.

For good dielectrics tanδ is insensitive to the frequency of the applied field. Depending on the response of the dielectric materials to the electric field or stress or temperature and then nature of dielectric constants, the dielectric materials can be grouped into different classes, namely ferroelectric/antiferroelectric, piezoelectric or pyroelectric .Subsequently, the brief introduction of such special dielectric materials is provided.

1.8. Group of dielectric materials

1.8.1. Ferroelectrics

Ferroelectric materials are special type of polar materials where the spontaneous polarizations possess at least two equilibrium states. The direction of the spontaneous polarization vector may be switched between those orientations by an electric field which appear as hysteresis loop as shown in **Fig.1.6**. All ferroelectric materials are piezo and pyroelectric materials. Analogous to ferromagnetic materials, ferroelectric materials have no net polarization due to formation of domains under normal conditions. When positive electric field is applied to ferroelectric material, polarization increases to saturation value known as saturation polarization (Ps), where all the dipoles are aligned parallel to one another. When the field is removed the polarization decreases to a remnant value, (P_r) and a coercive field, (E_c) is required to return the polarization to zero.

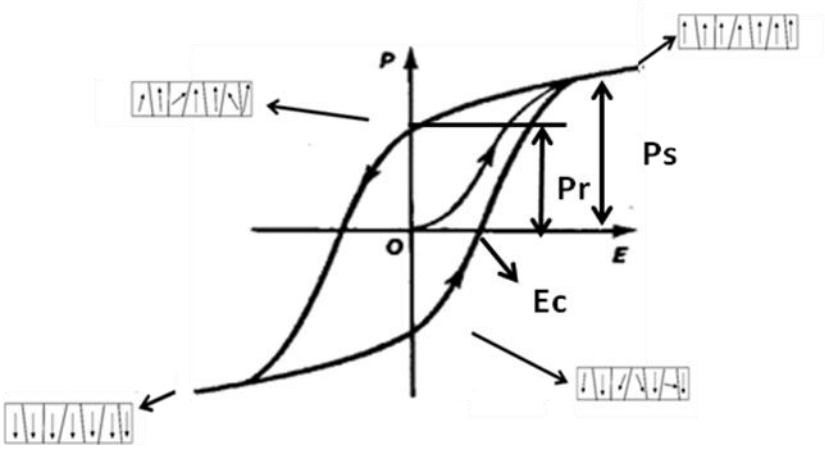

Fig.1.6: Hysteresis loop of ferroelectric material [45].

Depending on the structure of materials, the most of the polar dielectrics can be grouped to four classes as 1) Perovskite group, 2) Pyrochlore group, 3) tungsten-bronze group, 4) layered structure complex oxides group and 5) Hybrid composites group.

1.8.2. Perovskites

The most studied class of ferroelectric materials is perovskite group, which can also be divided into lead containing and lead free ferroelectrics. The dielectric properties of the ABO_3 perovskite materials have been investigated since long, due their ease of tunability by modifying the structure via A or B site substitutions as mentioned earlier. The average displacement of the Ti ions in $BaTiO_3$ along the c-axis from the centrosymmetric position gives the ferroelectricity. At the transition temperature (T_c~393 K), the tetragonal ferroelectric phase converts into paraelectric cubic phase. This transition temperature is also known as Curie temperature. Even though $BaTiO_3$ (BTO) has the easier synthesis methods, the narrow Curie transition

temperature (T_c) limits it to actual piezoelectric applications. The Curie temperature (T_c) of the $BaTiO_3$ can be increased by suitable substitution either at A or B site or at both sites. Unfortunately, although these type of materials have highest T_c, the relative permittivity at room temp is lower than the pure BTO [46]. Similar studies on isovalent ions with different radii such as Ca^{2+}, Ba^{2+}, Pb^{2+}, Cd^{2+}, Pr^{3+} and Mn^{3+} on the incipient ferroelectric, $SrTiO_3$ (T_c = 40K) indicates an increase in transition temperature [47]. In case of Pr doped $SrTiO_3$ ferroelectric behavior is observed [48]. Mn doped $SrTiO_3$ shows a broad dielectric maximum with relaxor like behavior [49] whereas Ba doped $SrTiO_3$ (BST) show adjustable Curie temperature. The T_C in BST varies almost linearly depending on Ba/Sr ratio [50]. The effect of B site substitution and simultaneous A and B site substitutions with the ions of different size and polarizability show similar onset of the ferroelectric phase transition have attracted much less importance. However, they are promising as superior lead-free or low lead content piezoelectric materials [51]. Another important series of ferroelectric material with perovskite structure are the niobates. $KNbO_3$ has an orthorhombic symmetry at room temperature. It is known that $KNbO_3$ and related compounds show a high curie temperature (T_c = 703 K). $(K,Na)NbO_3$ (KNN) is one of the best ferroelectric materials in the niobate series. Although, these materials have high curie temperature, the major problems associated with alkaline niobates are synthesis and sintering [52], due to sublimation of alkaline earth metal at high temperature leading to deviated initial stoichiometry. In order to minimize the above stated problems, several additives like CuO, MnO_2, and CeO_2 have been used [53]. These additives follow liquid phase sintering at lower temperature and facilitate densification. Alternate procedure involves the substitution at A and B site. For A site, several cations such as Li^+, Ba^{2+},

La^{3+}, Bi^{3+}, whereas for the B site Ti^{4+}, Sb^{5+} or Ta^{5+} are reported. Besides, use of powder sample of reduced particle size lead to sintered material at lower temperature [51,53].

1.8.3. Double perovskite

The simple perovskite structure (ABO_3) can be extended by substitutions, particularly of the A and B site cations. The substituent dopants may be located in the crystal lattice either randomly in the original perovskite structure, or the structure may become an ordered type in which the cations alternate regularly. Mostly only one cation is chosen for the A site substitution usually large species such as Sr^{2+}, Ba^{2+}, La^{3+}. Variation in the properties of double perovskite can also be studied by B site substitution. The most common substituents are the equiatom proportion of two ions with sufficiently different charge and size at B site, where charge or cation ordering is easily expected. The formula can be written as $A_2BB'O_6$ and can be described as the double perovskite. Structure of double perovskite is shown in the **Fig.1.7**

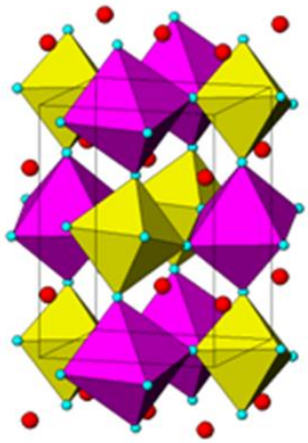

Fig.1.7: Schematic diagram of double perovskite structure. The octahedral units are shown for BO_6 and B"O_6 polyhedra. Isolated spheres are for A cation.

It has been observed that the charge difference between the B site cations is the most important factor for exhibiting cation order in perovskite structure. If the difference in the oxidation state is greater than two, highly ordered compounds are observed such as $A_2^{2+}B_1^{2+}B_{11}^{6+}O_6$ (eg; Sr_2FeWO_6) and $A_2^{2+}B_1^{1+}B_{11}^{7+}O_6$ (eg; Sr_2NaReO_6) compounds. If the charge difference is less than two, completely disordered or partially ordered structure is obtained. If the charge difference is equal to 2 then some of the compounds arrange in a partially, ordered structure (e.g. Sr_2FeSbO_6) and disordered structure can be achieved (e.g. Sr_2FeRuO_6). In the case of (La_2NiMnO_6) LNMO, it is expected that the Ni and Mn ions are respectively in the 2+ and 4+ oxidation states in the ordered phase, while both are in the 3+ oxidation state in the disordered phase. Ordering in perovskite also depends upon the some of the following factors as follows**:**

i. Size difference of the Cation

Cation ordering also depends on the size difference between the B site cations, if the size difference is higher, high degree of cation ordering can be expected. In case of Sr_2MTaO_6 (M^{3+}=Sc, Cr and Fe) even though charge difference of 2 for all, Sr_2ScTaO_6 exhibits more ordered structure followed by Sr_2CrTaO_6 and Sr_2FeTaO_6.

ii. Nature of the B site cation

Nature of the B site cation also has significant influence on cation ordering. $Sr_2FeSb^{5+}O_6$ has more cation order than $Sr_2FeTa^{5+}O_6$. This is due to preferential formation of Sb^{5+}-O-Sb^{5+} bonding. Since Sb^{5+} has only s and p orbitals, available for bonding, they preferentially form Sb^{5+}-O-Sb^{5+} bond whereas in case of Ta^{5+} d orbital are available for the bonding and hence it does not show preference for Ta^{5+}-O-Ta^{5+}

bond. Hence, a perfect intermixing of Fe^{3+} and Ta^{5+} is expected rather than Fe^{3+} and Sb^{5+}mixing. Hence, Ta^{5+} compounds are less ordered than the Sb^{5+} compounds. Along with the above stated points, the cation ordering also depends on the synthesis methods, annealing temperatures.

1.8.4. Tungsten–bronze structure

Tungsten-bronze structured materials have commercial importance as dielectric and ferroelectric materials. $PbNb_2O_6$ and $PbTa_2O_6$ [54] are among the first reported ferroelectric materials. $Sr_xBa_{1-x}Nb_2O_6$ ($0.25 \leq x \leq 0.75$) (SBN) [55] ceramics are ferroelectric with tetragonal tungsten bronze structure (TTB). The TTB structure consists of complex array of corner shared BO_6 octahedra as shown in the **Fig.1.8** Such unique arrangements of BO_6 octahedra, leads to interstitials available for different types of cations, thus the structure has the general formula $(A1)_2(A2)_4(C)_4(B1)_{12}(B2)_{28}O_{30}$. Filled bronzes have no vacant sites whereas unfilled bronzes have vacant C site and partially occupied A sites. In general, monovalent ions are filled in A1 site and B sites by tetra, hexavalent (i.e., Ti^{4+}, Nb^{5+}, Ta^{5+}, V^{5+} and W^{6+}). Often the C sites (being smaller), remain empty. Hence wide spectrum of Curie temperature and dielectric properties can be expected for the compounds of these families [56]. In case of $Sr_xBa_{1-x}Nb_2O_6$, the A1 site is occupied by both Ba and Sr ions whereas the A2 site is occupied by Ba ions and C is sites are empty. Out of six A1 and A2 sites only five positions are occupied by the Ba and Sr and one remains empty. Most of the physical properties including ferroelectric, pyroelectric and electrooptic can be altered by changing its composition. As the value of x increases in the composition, the transition temperature decreases linearly from 523K to 330 K. At

x~0.6, a crossover from normal ferroelectric to relaxor is observed in $Sr_xBa_{1-x}Nb_2O_6$ series [57].

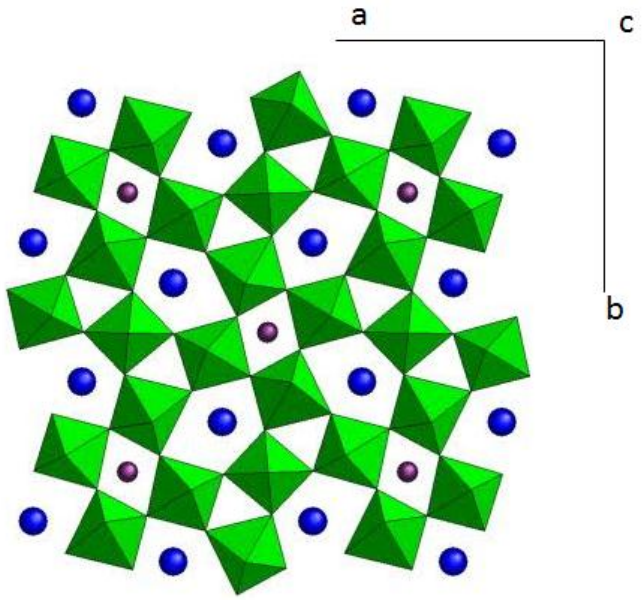

Fig.1.8: Schematic diagram of Tungsten-bronze structure. Isolated spheres are A1 and A2 cations in the octahedral frame of $B1O_6$ and $B2O_6$ units.

Doping of $Sr_{2-x}Ca_xNaNb_5O_{15}$ with La_2O_3 increases the dielectric constant to 1662 with transition temperature 471 K. $BaNb_2O_6$ has two polymorphic phases, tetragonal phase which transform to orthorhombic above 1473 K. The dielectric properties of each phase are significantly different; viz. tetragonal phase has high dielectric constant whereas low dielectric loss for orthorhombic phase is observed. Coates et al. showed that $BaNb_2O_6$ is ferroelectric with a transition temperature about 343K [58].

1.8.5. Layered structure (Aurivillius Structure)

Aurivillius type crystal structure was discovered by Aurivillius in 1949. The general formula of these structure is $Bi_2A_{n-1}B_n0_{3n+3}$ where n is the number of octahedral layers in the structure, A = Sr^{2+}, Ba^{2+}, Ca^{2+}, La^{3+}, Bi^{3+}, Pb^{2+}, K^{+}, B= cation suitable for octahedral configuration. Thus, B site cation is more size restrictive and is

typically occupied by Ti^{4+}, Nb^{5+}, Ta^{5+}, W^{6+}, Ga^{3+}, Al^{3+} and Mn^{3+} [59]. The structure consists of perovskite-like blocks of the form $(A_{n-1}B_nO_{3n+1})^{2-}$ sandwiched between two bismuth oxide $(Bi_2O_2)^{2+}$sheets. The number of perovskite layers can be 1, 2, 3 or more. Each can result in separate structure but perovskite layer and bismuth oxide layers are always in alternative position. Thus, it is possible to modify dielectric and ferroelectric properties by changing the chemical compositions. The effect of A site substitution is more useful than the B site substitution. Since cations at the B site have similar size, they do not play a major structural role in the polarization process. Most of the Aurivillius structures are orthorhombic at room temperature. After studying several isomorphic substitution Aurivillius developed the more general expression i.e., $(Me_2O_2)(Me^1_{m-1}B_nO_{3m-1})$. However in $Bi_4Ti_3O_{12}$, Me and Me' sites are occupied by the same ion. A large number of compounds with similar structure are known, some examples are $PbBi_2Nb_2O_9$ (m = 2), $BaBi_4Ti_4O_{15}$ and $CaBi_2Nb_2O_9$. $BaBi_4Ti_4O_{15}$ (BBT) has advantages over lead based materials as they have high fatigue resistance up to 10^{12} cycles. The majority of bismuth layer ferroelectrics have high Curie temperature (>673 K), low aging rate and low operational voltage [60].

1. 9. Polymer nano-composites

The need for pulse power energy storage systems with high energy density has led to the development of polymer composite systems. The electrical density of the dielectric material can be written as

$$E=1/2\ \varepsilon_0\ \varepsilon_{eff}\ E_b^2 \qquad [1.13]$$

Where, ε_{eff} is the effective dielectric constant and E_b is dielectric breakdown strength. Therefore, it is essential to develop dielectric materials which can meet the demands

of higher dielectric constant to increase the device capacitance and higher dielectric breakdown strength which will allow higher device operating voltage. Along with these two demands, development of low cost dielectric materials is also essentials. Generally organic polymers are low in cost but dielectric constant of these materials is also very low. The dielectric constant of the polymers can be increased by 1) introducing ceramic filler with high dielectric constant such as $BaTiO_3$ [61], $CaCu_3Ti_4O_{12}$ (CCTO) [62], $Pb(Mg_{1/3}Nb_{2/3})O_3$-$PbTiO_3$(PMNPT) [63], $Pb(Zr_xTi_{1-x})O_3$ [64], $Al@Al_2O_3$ [65], Al@C [66] into the polymer matrix. In order to obtain very high dielectric constant, large amount of ceramic fillers are required. In this process, at very high concentration of the ceramics, pores, voids, and imperfections are developed in the matrix which results in lowering the breakdown voltage. In addition, the ceramic particle loaded polymer loses its mechanical flexibility and poor quality composite films are obtained. 2) Another way is to prepare percolating systems by incorporating conductive fillers such as carbon black, carbon nanotubes, conductive fibres, or metal particles into the polymer matrix [67]. The effective permittivity is proportional to the filler (nano particle) loading. At higher filler loading, leakage current increases due to formation of conductive paths by conductive filler at percolation threshold. These problems can be avoided by the good dispersion of the nanoparticles of conductive filler in the polymer matrix. It can suppress the polarization losses generated from the interfacial moieties and also decreases the leakage current of device. This can be achieved by the effective filler shape and surface modification of the nanoparticles.

Polymer film	Dielectric constant	Maximum operating temperature (K)	Breakdown voltage (V/µm)	Dissipation factor % at 1 kHz	Energy density (J/CC)
Polypropylene (PP)	2.2	378	640	<0.02	1-1.2
Polycarbonate (PC)	2.8	398	528	<0.15	0.5-1
Polyester (PET)	3.3	398	570	<0.5	1-1.5
Polyvinylidene fluoride (PVDF)	12	398	590	<1.8	2.4
Polyethylene naphlate (PEN)	3.2	398	550	<0.15	1-1.5
Polyphenylene sulfide (PPS)	3.0	473	550	<0.03	1-1.5

Table 1.1: Breakdown voltage of different polymers [68].

These polymer nano-composites have many practical applications such as ferroelectric media for flexible FeRAM devices, integral thin film capacitors, electrostriction systems for artificial muscles and electric stress control devices. Some of the dielectric polymers for capacitor applications are shown in the **Table 1.1.**

1.10. Relaxor ferroelectrics

Relaxor ferroelectrics differ from the normal ferroelectrics in their ferroelectric transition temperature. The typical characteristics of relaxor are [69]:

- No distinct domain structure within the phase-transition temperature range.
- Dielectric response with respect to temperature does not follow the classical Curie-Weiss law. $\varepsilon_r = C/(T - T_c)$

Where, ε_r is the relative permittivity. The relaxor ferroelectrics are characterized by broad maximum and frequency dispersion of the dielectric permittivity at temperature around and below the T_m and its magnitude (ε_{max}) decreases with increasing frequency.

- There is no clearly defined hysteresis loop observed in the phase-transition range.
- Presence of a diffuse phase transition temperature.

Various models have been proposed for the possible mechanism of the dielectric relaxation. From the studies of Smolensk et al., it was thought to consist of chemical inhomogeneity with different concentration of dopants in micro regions gives rise to different curie temperatures [70]. A super-paraelectric model for the relaxor ferroelectrics was proposed by Cross which suggest that in the high temperature region, the micro polar regions are being dynamically disordered by thermal motion. The height of the barrier between domain states is directly proportional to the volume of the polar micro region. The polarizations with low thermal energies will be trapped into a preferential orientation and form a polar micro domain or cluster [71].This model is extended by Veihland *et al.* where the dispersion of the maximum dielectric constant temperature T_{max}, in terms of the AC frequency is described by the Vogel-Fulcher (V-F) relationship [72].

$$f = f_o \exp\left[-E_a/(T_{max}-T_f)\right] \qquad [1.14]$$

Where, f_o, E_a , and T_f are the fitting parameters.

The T_f is described as a static freezing temperature.

Relaxation behavior is mostly found in the lead based perovskite oxides. In case of $PbMg_{1/3}Nb_{2/3}O_3$ (PMN) disorder in the lattice brought by differences in ionic radii (0.64 Å vs. 0.72 Å), valence (5+ vs. 2+), and electronegativity (1.6 vs. 1.2 on the Pauling scale) between Mg^{2+} and Nb^{5+} ions on the B site, introduce local ordering charge fluctuations, which produce dipolar defects and results into relaxor behavior. In lanthanum modified lead zirconium titanate (PLZT), the substitution of lanthanum for Pb^{2+} produces randomly distributed Pb^{2+} vacancies and at high concentration of vacancies, relaxation behavior is observed. In case of $KTaO_3$ substitution of Nb^{3+} for Ta^{3+} and Li^{+} for K^{+}, produces off-site dipolar defects which lead to a relaxor state at low concentrations. Other lead perovskite oxides such as lead magnesium niobate (PMN), lead tin niobates (PSN), lead scandium tantalite (PST), lead indium niobates (PIN) also have the relaxor behavior.

1.11. Scope of the present thesis

In the aim of the present thesis, two different types of materials, either with fluorite or perovskite related structures, have been investigated for oxide ion conduction or dielectrics properties and they are explained sequentially. In the aspect of oxide ion conductor, several compositions such as $Ln_{1-x}Bi_xO_{1.5}$ ($0.00 \leq x \leq 0.50$) where Ln = Dy and Yb and pyrochlore-type $Pr_{2-x}Ca_xZr_2O_7$ ($0.00 \leq x \leq 0.20$) have been investigated and the results are explained in Chapters 3 and 4. In the interest of dielectric materials, perovskite related $Pr_2Ti_2O_7$ and Ln_2CoMnO_6 (Ln = Eu and Y) have been investigated and they are explained in Chapters 4 and 5. In addition, several organic and inorganic hybrid materials, like PVDF-M (M = Co, Ni) have been prepared and their electrical properties are explained in Chapter 6. Besides, electrical properties of some complex oxides like $InVO_4$, $CoFe_2O_4$ are also investigated and are

explained in Chapter 7. Each chapter is organized with the introduction relevant to the particular subject of the study and the scope for further study, followed by the details of preparation, characterization, and property evaluation of individual system. Finally all the results of the studies are summarized in Chapter 8.

CHAPTER 2
EXPERIMENTAL TECHNIQUES

2.1. Introduction

In this thesis preparation of various ceramic oxides and investigation of their electrical properties are focused. In this chapter, different types of preparation methods are briefly discussed. The conventional solid state, gel combustion methods were used to prepare ceramic oxides, while polyol route was adopted for preparation of metal nanomaterials. The prepared materials have been characterized by several analytical techniques, like X ray diffraction (XRD), Raman spectroscopy, FT-IR Spectroscopy, Scanning Electron Microscopy and Mössbauer spectroscopy. The functional properties of the prepared materials have been investigated by using Impedance Analyzer. The salient principle and scope of different experimental methods used are also discussed in this chapter.

2.2. Synthesis methods

Preparation of materials is the foremost aspect followed in material research. It is well known that the method of preparation is often selected depending on the nature of desired materials and their final applications. The preparation methods can be grouped as either high temperature ceramic methods or low temperature soft chemical methods. Each preparation method has certain advantage and disadvantage and thus adoption of a judicious preparation method is solely dependent on the desired products. Some of the adopted general methods of preparation of materials are explained below.

2.2.1. Solid-state reaction route

The solid-state process is a primitive, most conventional and widely used method to prepare polycrystalline ceramic oxide materials. It involves the mechanical mixing of the stoichiometric amounts of solid constituents (oxides/carbonates), repeated grindings and annealing at elevated temperatures, generally over a long

duration [73]. The formation of product and progress of the reaction is based on the diffusion of ions in solid state, which is an inherently slow process. The temperature chosen for the solid state reaction mainly depends upon the melting point of the solid reactants. Moreover, the ceramic oxides are high melting solids and hence, the reaction rate becomes extremely slow at lower temperature. Being the solid state reaction is a diffusion controlled process, the reaction rate follows a parabolic rate law as given below.

$$\frac{dx}{dt} = k.x^{-1} \qquad [2.1]$$

Where, x is the concentration of product (thickness of the product layer), t is the time and k is a constant. Since the reactants are mostly high melting refractory solids, only at high temperature ions can jump off from their normal lattice sites and diffuse through the crystals. Compared to solution processing, the solid state reaction occurs from a heterogeneous medium and thus they depend on several factors of the reactants. At a particular temperature, the reaction rate is fast in the initial stage and then progressively become slower due to the increasing barrier product layer in between the reactants which hinders the direct interaction of the two reacting solids. Usually, the solid state reactions are carried out by grinding the reactants to make a thoroughly mixed mixture of component solids. It can be mentioned here that the reaction rate depends to a large extent on the particle size of reactants, the degree of homogenization achieved on mixing and the intimacy of contact between the grains as well as annealing temperature. The area of contact between the reacting solids (their surface area) is also an important factor for enhancing the reaction of solids. The particle size of the reactants thus plays an important role in the solid state reactions, as

the decreasing the size, increases the surface area and hence increases the reactivity of the reactant particles. In order to increase the surface area, the reactants are crushed into finer powder. Further to increase the area of contact, the mixture of reactants are usually pressed into pellets. Most commonly, the repeated grinding and pelletizing after a heat treatment is essential for completion of the reaction. This is to bring fresh surfaces in contact and also to reduce the sizes of the reactant powders. Though the desired composition and phase can be managed by such solid state reactions, the process is often energy intensive and time consuming.

2.2.2. Soft chemical routes

Soft chemical routes are based on controlled chemistry of reactant ions. The problem of reactant heterogeneity of solid state reaction can be avoided by these soft chemical methods, as prefect homogeneity at molecular level is achieved in solutions state. The soft chemical methods employ a solvent medium from which, the required product can be isolated by precipitation, solvent evaporation etc. In the present work, two different soft chemical routes have been employed to prepare polycrystalline ceramic materials and metal nanoparticles. A detailed description of each of these synthesis methods is given as follows.

i. Gel combustion method:

Gel-combustion is an exothermic redox reaction between an oxidant viz., metal nitrate and a fuel such as citric acid, glycine, etc. The final product obtained by the combustion process has highest degree of phase purity and improved powder characteristics like, higher surface area, narrow size distribution of nanoparticles and better sinterabilty. In this thesis, nanocrystalline powder samples were prepared by gel-combustion process by using glycine as the fuel. Glycine (NH_2CH_2COOH) is a

zwitter ion forming compound having a carboxylic acid group at one end and amino group at the other end [74]. It is a low cost fuel which effectively complexes the metal ions of varying ionic sizes, preventing their selective precipitation. The powder properties such as crystallite size and surface area of the combustion-synthesized nano powders can be altered by changing the fuel content with respect to the oxidant. The amount of the fuel in the combustion reaction is fixed on the basis of principle of propellant chemistry [75]**.** According to the principle of propellant chemistry, for a stoichiometric redox reaction between a fuel and an oxidizer, the ratio (φ) of net oxidizing valence of metal nitrate to net reducing valency of fuel should be unity [76]. In such case the ratio of oxidizing-to-reducing valencies is called as stoichiometric ratio. The oxidant-to-fuel ratio less than that of stoichiometric ratio is termed as the fuel-deficient ratio and any ratio greater than this is termed as fuel-rich ratio. This oxidant-to-fuel ratio is an important parameter for gel combustion process as it governs the exothermicity of the combustion reaction and hence the flame temperature which thus governs the powder properties of final product. The typical chemical processes of a gel combustion reaction are explained below.

(a) Gel formation and combustion

The first step of the gel combustion is gel formation. In this step, the nitrate/oxynitrate salts of the metals of interest, in a required molar ratio, are mixed together in an aqueous medium to produce a transparent mixed metal-nitrate solution. Nitrates present in the reaction medium fulfill the requirement of oxidant by providing the oxygen for combustion of the fuel. Appropriate amount of suitable fuel (glycine, citric acid or urea) is then added to this mixed metal nitrate solution. The aqueous solution of fuel and oxidants is then dehydrated on a hot plate (at about 353-373 K)

which transformed to a viscous liquid (hereafter termed as gel). A pictorial representation of the gel formation step is depicted in **Fig.2.1a**. It may be noted that the thermal dehydration process is rather an important step, because any excess water left behind would lead to a sluggish combustion, deteriorating the phase purity and powder quality. The formation of the transparent viscous gel depends on the nature of the fuel, its amount and pH of the starting solution.

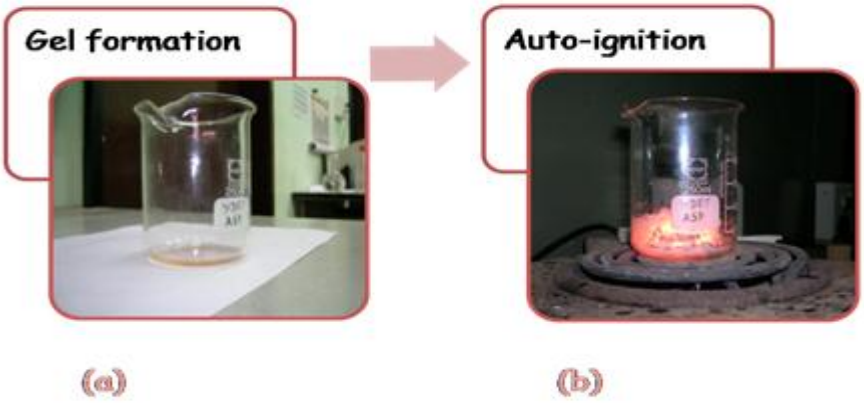

Fig.2.1: Steps involved in the gel-combustion method; (a) gel formation (b) auto ignition.

The obtained gel is further heated at a higher temperature (473-523K) where the combustion reaction is initiated or triggered. The very high exothermic decomposition of the fuel-oxidant precursor generated during the combustion reflects in the form of flame or fire and this processes is termed as auto-ignition (shown in **Fig.2.1b**). The auto-ignition is a very short-lived phenomenon as the flame persists for only about few (5-10) seconds. At this stage, the exothermic decomposition of fuel-oxidant results in a large voluminous powder. During the auto-ignition, gaseous products are evolved which dissipate the heat and fragment the product particle. Thus, the solid residual products are obtained as ultra-fine powders of oxide ceramics. However, the resultant product may be the desired phase, or semi-decomposed precursor having a

considerable amount of carbonaceous residue, depending on the nature and amount of fuel used.

(b). Advantages of the gel combustion process

1. Preparation of the precursor in the first step prevents the random redox reaction between a fuel and an oxidizer by the formation of homogeneous gel precursor. Thus, the possibility of local variations in the characteristics of the combustion-synthesized powders is very low.

2. As fuel and oxidant decompose, the final product does not require any special processing of the precursor such as washing etc.

3. Even though the time for which auto-ignition exists is very small, i.e. only for few seconds, most often the heat of combustion or flame temperature generated within this time is sufficient to produce the required phase. Hence, the combustion technique can be considered as time saving low temperature synthesis, which is not highly energy intensive.

(c). Precautions and limitations

Although the combustion process is known for its simplicity, few precautions are necessary while performing the experiments.

1. It is always advisable to perform the combustion process in a wide mouthed apparatus, with large volumes to avoid poor heat dissipation and for easy liberation of the gaseous products. Narrow opening container may lead to an explosion, due to the large swelling of viscous precursor and also the large volume of gaseous products eliminated, in addition, to the high exothermicity.

2. Combustion is a vigorous and spontaneous process wherein large amount of heat is released in a very short duration. Hence there must be an arrangement for safe ventilation which facilitates safe release of the gaseous products.

ii. Polyol method:

Polyol method is a very promising technique for the preparation of magnetic nanoparticles. In polyol process, polyalcohol not only acts as a solvent, but also as a mild reducing agent. When coupled with a base, it acts as a perfect medium for the reduction of metal salt precursors. In this polyol method the precursor salts are dispersed in a liquid polyol. The suspension is then heated up to reflux. During the polyol reaction, inorganic reactant precursor reacts with diols or alcohols, forming an intermediate which are reduced to form metal nuclei, and then metal nanoparticles. The nanoparticles obtained in the polyol method have surface adsorbed glycols and thus reduces the hydrolysis of fine metal nanoparticles which often occurs in the aqueous reaction process. Various polyols such as ethylene glycol, diethylene glycol, trimethylene glycol, propylene glycol and butylene glycol can be used in the polyol process. The polyol reaction can be followed by studying the a) Nucleation b) Surfactants c) Growth parameters. The adsorbed polymers on the surface of the nanoparticle lower the surface energy and develop a barrier for the aggregation of nanoparticles. Various polyols used for the reduction of metal salt precursors are shown in the **Fig.2.2.**

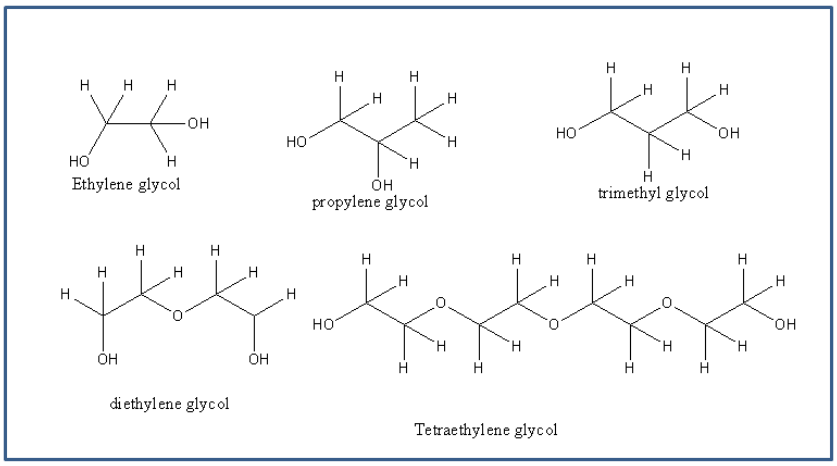

Fig.2.2: Molecular structure of various polyols used for the reduction of metal salt precursors.

2.3. Characterization techniques and instrumental details

The prepared materials have been thoroughly characterized prior to measurement of any of their properties. The phase and structural characterization of the materials have been carried out by powder XRD and vibrational spectroscopic methods, while morphological properties have been investigated using Scanning Electron Microscopic technique. Several supporting techniques, like Mössbauer, X-ray photoelectron spectroscopy (XPS) and Extended X-ray Absorption of Fine Structure (EXAFS) have been used to understand the local structure and oxidation states of various ions in certain system. In the following section the brief overview of the techniques use in this thesis work is explained.

2.3.1. XRD-technique

X-ray diffraction (XRD) was used for characterization as well as for detailed structural elucidation of the material. As the physical properties of solids (e.g., electrical, optical, magnetic, ferroelectric, etc.) depend on atomic arrangements of materials, determination of the crystal structure is important. The d spacing between

various planes in the unit cell of a crystal is of the order of wavelength of X-rays. Hence, XRD patterns are used to establish the atomic arrangement or structure of the materials. X-rays are produced when high-energy electrons, typically 30 keV, are bombarded at a metal target which is usually made of copper as shown in the **Fig.2.3**

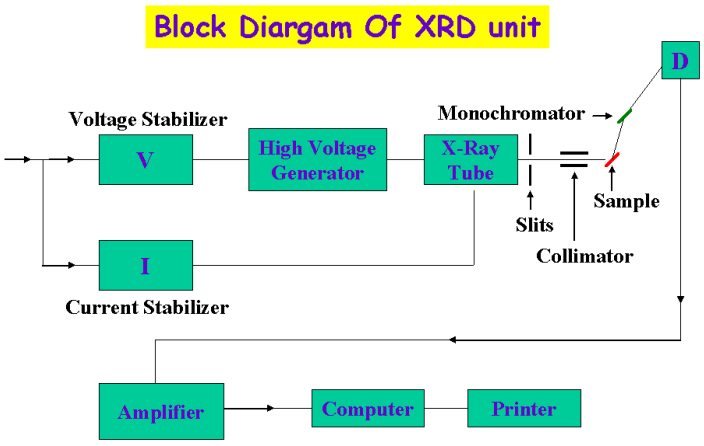

Fig.2.3: A typical block diagram of a powder XRD unit

From, this it clear that the prime components of a powder diffractometer is the source of X-ray, usually called x-ray tube, and the sample chamber and a goniometer for measuring the angles followed by a x-ray detector for measuring the intensity of diffracted X-ray beam. Besides there are several slits to reduce the divergence of the incident and diffracted beam and monochromator are also used**.** The most common method to generate X-ray is by the Bremsstrahlung process, where high energy electrons strike the metal target getting slowed down. In addition, if the energies of incident electron have sufficiently energy, they can ionize the atoms of the target by knocking an electron from inner orbital of atoms. Such ionization process leaves a hole in the inner orbital. The electron from a higher energy orbit or shell will jump down to replace the lost electron and the excess energy is released as monochromatic X-rays. In the overall process of interaction of electron with atoms results in X-ray

spectrum which consist of white radiation of broad spectrum of wavelengths, and a number of fixed, monochromatic wavelengths. Normally for X-ray diffraction, monochromatic radiation is required. In case of Cu target a transition from the 2p orbital of L shell to the K shell produces a Kα (λ = 1.5418 Å) X-ray, while the transition from 3p orbital of M shell to the K shell produces a Kβ (λ = 1.3922 Å) X-ray. The Kα radiation is more intense than the Kβ. Slight difference in energy for the 2 spin states causes the splitting of Cu Kα into Kα1 and Kα2. The more intensity Kα is used for the diffraction measurements and remaining unwanted radiations are filtered off by using Ni filter.

When X-ray interacts with the atoms in crystal they produce diffraction pattern. Schematic representation of the X-ray diffraction process is illustrated in **Fig.2.4.**

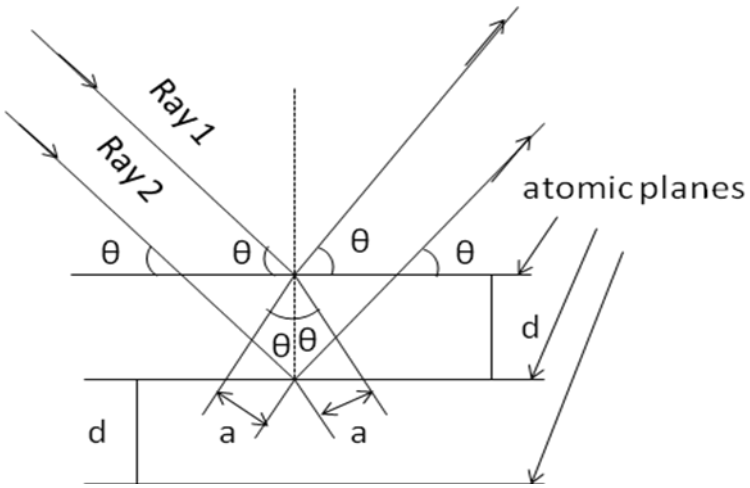

Fig.2.4: Schematic diagram of X-ray Diffraction process in crystal.

The X-ray (ray-1 of schematic-2.3 can interact with the upper part of the atomic planes and reflect with angle θ, equal to its angle of incidence. The ray-2 can travel down to the inner layer of atoms and then reflects back at an angle θ. In this process ray-2 travel extra distance equivalent to 2a. For this wave to be in phase with the wave

which reflected from the surface, the extra path difference should be a whole number multiple of wavelength. Therefore Bragg's equation can be written as:

$$n\lambda = 2d \sin \theta \qquad [2.2]$$

where, λ is the wavelength of the X-ray, θ is the angle of the diffracted X-ray coming out of the crystal, d is the inter spacing between the planes.

i. Powder XRD instrumental details

X-ray diffraction experimental setup consists of a source of X-rays and a detector for the detection of diffracted X-rays. X-rays are produced by bombarding high-speed electrons on a metal target in a sealed X-ray tube. It should be mentioned here that only a very small fraction of electron energy is used for the X-rays production and the rest is lost in heating the target element. During this process, the target element gets heated and hence, it requires a continuous cooling. The X-rays are emitted in all the directions and hence, slightly divergent X-ray beams are allowed to emit in a particular direction usually though a beryllium window (which allows to pass out the X-ray beam). The background and β-radiation are filtered using β filters, usually a thin plate of element with atomic number one to two unit below than that of the target element. The beam of X-ray passes through the soller and divergence slits and then fall on the sample. The fine grains of sample are generally spread uniformly over a rectangular area of a glass slide. The sample is adhered to the glass slide either using binders like collodion or grease or wax. The diffracted X-rays beams from the sample passed though several slits, like soller and receiving slits and then fall on a monochromator before detection. The monochromator separates out the fluorescent radiation as well as stray radiation scattered by the sample and gas molecules in the

sample chamber. The details of the typical X-ray spectra and the X-ray production and are explained in several monographs [77].

XRD can be used for several purposes, like 1) calculation of unit cell parameters, miller indices 2) identification of types of phases present in the material 3) to determine the phase purity of the sample 4) evaluation of the average crystallite size, etc.

ii. Lattice parameter determination

Theoretically, the lattice parameters are determined from the relationship between the distance, *d*, of two adjacent net planes and the (h k l) Miller indices of the reflection planes and is given by the equation

$$\frac{1}{d^2}=\frac{\frac{h^2}{a^2}Sin^2\alpha+\frac{k^2}{b^2}Sin^2\beta+\frac{l^2}{c^2}Sin^2\gamma+\frac{2hk}{ab}(Cos\alpha\cdot Cos\beta-Cos\gamma)+\frac{2kl}{bc}(Cos\beta\cdot Cos\gamma-Cos\alpha)+\frac{2lh}{ca}(Cos\gamma\cdot Cos\alpha-Cos\beta)}{1-Cos^2\alpha-Cos^2\beta-Cos^2\gamma+2Cos\alpha\cdot Cos\beta\cdot Cos\gamma} \quad [2.3]$$

$$V = abc\,(1-\cos^2\alpha-\cos^2\beta-\cos^2\gamma+\cos\alpha\cos\beta\cos\gamma)^{1/2} \quad [2.4]$$

where, V = volume of the unit cell a, b, c, α, β and γ are lattice parameters and h, k, l are the Miller indices. To solve crystal structures, quantitative measurements of intensity are necessary. Intensity of these diffracted beams depends on the atoms type and positions within a unit cell. The intensity of a diffracted beam, I_{hkl}, can be expressed as:

$$I_{hkl} \propto F^2_{hkl} mALP \quad [2.5]$$

F_{hkl} = structure factor, which can be written as;

$$F_{hkl} = \sum f_n \, exp\,[2\pi i(hx_n+ky_n+lz_n)]\,[-B_n sin^2\theta/\lambda^2] \quad [2.6]$$

Where,

f_n = atomic scattering factor of the n^{th} atom in the unit cell with the coordinates (x_n, y_n, z_n). It is directly proportional to atomic number, Z.

m = multiplicity factor the multiplicity factor takes into account the number of equivalent reflections that give rise to a single powder line.

L = Lorentz factor

The Lorentz factor is the correction for variation in the probability of a Bragg reflection occurring within a given diffraction angle. It corrects for the geometry of the diffractometer and is a simple function of θ [78].

A = absorption factor.

This factor accounts for absorption occurring within the sample, equating the proportion of incident and diffracted X-rays absorbed. The amount of radiation absorbed depends upon sample composition, diffraction angle and thickness, and varies according to the geometry of the diffraction method used.

P = polarization factor

This factor corrects for the unpolarized nature of X-rays produced by the X-ray tube. Diffracted beams are more intense, when the electric field vector is parallel or anti-parallel to the sample and are weakest when perpendicular. This correction is also a simple function of θ.

B_n = isotropic temperature factor

This accounts for the effect of thermal motion on intensity and is proportional to the mean square oscillations of the atoms, u_{iso}

$$B_n = 8\pi^2 \langle u^2_{iso} \rangle_n \qquad [2.7]$$

Another important method used to quantify each of the phases present is the Rietveld refinement method. Rietveld refinement analysis of X-ray powder diffraction data are used to refine structural parameters, such as atomic coordinates, occupancies, lattice

parameters, thermal parameters, etc. In the Rietveld refinement method experimental data are compared with theoretical line profile and intensity. The obtained theoretical proposed structure refined using a least-squares approach. Best fit model structure, achieved by adjusting parameters of the proposed structure, in order to minimize the difference between the experimental and calculated intensities.

iii. Determination of the average crystallite size

In order to determine crystallite size, XRD method is one of the simpler and best methods which can be used in the range of 2-100 nm. The diffraction peaks of the nano materials are broadened. The broadening of the Bragg peaks is due to the development of the lower crystallite size and internal stain. If the studied crystals are free from defects and micro-strains, peak broadening can be attributed to average crystallite size and diffractometer characteristics. From the broadness XRD peaks, the average crystallite size can be calculated by using Scherer's relation.

$$D = 0.9\ \lambda/\beta\cos\theta \text{ or } K\ \lambda/\beta\cos\theta \qquad [2.8]$$

Where, λ is wavelength of X-ray, β is FWHM in radian, θ is the Bragg angle and K is the Scherer constant. D is the crystallite size.

In the present work, a Philips 1710 diffractometer and rotating anode based X-ray diffractometer (Rigaku, Japan) were mostly used for the characterization process. Philips-1710 diffractometer is based on the Bragg-Brentano reflection geometry. The Cu Kα emissions from sealed tube are used as the incident beam. In the former set up, the diffracted beam is monochromatized with a curved graphite single crystal. The Philips (PW-1710) diffractometer has a proportional counter (Argon filled) for the

detection of X-rays where as rotating anode diffractometer has scintillator detector. The X-ray tube rating was maintained at 30 kV and 40 mA in both units.

2.3.2. X-ray photoelectron spectroscopy (XPS)

The basic components of XPS are X-Ray source, sample stage and electron analyser combined with detection system as shown in the Fig.2.5. XPS measurements are conducted in ultra-high vacuum (UHV). Interaction of sample with X-rays of sufficient energy emits the photoelectrons. Electron analyser measures the kinetic energy of the emitted electron. There is also a detector which measures the number of photo electron emitted.

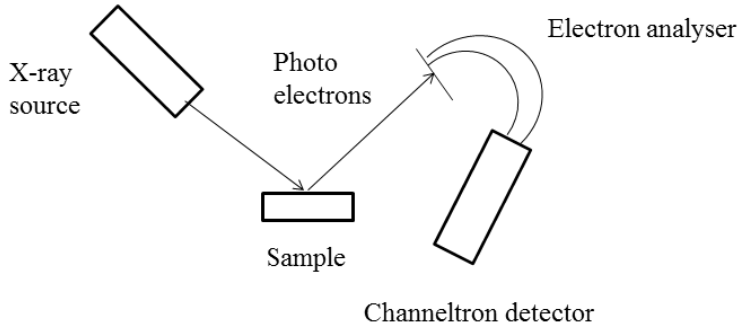

Fig.2.5: Schematic diagram of a XPS unit [79(a)]

When X-ray of energy higher than 1 keV exposed on the sample, electrons are liberated from the specimen sample by photoemission process. For each and every element, there will be a characteristic binding energy associated with each atomic orbital In photoemission process, atom absorbs the photon energy hυ, results the ejection of the core level electron. The characteristic parameter for the electron is its binding energy. The relation between these parameters is given by Eq. (2.9)

$$E_B = h\nu - E_K - W \qquad [2.9]$$

Where, E_B and E_K are the binding and the kinetic energy of the emitted photoelectron respectively, W is the spectrometer work function and hν is the photon energy. The excitation by X-rays may also cause electronic energy transitions within the atom that leads to emission of Auger electrons, which also appear in the spectra. The Auger electrons are not the main concern of XPS. The electrons emitted in XPS process contain information regarding electronic structure, chemical oxidation state and atomic composition. Thus, the XPS can provide the information on the shell structure. Since electrons emitted from atoms lying in layers deeper within the material have small chance for reaching the surface and being detected. Hence, this technique provides information about the atoms present within few uppermost atomic layers.

Since each element have different electronic binding energies, XPS can be used for elemental analysis. The binding energy of an electron is influenced by chemical environment around and oxidation state of the concerned atoms, the photo electrons from atoms of different binding states appear as generate, i.e. slightly shifted peaks. As a rule, binding with elements of higher electronegativity will shift the peaks to higher binding energy values and atoms with higher oxidation state shift the peak to higher binding energy values. Therefore, the technique is also useful for analyzing chemical bonding.

2.3.3. X-ray absorption spectroscopy

X-rays have sufficient energy to eject a core electron from an atom. Thus, X-ray intensity is decreased while transmitting though a material. Absorption of X-ray in a material depends on the elements present in it and energy of the incident X-rays.

The number of X-ray photons that are transmitted through a sample can be written as

$$I = I_0 e^{-\mu(E)t} \qquad [2.10]$$

$$\mu(E)t = -\ln I/I_0 \quad [2.11]$$

Where, I = intensity transmitted through the material, I_0 = X-ray intensity hitting the material, μ(E) = absorption coefficient, t = thickness of material the beam is passing through.

μ depends strongly on X-ray energy E, atomic number Z, density ρ and atomic mass A;

$$\mu \approx \rho Z^4/AE^3 \quad [2.12]$$

The plot of the mass absorption coefficients of matter against the incident X-ray energy or wavelength is called X-ray absorption spectrum (XAS). XAS gives the information about electronic and structural properties of a particular element in a material. Usually X-ray absorption spectroscopy (XAS) measures the variations in the X-ray absorption coefficients at energies near and above an X-ray absorption edge of an element, the total spectrum can be broken into two categories [79(b)];

1) XANES = X-ray Absorption Near-Edge Spectroscopy

2) EXAFS = Extended X-ray Absorption Fine Structure

i. Extended X-ray Absorption of Fine Structure (EXAFS)

The photoelectrons emitted from an atom due to the interaction of incident X-ray beam are scattered back by the surround atoms. The interference of the electron wave of the emitted and back scattered electrons interferes with the incident X-ray wave which results in a variation in the X-ray absorption pattern of the atom. When the electron waves of the outgoing and backscattered electrons are in phase, which happens with the X-ray having energy similar to absorption edge, the absorption of X-ray is maximum and appeared as a local maximum in the X-ray photo absorption spectra [79b]. At higher X-ray energy, the photoelectron has greater kinetic energy

and thus a shorter wavelength, resulting in destructive interference and a local minimum in photo absorption cross section. The physical origin of EXAFS is thus related to the electron scattering process and hence can provide information on the atomic species, arrangements of atoms and the bonding mechanisms. The schematic of EXAFS instrument is shown in Fig.2.6.

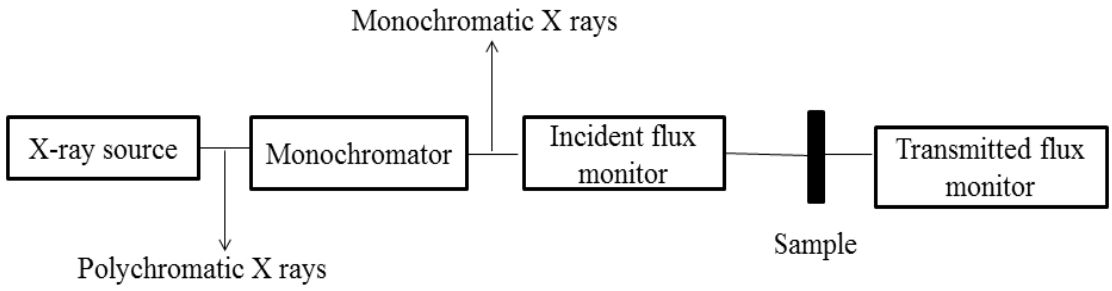

Fig.2.6: Schematic diagram of an EXAFS instrument [79(c)]

The synchrotron X- ray source is generally used in EXAFS, which gives the full range of X-rays and a monochromator uses the Braggs diffraction condition to select the particular energy. The monochromatic X-rays are then allowed to pass through the sample, which absorbs some of the incident electrons. The transmitted and incident X-ray fluxes are monitored, by gas ionization chambers.

In the present thesis certain XANES experiments have been carried out to ascertain oxidation states. The absorption experiments were carried out in transmission mode at the EXAFS beam line (BL-9) at the INDUS-2 synchrotron source at the Raja Ramanna Centre for Advanced Technology (RRCAT), Indore, India.

2.3.4. Vibrational spectroscopy

The vibrational spectroscopy is the most widely used spectroscopic technique for characterization of structural and in particular the local structure around an atom in a material. Mainly these methods are based on the interaction of electromagnetic

radiation with the different vibrational energy level in a molecule and thus they belong to molecular spectroscopy branch of spectroscopy.

In molecule, the total energy can be given as sum of all contributing components as given below

$$E = E_{rot} + E_{vib} + E_{elec} + E_{tran} + E_{spin} + E_{nucl}. \quad [2.13]$$

Interaction of electromagnetic radiation with a molecule can result in transition between various quantized energy states. The resonance between energy states of a molecule and electromagnetic wave occurs when energy of electromagnetic radiation (hν) matches to the difference between initial and final quantized energy states of molecule (ΔE) [80]

$$\nu\ (Hz) = \frac{c}{\lambda} \quad [2.14]$$

Where, c = velocity of light, while the λ and ν are wavelength and frequency of electromagnetic radiation, respectively.

Depending on the absorption region of electromagnetic radiation and energy state transition, different sorts of structural information can be obtained from such vibrational spectroscopy. When Infrared (IR) radiation interacts with the molecule or crystal lattice, transition between vibrational states of the atoms occurred by absorption of equivalent energies. These absorptions appeared as bands in the spectra which are generally presented in the unit wavenumber υ in cm^{-1}. The range of IR absorption spectra is 200-4000 cm^{-1}. The wave number of absorbance can be calculated by the harmonic oscillator model.

$$\upsilon = 1/2\pi c\sqrt{f/\mu} \quad [2.15]$$

Where c is the light velocity, f is the force constant in the atomic scale and spring constant for the macroscopic model and μ is the reduced mass defined by

$$\mu = m_A m_B / m_A + m_B \qquad [2.16]$$

Therefore, wavenumber of absorption is related to the force constant and reduced mass. Since the force constant is directly related to the chemical bond strength, the groups with stronger chemical bond and smaller the reduced mass m (mass effect) show absorption band at higher wavenumber. Assuming the molecule in the harmonic oscillator, the energy of vibrational levels can be written as below.

$$E_v = \left(V + \frac{1}{2}\right) h\omega \qquad [2.17]$$

The allowed transitions in between levels are defined by selection rules. Selection rule for allowed transition is $\Delta \upsilon = \pm 1$.

Modern IR instruments are based on Fourier transformation method, where the signal to noise ratio is improved considerably. In the FTIR instrument, all the frequency are used simultaneously to excite the all the vibrational modes of different types of bonds present in the sample.

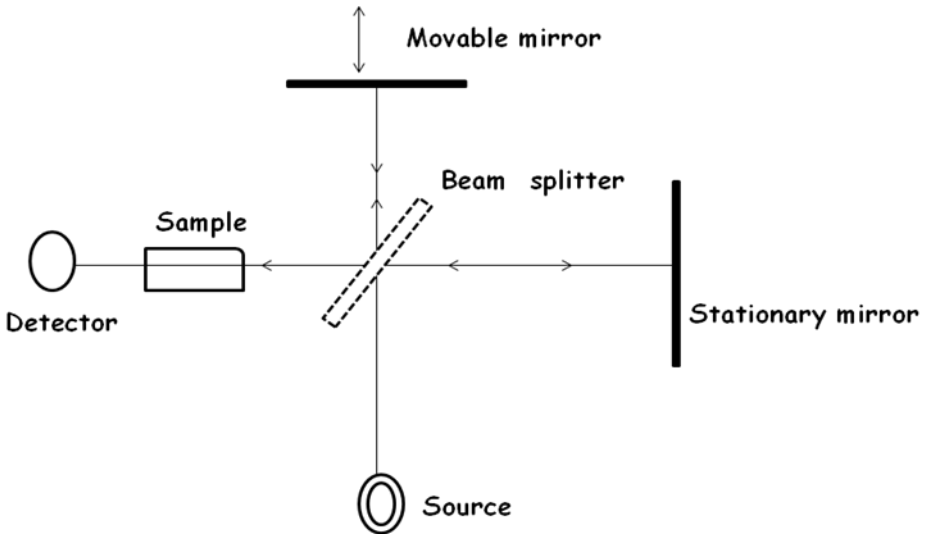

Fig.2.7: Schematic diagram of FTIR instrument [81]**.**

The construction of FT-IR instrument is based on Michelson interferometer and the typically ray sketch FT-IR is shown the **Fig.2.7**. The interferometer consists of a beam

splitter, a fixed mirror and a movable mirror that translates back and forth. A beam of IR emitted from the source is split into two parts by the beam splitter, one part is transmitted to the movable mirror and the other part is reflected to the fixed mirror. The fixed and moving mirrors reflect the radiations back to the beam splitter. Again, half of this reflected radiation is transmitted and half is reflected at the beam splitter, resulting a part of the beam passing to the detector and the second back to the source. The beam from the moving mirror has traveled a different distance than the beam from the fixed mirror. Thus, the outgoing beam to the detector is a combination of beams reflected from the fixed and moveable mirrors and hence, an interference pattern is created due to constructive and destructive interference of wavelengths depending on differences in the path traveled by the beams. This interference pattern is called an interferogram. This interferogram then goes from the beam splitter to the sample, where some energy is absorbed and some is transmitted to the detector. The detector reads the information of wavelengths simultaneously. To obtain the infrared spectrum, the detector signal is sent to the computer where time domain wavelength information is converted to wavelength versus intensity by an algorithm called a Fourier transform. The x-axis of FT-IR spectrum is typically displayed in "wavenumbers cm^{-1}". This unit is a product of the Fourier transform algorithm operating on the interferogram and is the reciprocal of the actual wavelength of radiation measured in centimeters at a point in the infrared spectrum.

In the present thesis IR data was recorded using a Bomem MB102FTIR (model 610) equipped with a DTGS detector.

2.3.5. Raman spectroscopy

Raman spectroscopy is a vibrational spectroscopy based on the interaction of monochromatic light with the electron cloud and bonds of a molecule. In such interaction, a part of the incident photon energy absorbed by the molecule and exited the molecule to a virtual energy state. As the molecule cannot remain within this virtual state, it relaxes to the ground state by emission of a photon whose energy is the same as that of the exciting radiation, which is elastic and known as Rayleigh scattering as shown in the **Fig.2.8**. There is no frequency shift in the emitted photon for Rayleigh scattering. However, if the molecule excitation or relaxation involves different energy levels then the frequency of scattered light is different from that expected in the elastically scattered process. This process is called Raman scattering. The emitted frequencies higher than elastically scattered frequency give anti stoke lines while those lower than elastically scattered frequency give stokes lines. The Raman spectra selection rule is analogues to the IR vibrational spectroscopy. It requires a changing induced dipole moment. Electron cloud of an atom or molecule, to be distorted from its normal shape by an external electric field [82].

$$\frac{d_\alpha}{d_Q} \neq 0 \qquad [2.18]$$

From group theory, if a molecule has a center of symmetry, vibrations that are Raman active will be inactive in the infrared, and vice versa. Also the scattering intensity is proportional to the square of the induced dipole moments.

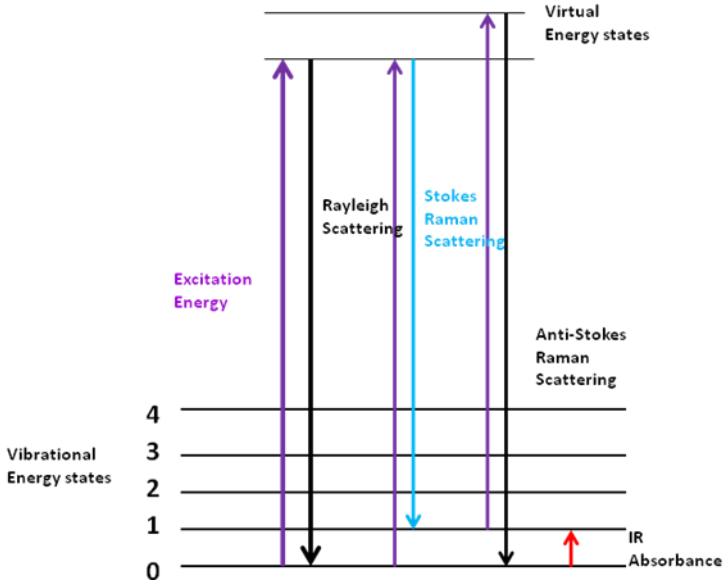

Fig.2.8: Schematic presentation of Raman Scattering.

The energy of Raman mode depends on the crystallographic location of atoms in the crystal and their local coordination including cell parameters, bond angle and type of coordination polyhedra and hence explicitly explains the structure of molecule and crystal. It can also directly identify local vibrational modes that are related to configurations of impurities or vacancies. Thus, the Raman scattering has been widely used to study short range order in disordered structures, micro or nano crystals, mixed oxides, impurities-doped semiconductors, alloys or compounds, and ion-implanted crystals. More detailed information on the identity and the location of the isolated defects can be obtained by Raman spectroscopy. Thus, Raman scattering provides important information on disordered materials, which is often observed consequence of chemical substitution and ion irradiation etc.

Raman spectrometer consists of four major components as shown in the **Fig.2.9**.

(1) Excitation source, which is generally a continuous-wave (CW) laser

(2) Sample illumination and collection system

(3) Wavelength selector

(4) Detection and computer control/processing systems.

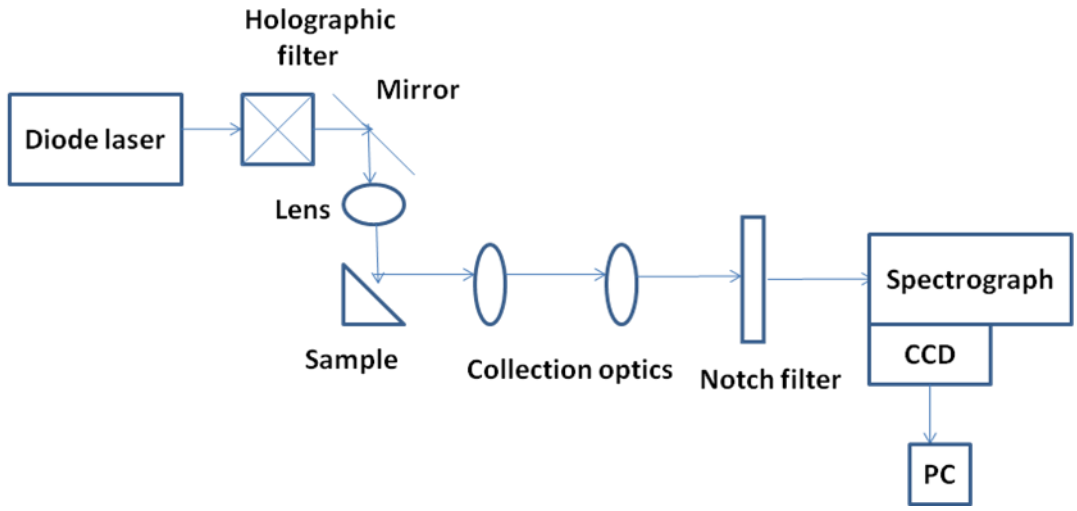

Fig.2.9: Block diagram of Raman spectrometer.

i. Source: To get high intensity signal the sources used in modern Raman spectroscopy should have high frequency as possible. Five of the most common lasers along with their wavelength (nm) used for Raman spectroscopy are; Argon ion (488 or 514.5 nm), Krypton ion (530.9 or 647.1 nm), Helium/Neon (632.8 nm), Diode laser (782 or 830 nm) and Nd:YAG (1064 nm).

ii. Sample illumination and collection system: Due to the lower intensity of the Raman scattering, the laser beam must be focused properly on to the sample. The focusing of laser can be achieved by small diameter of the laser beam (1mm to few μm). Collection optics consists of an achromatic lens system with a collecting lens and a focusing lens. The light gathering power of a lens can be expressed as F=f/D, where f is the focal length of the lens and D is the lens diameter. The smaller the value of F, higher is the light gathering power.

iii. Wavelength selector: Both prism, grating monochromator and spectrographs have been used extensively for measuring Raman spectra. Monochromators are still mainstay in this instrumentation.

iv. Detector: There are two different ways to detect and record Raman lines. The simple way is to gather the scattered light emerging through a glass window at the end of the Raman sample tube. Modern spectrometers have photomultiplier tubes which can do direct measurements and automatic scanning of a spectrum. The spectrum produced by the monochromator is passed through a slit which allows a narrow wavelength region to pass through which is focused on to a photomultiplier type detector. This detector employs an amplifier and a recorder to provide Raman spectrum. Modern Raman spectrometers uses CCD based detector for efficient and fast data acquisitions.

Raman spectroscopic measurements were carried out by using the Linkam variable temperature stage (Model-TS 1500) in back-scattering geometry. Scattered light was analyzed by using a home built 0.9 m single monochromator, coupled with an edge filter and detected by a cooled CCD.

2.3.6. Thermo-gravimetric Analysis (TGA)

Thermo-gravimetry or Thermo-gravimetric Analysis (TGA) measures the weight changes associated with thermally induced transitions. It uses a highly sensitive thermo-balance to measure the change in weight while heating or cooling the sample [83].**.** In TGA weight changes of a sample is being continuously recorded over a period of time under controlled heating rate in a specified atmosphere. The schematic diagram of TGA is shown in the **Fig.2.10**. A plot of mass change versus temperature (T) is referred as thermo-gravimetric curve. The TGA curve for the single decomposition consists of two characteristic temperatures, one the lowest temperature at which the onset of a mass change can be detected by thermo balance operating under particular conditions and other is the final temperature (T_f) at which the

particular decomposition completes. The difference $T_f - T_i$ is called as reaction interval. Thus, the resulting thermogravimetric curve (change in weight *versus* temperature) provides information about the thermal stability and also about the composition of any intermediate compounds that formed and also composition of the residue, if any.

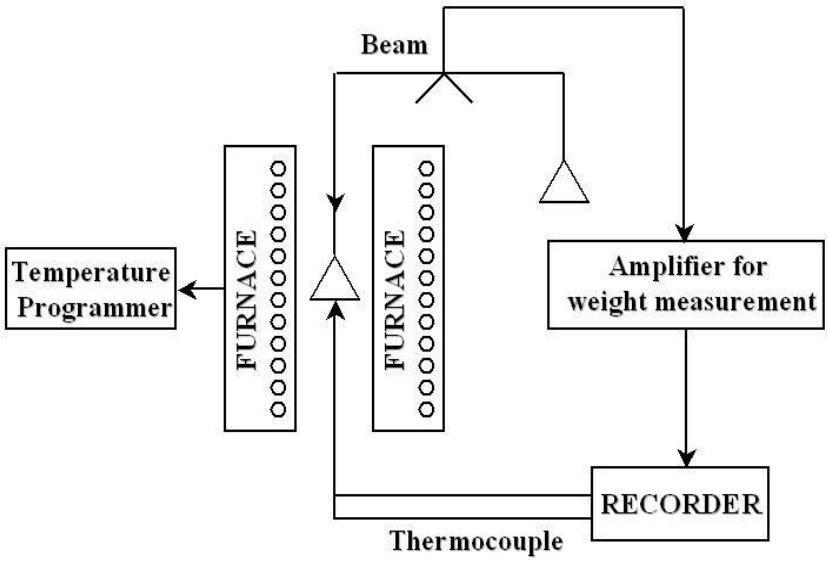

Fig.2.10: Schematic diagram of thermo-balance

In present thesis the TGA experiments were performed, using a SETARAM simultaneous TG/DTA instrument, Model 92-16.18, on the part of the dried gel precursors in the flowing air atmosphere with the heating rate of 10°C/min. Precursor (sample) and reference material (alumina) were placed in two identical platinum crucibles. The weight loss of the sample as a function of temperature was monitored with the help of a thermo-balance whereas difference in temperatures between sample and reference material, as well as sample temperature was monitored simultaneously using two thermocouples.

2.3.7. Scanning Electron Microscopy (SEM)

Electron microscopy has become important for all types of materials as it can be used to get the substantial information about the structure-property correlation including morphology, crystallographic defects, composition of phases and estimation of the crystallite size etc. Due to limited resolution, the above stated information cannot be obtained by optical microscopy. It mainly involves the interaction of the electrons with the sample. In the present thesis, Scanning Electron Microscopy (SEM) was used to study the morphology of sintered pellets. The principle and experimental particulars of SEM technique is given below.

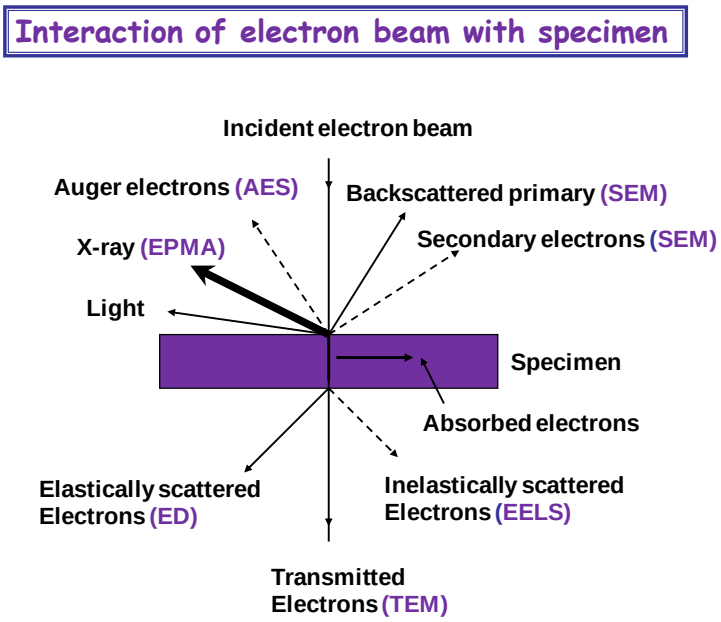

Fig.2.11: Depiction of different phenomena occurring on interaction of electron beam with material.

The scanning electron microscope (SEM) is one of the most versatile techniques used for the examination and analysis of the microstructure morphology and chemical composition characterizations. In which an electron beam is focused on the material and the signals resulting from the interaction of the beam with the surface

are recorded. Various interactions of electron beam with specimen are shown in the **Fig.2.11.** These interactions can be divided into two major categories elastic interactions and inelastic interactions. Elastic scattering results a change of direction without change of energy of electron. Such interactions are characterized by a wide-angle directional change of the scattered electron. In inelastic scattering, the electrons undergo changes in direction as well as energy. The outgoing electrons in an electron-sample interaction process considered in electron microscopes are three general types, viz. secondary electrons (SE), back-scattered electrons (BSE) and transmission of electrons. If the incident electrons are scattered through an angle of more than 90° they are called backscattered electrons (BSE). The inelastic scattering occurs through the varieties of interaction of incident electrons and atom of the sample, where substantial amount of energy of the electron is transferred to the atoms of sample. The excitation of the electrons by ionization process of atoms of sample leads to the generation of secondary electrons (SE) and energy of these secondary electrons are typically below 50 eV [84(a)].

In a typical scanning electron microscope, a well-focused electron beam is incident and scanned over the sample surface by two pairs of electro-magnetic deflection coils as shown in the **Fig.2.12**. Usually secondary (SE) and/or backscattered electrons (BSE), are collected by a detector and the resulting signal is amplified and displayed on a TV screen or computer monitor. The main components of a typical SEM are electron column, scanning system, detector(s), display, vacuum system and electronics controls. For SEM measurements sample should have the following requirements.

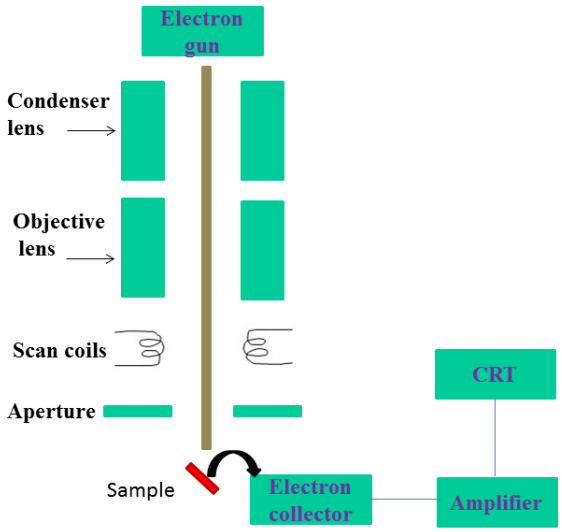

Fig.2.12: Schematic diagram of a SEM instrument [84(b)]

(1) The sample to be probed by SEM should be vacuum compatible. Electrons, being charged particles, require vacuum environment for traversing without any change in their number and density. Thus, the sample should be able to withstand vacuum of ~ 10^{-6} Torr, is required for SEM applications. Placing the sample in vacuum avoids their scattering by gas molecules, improving the measurements.

(2) The sample to be analyzed should be electrically conducting; otherwise there is a charge buildup on the sample due to accumulation of impinging electrons. This gives rise to the jumping of beam and makes the beam unstable. The surfaces of non-conductive materials are thus made conductive by coating with a thin film of gold or platinum or carbon.

The secondary electrons have low energies, so only those close to the surface can be detected. Besides the morphology, other information like elemental composition can be obtained from the analyses of the characteristic X-rays emitted by the excitation of inner shell electrons. The composition of the material can be

evaluated by Energy Dispersive X-ray spectroscopy (EDS) attachment to the SEM. Back-scattered electrons gives information about composition due to the Z-contrast, i.e. dependence of the number of back-scattered electrons to atomic number of atoms. Thus, back-scattered electrons can be used to determine local atomic number contrast, enabling distinction between different phases in the material. The technique is routinely used to study the microstructure evolution (grain size, porosity, etc.) of the sintered crystalline samples.

The technique was used to study the microstructure evolution (grain size, porosity, etc.) of the sintered samples. The instruments used in this thesis work were a mini SEM model SNE 3000M and scanning electron microscope (Zeiss, Gemany). Conductive copper/gold coating was applied on the sintered samples using 6" d.c. sputtering unit, model 6-SPT, manufactured by M/s. Hind High Vacuum, Bangalore.

2.3.8. Mössbauer spectroscopy

Mössbauer spectroscopy is one of the best techniques for identifying the electronic or magnetic structure such as its valence, spin state, or magnetic moment of the Mössbauer active atom. Mössbauer setup consists of the source, the absorber (sample) and the detector. The γ-ray emitted by the source pass through the sample and transmitted γ-rays are detected by radiation detector. The Mössbauer drive oscillates the source so that the incident γ-rays hit the absorber with a range of energies due to the doppler effect as shown in the **Fig.2.13**. Sometimes it is also possible to keep source stationary and oscillate the sample, as is done with synchrotron Mössbauer instrument. The technique belongs to nuclear spectroscopy, where nuclei in atoms undergo a variety of nuclear energy level transitions with the emission or absorption of gamma rays. These nuclear energy levels are influenced by their surrounding

environment and hence they appear as a change or split of these energy levels. These changes in the energy levels can provide information about the arrangement of the surrounding atom within a system. But there are two major obstacles in obtaining this information, one is the 'hyperfine' interactions between the nucleus and its environment are extremely small, and another is the recoil of the nucleus when the gamma-ray is emitted or absorbed prevents resonance.

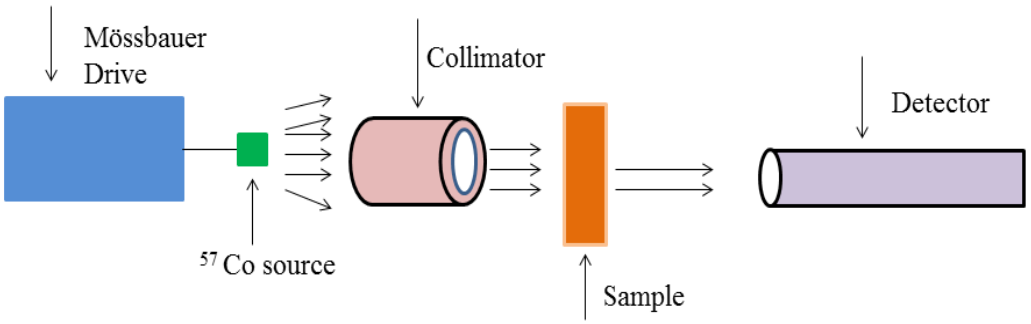

Fig.2.13: Schematic diagram of a Mössbauer setup [85]

For the analyses of emission and absorption of gamma rays by atoms in solids following three different situations need to be considered.

1) When atom in a solid emits a gamma ray, it recoils. The recoil energy can be calculated as:

$$E_\gamma = \frac{E_\gamma^2}{2MC^2} \qquad [2.19]$$

Where, E_γ is the gamma ray energy and M is mass of the recoiling atom. If the recoil energy is large compared to the binding energy of the atom in the solid, the atom will be completely dislodged from its lattice site.

2) If the recoil energy is larger than typical energies of lattice vibration but less than the binding energy, the atom dissipates the recoil energy by heating the surrounding solid.

3) If the calculated recoil energy is smaller than the phonon energies, it is possible for the atom to emit or absorb rays without recoiling. This is called as the M**ö**ssbauer effect.

Mössbauer effect can be detected in isotopes with very low lying excited states. Similarly, the resolution is dependent upon the lifetime of the excited state. These two factors limit the number of isotopes that can be used successfully for M**ö**ssbauer spectroscopy, the most commonly used isotope in Mössbauer spectroscopy is ^{57}Fe. In a Mössbauer experiment, a source and absorber with the same isotope of an atom are used [85]. The emitting ^{57}Fe results from electron capture phenomena in a ^{57}Co radioactive source, as shown in **Fig.2.14**.

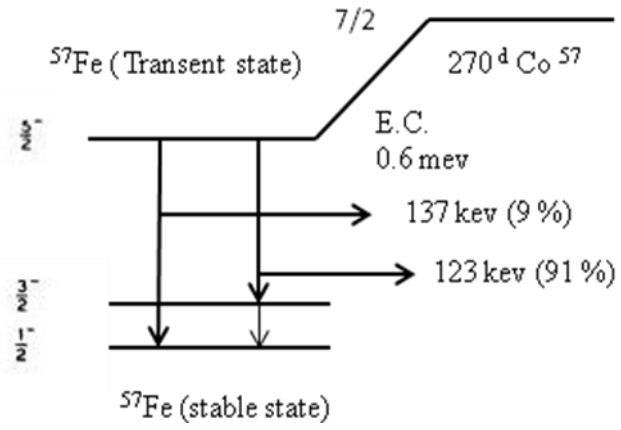

Fig.2.14: Decay scheme of ^{57}Co to ^{57} Fe (E.C. denotes electron capture) [86].

i. Magnetic splitting

Since Fe has cubic structure, no quadrupole splitting in the absorber is observed. The resonances are due to magnetic splitting of the ^{57}Fe nuclear levels which arise from the interaction of the nuclear magnetic dipole moment with the magnetic field due to its own electrons. The ground state of ^{57}Fe in a magnetic field B_z splits into two energy levels, which gives rise to the 14.4 keV gamma ray. Further,

each state is split into 2I+1 magnetic sublevel and allowed transitions must satisfy Δm = 0, ±1 selection rule as shown in the **Fig.2.15**. The energy difference between magnetic sublevels is $\Delta E = g\ \mu_N\ B$, where, μ_N is a nuclear magneton and the g factor is different for different levels and B is the magnetic field.

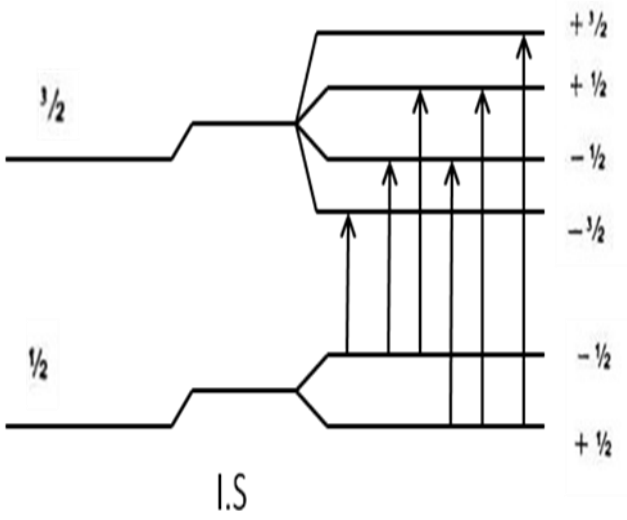

Fig.2.15: Magnetic splitting of nuclear levels. (Nuclear Zeeman Effect) [86].

ii. **Isomer shift or chemical shift**

The nucleus in an atom is always surrounded and penetrated by the electronic charge with which it interacts electrostatically. A nucleus in the excited state is larger than a nucleus in the ground state, so the nucleus in the excited state will have a larger overlap with the s-electron than when in the ground state. This will decrease the energy of the excited state relative to the ground state and any difference in the s-electron environment between the source and absorber produces a shift in the resonance energy for the transition. This shifts the whole spectrum positively or negatively depending upon the s-electron density, and sets the centroid of the spectrum

iii. Electric quadruple splitting

This splitting arises from the interaction between the gradient of the electric field at the site of the nucleus of the source and/or absorber and the quadrupole moment of the source or absorbing nucleus. This splits the nuclear energy levels as shown in the **Fig.2.16.**

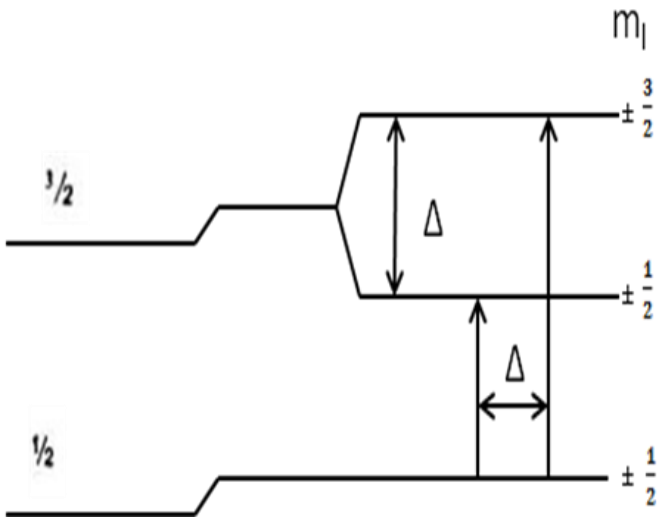

Fig.2.36: Quadrupole splitting for 3/2 to1/2 transition [86].

Mössbauer spectra (MS) at room temperature were recorded with a conventional spectrometer (Nucleonix Systems Pvt. Ltd., Hyderabad, India) operated in constant acceleration mode in transmission geometry with ^{57}Co source in Rh matrix of 50 mCi. The calibration of the velocity scale was done by using an enriched ^{57}Fe metal foil. The isomer shift values are relative to Fe metal foil (= 0.0 mm/s)

2.3.9. Electrical measurements

i. Impedance spectroscopy:

Impedance spectroscopy is a valuable electrochemical technique that can be used to characterize electrical properties of any material and its interface. Impedance

measurement is a sensitive indicator of wide varieties of chemical and physical properties, such as oxide ion conduction, diffusion, corrosion in materials. The basis of impedance spectroscopy involves the analysis of the impedance (resistance to alternating current) of the observed system with respect to the applied frequency and applied signal potential.

Electrochemical Impedance Spectroscopy (EIS) measures the response of the system with the application of a periodic small amplitude ac signal. The measurements carried out at different ac frequencies provide the information about the total opposition to the flow ac current in a circuit or in a substance. The net opposition is termed as impedance and thus the measurement is generally named as Impedance Spectroscopy. Such responses to ac field contain information about bulk conduction, ionic transport, grain boundary conduction, electrolyte-electrode interfaces and dynamics of bound or mobile charges etc. In impedance measurements, the resistance to the flow of the charges can be measured by measuring the current of the system with the applied potential.

From the fundamentals of AC theory, a pure sinusoidal voltage can be expressed as $E(t) = E_0 \exp(j\omega t)$, where t = potential at time t, E_0 = amplitude of the signal, ω = radial frequency. The relationship between radial frequency ω (radians per second), and frequency f (hertz) is described by, $\omega=2\pi f$. The output current of the system can be written as the $I(t) = I_o \exp(jwt+\Phi)$ where I_0 = amplitude Φ = phase difference. The value of Φ is positive when the voltage is leading the current, and is negative when the voltage is trailing the current.

According to Ohm's law, Impedance (Z) of the circuit at any frequency (ω) can be represented by as.

$$Z^* = Z_o \exp(-j\Phi)$$

$$Z^* = Z\cos\Phi - jZ\sin\Phi$$

$$Z^* = Z' - jZ'' \qquad [2.20]$$

Where, Z' = the real part of the impedance and is in phase,

Z'' = the imaginary part of the impedance and 90° out of phase

$j = \sqrt{-1}$, The phase difference Φ can be expressed by $\Phi = \tan^{-1}\frac{Z'}{Z''}$

Thus, the impedance for RC series circuit is given as

$$Z = R + \frac{1}{i\,\omega C} = R - \frac{i}{\omega C}, (where\ i = \sqrt{-1}) \qquad [2.21]$$

This means that, $Z' = R$ and $Z'' = -\frac{1}{\omega C}$

For a parallel RC circuit, the real and imaginary components are given by

$$Z' = \frac{R}{1 + (\omega RC)^2} \qquad Z'' = -\frac{\omega R^2 C}{1 + (\omega RC)^2}$$

A typical circuit containing a resistance and a capacitance in series and parallel are shown in **Fig.2.17.**

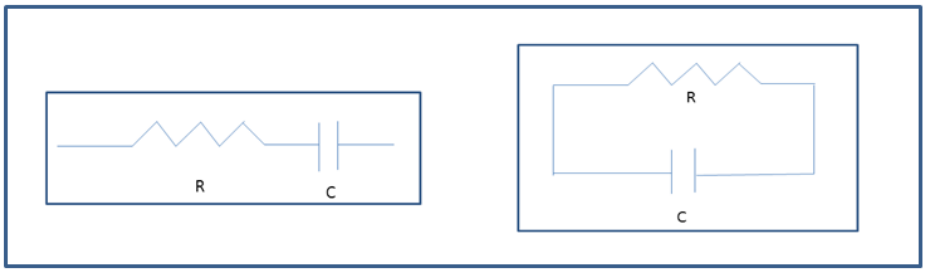

SERIES PARALLEL

Fig.2.17: Series and parallel arrangement of resistance and capacitance.

The impedance data is represented in the form of a complex impedance plot, where the x-axis shows the real component (Z') and y-axis shows the imaginary component (Z''). When plotted in the complex impedance plane for various frequencies (ω), a serial RC circuit will take the form of a spike, since R will be constant with ω. The graph representing the parallel RC combination is a semi-circle with its crest at a frequency ω = 1/RC and intercepts on the Z' axis at zero and R. Thus, the resistance values are derivable from the circular arc intercepts on the real axis. Using the values of resistances and the geometry (length/thickness and cross-sectional area) of the sample, the conductivity (σ) can be determined.

In this work, the ionic conductivity was measured in air, by impedance spectroscopy analysis using Solartron Impedance/Gain-phase Analyzer (S1 1290, U.K) Novocontrol Alpha AN impedance analyzer (Novocontrol Technologies, Germany) and Quatro nitrogen cryosystem in the frequency range 0.1 Hz to 1 MHz and the data was recorded through software ZView-2 and ZPlot-2.

Dielectric measurements

The complex dielectric constant (ε*) is expressed as

$$\varepsilon^* = \varepsilon' - i\,(\varepsilon'') \qquad [2.22]$$

Where, ε' is the real part of ε^* and is equivalent to the measured dielectric constant, ε'' is the imaginary part of ε^*

$$\varepsilon^*(\omega) = \varepsilon' - i\varepsilon'' = 1/\,[G\, i\omega\varepsilon_0\, Z^*(\omega)] \qquad [2.23]$$

Where G = geometrical factor defined as A/*l*

A = Area and *l* = thickness of specimen

$i = \sqrt{-1}$

ω = angular frequency = $2\pi f$

ε_0 = permittivity of free space = 8.85×10^{-14} F/cm

The ε' and ε'' were calculated from the complex impedance as below

$$\varepsilon' = 1/\omega\varepsilon_0 [Z''/Z'^2 + Z''^2]$$

$$\varepsilon'' = 1/\omega\varepsilon_0 [Z'/Z'^2 + Z''^2]$$

The complex electric modulus M* is the reciprocal of the complex permittivity ε*

$$M^* = 1/\varepsilon^*$$

$$M^* = M' + jM'' \quad [2.24]$$

Where, M' and M″ are, respectively, real and imaginary parts of complex electric modulus. The complex electric modulus spectra represent a measure of the distribution of ion energies in the structure.

Experimentally, dielectric measurements are usually made over a range of frequencies covering the audio frequency (~ 10^3 Hz), radiofrequency (~ 10^6 Hz) and microwave frequency (~ 10^9 Hz). The response of a dielectric to an alternating electric field is plotted as Cole-Cole complex permittivity diagrams similar to complex impedance plots. In this thesis, dielectric measurements were carried out using a Solartron Electrochemical Interface (S1 1287, U.K) in the frequency range 0.1 Hz to 1 MHz.

2.3.10. Magnetic measurements

The instrument used to study the magnetic property of a material is called as magnetometer. In this study, Superconducting Quantum Interference Device (SQUID) magnetometer was used to investigate the magnetic properties.

A SQUID (Superconducting Quantum Interference Device) is the most commonly used device for measuring magnetic fields. A magnetometer developed

using this device is known as SQUID magnetometer. It is used to characterize materials with highest detection sensitivity over a broad temperature range, using applied magnetic fields up to several Tesla. Schematic diagram of SQUID magneto meter is shown in the **Fig.2.18**.

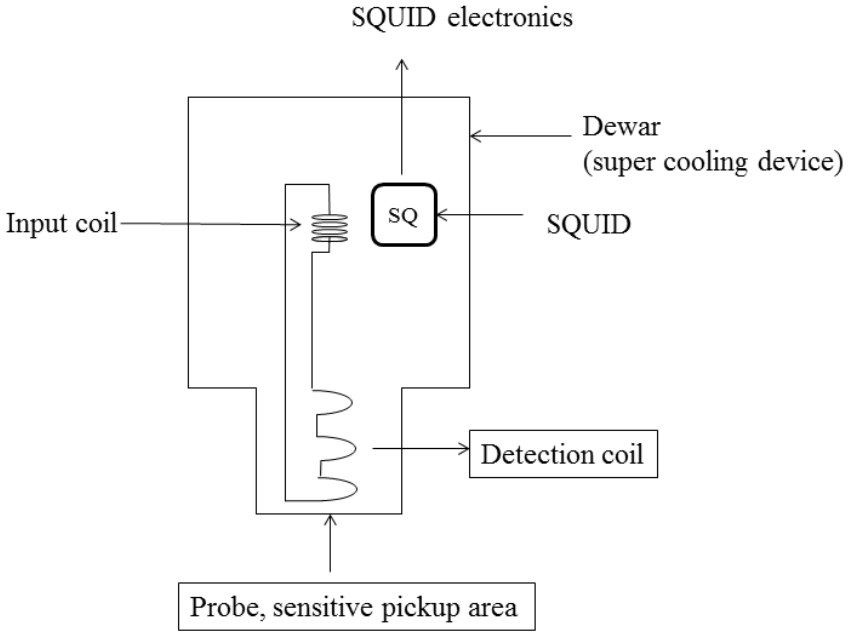

Fig.2.18: Schematic diagram of SQUID magnetometer .

A SQUID magnetometer consists of three main parts viz.

(1) Superconducting magnet: This is a solenoid made of superconducting wire. This solenoid must be kept at liquid helium temperature in a liquid-helium dewar. A uniform magnetic field is produced along the axial cylindrical bore of the coil. Currently, superconducting solenoids that produce magnetic fields in the range 5-18 Tesla are commercially available.

(2) Superconducting detection coil: This is a single piece of superconducting wire configured as a second-order gradiometer. It is coupled inductively to the sample. This pick-up coil system is placed in the uniform magnetic field of the solenoidal superconducting magnet.

(3) SQUID: This device responds to a fraction of the flux quantum. The SQUID is usually a thin film that functions as an extremely sensitive current-to-voltage-converter.

Magnetic measurements are done in SQUID magnetometer by moving the sample through the second-order gradiometer. The magnetic moment of the sample induces an electric current in the pick-up coil system. A change in the magnetic flux in these coils changes the persistent current in the detection circuit. Thus, the change in the current in the detection coils produces a variation in the SQUID output voltage proportional to the magnetic moment of sample. SQUID magnetometers are versatile instruments that can perform both DC and AC magnetic moment measurements.

In the present thesis work, the temperature and field dependent magnetic properties of the samples were investigated by using SQUID magnetometer (Quantum Design, USA

CHAPTER 3

PREPARATION AND CHARACTERIZATION OF OXIDE ION CONDUCTOR IN Bi_2O_3-Ln_2O_3 (Ln = DY AND Yb) SYSTEMS

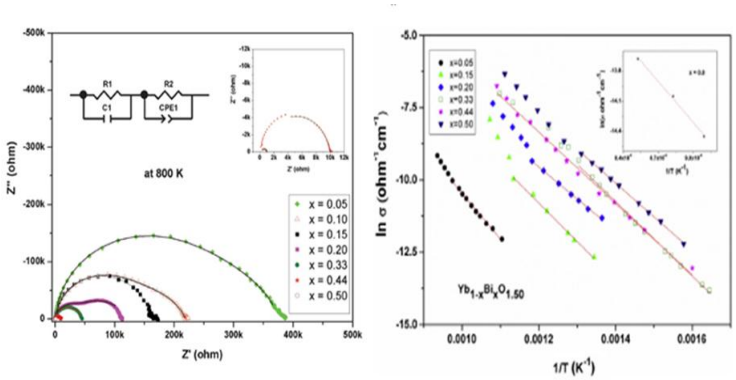

1. Phase evolution and oxide ion conduction behavior of $Dy_{1-x}Bi_xO_{1.5}$ ($0.0 \leq x \leq 0.5$) composite systems
K. Vasundhara, S. J. Patwe, A. K. Sahu, S. N. Achary and A. K. Tyagi
RSC. Adv. 3 (2013) 236-244.

2. Structural and oxide ion conductivity studies on $Yb_{1-x}Bi_xO_{1.5}$ ($0.0 \leq x \leq 0.5$) composites
K. Vasundhara, S. N. Achary, S. J. Patwe, A. K. Sahu, N. Manoj and A. K. Tyagi
J. Alloy. Compd. 596 (2013) 151-157.

3.1. Introduction

Over recent years, Bi_2O_3-based solid electrolytes with the fluorite-type FCC structure (space group $Fm\bar{3}m$) have gained much interest for several applications particularly in the field of fuel cells. Bi_2O_3 exists in four different polymorphs namely, α, β, γ and δ forms. The low temperature α-form is monoclinic and it transforms to high temperature cubic δ-form at 1003 K. The δ-phase is stable up to its melting point (1098 K). The δ-phase shows a large hysteresis at transition temperature while cooling to ambient temperature and often transforms to intermediate metastable phases instead of the ambient temperature α-phase. One of the two intermediate phases namely tetragonal (β) and body centered cubic (γ) are formed at a temperature 923 and 912 K, respectively. Silen had reported a fluorite-type (Fm3m) structure for δ-Bi_2O_3 where Bi^{3+} ions at *4a* site form a FCC lattice and oxygen ions occupy the tetrahedral *8c* interstitial sites [87]. Since there are six oxygen ions available, two of the eight tetrahedral sites remain as random vacant sites (vacancies). The Gattow model [88] shows the equal possibility of tetrahedral site occupancy by oxygen ions and no preferential vacancy in δ-Bi_2O_3 as proposed in Silen model. Later it has been understood that the vacancies can order in the structure of δ-Bi_2O_3 and most commonly they order in <111> direction. The vacancy ordering in δ-Bi_2O_3 has attracted more attention to understand its temperature dependent electrical property and defect structure. Willis [89] reported displacement of O^{2-} from *8c* site along <111> direction. Thus, the O^{2-} ions occupy 32 equivalent positions (32*f*). The occupancy of oxide ions is 6/32. From the neutron diffraction studies on the δ-Bi_2O_3, Battle et al. [90] concluded a defective fluorite structure, where 43% of oxide io

occupy the normal *8c* sites while the remaining 57% are displaced along the <111> directions.

Due to the highly defective anion structure, δ-Bi_2O_3 has attracted attention as an oxide ion conductor. Hawing [91] had reported a systematic study on electrical conductivity of β, γ and δ-phases of Bi_2O_3. The α-Bi_2O_3 has the electronic conductivity and lowest ionic conductivity due to ordered arrangement of anions. Oxide ion conductivity is observed dominatingly only in the metastable β and γ-phases. In the temperature range of 923-1023 K, i.e. in the δ-Bi_2O_3 phase region, a rapid increase in the conductivity with O^{2-} as major charge carriers has been attributed to the presence of mobile oxide ions in a highly disordered anion sublattice. Thus, disorder fluorite structure is the main reason for high conductivity of δ-Bi_2O_3 and that facilitate diffusion of O^{2-} along the <111> directions, i.e. the oxide ions move along a path towards an empty octahedral site at the cube centre. Further, the asymmetric arrangements of anions due to the lone pair *($6s^2$)* of Bi^{3+} ions and highly polarizable nature of Bi^{3+} ions are other favourable features for the oxygen mobility in δ-Bi_2O_3 [92]. The ionic conductivity of δ-Bi_2O_3 is ~ 1 $\Omega^{-1}cm^{-1}$at 1003 K, which is about one to two orders higher than that of stabilized zirconia at this temperature.

Even though δ-Bi_2O_3 has high ionic conductivity, its usage as an oxide ion conductor is limited due to its stability only in a narrow temperature range. It has been observed that a partial substitution of Bi^{3+} by isovalent or heterovalent cations stabilizes the high temperature δ-Bi_2O_3 phase at ambient temperature. High ionic conductivity in stabilized δ-phase with multiple cations of iso or hetero valence, has also been reported in literature [4]. Doping of di, tri, penta or hexavalent metal ions in

Bi_2O_3 also lead to conductive phases similar to cubic δ-Bi_2O_3 type or rhombohedral distorted phases. For the stabilization of δ-Bi_2O_3, rare-earth ions are considered as suitable dopants due to their similar charge and ionic radii. Among all the rare earth cations, Er^{3+} can stabilize the δ-phase with a minimum dopant concentration, viz. ($Bi_{0.8}Er_{0.2}O_{1.5}$) and exhibit higher conductivity [4]. Literature also revealed that the Bi_2O_3 based electrolytes are unstable under reducing environment. Even at 873 K, a rapid degradation of electrolyte has been observed at an oxygen partial pressure of about 10^{-13} atm [93]. In order to circumvent such problems arising from the direct contact of electrolyte and fuel, usage of thin barrier layer of stable oxide ion conducting YSZ had been proposed. However, such approaches may also fail to prevent the reactivity of the electrolytes due to formation of several stable phases of Bi_2O_3-ZrO_2 system [94]. Thus, the potential of the δ-Bi_2O_3 based solid electrolytes is limited for actual applications till date. Hence, for a practical application, the thermodynamic and structural stability of the electrolyte in reducing atmospheres and operation temperature needs more research attention. In view of these problems associated with Bi-rich systems, reduced contribution of the reactive Bi_2O_3 in electrolyte or Bi-deficient phases in Bi_2O_3-Ln_2O_3 may be promising materials for practical applications. The ordering of cations and anions in such Bi deficient phases can render more structural and chemical stability to them compared to the δ-Bi_2O_3. At an optimum concentration of Bi_2O_3 in Bi deficient compounds can thus lead to a significant improvement on the stability but with a partial loss on conductivity. In order to study the potential of Bi_2O_3 deficient compositions as electrolytes, the phase evolution and electrical properties in $Ln_{1-x}Bi_xO_{1.5}$ (Ln = Dy and Yb; $0.0 \leq x \leq 0.50$) system have been investigated and they are presented in this chapter.

3.2. Experimental method

A series of compositions $Ln_{1-x}Bi_xO_{1.50}$ (Ln^{3+} = Dy^{3+} and Yb^{3+}; $0.00 \leq x \leq 0.50$) were prepared by solid state reaction of stoichiometric amounts of component binary oxides (Dy_2O_3, 99.9 %, Aldrich, Bi_2O_3, 99.9 %, Aldrich, Yb_2O_3 99.9 %, Aldrich). All the reactants were preheated (Ln_2O_3 at 1073K and Bi_2O_3 at 773 K) to remove any carbonate, hydroxide and adsorbed water molecules. Appropriate amounts of Bi_2O_3 and Ln_2O_3 were thoroughly homogenized in a mortar and pestle. The finely ground homogenized mixtures were pressed into pellets of 1 cm diameter and 2 to 3 mm height. These pellets were heated at 973 K for 24 h in platinum crucible. After first heat treatment pellets were re-homogenized, pelletized and then sintered at 1173 K for 24 h. The sintered products were characterized by XRD and Raman spectroscopy and electrical properties were measured by ac impedance measurements.

3.3. Results and discussion of $Dy_{1-x}Bi_xO_{1.50}$ ($0.00 \leq x \leq 0.50$)

3.3.1. XRD studies

The powder XRD patterns of all the sintered samples are depicted in **Fig.3.1**. The powder XRD data of one end member, x = 0.00 (i.e. Dy_2O_3), shows the characteristic reflections of cubic C-type rare-earth oxide lattice. All the observed reflections could be indexed on the body centered cubic lattice with unit cell parameter *a* = 10.6606(2) Å, which is in agreement with that earlier, reports for Dy_2O_3 (JCPDS-PDF: 43-1006). As the Bi^{3+} content in the nominal composition $Dy_{1-x}Bi_xO_{1.5}$ increases, several new reflections in addition to the reflections attributable to Dy_2O_3 but different from the Bi_2O_3 have appeared. The appearance of new reflections can be due to the formation of a new phase in this system. With the increase in Bi concentration, a systematic increase in intensity of the reflections of the new phase

with a concomitant decrease in intensity of the reflections of Dy_2O_3 type phase was observed. The reflections attributable to the Dy_2O_3 type phase observed in different nominal compositions were indexed on similar body centered cubic lattices and the refined unit cell parameters are given in **Table 3.1**.

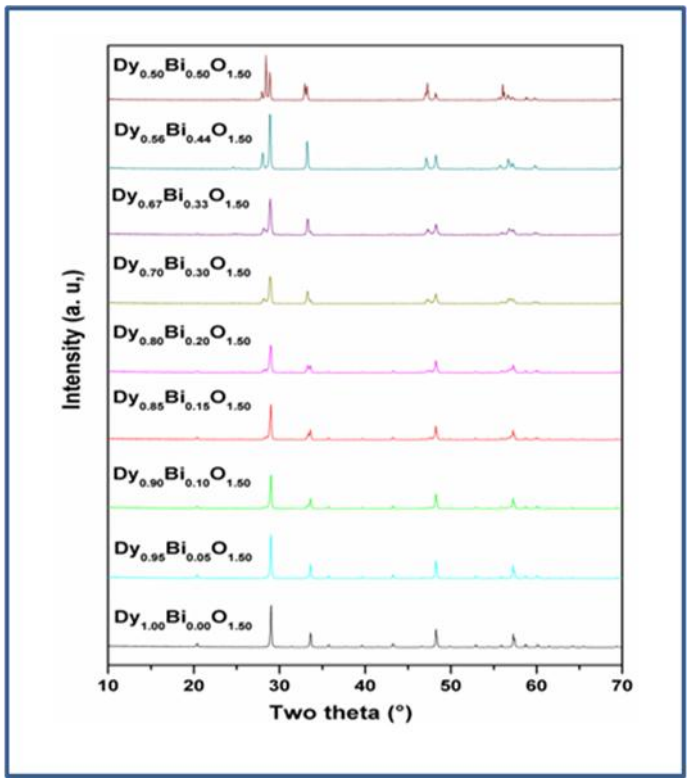

Fig.3.1: Powder XRD patterns of nominal compositions $Dy_{1-x}Bi_xO_{1.5}$ ($0.00 \leq x \leq 0.50$).

Further details of the phases were obtained from the analyses of the unit cell parameters and refinement of the powder XRD data. From the XRD data and unit cell parameters of C-type phases in the studied compositions, it was observed that the unit cell parameter has an increasing trend with the increasing values of x in $Dy_{1-x}Bi_xO_{1.5}$ series and this trend is observed up to x = 0.15. This suggests that Bi^{3+} is partially incorporated in the Dy_2O_3 lattice. However, the nonlinear variation of the unit cell

parameter suggests a possible inter-diffusion of Bi^{3+} ions in between the two coexisting phases leading to a variable concentration of Bi^{3+} ion incorporation in them.

The crystal structure and crystal chemistry of A_2O_3 type sesquioxides have been a subject of research interest for a long time. It has been well understood that the structure is mainly governed from the ionic radii of the A^{3+} ion [7a]. A_2O_3 compositions with $r_A{}^{3+} \leq 0.7$ Å, mainly crystallize in the corundum type structure where the trivalent cations form ideal octahedra. However, compounds with larger $r_A{}^{3+}$ crystallize in various rare-earth oxide type structures, where the cations have distorted octahedral or seven or eight fold coordination. These structures can be grouped to three categories, namely hexagonal (A-type), monoclinic (B-type), and cubic (C-type) [95]. Besides these, several other distinct structure types have been observed in various A_2O_3 type compounds. Depending on composition and external variables like pressure or temperature a number of structural variants are known and they have been recently reviewed by Manjon and Errandonea [96]. The structure of lighter rare-earth oxides has cubic lattice (C-type) which is closely related to the fluorite type lattice with ¼ of oxygen sites vacant. The ordered arrangement of the vacancies leads to two different site symmetry for the cations, which lower the symmetry of the lattice from face centred cubic Fm3m to body centred Ia-3. Almost all the sesquioxides of heavier lanthanides, In_2O_3 and Mn_2O_3 exist in such C-type structures, which can be explained as distorted AO_6 octahedra, where A = trivalent cation. As mentioned in the introduction section, the structure of other end member, Bi_2O_3 can exists in a number of structure types. The ambient temperature, α-Bi_2O_3 has a monoclinic structure where the lattice is formed by stacking of layers of Bi^{3+} and O^{-2} ions. This arrangement results in a distorted trigonal bipyramidal configuration where

the $6s^2$ lone pair of Bi^{3+} and two oxygen atoms at shorter Bi-O bond length form the basal triangle and other two oxygen atoms at longer Bi-O bond lengths form apices [91].

x	Nominal composition	Phases Identified				
			a (Å)	c (Å)	V $(Å)^3$	Z
0.00	$Dy_{1.00}Bi_{0.00}O_{1.50}$	C	10.6606(2)		1211.57(3)	32
0.05	$Dy_{0.95}Bi_{0.05}O_{1.50}$	C R	10.6630(2) *	- -	1212.39(4) -	32 3
0.10	$Dy_{0.90}Bi_{0.10}O_{1.50}$	C R	10.6639(2) *	- -	1212.67(4)	32 3
0.15	$Dy_{0.85}Bi_{0.15}O_{1.50}$	C R	10.6644(2) 3.7817(3)	- 3.4080(10)	1212.87(4) 116.52(2)	32 3
0.20	$Dy_{0.80}Bi_{0.20}O_{1.50}$	C R	10.6619(3) 3.7780(3)	- 9.4773(9)	1212.01(5) 117.15(2)	32 3
0.30	$Dy_{0.70}Bi_{0.30}O_{1.50}$	C R	10.6629(5) 3.7758(2)	- 9.4912(7)	1212.36(10) 117.19(1)	32 3
0.33	$Dy_{0.67}Bi_{0.33}O_{1.50}$	C R	10.6612(7) 3.7744(2)	- 9.4914(8)	1211.78(13) 117.10(1)	32 3
0.44	$Dy_{0.66}Bi_{0.44}O_{1.50}$	R	3.7728(1)	9.5541(6)	117.77(1)	3
0.50	$Dy_{0.50}Bi_{0.50}O_{1.50}$	R F	3.7722(2) 5.4366(3)	9.5713(7) -	117.95(1) 160.69(1)	3 4

Table 3.1: Details of phase analysis of $Dy_{1-x}Bi_xO_{1.5}$ system ($0.00 \leq x \leq 0.50$).

C = Cubic C-type rare-earth oxides related

R= Rhombohedral

F = δ-Bi_2O_3 type (fluorite) * Not determined due to very weak reflections

This structure is also closely related to fluorite lattice with ¼ of anions sites vacant. At higher temperature, Bi_2O_3 transforms to a cubic fluorite type (δ-Bi_2O_3) structure by complete disordering of anion and vacant sites. In addition to these ionic structures, several molecular structures are also known for some lone pair containing A_2O_3 type compounds, viz. Sb_2O_3, As_2O_3 etc. [97]. Due to such complexity of crystal chemistry of A_2O_3 type compounds, ordered lattices and different polymorphs can be easily expected in $Dy_{1-x}Bi_xO_{1.5}$ system.

In addition, the stabilized fluorite phases often show anion or cation ordering which leads to various ordered lattices. Thus, the possibility of getting ordered phase is very common in the cation substituted Bi_2O_3 lattices. Hence, analysis of weak peaks and profile of the XRD patterns were carried out. The analyses of the XRD data of the compositions with $0.0 \leq x < 0.44$ revealed no distortion or ordering in the C-type phase. Watanabe et al. [98] have reported a gradual transformation of fluorite-type stabilized face centered cubic lattice of $Bi_{0.68}Dy_{0.32}O_{1.5}$ to a body centered cubic lattice ($I2_13$) with unit cell parameter a = 10.987 Å. The disordered anions of the δ-Bi_2O_3 type phase slowly relaxed to ordered sites of such body centered cubic lattice. The authors had also suggested that the transformed body centered cubic lattice is closely related to the C-type rare-earth oxide lattice. However, the occupation of oxygen in two non-equivalent sites lower the symmetry in stabilized body centered cubic lattice of the rare-earth doped Bi_2O_3 compared to the C-type lattice. The maximum observed unit cell parameter of the present study (a = 10.6644(2) Å for x = 0.15) is only marginally higher than that of pure Dy_2O_3. The larger ionic radii and highly asymmetric electron configuration of Bi^{3+} may be a plausible reason for very low

solubility of Bi^{3+} in the Dy_2O_3 lattice. Besides, no additional reflections attributable to low symmetry space group ($I2_13$) lattice or any other polymorph of A_2O_3 type compounds were observed in XRD patterns of any $Dy_{1-x}Bi_xO_{1.5}$ compositions. The limited solubilities of Bi_2O_3 in the rare-earth oxide lattice retaining the C-type structure have been reported earlier in literature [99]. The maximum solubility of Bi_2O_3 (~ 15 mol %) has been reported in Gd_2O_3, while the solubility decreases with increasing or decreasing the ionic radii of the rare-earth ions with respect to Gd^{3+}, viz. about 8 mol % in hexagonal Pr_2O_3 and about 2 mol % in cubic Yb_2O_3. From the variation of unit cell parameters of the present investigation, it can be suggested that the solid solubility of Dy_2O_3 in Bi_2O_3 remains within 2 mole % as in the cases of Yb_2O_3.

In order to understand the nature of the new coexisting phases, the diffraction data observed for the higher Bi^{3+} containing composition, viz. x = 0.33 to 0.50 were compared. The reflections attributable to the above mentioned C-type phase are not observed at the composition with x = 0.44 as shown in **Fig.3.2**. All the observed intense reflections observed for the $Dy_{0.56}Bi_{0.44}O_{1.5}$ composition could be indexed on a rhombohedral lattice with unit cell parameters as: a = 3.772 and c = 9.5482 Å. The unit cell parameters of this rhombohedral phase identified in the studied nominal compositions are summarized in **Table 3.1**. The formation of rhombohedral phase in the bismuth rich (viz. x > 0.65) compositions of Bi_2O_3-Ln_2O_3 systems have been reported earlier [3,99c,100]. Typical unit cell parameters of such rhombohedral phase can be compared to the present observed parameters as: $a \sim a_h$ and $c \sim 3 \times c_h$ (where a_h and c_h are present observed unit cell parameters). A comparison of the unit cell parameters of the rhombohedral phase observed in various nominal composition

indicates that the *a*-axis systematically decreases with the increase in the concentration of Bi^{3+} while the *c*-axis show an increasing trend. A wide homogeneity range of Bi^{3+} and Dy^{3+} with a concomitant cation distribution in the lattice may be the reason for such variation of unit cell parameters. By considering the existence of both rhombohedral and C-type phases, all the compositions for $0.00 \leq x \leq 0.44$ can be explained as a composite system.

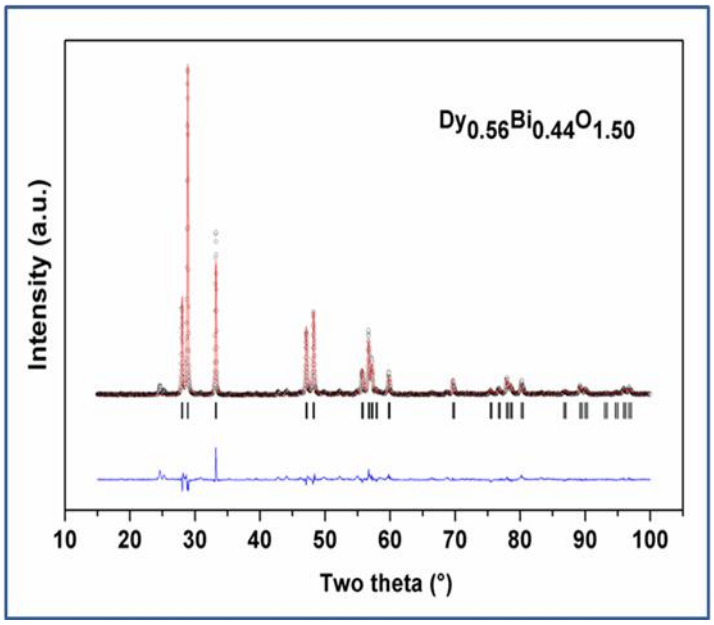

Fig.3.2: Rietveld refinement plot for the powder XRD data of $Dy_{0.56}Bi_{0.44}O_{1.5}$.

In all these rhombohedral phases appreciably lower ionic conductivity was observed compared to the δ-Bi_2O_3 type phases, which have been explained by the ordering of anions. A number of reports dealing with structural and phase transition aspects of such rhombohedral phases are available in literature [100]. Most of these rhombohedral phases show homogeneity ranges which dependent on the ionic radii of the rare-earth ions. Besides, two different types of rhombohedral phases, namely β1 and β2 have been reported in literature, which have almost identical XRD patterns as well as unit cell parameters [99c,100]. However, the difference of the two types of

rhombohedral phases has been concluded from the thermodynamic stability and nature of temperature induced phase transitions [100]. Further investigations by electron microscopy revealed two different types of modulated structures in such bismuth rich rhombohedral phases.

The phases observed in rare-earth rich compositions have diversified symmetry. Structural details of several of Ln_2O_3 rich compositions in Bi_2O_3-La_2O_3/Nd_2O_3 systems are available in literature [101]. An orthorhombic tunnel like structure has been reported for $Bi_8Ln_{10}O_{27}$ composition with only La as rare-earth cation [102]. Horlyn et al. [101d] investigated a series of $Bi_3Ln_5O_{12}$, for Ln = La to Lu compositions and assigned rhombohedral lattices to all of them. The rhombohedral unit cell parameters observed in the present study are similar to those reported by Horlyn et al. [101d] Chen et al. [101c] and Walcryz et al. [103] have reported a monoclinic (C2/m) lattice for $Bi_2La_4O_9$ and $Bi_2Nd_4O_9$ compositions. The reported monoclinic cell is very closely related to the rhombohedral lattice of the present study as well as that reported by Horlyn et.al. [101d]. Drache et.al. [100] have explained a close relation of the rhombohedral and monoclinic lattice with fluorite-type lattice of δ-Bi_2O_3. Further inferences about the observed rhombohedral phases were obtained from the detailed structural investigations on $Dy_{0.56}Bi_{0.44}O_{1.50}$ composition. The average structure for the rhombohedral phase observed at $Dy_{0.56}Bi_{0.44}O_{1.5}$ was obtained by the Rietveld refinement of the powder XRD data by using a cation disorder model reported earlier for such non-stoichiometric rhombohedral phases. In this initial structural model, Bi and Dy are statistically occupied on *3a* (0,0,0) sites *(occ.* Dy:Bi = 0.56:0.44) while anions are occupied on *6c (0,0,z)* sites (*occ.* = 0.75) of space group R-3m. The refined unit cell parameters are: *a* = 3.7728(1) Å and *c* =

9.5541(5) Å, V = 117.77(1) Å^3, Z = 3, (the corresponding rhombohedral unit cell parameters are: a = 3.8584(2) and α = 58.538(2)°, Z = 1) and final refined oxygen position coordinates are: (0, 0, 0.251(2)). The refined structural parameters and the observed as well as calculated XRD patterns for $Dy_{0.56}Bi_{0.44}O_{1.5}$ are shown in **Fig.3.2**.

It can be mentioned here that the above assigned rhombohedral unit cell cannot index a number of weak reflections observed in the XRD pattern of $Dy_{0.56}Bi_{0.44}O_{1.50}$. Thus, the exact structure is a superstructure of this rhombohedral lattice. All the observed weak reflections could be indexed on rhombohedral lattice with unit cell parameters: a = 15.21 and c = 19.67 Å, which can be related to the basis rhombohedral cell as: $a \sim 4 \times a_h$ and $c \sim 2 \times c_h$. The formation of superstructure has been reported for several rare-earth oxide rich compositions, viz. Watanabe [104] has reported a hexagonal superstructure with unit cell parameters, a = 22.865 and c = 19.036 Å for the compositions $Bi_{0.425}Y_{0.575}O_{0.15}$, while Walcryz et al. [103] have reported a rhombohedral superstructure with unit cell parameters, a = 31.67 and c = 19.93Å for $Bi_2La_4O_9$. Besides these hexagonal superlattices, several other distorted monoclinic and triclinic lattices have also been assigned for similar rare-earth rich compositions [101a,103,105]. Earlier, a possible anion ordering has been mentioned for the average rhombohedral structure of $Bi_3Ln_5O_{12}$ (RE = Rare-earth ions) [101d], and $Bi_2La_4O_{4.5}$ [103] etc. It has also been mentioned that the structure of rhombohedral phase is closely related to the structure of fluorite-type δ-Bi_2O_3 and hexagonal (A-type) La_2O_3 and acts as a bridge between fluorite to La_2O_3 type structural transition. The unit cell parameters reported for rhombohedral superstructure observed by Wolcyrz et al. [103] can be related to the presently observed unit cell parameter of rhombohedral supercell of $Dy_{0.56}Bi_{0.44}O_{1.5}$ by doubling

the *a*- and *b*-axes. However, no structural details for such superstructures have been reported in literature, and thus the direct refinement of observed XRD data could not be carried out in the thesis work.

The observed powder XRD pattern of the compositions with x = 0.50 indicates several intense reflections in addition to the reflections due to the above mentioned rhombohedral lattice (**Fig.3.3)**. These extra reflections could be indexed on a fluorite-type lattice, with unit cell parameter a = 5.437 Å. Earlier studies of Verkerk and Burggraaf [27a] on bismuth rich compositions of Bi_2O_3-Dy_2O_3 system indicate that with 25-52 mole % Dy_2O_3 the fluorite type δ-Bi_2O_3 can be stabilized at ambient temperature. The authors have also observed that for lower Dy_2O_3 (i.e. below 25 mol %) compositions, the fluorite-type δ-Bi_2O_3 phase can also be stabilized by quenching from higher temperature. In order to determine the cation ratio and phase fraction, Rietveld refinement of the XRD data were carried out by GSAS software package. The earlier mentioned rhombohedral phase with composition $Dy_{0.50}Bi_{0.50}O_{1.5}$ and fluorite type phase with stoichiometry $Dy_{0.5}Bi_{0.5}O_{1.5}$ were taken as initial structural model for Rietveld refinement. The refined unit cell parameters for the rhombohedral phase are: a_h = 3.7722(2), c_h = 9.5715(7) Å, V = 117.95(1) $Å^3$ and those of fluorite-type phase are: a = 5.4366(2) Å, V = 160.69(1) $Å^3$. The details of other structural parameters are given in **Table 3.2.**The final Rietveld refinement plot for $Dy_{0.5}Bi_{0.5}O_{1.5}$ composition is shown in **Fig.3.3**.

Rhombohedral		Cubic	
a = 3.7722(2) Å c = 9.5715(7) Å V = 117.95(1) Å^3		a = 5.4366(2) Å V = 160.69(1) Å^3	
Dy/Bi (occ. 0.49:051)	*3a: 0,0,0* *U_{iso} = 0.023(2) Å^2*	Dy/Bi (occ. 0.50:050)	*4a: 0,0,0* *U_{iso}* = 0.031(1) *Å^2*
O (occ. 0.75)	*6c: 0,0, 0.243(2);* *Uiso = 0.016(11) Å^2*	O (occ. 0.75)	*8c: 0.25,0.25,0.25;* *Usio = 0.067(14) Å^2*
Wt fractions	48.6(4) %(	51.4(4) %	
Rp: 0.17, Rwp: 0.22, χ^2 = 1.95.			

Table 3.2: Refined structural details for nominal composition $Dy_{0.5}Bi_{0.5}O_{1.5}$

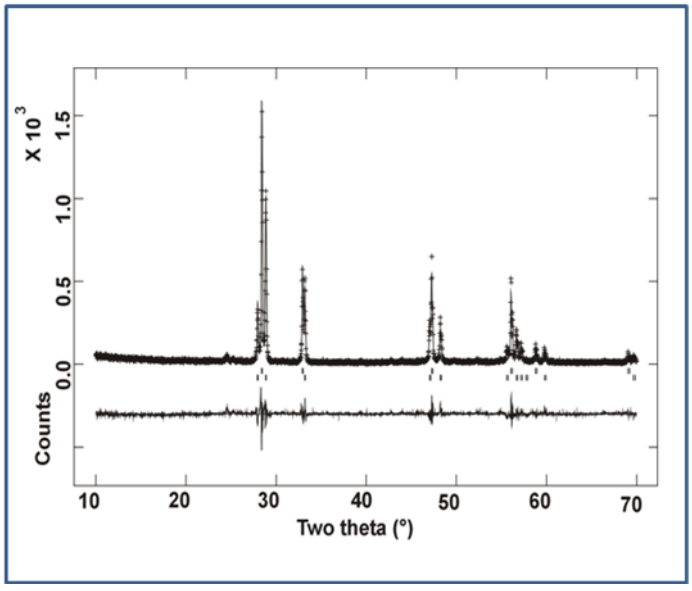

Fig.3.3: Rietveld refinement plot for $Dy_{0.50}Bi_{0.50}O_{1.5}$ composition (rhombohedral: lower vertical marks and fluorite: upper vertical marks).

A comparison of the unit cell parameter observed for fluorite-type δ-Bi_2O_3 with those reported by Verkerk and Burggraaf [27a] suggests that the composition of the fluorite

phase is close to nominal composition $Dy_{0.5}Bi_{0.5}O_{1.50}$. Further occupation of the cation sites of the fluorite type phase was refined by constraining the total metal ion at *4a* site to unit. The cation ratio did not show any appreciable variation from that expected for $Dy_{0.50}Bi_{0.50}O_{1.50}$. Thus it can be suggested that the rhombohedral and fluorite type δ-Bi_2O_3 phases are stable competing phases at x = 0.50 and later is more preferred phase for $x \geq 0.50$. Further it can be mentioned here that no triclinic phase similar to $BiYbO_3$ [105] is formed in the adopted preparation condition.

In summary, it can be concluded that the $Dy_{1-x}Bi_xO_{1.5}$ ($0.00 < x \leq 0.50$) system has three different phases, namely, a feebly Bi doped rare-earth oxide type, a fluorite related rhombohedral and a fluorite-type phases. Both, the rare-earth oxide type and rhombohedral type phases have a homogeneity range as observed from the variation of unit cell parameters. All the compositions, except x = 0.44 exists as a composite of two phases.

3.3.2. SEM studies

The SEM micrographs of representative samples obtained after sintering at 1173 K are shown in **Fig.3.4**. The SEM micrograph of the samples shows that one of the two coexisting phases has well developed grains compared to other. The compositions of metal ions of some representative compositions were verified by point EDS scan and they are given in **Table 3.3.** The homogeneous distributions of elements are confirmed by line EDS scan. As shown in the **Fig.3.5**. A comparison of the SEM micrographs shows very well developed grains for the compositions with higher Bi^{3+} content compared to the lower Bi^{3+} ones. These features corroborate to the findings of the XRD study. The poor sinterabilty is evident for the C-type phases

having excess of Dy_2O_3, which can be attributed to the higher melting temperature of rare-earth oxides.

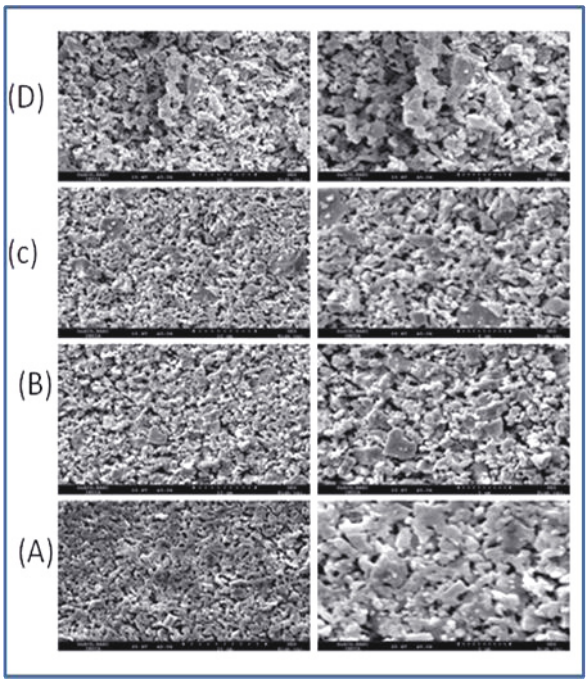

Fig.3.4: SEM images of $Dy_{1-x}Bi_xO_{1.5}$ (A: x = 0.05; B: x = 0.20; C: x = 0.33 and D: x = 0.50) pellets recorded at different magnifications. (Left column is at 3K and right column is at 5K magnification).

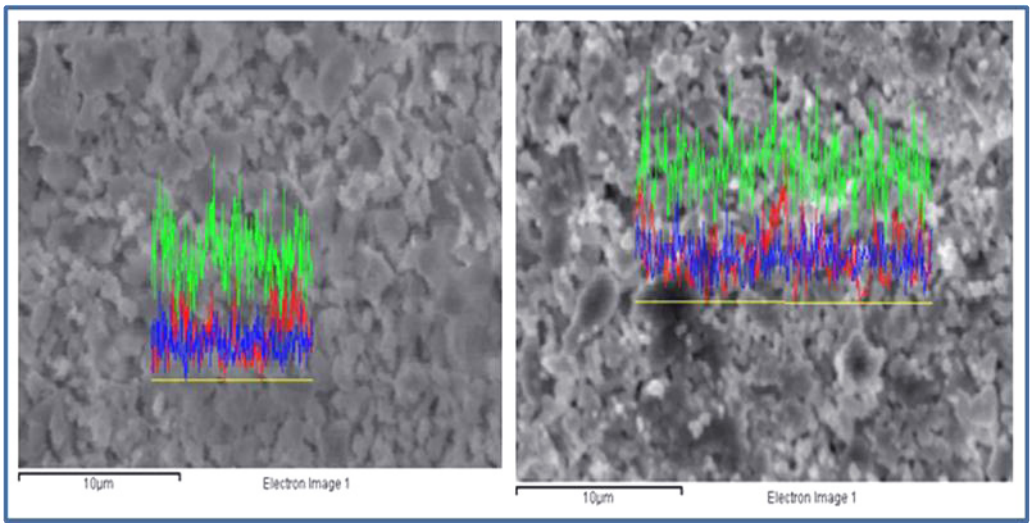

Fig.3.5: Shows the EDS line profile $Dy_{0.56}Bi_{0.44}O_{1.5}$ and $Dy_{0.50}Bi_{0.50}O_{1.5}$ (Blue: Bi, Green: Dy and Red: O.

Nominal compositions	Point	Observed elemental concentration (%)			Expected elemental concentration (%)		
		Dy	Bi	O	Dy	Bi	O
$Dy_{0.56}Bi_{0.44}O_{1.50}$	1	26.87	13.13	60.00	26.8	13.2	60.0
	2	25.79	14.21	60.00			
$Dy_{0.67}Bi_{0.33}O_{1.50}$	1	22.60	17.40	60.00			
	2	22.76	17.74	60.00	22.8	17.6	60.0
	3	22.92	17.08	60.00			
$Dy_{0.50}Bi_{0.5}O_{1.50}$	1	20.08	19.16	60.00	20.0	20.0	60.00
	2	18.91	21.08	60.00			

Table 3.3: Analysis of elemental compositions from point EDS spectrum.

3.3.3. Ionic conductivity studies

Further to understand the electrical properties, the *ac* conductivities of all the compositions were studied from ambient to 973 K. At ambient temperature, the impedance spectra show noisy features indicating highly resistive behavior and impedance beyond the measurable limit of the instrument. Proper semicircles displaying real and imaginary parts of impedance could be obtained only above 673 K. therefore the data measured above this temperature were used for extracting the conductivity information. Typical Cole-Cole plots for some representative compositions at a temperature are shown in **Fig.3.6.** In the frequency range of 0.1 Hz to 10 MHz, two overlapping semicircles were observed for all the compositions. However, two distinct semicircles indicating two different types of relaxation phenomena were observed for the composition with x = 0.20. As observed from the XRD data, the rhombohedral phase is appreciably developed along with the cubic C-type phase at this composition. This may results in two different conduction

mechanisms leading to two distinct semicircles in Cole-Cole plot. At low frequency end the spike like feature attributable to electrode phenomena or semicircle attributable to other contributions were not observed.

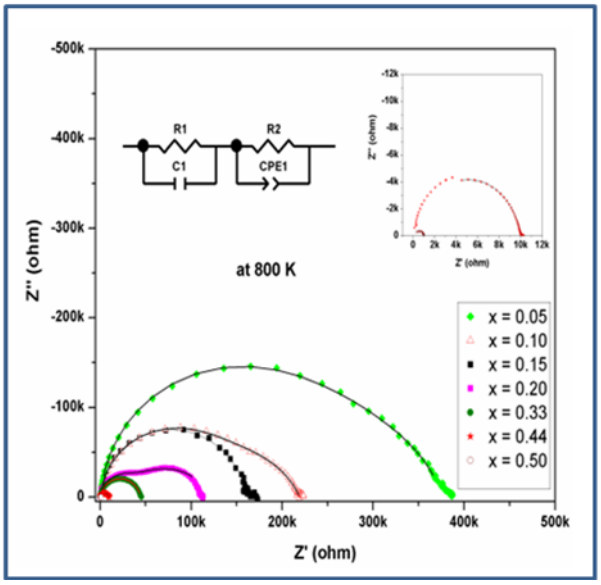

Fig.3.6: Typical Cole-Cole plots of in $Dy_{1-x}Bi_xO_{1.50}$ ($0.00 \leq x \leq 0.50$) at 800 K (insets Fig indicates Cole-Cole plots of x = 0.50 and 0.44). (Solid lines indicate fit data of equivalent circuits).

The analyses of the impedance data were carried out by considering equivalent circuit models by using *ZView* ver. 3.1 (Scribner Associates, Inc.). The impedance data observed in between 1 kHz to 1 MHz were used for the non-linear least square fitting. The observed impedance data at higher temperature could be modelled by using one RC and one R-CPE (R = resistance, C = capacitance and CPE= constant phase element) circuits in series configuration. The equivalent circuit and the corresponding fit data are shown in **Fig.3.6**. The total conductivity *(σ)* were calculated by using the relation σ = (1/R)l/a, where R = total resistance, *l* and *a* are thickness and cross sectional area of sample pellets. The conductivity of each sample was extracted from the observed resistance at different temperature and they are depicted in **Fig.3.7**.

The temperature dependent conductivity of various samples could be fitted with Arrhenius relations: $\ln\sigma = \ln\sigma_0 - E_a/kT$, (where σ_0 = pre exponential factor, E_a = activation energy, k = Boltzmann's constant). The activation energy for different compositions as obtained from the Arrhenius relation are given in **Table 3.4**. The typical conductivities of $Dy_{1-x}Bi_xO_{1.5}$ compositions at 800 K are also included in **Table 3.4**. Activation energy for all the studied compositions is marginally different and they all remain within the range of 1.1 to 1.2 eV. However, the pre-exponential factor increases systematically with the increase in Bi^{3+} content. Besides, a sharp rise in pre-exponential factor is observed for the composition with x = 0.50. From the **Fig.3.6**, it can also be seen that the radius of the semicircle decreases systematically with the increasing values of x in $Dy_{1-x}Bi_xO_{1.5}$, which indicates a systematic increase in conductivity with increase in x values. A comparison of the conductivity of the investigated compositions suggests that at any temperature conductivity increases with increasing Bi^{3+} content (inset in **Fig. 3.7** and **Table 3.4)**. Typical conductivity of $Dy_{0.95}Bi_{0.05}O_{1.50}$ and $Dy_{0.80}Bi_{0.20}O_{1.50}$ at 800 K are 7.5×10^{-7} and 4.6×10^{-6} S/cm, respectively. However, those of $Dy_{0.56}Bi_{0.44}O_{1.50}$ and $Dy_{0.50}Bi_{0.50}O_{1.50}$ are about 6.4×10^{-5} and 8.1×10^{-4} S/cm, respectively. The lower conductivity in low Bi containing samples can be attributed to poor oxygen transport in C-type cubic lattice. However, as the bismuth content increase in these composition, the contribution from the rhombohedral phase becomes appreciable and that enhances the net conductivity. The conductivity of rhombohedral phase is about one order higher than that of the C-type cubic phase. This can be attributed the under occupied disordered anion sites of rhombohedral phase compared to the fully occupied ordered anion sites of the C-type cubic phases. Besides, the rhombohedral phase has layers of disordered anions with

vacancies, which can favor the anion migration due to unhindered two dimensional channels in a layer.

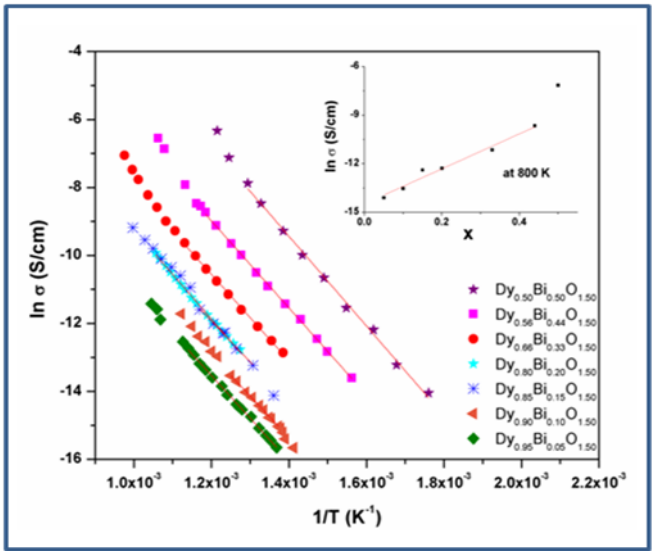

Fig.3.7: Variation of conductivity of $Dy_{1-x}Bi_xO_{1.50}$ with temperature (variation of conductivity with composition x at 800 K is shown as inset).

x	Composition	E_a(ev)	σ (ohm^{-1}cm^{-1}) at 800 K
0.05	$Dy_{0.95}Bi_{0.05}O_{1.50}$	1.11	7.5×10^{-7}
0.10	$Dy_{0.90}Bi_{0.10}O_{1.50}$	1.14	1.3×10^{-6}
0.15	$Dy_{0.85}Bi_{0.15}O_{1.50}$	1.13	4.2×10^{-6}
0.20	$Dy_{0.80}Bi_{0.20}O_{1.50}$	1.17	4.6×10^{-6}
0.33	$Dy_{0.67}Bi_{0.33}O_{1.50}$	1.20	1.4×10^{-5}
0.44	$Dy_{0.66}Bi_{0.44}O_{1.50}$	1.18	6.4×10^{-5}
0.50	$Dy_{0.50}Bi_{0.50}O_{1.50}$	1.19	8.1×10^{-4}

Table 3.4: Activation energy, pre-exponential factor and typical conductivity at 800 K.

Also, it needs to be noted here that the all the compositions have identical oxygen stoichiometry due to the isovalent character of Bi^{3+} and Dy^{3+}. Thus, the increasing ion mobility might be related to the facile percolation pathway in the rhombohedral structures. The better grain growth of the composites phases observed in the Bi^{3+} rich compositions might be a favorable condition for creating channels for the anion migration. In addition, Bi^{3+} has higher polarizability due to the presence of lone pair, which favours the ionic conductivity of anions.

The significantly higher conductivity at the composition with x = 0.50 can be attributed to the coexisting fluorite-type δ-Bi_2O_3 phase. As mentioned earlier, the δ-Bi_2O_3 and rare-earth doped stabilized δ-Bi_2O_3 type phases are fast oxide ion conductors due to excessive anion vacancy and disordered lattice. Though the electrical conductivity is appreciably high, the thermal and electrical stability of this composition will be limited due to the metastable nature of fluorite-type phase. However, the identified rhombohedral phase, though has lower conductivity compared to δ-Bi_2O_3 type phase but it has significantly higher conductivity compared to zirconia based ionic conductors. The ordered arrangements as inferred from the superstructure reflections may render a better structural stability to it compared to δ-Bi_2O_3 type phases. Further investigation on structural stability and conduction mechanism will be useful for delineating the potential of this ordered phase.

In order to investigate, the effect of nature of ionic radius of rare-earth ion and to compare with the result of the $Dy_{1-x}Bi_xO_{1.50}$ ($0.00 \leq x \leq 0.50$), an additional system, $Yb_{1-x}Bi_xO_{1.50}$ ($0.00 \leq x \leq 0.50$) is being explained in following section.

3.4. Result and discussion of $Yb_{1-x}Bi_xO_{1.50}$ ($0.00 \leq x \leq 0.50$)

3.4.1. XRD studies

The typical powder XRD patterns of the $Yb_{1-x}Bi_xO_{1.5}$ samples obtained after final sintering are shown in **Fig.3.8**. The phases present in various nominal compositions were identified by comparing XRD patterns of the successive compositions as well as with earlier reported standard X-ray diffraction data for end members i.e. Yb_2O_3 and Bi_2O_3. The XRD pattern for x = 0.00, agrees well with the reported data for cubic Yb_2O_3 (JCPDS-PDF 43-1037). All other compositions, i.e. with $x \geq 0.05$ show coexistence of a cubic rare-earth oxide (C) type and a fluorite (F) type phases. The increasing trend of intensity of the reflections attributable to F-type phase with the increase in x (**Fig.3.8**) suggests that the addition of Bi_2O_3 preferentially forms F-type phase. Further analyses of the diffraction patterns were carried out by Rietveld refinement of the XRD data. The details of the structural parameters of the different phases observed in this system are summarized in **Table 3.5**. Typical Rietveld refinement plots for the two end members of the studied system are shown in **Fig.3.9**. It is observed that the unit cell parameter of C-type phase increases from 10.4281(2) Å (at x = 0.00) to 10.4372(1) Å (at x = 0.05) and then remain almost unchanged with increasing x. This feeble expansion of unit cell parameter can be attributed to the incorporation of larger Bi^{3+} ion in the C-type lattice of Yb_2O_3. However, the presence of secondary phase even in the composition with x = 0.05 suggests only a limited incorporation of Bi^{3+} ions in the C-type lattice. It can be mentioned here that the structure of the C-type cubic lattice is closely related to the fluorite type lattice with ¼ of oxygen sites as vacant. The formation of body centered cubic lattice (space group $I2_13$) due to relaxation of oxide ions from disordered sites to

ordered sites has been mentioned in the discussion of XRD results of Dy_2O_3-Bi_2O_3 section. In this system also no evidence for the anion ordering has been observed either in C- type or F-type phases.

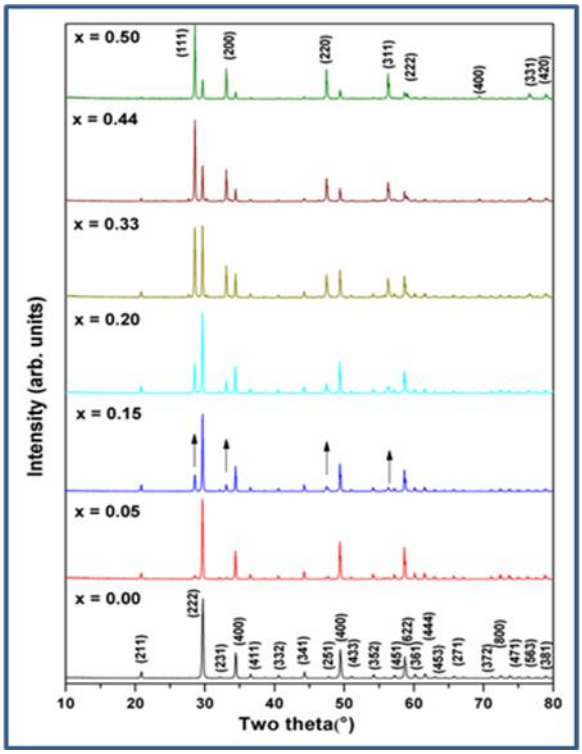

Fig.3.8: Powder XRD patterns of $Yb_{1-x}Bi_xO_{1.5}$ compositions. (indices for reflections of C-type phase are marked in bottom panel and for F-type phase are marked in top panel).

A comparison of the unit cell parameters of the F-type phases revealed almost similar values for all the fluorite-type phases observed in different nominal compositions (**Table 3.5**). This further confirms that the fluorite-type phase is formed with Bi_2O_3 lattice saturated with Yb^{3+} ions. The stabilization of δ-phase and the solubility of Yb_2O_3 in Bi_2O_3 have been reported in literature [106]. A comparison of unit cell parameters of various reported fluorite-type $Bi_{1-y}Yb_yO_{1.50}$ phases indicates a decreasing trend with the increase in y, viz. a = 5.519 Å ($Bi_{0.867}Yb_{0.143}O_{1.50}$) [JCPDF-41-02819], 5.469 Å ($Bi_{0.75}Yb_{0.25}O_{1.50}$), 5.419(1)Å and ($Bi_{0.65}Yb_{0.35}O_{1.50}$) [106] etc.

This observation is in accordance with the smaller ionic radius of Y^{3+} compared to Bi^{3+}. The unit cell parameters of the present observed F-type phases are comparable to the values earlier reported for $Bi_{0.65}Yb_{0.35}O_{1.50}$[106b]. Thus, it can be suggested that the F-type phase of the present study has a composition close to $Yb_{0.35}Bi_{0.65}O_{1.5}$. Considering $Yb_{0.35}Bi_{0.65}O_{1.5}$ as the composition of fluorite type phase, quantitative analyses of the XRD data of $Yb_{0.50}Bi_{0.50}O_{1.50}$ indicated the fraction (wt %) of F- and C-type phases are 24(1) % and 76(1) %, respectively

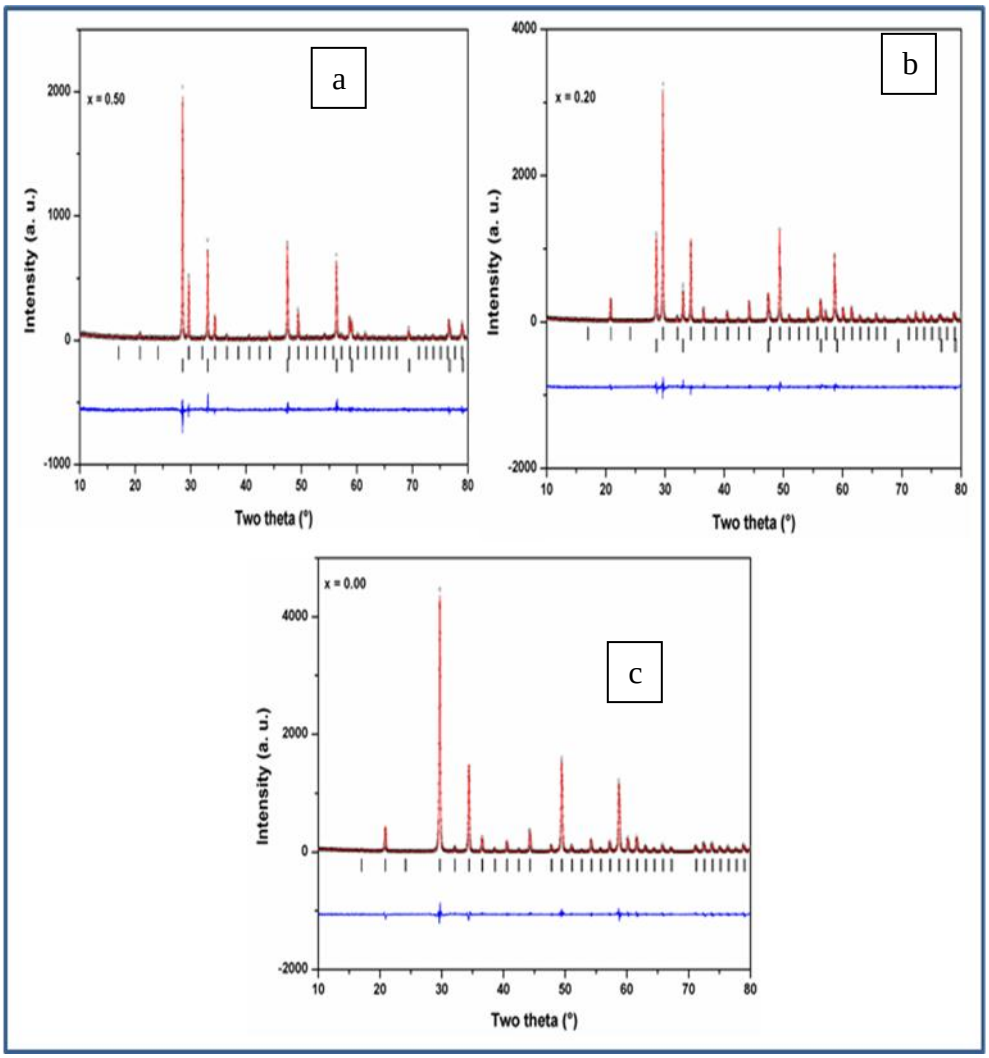

Fig.3.9: Rietveld refinement plots for representative $Yb_{1-x}Bi_xO_{1.50}$ compositions. (vertical ticks indicates Bragg positions. upper: (a,b: C-type)(c: F-type).

x	Nominal composition	C-Type						F-Type				R_p. R_{wp}, χ^2
		a (Å)	*V(Å)^3*	*Yb2 (x,0,1/4)*	*O (x,y,z)*	*Bov (Å)^2*	*R_F*	*a (Å)*	*V (Å)^3*	*Bov (Å)^2*	*R_F*	
0.00	$Yb_{1.00}Bi_{0.00}O_{1.50}$	10.4281(2)	1134.02(3)	-0.0322(1)	0.391(1), 0.154(1), 0.383(1)	0.32(5)	2.49	-	-			10.4, 15.7, 1.47
0.05	$Yb_{0.95}Bi_{0.05}O_{1.50}$	10.4372(1)	1136.99(2)	-0.0326(1)	0.387(1), 0.151(1), 0.382(2)	0.26(6)	2.94	5.4165(12)	158.91(6)	4.0(5)	5.40	12.5, 19.3, 1.31
0.10	$Yb_{0.90}Bi_{0.10}O_{1.50}$	10.4368(1)	1136.84(3)	-0.0323(2)	0.392(1), 0.151(1), 0.384(2)	0.29(7)	2.78	5.4191(7)	159.14(4)	3.9(3)	3.67	12.7, 18.9, 1.48
0.15	$Yb_{0.85}Bi_{0.15}O_{1.50}$	10.4363(1)	1136.68(2)	-0.0323(2)	0.392(1), 0.156(1), 0.384(2)	0.34(7)	2.57	5.4176(4)	159.01(2)	3.6(2)	3.09	12.5, 17.1, 1.64
0.20	$Yb_{0.80}Bi_{0.20}O_{1.50}$	10.4365(1)	1136.76(3)	-0.0323(2)	0.391(2), 0.153(2), 0.385(2)	0.50(8)	2.94	5.4181(3)	159.05(1)	3.9(1)	2.55	12.2, 16.9, 1.49
0.33	$Yb_{0.67}Bi_{0.33}O_{1.50}$	10.4361(3)	1136.61(5)	-0.0326(3)	0.393(3), 0.151(3), 0.391(3)	0.4(1)	5.11	5.4176(2)	159.01(1)	4.1(1)	4.11	14.1, 20.0, 1.84
0.44	$Yb_{0.56}Bi_{0.44}O_{1.50}$	10.4361(4)	1136.62(7)	-0.0317(4)	0.392(4), 0.157(4), 0.392(4)	0.3(1)	9.26	5.4180(2)	159.05(1)	4.3(1)	4.30	14.9, 20.8, 2.24
0.50	$Yb_{0.50}Bi_{0.50}O_{1.50}$	10.4343(4)	1136.03(8)	-0.0321(5)	0.396(5), 0.151(5), 0.395(5)	0.4(2)	8.76	5.4177(1)	159.02(1)	3.8(1)	2.69	14.3, 19.9, 1.44

Table 3. 5: Refined unit cell and structural parameters of the C- and F- type phases in $Yb_{1-x}Bi_xO_3$ compositions.

C-Type: Yb_2O_3 type phase, Space group: *Ia-3* (No. 206). Yb1: *8b (¼,¼,¼)*; Yb2: *24d (x, 0, ¼)*; O: *48e (x,y,x).*

F-Type: Fluorite type δ-Bi_2O_3 phase, Space Group: *Fm3m* (No. 225). Bi:Yb: *4a (0,0,0)*, occ. 0.65:35; O: *8c (¼,¼,¼)*, occ: 0.75.

Further, in any of the present observed XRD patterns no evidences for the formation of earlier reported cation or anion ordered phases like orthorhombic ($Bi_8Ln_{10}O_{27}$, $Bi_{17}Ln_7O_{36}$ types) [102,105], rhombohedral ($Bi_3Ln_5O_{12}$ type) [101d], monoclinic ($Bi_2Ln_4O_9$ type) [101c,103,107] or triclinic $BiYbO_3$ type [105] are observed. Thus, from the XRD studies it can be concluded that the Bi^{3+} deficient region of $Yb_{1-x}Bi_xO_{1.50}$ system exist as composites of feebly Bi^{3+} doped Yb_2O_3 and fluorite type $Bi_{1-y}Yb_yO_{1.50}$ with y ~ 0.35 composition. The observed powder XRD patterns do not show any evidence for the formation of high pressure or moderate temperature phases of Bi_2O_3 as mentioned earlier. Thus, the existence of fluorite-type δ-Bi_2O_3 phase and C-type body centered cubic phase is concluded from the present XRD study.

3.4.2 Raman spectroscopic studies

In order to further understand the nature of phases formed in this composite system, Raman spectroscopic investigations were carried out. Raman spectroscopy being a sensitive method to study the local coordination spheres, the exact nature of bonding and distortion around the ions can be clearly obtained.

The typical Raman spectra of the final sintered $Yb_{1-x}Bi_xO_{1.5}$ samples are shown in the **Fig.3.10**. The Raman spectrum of x = 0.00 composition shows a strong band at 365 cm^{-1} and several weak bands at 97, 121, 134, 135, 315, 340, 439, 469 and 612 cm^{-1}. All these observed Raman bands are in agreement with the C-type cubic structure of Yb_2O_3 [108]. From the factor group analyses, 22 Raman active modes have been predicted for C-type cubic lattice of rare-earth sesquioxides [109]. However, all the Raman modes have never been observed experimentally and most often the strong mode observed around 365 cm^{-1} is used as a characteristic of C-type cubic

structure [108-109]. This high intensity Raman mode has been assigned to a combination of stretching and bending (F_g+A_g) mode, i.e. due to oxygen motion and deformation of YbO_6 octahedral units where large variation in polarizability occurs [108-109]. Comparing the earlier reported modes for C-type sesquioxides, the low frequency Raman modes (below 135 cm^{-1}) observed for x = 0.00 composition can be assigned to the oscillation of the O-Yb-O and Yb-O-Yb bond angles and a weak mode around 612 cm^{-1} can be assigned to the pure stretching (A_g) mode of Yb-O bonds [110].

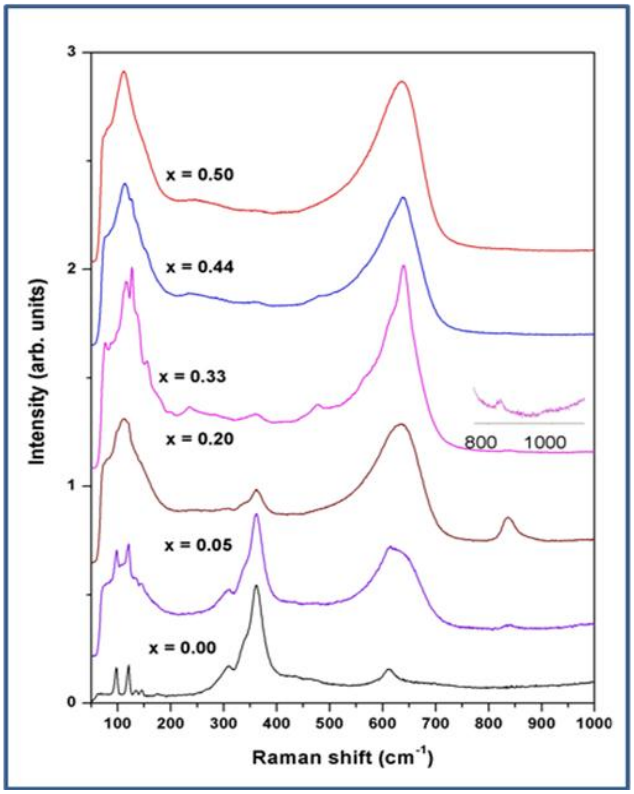

Fig.3.10: Raman spectra of $Yb_{1-x}Bi_xO_{1.50}$ compositions.

The evolution of Raman spectra with the increasing Bi^{3+} contents indicates the appearance of a new intense and broad peak around 650 cm^{-1} in addition to the peaks due to C-type phase. This new peak could be assigned to fluorite-type δ-Bi_2O_3 phase. The Raman spectra of stabilized δ-Bi_2O_3 type phase usually show two broad intense

peaks, one at medium frequency (around 580-640 cm^{-1}) due to the deformation of the oxygen defect containing cubic BiO_8 polyhedra and another below 200 cm^{-1} due to the bending or rotation of Bi-O-Bi or O-Bi-O [109,111]. The Raman spectrum observed for x = 0.50 composition shows two broad peaks around 116 and 638 cm^{-1}, which can be assigned to the F-type stabilized δ-Bi_2O_3 phase. Significantly broadened peaks are usually observed in F-type δ-Bi_2O_3 phase due to disordered oxygen defects in the structure. The presence of C-type phase at the composition with x = 0.50 is inferred from the existence of a weak peak at 365 cm^{-1} attributable to the most intense line of the C-type Yb_2O_3. Such features are observed in the Raman spectra of all intermediate compositions, which confirm the coexistence of C-and F-type phases in them. However, the Raman spectra of the composition with x = 0.05, 0.20 and 0.33 show a new peak around 840 cm^{-1}, which is not observed in fluorite type or C-type phase of rare-earth sesquioxides or any other intermediate ordered phases reported in Ln-Bi-O system [108a,111]. Mandal et al. [108b] have observed a similar peak in anion rich C-type solid solution compositions. In the present case any anion excess structure is not expected due to similar oxidation states of Yb^{3+} and Bi^{3+}. Comparison of Raman spectra of various phases Bi_2O_3 indicates that γ-Bi_2O_3 which is formed at an intermediate temperature between 700-750°C, has a peak around 827-840 cm^{-1} [112] Thus, the present observed peak around 840 cm^{-1} might be due to the presence of small amount of γ-Bi_2O_3 which could not be detected by XRD studies. Further, it can be noticed from the Raman spectra of the x = 0.33 and 0.44 compositions, the intense Raman modes assigned to the stabilized fluorite type solid solution phase has several shoulder like features (around 476, 564, 614 cm^{-1}). These peaks might be due to local ordering of Yb^{3+} and Bi^{3+} within the stabilized F-type Bi_2O_3 phase but without any

long range ordering to assign any distinct intermediate phases. Earlier, Rubben et al. [111] have reported a number of overlapping Raman modes between 50 to 600 cm^{-1} in the triclinic $YbBiO_3$ and orthorhombic $Yb_7Bi_{17}O_{36}$ (i.e. x = 0.50 and x = 0.71). Thus, a possible formation of smaller domains of such phase in these compositions cannot be ruled out. The XRD patterns reported for such complex phases have several new peaks as well as splitting of intense peaks [105,113]. However, the XRD patterns of the present studied compositions do not show such features. Thus, it can be suggested that the F-type phase observed in this study may have local clustering of defects which are not reflected in long range periodicity.

Hardcastle and Wachs [109] have reviewed Raman spectra of a large number of diversified bismuth containing compounds and proposed an empirical relation between stretching frequencies (ν) and Bi-O bond lengths of BiO_n polyhedra. According to the authors, stretching frequency (ν) and distance between the Bi and O of BiO_n polyhedra (d) are related as $\nu(cm^{-1}) = 92760 \times e^{-2.511d})$. In F-type phases, the observed peak around 638 cm^{-1} indicates a Bi-O bond length of about 1.98 Å. From the XRD studies, the average (Bi,Yb)-O bond lengths are 2.34 Å (for F-type phases) and 2.12 to 2.35 Å (for C-type phases). Due to smaller ionic radii of the Yb^{3+} (0.87 Å) compared to the Bi^{3+} (1.03 Å), the formations of local clusters with a range of bond lengths in F-type phase are expected and they may be reflected in a number of Raman peaks. This suggests that the F-type structure observed in rare-earth doped Bi_2O_3 phases is likely to have highly distorted coordination polyhedra. Thus, from the X-ray diffraction and Raman spectroscopic studies, it can be inferred that all the compositions except x = 0.00 have coexistence of the F- and C-type phases.

3.4.3. SEM studies

The SEM images of some representative sintered samples are shown in **Fig.3.11.** The SEM images of $Yb_{0.95}Bi_{0.05}O_{1.5}$ revealed porous structure and poor grain growth, while the compositions with higher x values have well grown and inter-connected grains. The poor sinterability for the C-type phases is evident from the higher melting temperature of Yb_2O_3 compared to Bi_2O_3 as in the case of Dy_2O_3-Bi_2O_3 system.

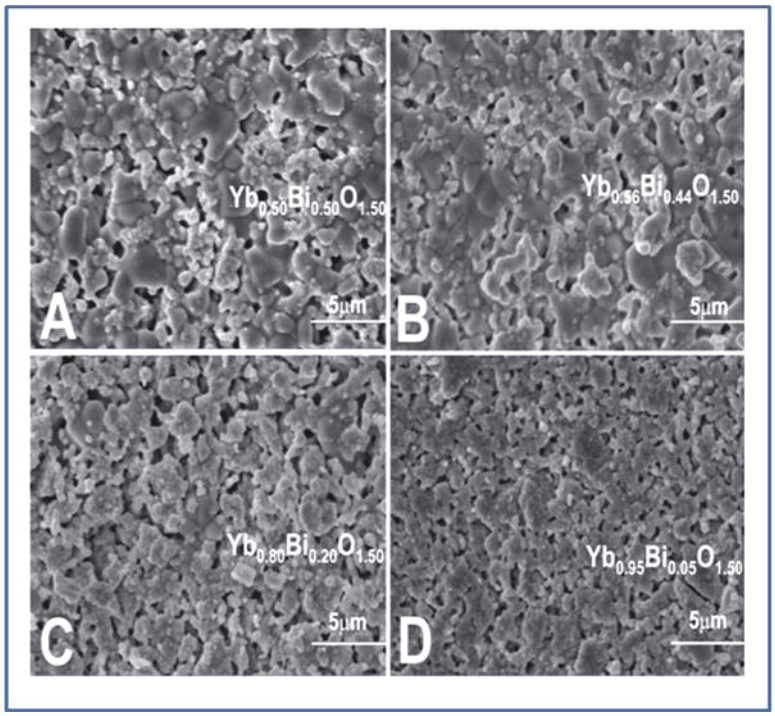

Fig.3.11: SEM images of $Yb_{1-x}Bi_xO_{1.5}$ compositions (A: x = 0.5; B: x = 0.44; C: x = 0.20and D: x = 0.05) at 10K magnification.

3.4.4. Electrical properties

The electrical properties of the sintered samples (~ 90 % of theoretical density (TD) of all except for x = 0.00 (~ 65 % of TD) were investigated from the *ac*-impedance measurements. The *ac* conductivities of all the compositions were studied from ambient to 973 K. Reliable impedance data could be measured only above 673 K

for compositions with x ≥ 0.05 and they were analyzed. Typical composition and temperature dependent Z' vs Z'' plots are shown in **Fig.3.12 (a and b)**.

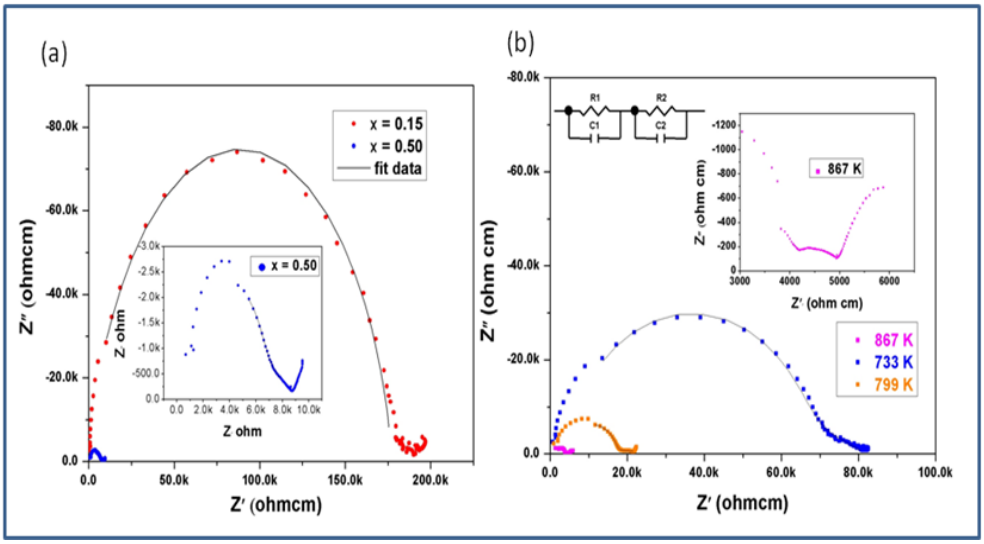

Fig.3.12: (a). Typical Z' vs Z'' plots for x = 0.15 and 0.50 compositions of $Yb_{1-x}Bi_xO_{1.50}$ at 773 K (inset shows expanded data observed for x = 0.50) (b). $Yb_{0.80}Bi_{0.20}O_{1.50}$ at 867,733 and 799 K (inset shows expanded data observed at 867 K) (Fit data are shown as solid lines).

All the data show large semicircles at high frequency end while very weak small and depressed semicircles at the low frequency end. The impedance data observed below the electrode responses (i.e. ~ 10^6 Hz) were analyzed by using equivalent circuit models. The diameters of the arcs indicate the low resistance of the grain boundaries compared to the bulk grains. Due to the highly overlapping contributions of the grain and grain boundaries, the data could not be explained by the simple circle fitting method. Hence all the data analyses were carried out by non-linear least square (NLLS) analyses assuming different equivalent circuit models. It is important to note here that the high temperature impedance data needs different equivalent circuit models for better NLLS regression. For example, at lower temperature the data of all the samples can be modeled by considering two RC circuits while as the temperature increases one

diffusive capacitor component is required to model the data. The impedance data for the compositions with x ≥ 0.05 were analyzed by using two *RC* or one *RC* and one *R-CPE* (R = Resistances, C = Capacitance and CPE = Constant Phase Element) circuits in series configuration.

The total conductivity (σ) of the studied samples was extracted from the measured total resistances and they are shown **Fig.3.13**. The variation of conductivity with temperature could be fitted with Arrhenius equation ($ln\sigma = ln\sigma_0 - E_a/kT$), where σ_0 = pre exponential factor, E_a = activation energy, k = Boltzmann's constant). Typical conductivities and activation energies for different compositions are given in **Table 3.6**.

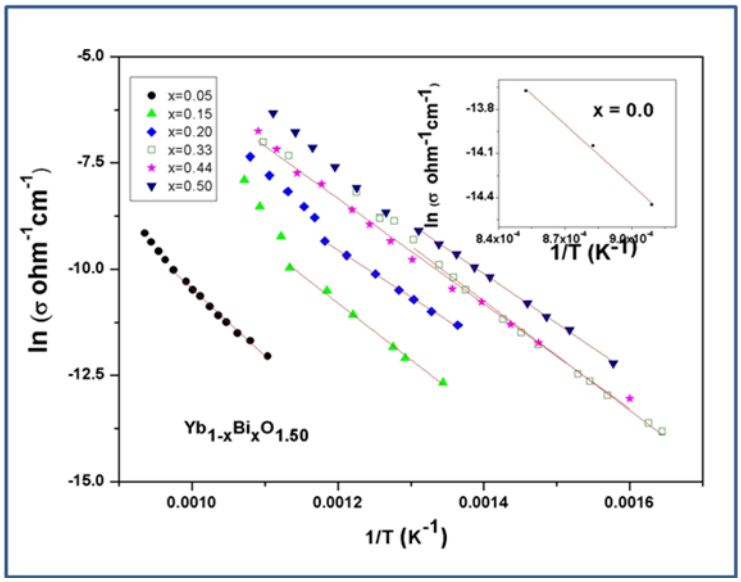

Fig.3.13: Variation of conductivity of $Yb_{1-x}Bi_xO_{1.50}$ compositions with temperature (variation of conductivity Yb_2O_3 is shown as inset). Continuous lines are Arrhenius equation data.

Pure Yb_2O_3, does not exhibit any reliable impedance data up to about 1100 K. The impedance data for Yb_2O_3 could be well explained by using two RC circuit elements in series combination. The observed conductivity of Yb_2O_3 at 1100 and 1173 K are

about 5.3×10^{-7} and 1.1×10^{-6} $ohm^{-1}cm^{-1}$, respectively [114]. Typical values of resistances for the grain interior and grain boundary for Yb_2O_3 at 1100 K are about 1.8×10^4 and 3.4×10^5 ohm, respectively. The higher resistance offered at the grain boundary compared to the grain interior implies the tunneling of anions in the ordered lattice of the grains compared to the grain boundary. Subba Rao et al. [114] have investigated the electrical properties of a series of rare-earth oxides and revealed very low conductivities ($\sim 10^{-9}$ $ohm^{-1}cm^{-1}$) below 923 K. Predominantly electronic conductivity in the rare-earth sesquioxides have been reported in literature. This is in accordance of the present temperature dependent electrical behavior of Yb_2O_3. It can be mentioned here that the C-type cubic lattice of Yb_2O_3 is closely related to anion deficient fluorite structure. But the ordered arrangements of anions in C-type lattice inhibit the ease of anion migration. At higher temperature due to large contribution of vibration energy to overcome the activation barrier of the anion diffusion renders ionic conductivity in them. As mentioned earlier, the compositions with $x > 0.0$ have a coexisting fluorite-type phase and the fraction of this phase systematically increases with the increase in the x values. The phase fraction of the fluorite-type phase is reflected in their electrical properties. The impedance data for the compositions with $x = 0.05$ were analyzed with one RC and one R-CPE circuit in series configuration while those with higher values x were analyzed by using two R-CPE circuits in series configuration. Besides, the compositions with $x \geq 0.2$ show deviations in the variations of conductivities with temperature. Often, such discontinuities are not observed in stabilized single phasic δ-Bi_2O_3 phase. The observed discontinuity might be related to relaxation of lattice strain in the composite phases. Changeover of conduction mode in the due to breaking of defect clusters. It can be mentioned here

that the conductivity observed even at x = 0.20 (4.1×10^{-4}ohm^{-1} cm^{-1}, at 900 K) is significantly higher compared to that reported for 8-YSZ (~ 1×10^{-4}ohm^{-1}cm^{-1}) at similar temperature [115]. However, the maximum observed conductivity in the studied composites is lower compared to that reported for fluorite type $Bi_{0.75}Y_{0.25}O_{1.5}$ and doped CeO_2 based electrolytes [27a,116].

x		$\sigma_{765\ K}$ (Scm^{-1})	$\sigma_{900\ K}$ (Scm^{-1})	E_a (eV)
0.00	$Yb_{1.00}Bi_{0.00}O_{1.50}$	-	-	-
0.05	$Yb_{0.95}Bi_{0.05}O_{1.50}$	-	5.9×10^{-6}	1.36
0.15	$Yb_{0.85}Bi_{0.15}O_{1.50}$	5.6×10^{-6}	2.0×10^{-4}	1.15
0.20	$Yb_{0.80}Bi_{0.20}O_{1.50}$	2.2×10^{-5}	4.1×10^{-4}	0.95
0.33	$Yb_{0.67}Bi_{0.33}O_{1.50}$	9.0×10^{-5}	7.6×10^{-4}	1.11
0.44	$Yb_{0.56}Bi_{0.44}O_{1.50}$	5.7×10^{-5}	9.0×10^{-4}	1.06
0.50	$Yb_{0.50}Bi_{0.50}O_{1.50}$	1.1×10^{-4}	1.8×10^{-3}	1.01

Table 3.6: Typical conductivities (σ) and activation energies (E_a) of $Yb_{1-x}Bi_xO_3$ composites.

In addition, it is observed that the typical conductivities for the compositions with $0.33 \leq x \leq 50$ have nearly similar magnitude and behavior. This may be attributed to the predominant conductivity of the stabilized fluorite phase. However, at lower x values, the conductivities arise from the grains of fluorite phase and interfacial conductivity of the stabilized δ-Bi_2O_3 and Yb_2O_3 phases. The low interfacial resistances due to the highly defective arrangement of ions of the two coexisting phase is an important factor to enhance the ionic conductivity. Several studies indicating such enhancement of ionic conductivity by addition of secondary phases to a moderate or non conducting material are reported earlier [117]. The ease of percolation of ions

at the interface due to highly defective and relaxed arrangement structure has been attributed to such behavior [117-118]. A comparison of compositional dependent Cole-Cole plots of $Yb_{1-x}Bi_xO_{1.50}$ suggests that the grain boundaries has highly depressed semicircle with low resistance than the grains. Thus, the interface of the resistive Yb_2O_3 and conducing δ-Bi_2O_3 plays a dominating role in governing the total conductivity of the present study.

3.5. Conclusion

Detailed analyses of phases in $Ln_{1-x}Bi_xO_{1.5}$ ($0.00 \leq x \leq 0.50$) [Ln = Dy and Yb] systems were performed. In case of $Dy_{1-x}Bi_xO_{1.5}$, composite systems coexistence of C-type cubic and rhombohedral or rhombohedral and δ-Bi_2O_3 type phases were observed in all compositions except x = 0.44. In case of $Yb_{1-x}Bi_xO_{1.5}$ ($0.00 \leq x \leq 0.50$) composite system, Bi^{3+} doped Yb_2O_3 and about 35 % Yb^{3+} doped Bi_2O_3 phases were observed. An appreciable dispersion of Bi-O bonds in the F-type phase is indicated in Raman spectroscopy study. The ionic conductivity studies of both the composites revealed a systematically increasing trend with temperature and Bi^{3+} content. The activation energies obtained by the Arrhenius equation are marginally different in all the studied compositions, while the pre-exponential factor increases with Bi^{3+} content. Among the Dy_2O_3 and Yb_2O_3 the bond energy of Yb-O is greater than the Dy-O. Hence, $Yb_{1-x}Bi_xO_{1.50}$ ($0.00 \leq x \leq 0.50$) expected to show lower conductivity. However, the size difference between Yb^{3+} and Bi^{3+} is more compared to Dy^{3+} and Bi^{3+}. Due to this large size difference, small substitution of dopant results in the large distortion in the host lattice and preferentially stabilizes the fluorite phase in $Yb_{1-x}Bi_xO_{1.50}$ ($0.00 \leq x \leq 0.50$). Hence $Yb_{1-x}Bi_xO_{1.50}$ compositions have the comparable conductivity as those of $Dy_{1-x}Bi_xO_{1.50}$ compositions.

CHAPTER 4

STUDIES ON STRUCTURAL AND ELECTRICAL PROPERTIES OF $Pr_2B_2O_7$ TYPE COMPOUNDS (B^{4+} = Zr^{4+} AND Ti^{4+})

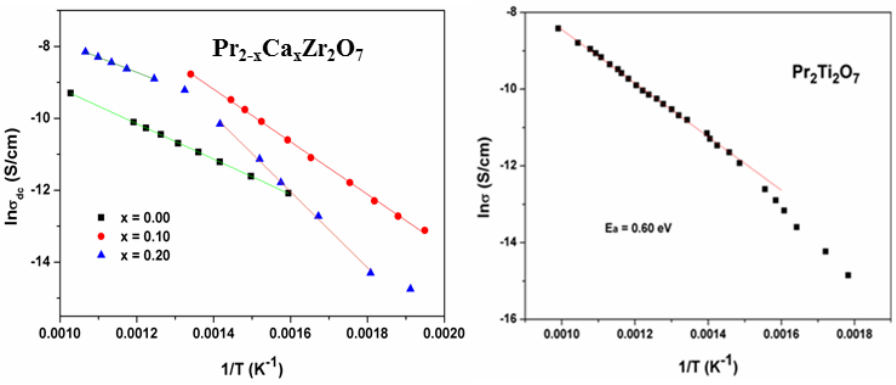

1. Structure, thermal and electrical properties of calcium doped pyrochlore type praseodymium zirconate
   K. Vasundhara, S. N. Achary and A. K. Tyagi
   Int. J. Hydrogen Energy 40 (2015) 4252-4262.

2. Structure and electrical properties of layered perovskite type $Pr_2Ti_2O_7$: Experimental and theoretical investigations
   S. J. Patwe , **K. Vasundhara**, N. P. Salke, S. K. Deshpande, R. Rao, M. K. Gupta, R. Mittal, S. N. Achary and A. K. Tyagi
   J. Mater. Chem. 3 (2015) 4570-4584.

4.1. Introduction

$A_2B_2O_7$ type compositions with A = trivalent rare-earth ions and B = tetravalent ions, like Ti^{4+}, Zr^{4+}, Hf^{4+} and Sn^{4+}, have been of interest due to their interesting crystal chemistry and several technological applications. Depending on the radius of the cations, the $A_2B_2O_7$ type compositions of rare-earth ions can be grouped in three categories, namely fluorite ($r_A/r_B < 1.48$), pyrochlore ($1.48 < r_A/r_B < 1.78$) and perovskite-type ($r_A/r_B > 1.78$) structures [5a]. Thus, wide varieties of structure-types are expected for the $A_2B_2O_7$ compositions and each structure-type forms a specific domain of technological application. In the fluorite-type $A_2B_2O_7$ composition, both A and B cations are randomly distributed over the cation positions of the fluorite lattice while one anion vacancy and oxygen atoms are randomly distributed over the anion positions of the fluorite lattice. Thus, both the metal ions have cubical coordination of oxygen ion and vacancy as cube corner. In the pyrochlore-type structure of the $A_2B_2O_7$ composition, the A and B cations form eight and six coordinated polyhedra, respectively [5a]. The structure of pyrochlore is closely related to the fluorite structure except the cations and vacancies are ordered in the former. Such ordering transforms the Fm3m symmetry of the fluorite to Fd3m symmetry in pyrochlore and double the unit cell parameter. The preferential coordination of the cations is favored only in appropriate cation combinations governed by the ratio of radius of the cations (r_A/r_B = 1.46 to 1.78) and thus, the structure is formed only with cations of appropriate ionic radii and charge combinations. In the perovskite-type structure of the $A_2B_2O_7$ composition, the B cations form six coordinated polyhedra and form a network similar to the ReO_3 type structure and a part of the A-type cations are occupied in the interstices of the octahedral frame while others form distinct coordination. The

positions of later cation fraction slice the perovskite-type network and thus makes the structure as a layered perovskite structure. Such layered perovskite structure exhibit diversified symmetries, ranging from tetragonal, orthorhombic and monoclinic, depending on the distortion and tilting of the octahedra in the lattice. For Ti^{4+} as B site cation, the $A_2B_2O_7$ type rare-earth (RE) titanates form monoclinic perovskite-type structure for RE = La, Nd and Pr while rest of the lanthanides form cubic pyrochlore-type structure [119]. The monoclinic perovskite-type titanates have been of attraction due to their high Curie temperature ferroelectric and piezoelectric properties, high dielectric constants, non-linear optical and photocatalyic properties [120].

In order to investigate the structure dependent properties, two different materials from these two classes, namely $Pr_2Zr_2O_7$ (pyrochlore-type) and $Pr_2Ti_2O_7$ (perovskite-type) have been selected and their detailed structural and electrical properties have been investigated. The salient details of these studies are explained in this chapter.

4.2. Pyrochlore-type $Pr_2Zr_2O_7$

The pyrochlore-type structure has been reported for $Ln_2Zr_2O_7$ (Ln–Rare-earth) type zirconates [121]. Among the rare-earth zirconates, the zirconates of Pr and Ce have additional importance due to the possible existence of multivalent cations in the structure. Materials exhibiting both ionic as well as electronic conduction, called as Mixed Ionic Electronic Conduction (MIEC) materials, which can be promising electrodes for effective transfer of the oxygen to the electrolytes in SOFC [122]. Thus, such MIEC materials are desired for effective fuel cell, as the undue degradation of electrode and electrolyte interface under operation can be circumvented. The oxygen stoichiometry of such pyrochlore-type materials can be controlled by aliovalent

substitution of the A or B site cations. In order to increase oxide ion conduction, a number studies with alio or isovalent cation substituted pyrochlore structure are reported in literature [121a-d,121h,123]. It is observed that, the isovalent substitution stabilizes the structure in a wider range and ionic conductivity is governed by the anion or cation ordering in the lattice [121h,123c,124]. However, aliovalent (A^{2+}) substitution of the rare-earth sites is only limited due to preferential formation of secondary phases. The studies on $Sm_{2-x}Ca_xZr_2O_{7-\delta}$ indicate the formation of single phase pyrochlore structure within x = 0.20 [123a]. The oxygen ion conductivity of such solid solutions shows an increasing trend with increasing Ca^{2+} contents. Similar studies on electrical properties of $Y_{2-x}Ca_xTi_2O_{7-\delta}$, $Gd_{2-x}Sr_xZr_2O_{7-\delta}$, $Nd_{2-x}Sr_xZr_2O_{7-\delta}$, $La_{2-x}Ca_xZr_2O_{7-\delta}$ etc. indicate an increasing conductivity with the increase in alkaline earth metal concentrations, which have been attributed to the increasing anion vacancies in the structure [121b,123a,123b]. However, in such alkaline earth substituted pyrochlores, the segregation of perovskite-type phase beyond solubility limit decreases conductivity. Studies on single phase pyrochlore-type $La_{2-x}Ca_xZr_2O_{7-\delta}$ ($0.0 \leq x \leq 0.07$) compositions show maximum conductivity at x = 0.05 [121b]. The variations of ionic conductivity in these compositions have been explained on the basis of concentration and clustering of vacancies. Most importantly, the rare-earth pyrochlores, in particular the lighter rare-earth ions can exhibit proton conduction as well as oxide ion conduction depending on the conditions of measurements. It can be envisaged that the cations exhibiting multiple valences can be of importance to introduce electronic conductions. As mentioned earlier, the possible existence of mixed valence states of Ce or Pr, the zirconates of Ce and Pr are likely to be important candidates for such properties. It has been reported in literature that the pyrochlore-

type cerium zirconates can easily introduce mixed Ce^{3+} and Ce^{4+} which are effective to control the ionic and electronic conduction [121a,121c-g]. The higher stability of Pr^{3+} compared to the Ce^{3+} is expected to make $Pr_2Zr_2O_7$ better mixed ionic and electronics conductor. Also, it has been reported in literature that substitution of Pr^{3+} in zirconia and other oxide ion conductors exhibit electronic conductivity along with ionic conductivity. In this present study, the structural and electrical properties Ca^{2+} substituted pyrochlore-type $Pr_2Zr_2O_7$ have been investigated and they are presented in subsequent section.

4.3. Experimental method

4.3.1. Preparation of $Pr_{2-x}Ca_xZr_2O_7$ ($0.0 \leq x \leq 0.20$)

Stoichiometric compositions of $Pr_{2-x}Ca_xZr_2O_7$ ($0.0 \leq x \leq 0.20$) ceramic samples were prepared by a combined gel combustion and high temperature reaction method. Reagent grade chemicals such as Pr_6O_{11}, $Ca(NO_3)_2$ and zirconium oxy nitrite [$ZrO(NO_3)_2$] were used as starting materials for preparation. Weighed quantities of appropriate reactants for desired composition were dissolved in 1:1 ratio of HNO_3:H_2O solution. Calculated amount of glycine was added to the above solution. The solution was slowly heated until the solution becomes viscous gel which on further heating undergoes auto-ignition and form fluffy powder product. The synthesized powder was calcined at 973 K to remove the residual carbon in the sample. The pellets of calcined powder were then heated at 1523 K for 48h under flowing Argon-Hydrogen (95:5 volume ratio) atmosphere.

4.3.2. Preparation of $Pr_2Ti_2O_7$

The polycrystalline sample of $Pr_2Ti_2O_7$ was prepared by solid state reaction of appropriate amounts of Pr_6O_{11} and TiO_2. Pr_6O_{11} was preheated at 1073 K to remove

any adsorbed moisture and lower valent Pr^{3+} then desired for stoichiometry. TiO_2 was heated at 1273 K to remove any adsorbed moisture or hydroxyl groups. About 7 g of the homogenous mixture was prepared by mixing stoichiometric amounts of the reactants in acetone media. The mixed powder were pressed into pellets of about 1 inch diameter and 5 mm height and slowly heated to 1173 K and held for about 24 h and then cooled to ambient temperature. The pellet was rehomogenized and heated at 1100°C for another 24 h. The completion of the reaction is ensured in after this heating step. The pellet was again rehomogenzied and pelletized to 1 cm diameter and 2 mm height and then sintered at 1473 K for 24 h and slowly cooled (at the rate of 2 °C/min) to ambient temperature. Well sintered pellets of dark green color were obtained after this heat treatment and they were used for all the studies.

The final products [$Pr_{2-x}Ca_xZr_2O_7$ ($0.0 \leq x \leq 0.20$)] were characterized by X-ray diffraction (XRD) technique by using X'Pert Pro powder X-ray diffractometer (PANalytical, Netherland). CuKα radiation (λ = 1.5406 and 1.5444 Å) was used for recording the diffraction pattern. Diffraction data were collected in the two theta range of 10-80°, with step width and step time of 0.02° and 3 sec. Whereas, in case of $Pr_2Ti_2O_7$ the product was characterized powder XRD data recorded on a rotating anode based X-ray diffractometer (Rigaku, Japan) using monochromatized Cu-Kα radiation. Powder sample of $Pr_2Ti_2O_7$ was pressed into a groove of about 1 mm of a glass sample holder and XRD data were collected from 5 to 100° with step width of 0.02° and time per step is 5 sec.

The *in situ* high temperature XRD patterns of both the samples were recorded in static air on a Philips X'Pert Pro diffractometer equipped with Anton Parr high temperature attachment. The XRD patterns were recorded in the two-theta range of

10-70° with step width and step time as 0.02° and 1.5 seconds, respectively. The powder XRD data were analyzed by Rietveld refinement program using GSAS and Fullprof 2000 software packages. The Raman spectra of the $Pr_{2-x}Ca_xZr_2O_7$ ($0.0 \leq x \leq 0.20$) compositions were recorded in the frequency range of 200 to 800 cm^{-1} using STR-300 micro-Raman spectrometer (SEKI Technotron, Japan). Whereas in case of $Pr_2Ti_2O_7$ Raman spectroscopic measurements at high temperature in the range 298–1073 K were carried out using the temperature stage from Linkam (Model-TS 1500). The spectra were recorded in back-scattering geometry. Samples were excited at 532 nm (power ~20 mW at the sample spot) and the scattered light was detected by a thermo-electric cooled charge-coupled device (CCD).

Thermal stability and oxidation behavior of the sample was studied by thermogravimetry using Setaram thermobalance in dry oxygen and argon atmosphere. The thermogravimetric (TG) and differential thermal analyses (DTA) traces were recorded by heating about 100 mg of sample to 1673 K on the thermobalance. Typical heating rate 10 K/min was used for recording the TG-DTA data. The residue obtained after heating the TG-DTA runs were also characterized by powder XRD data.

For impedance measurements, a cylindrical pellet of about 80 % of theoretical density was used. Platinum paste was applied on two parallel faces for better electrical contacts. The dielectric properties of the pellets were measured in a parallel-plate capacitor configuration using flat gold-plated electrodes. Low temperature (173 to 473 K) impedance measurements were carried out by using Novocontrol Alpha AN impedance analyzer (Novocontrol Technologies, Germany) and Quatro nitrogen cryosystem. The complex dielectric data were recorded at a series frequency range of 100 Hz to 5 MHz at several temperatures while heating from 173 K to 473 K. The

electrical properties between RT to 1073 K were investigated by using an impedance analyzer (Solartron 1260, Hampshire, U.K). The impedance data were measured in the frequency range of 1MHz to 1 Hz at several temperatures while heating the sample. The dielectric and impedance data were analyzed by using Winfit and Z-view software packages.

The microstructure of $Pr_2Ti_2O_7$ sintered samples was studied by using scanning electron microscope (Ziess Germany). The micrographs at different magnifications were recorded on sintered and fractured surfaces of pellets. The field dependent electric polarizations (PE-loops) were recorded at ambient temperature by using Aixacct TF2000 (Aixacct GmbH, Germany) ferroelectric analyzer. Polarization data were measured by using platinum paste coated sintered sample at several ac frequencies.

4.4. Results and discussion of $Pr_2Zr_2O_7$

4.4.1. XRD studies

The powder XRD patterns of the $(Pr_{1-x}Ca_x)_2Zr_2O_7$ compositions obtained after heating at 1523 K for 10 h are shown in **Fig.4.1**. Formation of single phase pyrochlore- type structure was observed for the x = 0.00 and 0.10 compositions while the composition with x = 0.20 indicates the presence of additional segregated phase (marked in **Fig.4.1**). The additional peaks observed (at two-theta ~ 29.5, 34.2, 58.5°) in the XRD pattern of the composition with x = 0.20 could be assigned to CaO stabilized ZrO_2 (JCPDF-84-1829) phase (CSZ). A comparison of the XRD patterns for the compositions with x = 0.1 and 0.2 with that of x = 0.00 indicates that the positions of peaks shift appreciably towards higher angle up to x = 0.1 and then marginally even at x = 0.20. These facts indicate contraction of the unit cell volume with increasing

Ca^{2+} content and limited solubility of Ca^{2+} in $Pr_2Zr_2O_7$ lattice. The observed unit cell parameter of the pyrochlore phase for the compositions with x = 0.00, 0.10 and 0.20 are: 10.7096(1), 10.6835(3) and 10.6798(4) Å, respectively. The observed unit cell parameters of x = 0.00 composition is little higher than those reported earlier in literature [125].

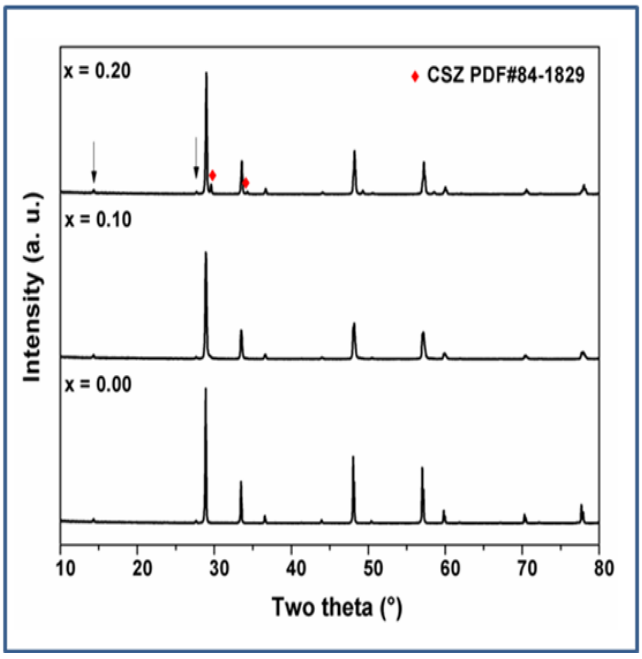

Fig.4.1: Powder XRD pattern of $Pr_{2-x}Zr_2Ca_xO_7$ (x = 0.0, 0.1 and 0.2) compositions.

In such pyrochlore structures, the variation of unit cell parameters can be governed by three independent contributions, like decreasing average ionic radii due to substitution of smaller cation, i.e. Ca^{2+} (radius Ca^{2+}_8 = 1.112 Å) in place of Pr^{3+} (radius Pr^{3+}_8 = 1.126 Å), partial conversion of Pr^{3+} to Pr^{4+} (radius Pr^{4+}_8 = 0.96 Å) and oxygen vacancies in the structure. Though the samples have been prepared under reducing atmosphere, the oxidation of Pr^{3+} to Pr^{4+} or excess anion in the lattice cannot be completely excluded while handling the sample in air. However, the larger unit cell parameters compared to that reported values [125] for x = 0.00 composition indicate

the oxidation of Pr^{3+} is not significant in the present studied sample, which would have led to contraction of unit cell. Thus, the decreasing value of the lattice parameter at the composition x = 0.1, can be attributed to the contraction of the unit cell volume due to substitution of Ca^{2+} in Pr^{3+} site and increasing oxygen vacancies. Further the separation of the CSZ type phase indicates that the solubility of Ca^{2+} ions in $Pr_2Zr_2O_7$ is less than 10 %.

4.4.2. Raman spectroscopic studies

Raman spectra of all samples in the series $Pr_{2-x}Ca_{2x}Zr_2O_7$ ($0.0 \leq x \leq 0.2$) in the wavenumber range of 150 to 1000 cm^{-1} are shown in the **Fig.4.2**.

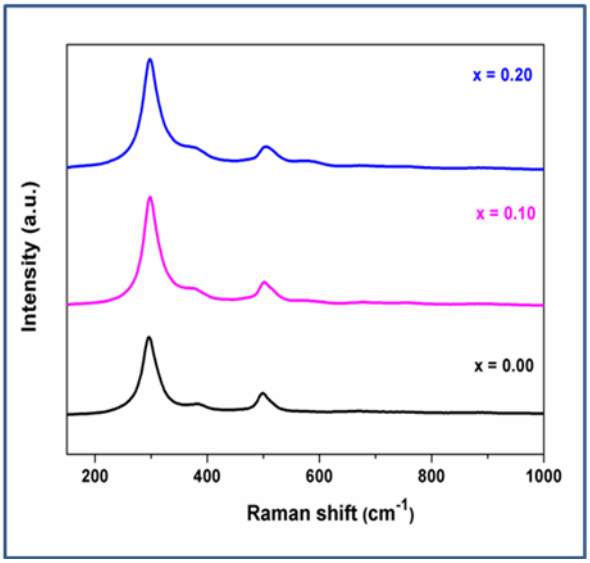

Fig.4.2: Raman spectra of $Pr_{2-x}Zr_2Ca_xO_7$ (x = 0.0, 0.1 and 0.2) compositions.

According to group theory, the cubic pyrochlore (space group; Fd3m) has six Raman active modes distributed as $A_{1g} + E_g + 4F_2g$ [126]. Out of the six Raman active modes, one of the F_{2g} mode involves the O2 (*8a* site) oxide ions while all other F_{2g} as well as the A_{1g} and E_g, modes are associated with the O1 (*48f* site) ions. The Raman vibration modes of pyrochlore structures are mainly originating from the motion or vibration of the oxide ions rather than the cations. It can be mentioned here that materials with

pyrochlore structure can exhibit more number of modes due to the violation of selections rules. Such selection violations have been attributed to the change in local symmetry and coordination due to intrinsic or extrinsic defects which may activate Raman inactive modes or break the k≠0 requirements [126]. Also, several overtones are possible to observe in Raman spectra of pyrochlore [126b]. Four clear Raman modes (E_g, A_{1g} and two F_{2g}) observed at 297, 386, 499 and 579 cm^{-1} for the studied $Pr_2Zr_2O_7$ sample are in agreement with the isostructral pyrochlores reported in literature [123a,126-127]. In addition, the Raman spectra indicate several other modes, which are not generally observed in the pyrochlore-type rare-earth zirconates. This suggests that the pyrochlore structure $Pr_2Zr_2O_7$ may have distortion or defects due to cation disordering (anti-sites), interstitial anion and oxidation of Pr^{3+} to Pr^{4+}. It can be expected that small amounts of Pr^{3+} may also be oxidized to Pr^{4+} in oxygen or air atmosphere retaining pyrochlore structure similar to the Ce^{3+} pyrochlores [121c,121d]. The retention of structure in all the samples in air at higher temperature has been concluded from the thermogravimetry and *in situ* high temperature XRD studies. The presence of Pr^{4+} in the samples is evident from the electrical conductivity measurements explained later in this chapter. Thus, more number of Raman modes due to symmetry violation in this system is not unexpected in this system. A comparison of the Raman spectra of the Ca substituted compositions with the unsubstituted sample indicates a close similarity in all.

The observed Raman modes of different compositions and their assignments are summarized in **Table 4.1**. The low frequency modes around 159 and 237 cm^{-1} are observed in x = 0.00 composition, while only a weak shoulder like feature at 237 cm^{-1} is observed in compositions with x = 0.1 and 0.2. The low frequency modes (below

237 cm^{-1}) are likely to be originating from the O(2)Ln_4 tetrahedra or motion of Ln^{3+} ions [126a]. The intense mode observed at 297 cm^{-1}, can have contribution from the E_g and one of the F_{2g} modes which correspond to the bending vibration mode of O-Pr(Ca)-O linkage. The A_{1g} modes around 500 cm^{-1} in $A_2B_2O_7$ pyrochlore structure have been attributed to the bending vibration modes of O-B-O of the BO_6 octahedra with some contribution from B-O or A-O stretching, while the F_{2g} modes are related to the A-O stretching and deformation of the AO_8 polyhedra of pyrochlore lattice.

Modes	x = 0.00 (cm^{-1})	x = 0.10 (cm^{-1})	x = 0.20 (cm^{-1})	Remark
	159	162	169	Motion of Ln^{3+} or vibration of OLn_4 tetrahedra
F_{2g}	237	-		″
F_{2g}	297	299	298	O-B–O bending
E_g	385	379	378	B–O stretch with mixture of A–O stretch and O–B–O bending vibrations
A_{1g}	498	502	505	O–B–O bend with mixture of B–O and A–O stretch
F_{2g}	579	583	581	B–O stretch
	740	760	754	Distortion in BO_6 or overtone of E_g
	879	891	888	Possibly B–O stretch

Table 4.1: Raman modes of $Pr_{2-x}Ca_xZr_2O_7$ compositions.

The E_g mode around the frequency 383 cm^{-1} observed for the composition with x = 0.00 can be attributed to the Zr-O stretching vibration mode with some contribution of O-Zr-O bending and Pr-O stretching vibrations. This mode shows a noticeable shift towards lower frequency with increasing values of x **(Table 4.1)**. As the system may have Pr^{4+} in the structure, the Zr-O bonds may be weakened due to

stronger Pr^{4+}-O^{2-} interaction. In the Ca^{2+} substituted samples, the fraction of Pr^{4+} is likely to be higher then undoped sample. This observation is further supported from the electrical measurements. Also, the presence of Ca^{2+} may affect the Ca-O-Zr angle and consequently deforms the O-Zr-O angle. The modes involving the ZrO_6 octahedra (F_{2g}: 579 cm^{-1}) are also broadened but no significant shift in the frequencies is observed. The high frequency modes, above 700 cm^{-1} are likely to appear in doped system due to several reasons, like symmetry violation and disorder in structure which are mainly from the B-O stretching and distortion of the BO_6 octahedra.

4.4.3. Thermo-gravimetric results

Further to understand the thermal stability of the $Pr_{2-x}Ca_xZr_2O_7$, thermo-gravimetric (TG) analyses and *in situ* high temperature XRD studies were carried out while heating the samples from ambient temperature. Typical TG traces recorded for x = 0.0, 0.10 and 0.2 are shown in **Fig.4.3**.

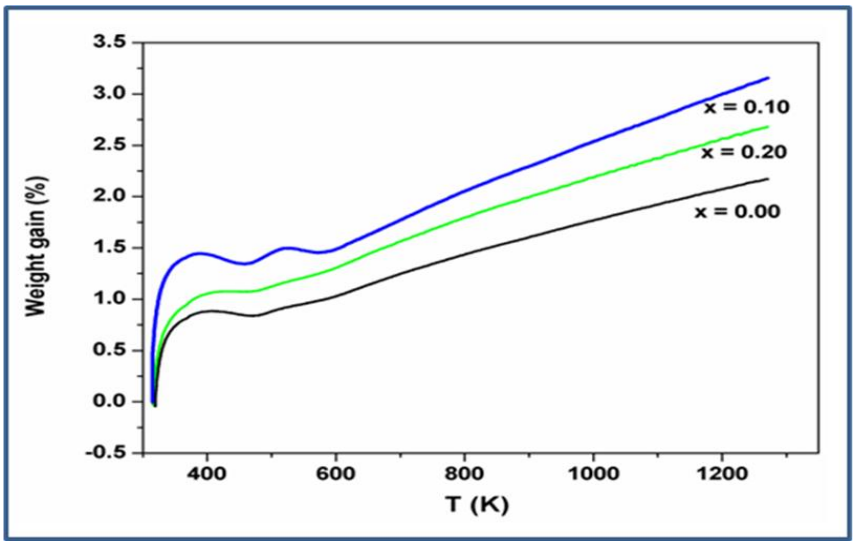

Fig.4.3: Thermo-gravimetric traces $Pr_{2-x}Ca_xZr_2$ (0.0, 0.1 and 0.2), recorded while heating in flowing air (Initial rises in weight is instrumental artifacts).

The TG traces shows a maximum of about 1-1.25% gain from 473 K up to 1073 K. This attributes to incorporation of about of 0.38 to 0.45 atoms of oxygen per formula

unit. According to the earlier structural studies on oxygen rich pyrochlore-type phases [121d], it can be mentioned here that the structure does not deviate from ideal Fd3m symmetry up to $O_{7.5}$. Further, due to the segregation of Ca stabilized ZrO_2 phase and existence of sizeable amount of lower valent Pr^{3+}, the stoichiometry is not expected to exceed from $O_{7.5}$. In this system, all the Pr^{3+} does not oxidize to Pr^{4+} as in the case $Ce_2Zr_2O_7$ pyrochlore, where the complete Ce^{3+} oxidized to Ce^{4+} at higher temperature. This can be due to the higher stability of Pr^{3+} compared to Ce^{3+} in oxidizing atmosphere. Hence all the compositions are likely to have coexisting Pr^{3+} and Pr^{4+} ions, which are likely to influence to their electrical properties.

The retention of cubic pyrochlore structures at elevated temperature is revealed in the *in situ* high-temperature XRD (HT-XRD) patterns of the samples (**Fig. 4.4(a-c)**). In all the cases, characteristics peaks of parent phase are retained in the HTXRD patterns, except their positions shift towards lower angle due to expansion of the lattice. Since the peaks due to platinum (Pt) strip (used as sample holder-cum-heater) are also observed in the *in situ* high-temperature XRD patterns, the analyses of diffraction data have been carried out by considering structures of both cubic pyrochlore and Pt together. The secondary phase, calcium stabilized zirconia (CSZ) observed at the composition with x = 0.20, also show similar thermal expansion. The unit cell parameters of the pyrochlore phase of different compositions at different temperature were obtained by fitting the observed profile by Lebail refinement method and they are depicted in **Fig. 4.5**. From the HTXRD studies, it was observed that the unit cell parameters show a gradual increasing trend with increasing temperature without any anomalous effects as observed in the related pyrochlore systems [121d].

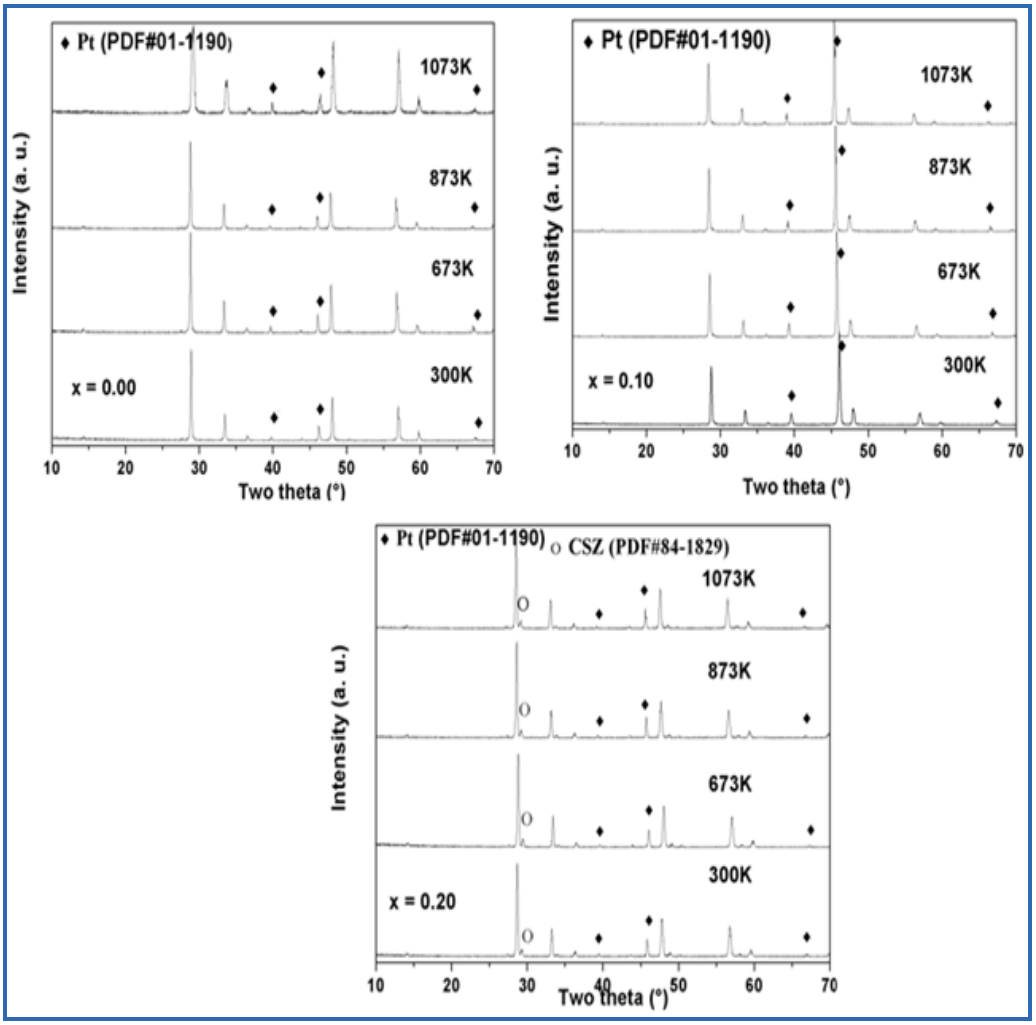

Fig.4.4: HT-XRD patterns of the $Pr_{2-x}Ca_xZr_2O_7$ at selected temperatures; (a) X = 0.0, (b) 0.1 and (c) 0.2.

The temperature dependent unit cell parameters in such pyrochlore lattices are governed by several different contributions, like decreasing ionic radii of the A site cation due to oxidation of trivalent cations, incorporation of excess anions in the lattice, thermal contribution to the anharmonic vibrations and masking of expansions due to vacancies [121c,121d]. Earlier, studies in such pyrochlore lattices show that the expansion of the unit cell due to the thermal expansion and incorporation of excess oxygen is nullified by the contribution from reduction of ionic radii from the oxidation of Ln^{3+} to Ln^{4+} [121c,121d], where Ln= Ce, Pr. The variation of unit cell parameters

with temperature suggests that the oxidation in the structure is not significantly affecting the thermal expansion behaviour. The observed unit cell parameters at 873 K are: 10.7616(3), 10.7383(7) and 10.7385(4) Å for x = 0.00, 0.10 and 0.20 compositions, respectively. The typical values of average thermal expansion coefficients for x = 0.00, 0.10 and 0.20 compositions are: 8.4×10^{-6}, 11.3×10^{-6} and 11.7×10^{-6} K^{-1}, respectively. The observed thermal expansion coefficient for x = 0.00 is lower than the value (9.3×10^{-6} K^{-1}) reported by Fu-Kang et al. [121g]. The difference can be attributed to the differences in the Pr^{3+}, Pr^{4+} and oxygen contents in the samples. The increasing values of thermal expansion coefficient with the Ca^{2+} concentration can be attributed to the larger expansion of Ca-O bonds compared to the Pr^{3+}-O^{2-} or Pr^{4+}-O^{2-} bonds.

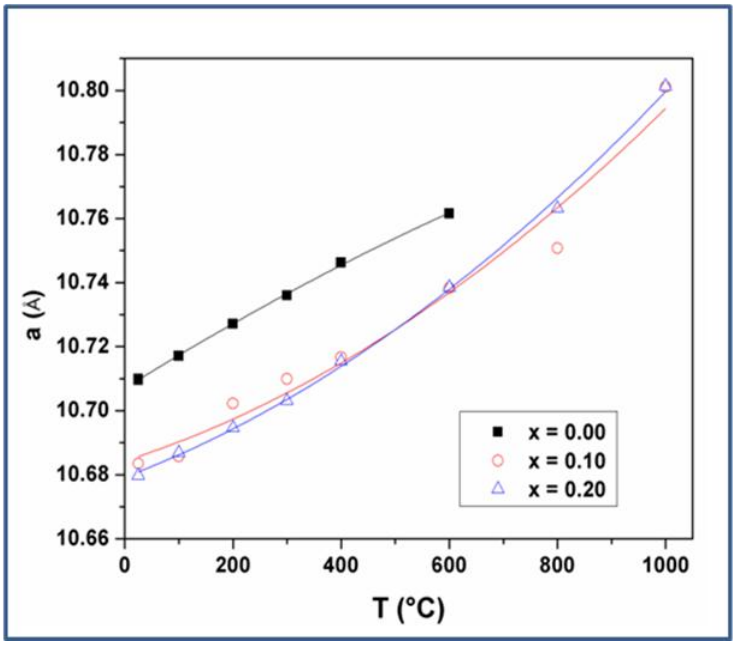

Fig.4.5: Variation of unit cell parameters of the $Pr_{2-x}Ca_xZr_2O_7$ (x = 0.0, 0.1 and 0.2) with temperature.

4.4.4. Electrical properties

The impedance data collected at different temperature were fitted by using equivalent circuit model considering one constant phase element (CPE) and one

resistance in parallel. The extracted conductivities of different compositions at different temperature are shown in **Fig.4.6.** Temperature dependence of the conductivity can be described by modified Arrhenius relation ($\sigma T = \sigma_o exp(E_a/k_bT)$, where, pre-exponential term (σ_o) is a measure of the number of mobile ions and hoping distance as well as frequency, and E_a is the activation energy for the electrical conduction process, k_b is the Boltzmann constant and T is the absolute temperature). From the slope of the Arrhenius plots, the obtained activation energies for conduction are: 0.42 eV (for x =0.00) and 0.63 eV (for x = 0.10). In addition, it can be observed that the conductivity of the composition with x = 0.20, shows deviation above 723 K, which can be due to the additional interfacial contribution due to the segregated secondary phase (CSZ) which is detected by XRD studies or involvement of different transport mechanisms. The activation energies for conduction as obtained from the slope of Arrhenius relations are: 0.97 eV (from ambient to 700 K) and 0.38 eV (above 755 K). At high temperature the composition with x = 0.20 shows lower activation energy (0.38 eV) which can be attributed easier hopping of ions and activated anion defects at higher temperature. It can be mentioned here the conductivity increases with the increasing of the Ca^{2+} in the compositions and maximum conductivity is observed at x = 0.10. In the present studied system, the appreciable conductivity due to hopping of electrons from Pr^{3+} to Pr^{4+} can be expected. The electrical properties of the $Pr_{2-x}Ca_xZr_2O_7$ can be closely related to the ceria based fluorite or pyrochlore type systems [128], where the presence of mixed valence of cations decreases by the incorporation of lower valent cations. It is observed that the conductivity increases with the temperature which is the evidence for the thermally activated oxide ion migration process in this series. However, the activation energies show an increasing trend with

x. This might be due to reduction in the unit cell parameter with increasing Ca^{2+} ions concentration, where the percolation of ions is hindered. Besides, the distribution of Pr^{3+}, Pr^{4+} and Ca^{2+} would result the clustering of defects which may also decrease the mobility of oxide ion. Also, the activation energy of the x = 0.00 composition is similar to the electronic conducting materials, while the activation energies of doped samples are similar to ionic conductors. Thus the hopping of electrons from Pr^{3+} to Pr^{4+} can also be a reason for conductivity [121c,121g]. The pre-exponential factor also show similar trend as activation energy, which indicates that the reduction of effective oxygen ions for migration with increasing the Ca^{2+} concentration.

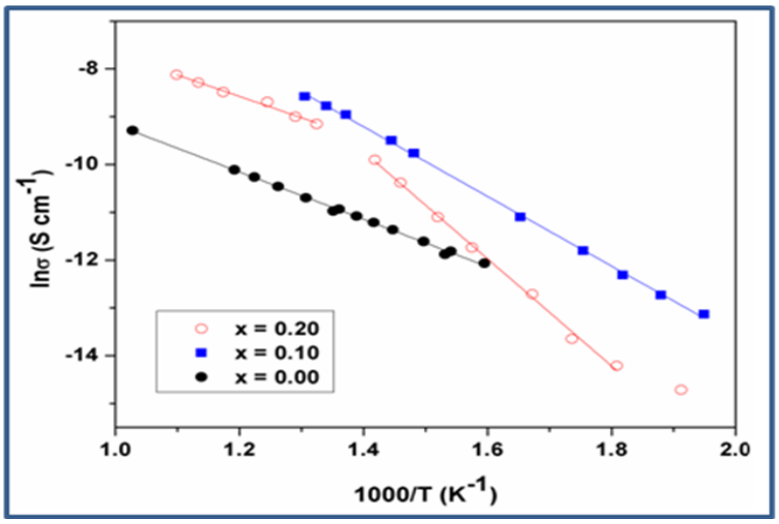

Fig.4.6: Variation of total conductivity of the $Pr_{2-x}Ca_xZr_2O_7$ (x = 0.0, 0.1 and 0.2) with temperature (continuous lines are fitted by Arrhenius equation).

Further the *ac*-conductivities of the samples were obtained from the frequencies dependent impedance data by relations, $\sigma^* = (l/A)\ Y^*$, where $Y^* = 1/Z^*$ and σ^*, Y^* and Z^* are complex conductivity, admittance and impedance, respectively. The variations of real part of the *ac*-conductivities (σ') with frequency at several temperatures are shown in **Fig. 4.7 (a-c).** In all the cases, the increase in conductivity with increasing temperature supports the thermal activation process as observed

commonly for the ceramic conductors. The conductivity data show universal power law ($\sigma' = \sigma_{dc} + A\omega^n$, where A and n are constants) type behavior [129] for x = 0.00 and 0.10 compositions. However, the composition with x = 0.20 shows different behavior, which can be related to the presence of two phases observed in this system.

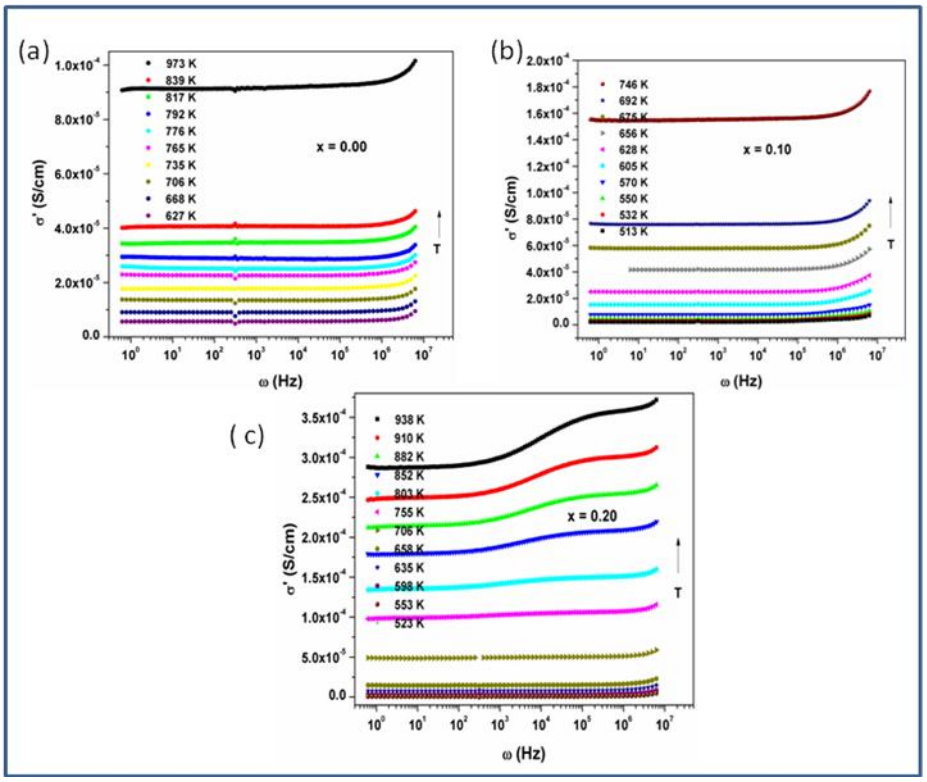

Fig.4.7: Variation of real part of ac conductivity of the $Pr_{2-x}Ca_xZr_2O_7$ (x = 0.0, 0.1 and 0.2) with frequency. (a) x= 0.0, (b) x= 0.1 and (c) x= 0.2.

The σ_{dc} conductivity data for samples extracted by extrapolating the frequency dependent σ' to the low frequency regions are shown in the **Fig.4.8**. The low frequency dispersion due to interfacial or space charge polarization was observed only at higher temperature (viz. above 673 K), which could be attributed to appreciable ionic diffusion only at higher temperature. The extrapolated σ_{dc} are frequency independent and mainly attributed to the electronic conductions in this system. The activation energy obtained by fitting the variation of σ_{dc} with temperature as $\sigma_{dc} = \sigma_o \exp(E_a/k_bT)$ are 0.42, 0.63 and 0.91 eV for the composition with x =0.00, 0.10 and

0.20, respectively. A comparison of the conductivities obtained from the Nyquist plots and from power law approximation show similar trend with compositions. The σ_{dc} increases **(Fig.4.8)** from x = 0.00 to 0.10 and then decreases at x = 0.20. The decrease at x = 0.20 can be attributed to the blocking of carrier transportation at the intervening secondary phase.

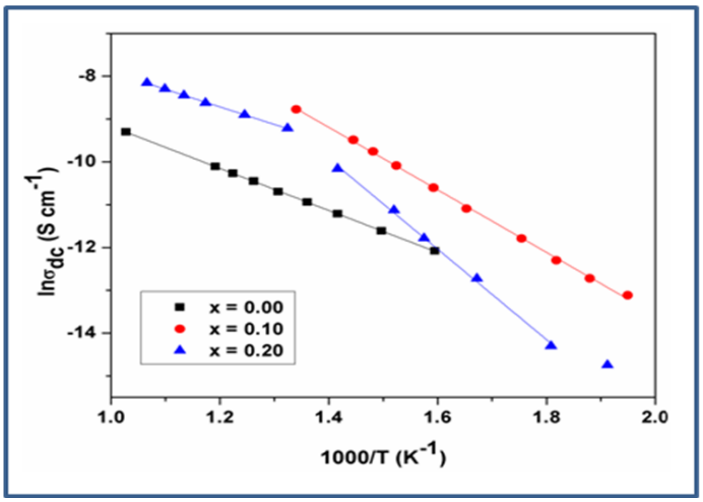

Fig.4.8: Variation of dc conductivity of the $Pr_{2-x}Ca_xZr_2O_7$ (x = 0.0, 0.1 and 0.2) with temperature. Continuous lines are fitted by Arrhenius equation.

The frequency dependent terms are in general indicative of the contribution and mechanism of the ionic transports. For the composition with x =0.00, the values of A are in the range of 1.2×10^{-10} to 7.3×10^{-13} S/cm and the values of n are in the range of 0.71 to 0.98 (in between 623 K to 923 K). The values of n are the indicatives of the conduction process in the system and they approach towards 1 for ideal long range path of diffusion modes of conduction [129-130]. The observed values of n suggest a long range ideal diffusion process as commonly expected for a pyrochlore structure. However, in the substituted samples values of n have varies from 0.40 to 0.93 (in between 673 K-873 K) suggests a contribution from hopping processes in disordered and ordered structures.

From the observed electrical properties, it is inferred that the transport of electrons has an important role on the conductivity of the $Pr_2Zr_2O_7$ than ionic conductivity. With increasing temperature, the ac-conductivities of samples show low frequency dispersion due to electrode polarization originating from ion migration.

4.5. Perovskite-type $Pr_2Ti_2O_7$

As mentioned earlier, among the $A_2B_2O_7$ type rare-earth (RE) titanates, the monoclinic perovskite type structure is formed with RE = La, Nd and Pr while all others form cubic pyrochlore type structure [119]. These monoclinic titanates exhibit ferroelectric properties due to their structural features. Ferroelectric transition of $Pr_2Ti_2O_7$ depends on the nature of sample preparation. Sun et al. [131] have reported coupled magnetism and ferroelectric properties in nanocrystalline $Pr_2Ti_2O_7$, where the magnetism is associated to the oxygen vacancies while the ferroelectric is expected arise from the structural features. Besides, the authors have reported ferroelectric transition at around 570 K in $Pr_2Ti_2O_7$, which is lowest temperature reported among the monoclinic $Ln_2Ti_2O_7$ [131]. The frequency and temperature dependent dielectric study confirm the transition as the ferroelectric transition and the lowering of T_c has been attributed to the crystallite size effects. The structure of $Ln_2Ti_2O_7$ (Ln = La and Nd) has been explained by a monoclinic ($P2_1$) lattice [119,132]. However, later a closely related orthorhombic ($Pbn2_1$) has been assigned for the structure of $La_2Ti_2O_7$ [133]. In addition, Scheunemann & Müller-Buschbaum [133a] and Harvey et al. [134] have reported a monoclinic superstructure with $P2_1$ for the structure of $Nd_2Ti_2O_7$. High temperature structural studies on $La_2Ti_2O_7$ indicate a structural transition from $P2_1$ to $Cma2_1$ above 1326 K and both low and high temperature phases differ by the shift of the rare-earth ions and distortion as well as tilt of the TiO_6 octahedral units

[135]. From the structural analyses, the authors have indicated the polarization in these structure arises mainly from shift of the rare-earth ions and partly from the rotation of the deformed octahedral TiO_6. Recently, Ishizawa et al. [136] have investigated the crystal structure of $Nd_2Ti_2O_7$ and indicated that the subcell represents the actual structure of $Nd_2Ti_2O_7$ and it is related it to the earlier super-structure by the differences in shift of cations along one of the axes, i.e. along the polarization direction. From density functional calculations, Pruneda et al. [137], Zhang et al. [138] and Xioa et al. [139] have reported structure and elastic properties of cubic phase of $La_2Ti_2O_7$ and $Nd_2Ti_2O_7$, which have never been observed experimentally. Theoretical analysis of Lopez-Perez and Iniguez indicated transformation from $Cmc2_1$, the real high temperature structure of $La_2Ti_2O_7$ to paraelectric (Cmcm) structure is related to shift of cations and distortion of octahedra and is a topological ferroelectric transition. Similar studies on $La_2Ti_2O_7$ and $Nd_2Ti_2O_7$ by Bruyer and Sayede indicated that the monoclinic ($P2_1$) structure is stable phase at ambient condition. This study also indicates that the ferroelectric to paraelectric phase transition may also occur through the $P2_1$ to $P2_1/m$ structural transition. However, the prototype $P2_1/m$ or Cmcm phases have never been observed experimentally for any of these titanates up to melting temperature. In view of this uncertainty in literature, the composition $Pr_2Ti_2O_7$ is prepared and its structure and electrical properties have been studied in a wider range of temperature and frequency.

4.6. Results and Discussion of $Pr_2Ti_2O_7$

4.6.1. XRD studies

The observed reflections of the powder XRD data of $Pr_2Ti_2O_7$ (PTO) sample obtained after final sintering are quite similar the reported monoclinic (JC-PDS-PDF:

35-0267) as well as orthorhombic phases (JC-PDS-PDF: 35-0224). As mentioned in earlier, the structure of $Pr_2Ti_2O_7$ and analogous rare-earth titanates has been explained by diversified symmetries, viz. monoclinic ($P2_1$ and $P2_1/m$) and orthorhombic ($Pna2_1$, $Cma2_1$ and Cmcm). The ferroelectric phase of PTO is likely to have $P2_1$, $Pna2_1$ or $Cmc2_1$ symmetry while the paraelectric phase is likely to have monoclinic $P2_1/m$ or orthorhombic Cmcm symmetry. It can be mentioned here that all the structures are closely related and hence their XRD patterns show only marginal differences. In order to characterize the structure of PTO, the reported structural details of monoclinic ($P2_1$) and orthorhombic (Pna21 and Cmc21) were considered. Models for other structures are obtained by structural transformations. The Rietveld refinements of the powder X-ray diffraction (XRD) were carried by considering all the possible models based on $Ln_2Ti_2O_7$ and related structure types. The diffraction peaks and background were modeled by using pseudo-Voigt profile function and shifted Chebyschev polynomial function, respectively. Initially background parameters along with the scale were refined and the unit cell parameters, half-width (U, V and W) and mixing (η) parameters of pseudo-Voigt function and peak asymmetry correction were added to the refinement cycle. All the intense peaks could be explained by all the considered models. However, the intensity of some weak peaks, in particular peaks at two theta ~ 18.2, 35.0, 37.5° etc. favour for an orthorhombic $Pna2_1$ [133b] and monoclinic ($P2_1$) [134] structures compared to the orthorhombic $Cmc2_1$ or Cmcm structures [132b]. The refinement of the structural parameters with all the reported models were subsequently carried out to further confirm the structure of PTO and the goodness of the refinements were observed from the residuals (R-values) and difference plots. The

refined unit cell parameters and the residuals of the refinements with different structural models are summarized in **Table 4.2**.

	$P2_1$ (4)	$Pna2_1$ (33)	$Cmc2_1$ (36)	$P2_1/m$ (11)	Cmcm (63)
a Å	7.71516(111)	25.7197(4)	3.85753(7)	7.71461(21)	3.85730(9)
b Å	5.48784(7)	7.71509(12)	25.7194(5)	5.48743(12)	25.71973(63)
c Å	13.00417(22)	5.48767(9)	5.48772(12)	13.0036(4)	5.48718(14)
β (°)	98.552(4)			98.531(7)	
V $Å^3$	544.468(15)	1088.919(30)	544.455(18)	544.397(27)	544.376(22)
ρ (gm/cc)	5.973g/cc	5.973g/cc	5.973g/cc	5.974g/cc	5.974g/cc
R_p	0.0616	0.0804	0.0834	0.1192	0.1066
Rw_p	0.0775	0.1001	0.1084	0.1496	0.1433
$\chi 2$	3.758	5.899	6.791	10.64	10.72
R_{F2}	0.0630	0.0892	0.1008	0.1856	0.1603

Table 4.2: Comparison of structural models of $Pr_2Ti_2O_7$.

A comparison of the analyses of the residuals obtained in different models indicates the monoclinic ($P2_1$) structure with unit cell parameters a = 7.7152(1) Å, b = 5.4878(1) Å, c = 13.0042(2) Å and β= 98.552(4)° shows the best fit for the observed diffraction data. In addition, the monoclinic unit cell reported by Scheunemann and Mueller-Buschbaum [133a] and Harvey et al. [135] also indicates similar residuals with the unit cell parameter is doubled along the c-axis. Despite the structure consists of twice the number of atoms in asymmetry unit and larger unit cell, no better

residuals as well as profile could be obtained. Hence, these two models were neglected for further consideration. The typical Rietveld refinement plot of the final cycle is shown in **Fig.4.9.**

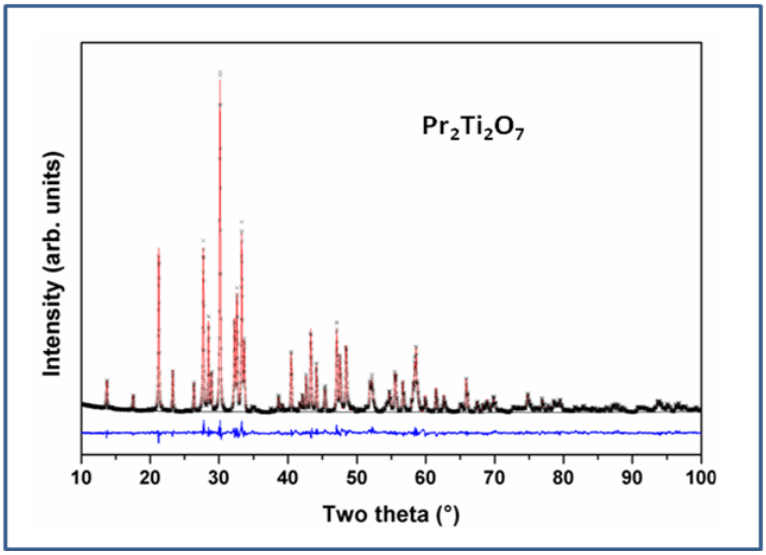

Fig.4.9: Rietveld refinement of $Pr_2Ti_2O_7$.

4.6.2. SEM studies

The characterized samples of PTO have been further investigated by scanning electron microscopy to understand their micro structural features.

The SEM pictures of the top and fractured surfaces of the prepared pellets are shown in **Fig.4.10**. Irregular micron sized well connected grains were observed under the preparation condition. However, the observed grains were quite different in shape and connections from the samples prepared from the low temperature solution processing and spark plasma sintered samples. As reported earlier, the higher sintering temperature lead of the oriented grain growth in such layered titanates. However, in the present case no such preferred orientation or well developed facets are observed under this sintering condition. The differences might be attributed to the differences in the sintering temperature. Since the sample shows a partial decomposition at higher

temperature, explained in later in this chapter, the high temperature sintering might lead to a difference in composition and/or oxidation state of cations, and hence it was avoided.

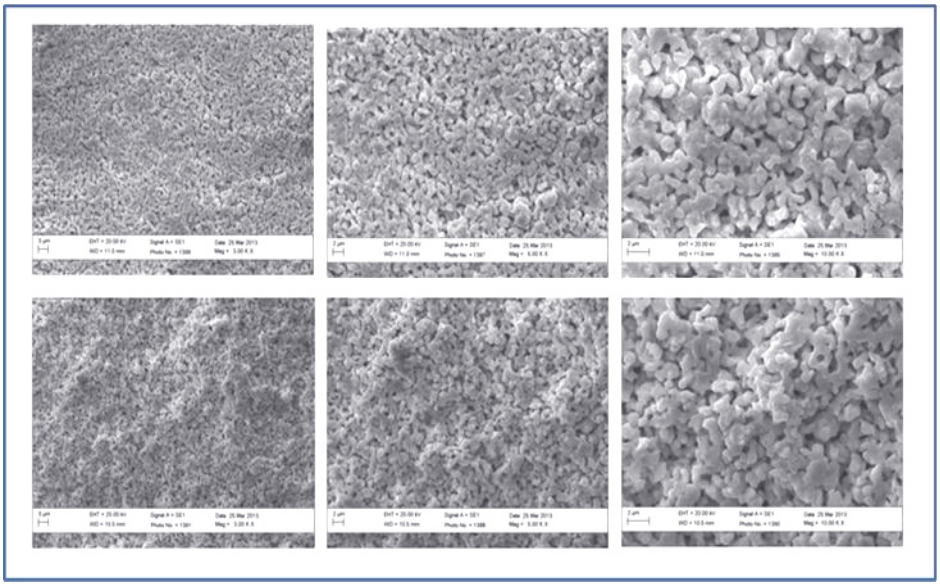

Fig.4.10: SEM images of $Pr_2Ti_2O_7$ (Top row: Top surface; bottom row: Fractured surface).

4.6.3. Thermo-gravimetric results

The thermal characteristics of $Pr_2Ti_2O_7$, the thermo-gravimetric studies in oxygen and also in inert atmosphere were carried out. Typical TG-DTA traces while heating the sample in oxygen or argon while heating from ambient to 1673 K are shown in **Fig.4.11**. No weight gain of the sample, as seen from the TG traces, suggests the retention of the 3+ state of praseodymium till the highest temperature. Deviation in the DTA pattern above 1073 K was observed in DTA traces recorded both in oxygen or argon. Onset of endothermic peak above 1573 K was observed which coincides with the reported ferroelectric to paraelectric transition of PTO but clear DTA peak could not be seen due to temperature literature.

The XRD patterns of the residue obtained after TG-DTA runs indicate the presence of the original monoclinic $P2_1$ structure **Fig.4.12.** However, several extra

reflections attributable to Ti rich perovskite type phase, ($Pr_2Ti_4O_9$) were observed in both the XRD patterns. This suggests a possible decomposition of the $Pr_2Ti_2O_7$ composition at higher temperature.

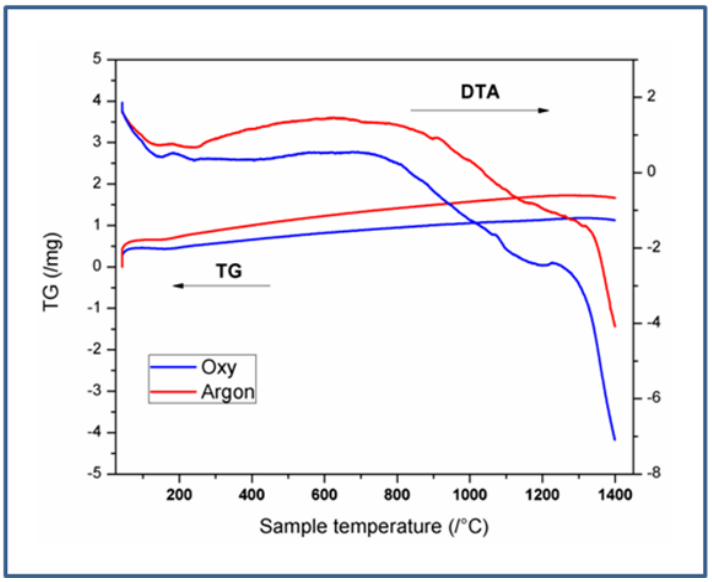

Fig.4.11: TG/DTA curves of $Pr_2Ti_2O_7$ while heating from ambient to 1673 K. (Heating rate = 10 K/min).

The Rietveld refinement of the powder XRD pattern of the samples obtained after TG runs suggests no significant change the unit cell or structural of the PTO lattice compared to the original ambient temperature phases. Gao et al. [120d] have observed a dielectric anomaly around 1023 K which the authors have attributed to the ferroelectric to paraelectric phase transition. The lowering of the ferroelectric T_c has been attributed to the preparation procedure and/or nanocrystalline nature of the sample. However, in the DTA there was no anomaly around this temperature but, dielectric anomaly around this temperature with no structural change is observed from the in situ high temperature XRD or Raman spectroscopic studies. This can be either due to the absence of any structural transition or transition accompanied by a very low energy change. In order to understand the high temperature behavior of the PTO, in

situ variable temperature powder XRD studies were carried out and they are explained below.

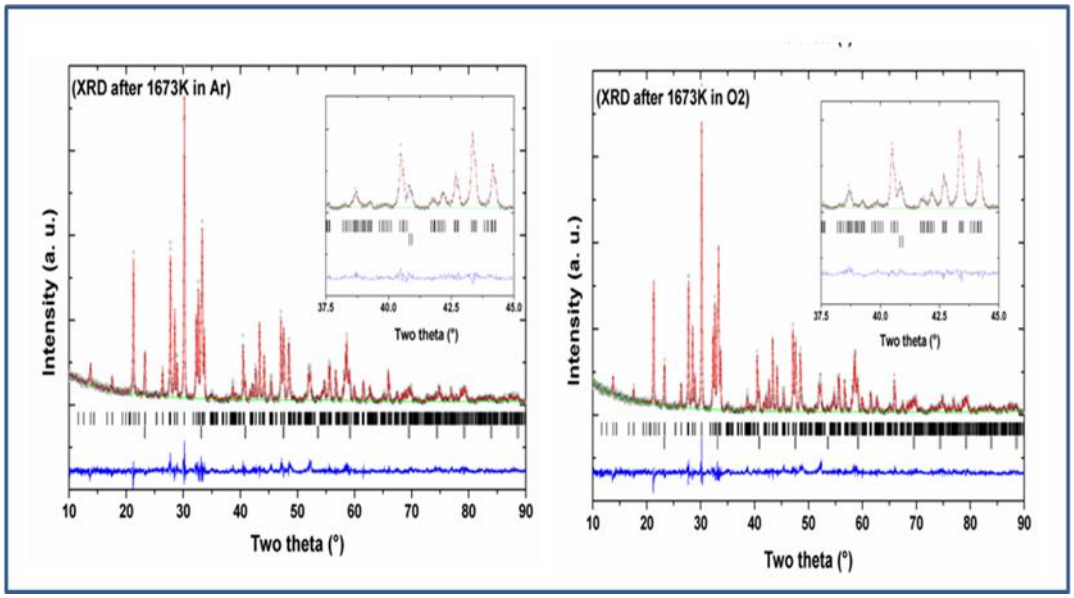

Fig.4.12: XRD patterns of $Pr_2Ti_2O_7$ recorded after heating at 1673 K.

(Argon)

a = 7.7158(2) Å, b = 5.5878(2) Å, c = 13.0031(4) Å, β = 98.572(6)°, V =

(Oxygen)

a = 7.7159(2), b = 5.5878(2), c = 13.0021(3), β = 98.582(4)°, V = 544.39(2) $Å^3$.

The vertical ticks in lower panel indicate Bragg positions of $Pr_2Ti_4O_{11}$

Powder XRD patterns of PTO recorded at successive temperatures between ambient to 1273 K are shown in **Fig.4.13.** The XRD patterns recorded at higher temperature are almost similar to that observed at ambient temperature except the shift in positions due to thermal effect. Considering the refined structural parameters from the ambient temperature data, the XRD data recorded at different temperatures were refined by Rietveld refinement method. The refined unit cell parameters observed for ambient temperature phases are comparable to those observed in ex situ ambient temperature data. The observed unit cell parameters at different temperatures are given in **Table 4.3**.

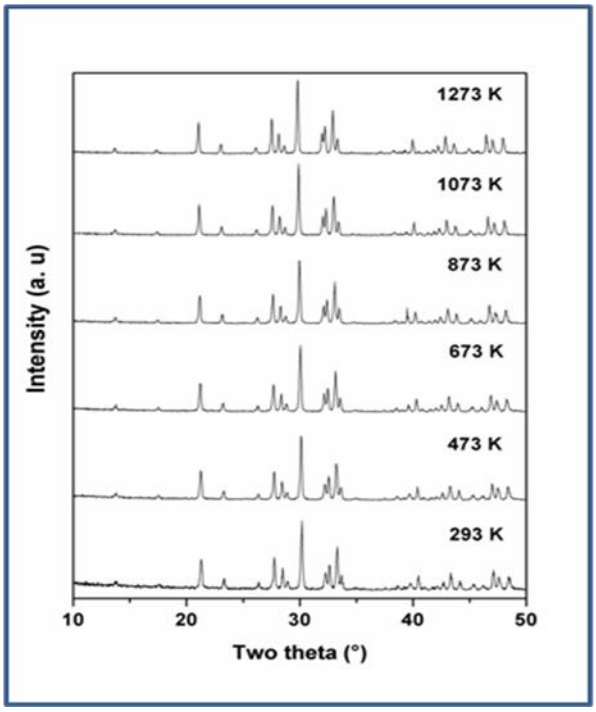

Fig.4.13: Typical powder XRD patterns of PTO recorded at different temperatures.

A comparison of the variations of unit cell parameters observed at different temperatures indicates a smooth variation with temperature. In order to see the possible phase transition, the XRD data recorded at and beyond 873 K were also analyzed by considering the possible symmetries of paraelectric ($P2_1/m$; Cmcm) and ferroelectric ($Cmc2_1$) phases. However, the observed peaks, in particular the differentiating peak at two-theta ~ 37.5°, could not be accounted by these models. This suggests that the ferroelectric to paraelectric phase transition is above 1273 K, as observed in other analogous titanates [119-120,140]. Earlier studies on an isostructural compound, $La_2Ti_2O_7$, indicated a structural transition from ferroelectric ($P2_1$) to another ferroelectric ($Cmc2_1$) transition in between 993 to 1053 K [135], which is similar to that reported for $Ca_2Nb_2O_7$. In a recent study, Hererra et al.[141] have reported both $P2_1$ and $Cmc2_1$ structures of $La_2Ti_2O_7$ at ambient temperature, in the sample prepared from xerogel by heating at 1073 and 1273 K, respectively. However,

the reported XRD pattern indicated poorly crystalline nature of the phase where the differentiation of these two symmetries is remote. In the present study and earlier studies on $La_2Ti_2O_7$ and related materials, the samples prepared at higher temperature show only $P2_1$ structure at ambient temperature [132b,135-136]. Since the differentiation of these probable symmetries is extremely difficult as they are mainly based on the presence or absence of weak reflections, the claim for the stabilization of $Cmc2_1$, which is also energetically unfavorable compared to $Pna2_1$ or $P2_1$ structures, cannot be relied. Thus, it suggests no structural transition in PTO up to 1273 k.

Temp (K)	a (Å)	b (Å)	c (Å)	β (°)	V $(Å)^3$
300	7.7184(4)	5.4898(3)	13.0076(9)	98.59(2)	544.98(6)
473	7.7336(3)	5.5003(2)	13.0224(7)	98.57(2)	547.75(4)
673	7.7518(3)	5.5135(2)	13.0423(7)	98.56(2)	551.21(4)
873	7.7683(3)	5.5246(2)	13.0613(7)	98.59(1)	554.26(4)
1073	7.7882(3)	5.5387(2)	13.0833(7)	98.58(1)	558.05(4)
1273	7.8107(3)	5.5543(2)	13.1080(6)	98.59(1)	562.28(4)

Table 4.3: Refined unit cell parameters of $Pr_2Ti_2O_7$ at different temperatures.

4.6.4. High-temperature Raman spectroscopic studies

Further to confirm the high-temperature behavior of PTO, *in situ* high-temperature Raman spectroscopic investigations were carried out. Raman modes being sensitive to the variation of local coordination and distortion as well as to

symmetry, the analyses of temperature dependent Raman mode can provide clear information on these features. At ambient conditions, $Pr_2Ti_2O_7$ has monoclinic structure with space group $P2_1$ and four formula units per unit cell which gives 132 normal modes. Factor group analysis gives irreducible representations for optic and acoustic modes as Γ_{optic} = 65A+64B and $\Gamma_{acoustic}$ = A+2B, respectively. At ambient temperature 32 distinct Raman modes could be clearly identified as shown in the **Fig.4.14**. The less number of observed Raman modes than expected may be due to the degeneracy or weak nature of some modes**. Fig.4.15** shows the Raman spectra of PTO at different temperatures in between 298-1073 K.

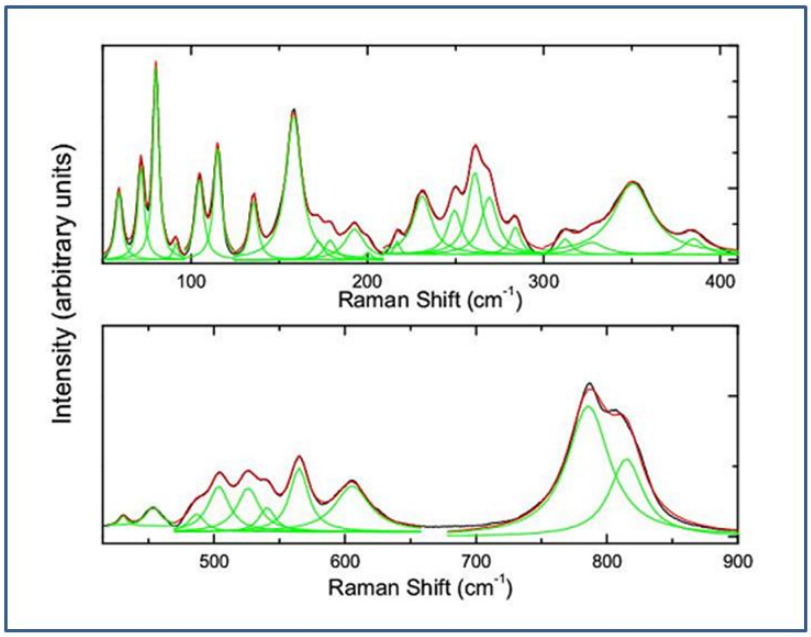

Fig.4.14. Raman spectra of $Pr_2Ti_2O_7$ at ambient conditions. The green lines indicate fitted profile with 32 distinct peaks.

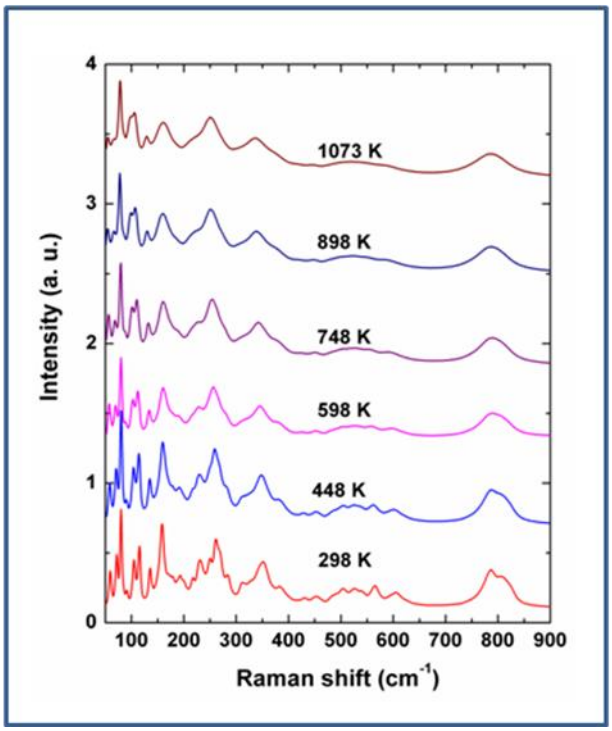

Fig.4.14: Raman spectra of $Pr_2Ti_2O_7$ at different temperatures.

Low frequency modes in the range 50-490 cm^{-1} were attributed to the Pr-O vibrations [142]. Modes in the range 490-575 cm^{-1} are assigned to distorted TiO_6 octahedron. The modes above 600 cm^{-1} were assigned to stretching modes of Ti-O vibrations. The evolution of Raman modes with temperature were followed by comparing with the modes observed at ambient temperature.

The temperature dependencies of Raman modes of PTO are shown in **Fig.4.16**. It was observed that with increasing temperature all the Raman modes were broadened and hence most of the weak intensity modes could not be observed at higher temperatures. From the variations of mode frequency with temperature, it can be seen that almost all the mode frequencies decrease with increasing temperature.The linearly decreasing trend of most of modes in the temperature range of 298-1073 K indicates the anharmonicity in $Pr_2Ti_2O_7$ is predominantly due to three phonon decay process. However, the typical trends of the modes show anomalous behavior. The lattice mode

at 158 cm^{-1}, the mode at 312 cm^{-1} due to Pr-O vibration, and the mode at 785 cm^{-1} due to Ti-O stretching vibration show increasing trend with temperature.

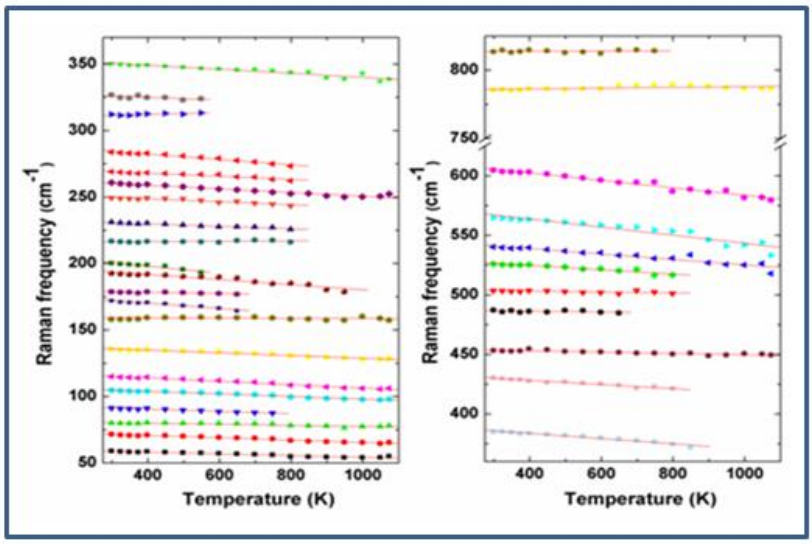

Fig.4.15: Temperature dependence of Raman mode frequencies of $Pr_2Ti_2O_7$.

Table 4.4 shows the temperature coefficients of Raman mode frequencies of $Pr_2Ti_2O_7$. The modes at 217 due to Pr-O stretching vibration and 814 cm^{-1} due to Ti-O stretching vibration show negligible temperature dependencies. This anomalous temperature dependency might be due to symmetrization of the PrO_n and TiO_6 polyhedra Earlier low temperature Raman spectroscopic studies on $Pr_2Ti_2O_7$ indicated similar temperature dependencies while the modes 194, 384 and 785 cm^{-1} show anomalous behaviour as the present study [143]. The phonon-phonon anharmonic interaction at higher temperatures cause change in frequency with temperature and they can have contribution from the cubic and quartic terms vibrational energies. The cubic and quartic anharmonicity terms are responsible for decreasing and increasing behavior of temperature dependent frequency. Also a ferroelectric system as in the present case is likely to have soft modes, and they can show anomalous behaviour. However, the details of the mode analyses have not been carried out to support this at this stage.

Sr. No	ω (cm^{-1})	dω/dT cm^{-1}/K	Sr. No	ω (cm^{-1})	dω/dT cm^{-1}/K
1	59	-0.0070	17	269	-0.012(1)
2	72	-0.0090	18	284	-0.020(1)
3	80	-0.004(1)	19	312	0.006(2)
4	91	-0.009(1)	20	327	-0.010(4)
5	105	-0.0100	21	350	-0.015(1)
6	115	-0.0130	22	385	-0.022(1)
7	136	-0.010(1)	23	431	-0.017(1)
8	158	0.03	24	453	-0.005(1)
9	172	-0.019(2)	25	487	-0.003(2)
10	179	-0.004(1)	26	504	-0.003(1)
11	193	-0.019(2)	27	526	-0.018(2)
12	200	-0.027(4)	28	540	-0.023(2)
13	217	0.001(1)	29	565	-0.034(3)
14	231	-0.010(1)	30	605	-0.031(1)
15	249	-0.012(1)	31	785	0.003(1)
16	261	-0.014(1)	32	814	0.001(2)

Table 4.4: Temperature coefficients of Raman modes (ω) of $Pr_2Ti_2O_7$.

4.6.5. Electric polarization studies

The measurement of electric polarization (P) with applied potential (E) at ambient temperature show typical ferroelectric like loops and is in agreement with the ferroelectric nature of PTO. Typical PE loops recorded at different applied field and different ac-frequencies are shown in **Fig.4.17**.

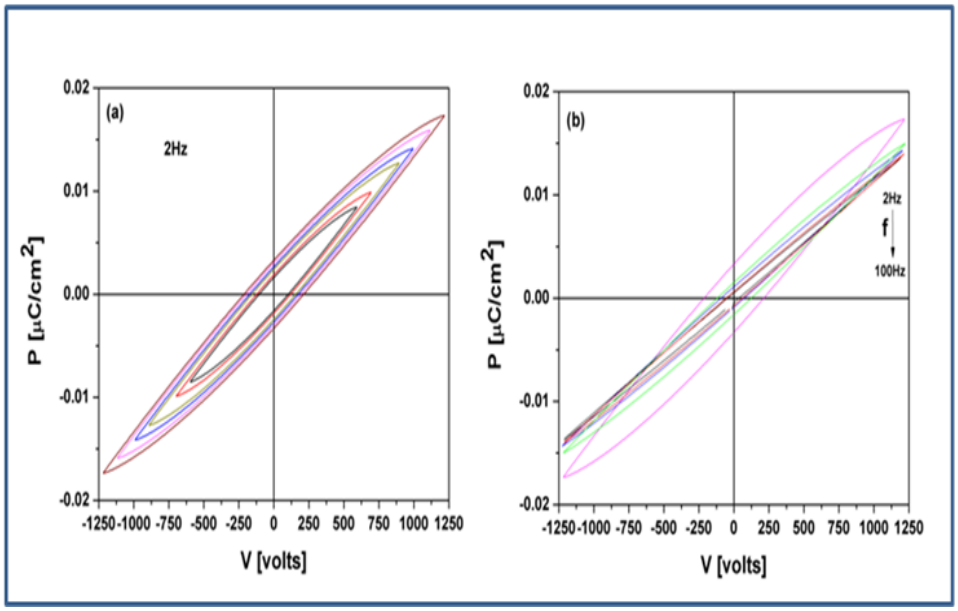

Fig.4.16: Ambient temperature PE loops of $Pr_2Ti_2O_7$ measured at different applied voltage and applied ac-frequency.

No saturation of polarization was observed up to the maximum applied voltage of this study. This might be due to higher loss arising from low density of the studied pellets. Besides, a maximum polarization and remanent polarization increases with decreasing frequency, which suggests the polarization originate from the dipolar rotation. The observed maximum polarization (Ps), remanent polarization (P_r) and coercive field (E_c) are: 0.017 μC/cm^2, 0.005 μC/cm^2 and 235 V, respectively. Typical loss current of about 0.1μamp is observed at 1200 V.

4.6.6. Electrical properties

Additional electrical properties of PTO were studied by the impedance spectroscopy. The temperature dependent permitivity and loss spectra in between 173 to 473 K are shown in **Fig.4.18**.

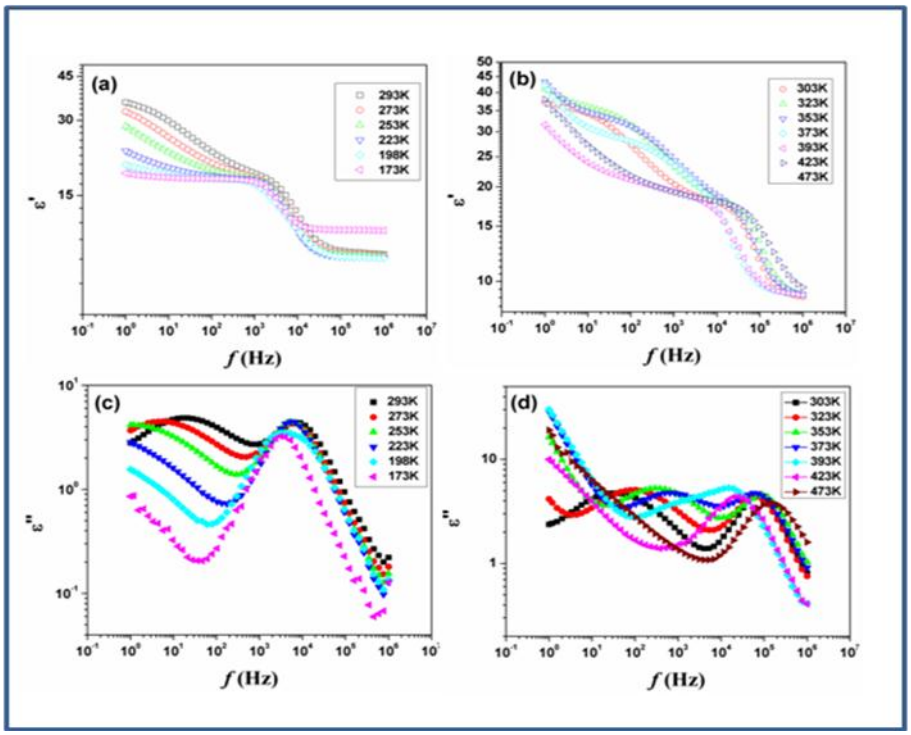

Fig.4.17: Temperature dependent ε'(a and b) and ε'' (c and d) of $Pr_2Ti_2O_7$ in low temperature region.

In both the spectra two different types of dielectric responses were clearly observed in the studied frequency range. The low frequency relaxations show significant temperature dependence, with the loss peak moving towards higher frequencies as the temperature rises, whereas the high frequency relaxation was almost invariant with temperature. The permittivity spectra recorded up to 473 K show almost similar behavior. However, at still higher temperature the permittivity shows sharp rise at lower frequency compared to that at higher frequency. A comparison of the temperature dependent permittivity and loss features suggests that at higher temperature an appreciable ion migration causes interfacial polarization leading to sharp rise in permittivity due to the Maxwell Wagner (MW) effect

The frequency-dependent complex permittivity $\varepsilon^*(\omega)$ can be most generally represented by the Havriliak-Negami (H-N) model as given below [144]

$$\varepsilon^*(\omega) = \varepsilon_\infty + (\varepsilon_s - \varepsilon_\infty)/[1+(i\omega\tau)^\alpha]^\beta \qquad [4.1]$$

where $\omega=2\pi f$ is the angular frequency, τ is the relaxation time, ε_s and ε_∞ are the low and high frequency values of permittivity, respectively, $i = \sqrt{-1}$, and α and β are exponents such that $\alpha > 0$, $\alpha\beta \leq 1$. The contribution due to electrical conductivity can be incorporated by adding the term $(-i[\sigma_{dc}/(\varepsilon_0\omega)]^n)$ to Eq. (4.1), where σ_{dc} is the *dc*-conductivity, ε_0 is the permittivity of free space, and $n \approx 1$. This dielectric data further analyzed these two dielectric responses by fitting two H-N relaxation models and a conductivity contribution to the measured dielectric loss spectra as below.

$$\varepsilon^*(\omega) = \varepsilon_\infty + \frac{\varepsilon_s - \varepsilon_\infty}{[1+(i\omega\tau_1)^{\alpha_1}]^{\beta_1}} + \frac{\varepsilon_s - \varepsilon_\infty}{[1+(i\omega\tau_2)^{\alpha_2}]^{\beta_2}} - i[\sigma_{dc}/(\varepsilon_0\omega)]^n \qquad [4.2]$$

Where, the subscripts 1 and 2 correspond to the low and high frequency relaxations, respectively. A representative fitted curve ε" of PTO with Havriliak-Negami (H-N) model is shown in the Fig.4.19.

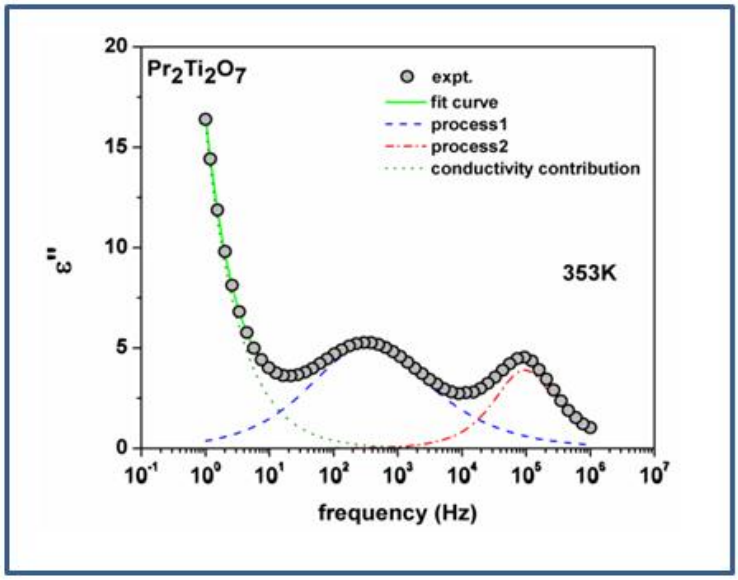

Fig.4.19: Typical fittings of ε" of PTO with Havriliak-Negami (H-N) model

The relaxation time τ_1 extracted from this fitting was found to follow the Arrhenius relation Eq.(4.3) which suggest the relaxation is a thermally activated process

$$\tau_1 = \tau_0 \exp(E_1 / k_B T) \qquad [4.3]$$

Where, τ_0 is a pre-exponential factor, E_1 is the activation energy, and T is the temperature of measurement. The typical Arrhenius plot of the relaxation time τ_1 is depicted in **Fig.4.20**. In contrast to τ_1, the relaxation time (τ_2) for the second (high frequency) process does not show any strong trend with temperature (see inset in **Fig.4.20**).

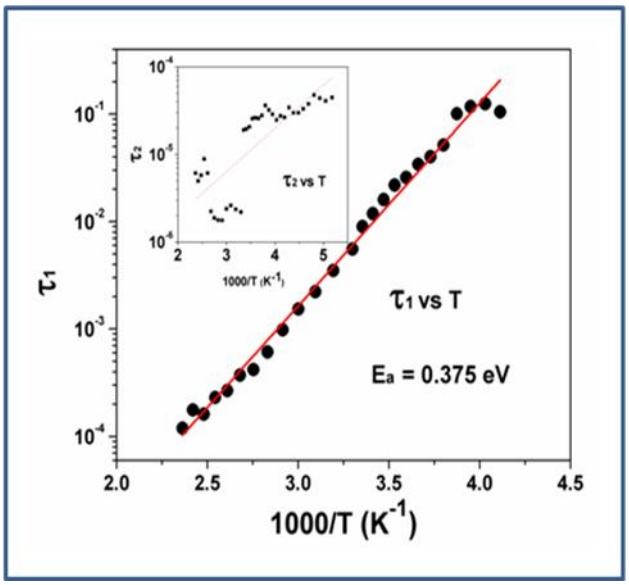

Fig.4.20: Typical Arrhenius fit for low temperature relaxation (τ_1) of $Pr_2Ti_2O_7$. The temperature dependency of τ_2 is shown as inset.

Thus, the first relaxation is a thermally activated process, and can be attributed to the Maxwell-Wagner polarization arising from the grain boundaries. This was further confirmed by the observation that the 'dielectric strength' (ε_s-ε_∞) decreases with temperature, as shown in **Fig.4.21**. Similar to the relaxation time, the behavior of dielectric strength for the second relaxation is also quite different as seen in **Fig.4.21**,

and thus it can be concluded that the relaxation was not due to the Maxwell-Wagner effect. It appears that this relaxation may have dipolar origin and related to the realignment of the dipole domains as the applied electric field oscillates. The Maxwell-Wagner relaxations due to grain boundaries are essentially a low frequency phenomenon, since the interfacial polarization cannot follow the applied ac field at higher frequencies, and thus, the dielectric strength diminishes with temperature [145]. The value of permitivity (dielectric constant) measured in this study is around 18 at 10 kHz and remains almost unchanged with temperature. This value is somewhat lower than that observed for $Pr_2Ti_2O_7$ by Gao et al. [120d] but close to that obtained by Sun et al. [131] for nanocrystalline $Pr_2Ti_2O_7$. The low values of loss tangent, viz. 0.2-0.3 at 10 kHz, indicate the low loss characters of PTO in between 173 to 473 K.

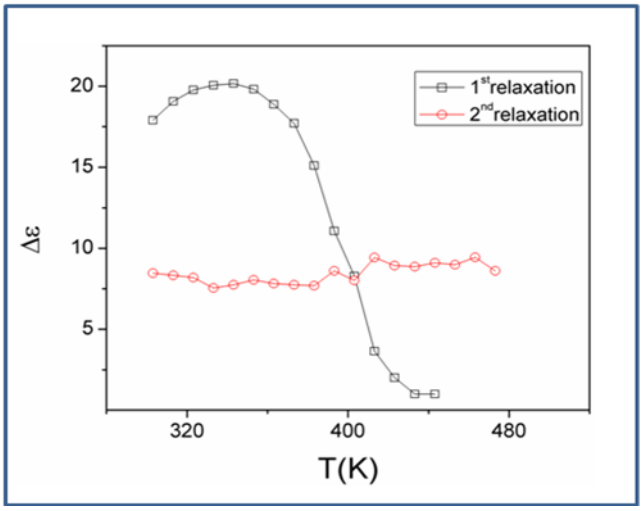

Fig.4.21: Variation of dielectric strength of the two low temperature relaxations of $Pr_2Ti_2O_7$ with temperature.

The temperature dependent dielectric constants indicate a ferroelectric like transition at lower temperature (~ 673 K) as observed by Sun et al. [131], despite the crystalline nature of all the samples. To follow the dielectric properties at still higher temperature, the impedance spectroscopic studies at higher temperature were carried

out. The variation of permittivity and *tanδ* with temperature are shown in **Fig.4.22.** The temperature dependent permittivity shows a peak like feature around 673 K. Besides with increasing frequency, a gradually decreasing trend of permittivity and shifting of peak temperature towards higher temperature are observed. The variation of peak temperature with frequency follows Arrhenius relation and thus again support for a thermal activated process in PTO. At lower frequencies, sharp rise in permittivity was observed. Such behaviours are expected for ionic conductors due to polarization of electrodes. This again suggests that the low frequency dielectric anomaly is not related to the polar orientation. A sharp increase in loss tangent at higher temperature was observed in the variation of *tanδ* with temperature. Though the values of loss tangent are small at lower temperature, they show considerably larger values at higher temperature. Thus, at higher temperature, PTO shows appreciable ionic conduction either due to formation of intrinsic defect or annihilation of defect clusters. Thus, the dielectric anomaly is related to ionic movement in the system.

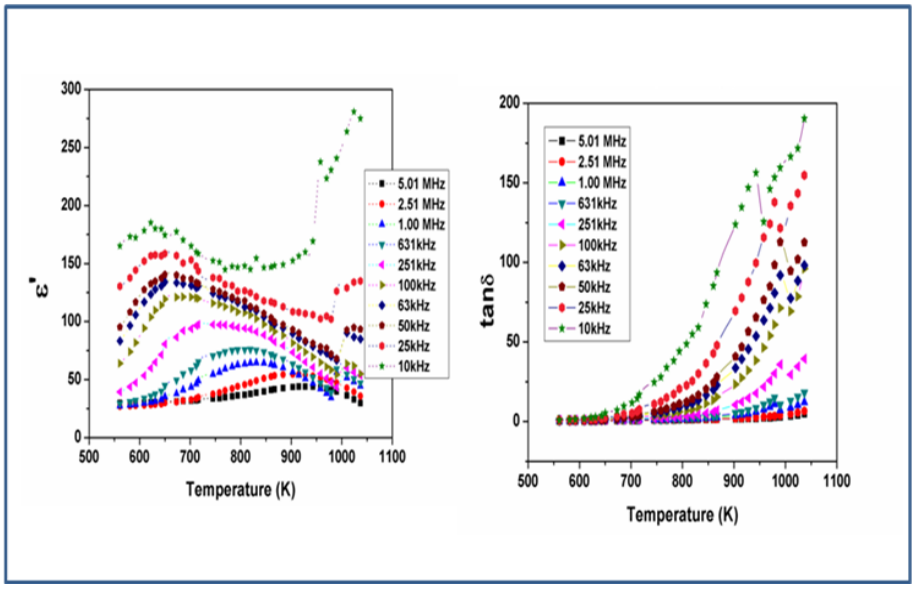

Fig.4.18: Temperature dependent ε' (left column) and tanδ (right column) of $Pr_2Ti_2O_7$ at selected frequencies in high temperature region.

In order to understand the electrical conductivity, the total conductivity was extracted from the impedance data and the temperature dependent conductivities are shown in **Fig.4.23**. A discontinuity in conductivity with an appreciable decrease in the activation energy is observed above 873 K. The measured activation energy in between 673-873 K is 0.60 eV. The observed activation energy is more similar to that for an ionic conductor at lower temperature while the same at higher temperature might be due to the mixed conduction as observed earlier in $Pr_2Zr_2O_7$ and other related systems [146] From the dielectric and impedance data it was observed that the electrical properties of $Pr_2Ti_2O_7$ are cumulative effects of the grain boundary and ionic and/or electronic defects.

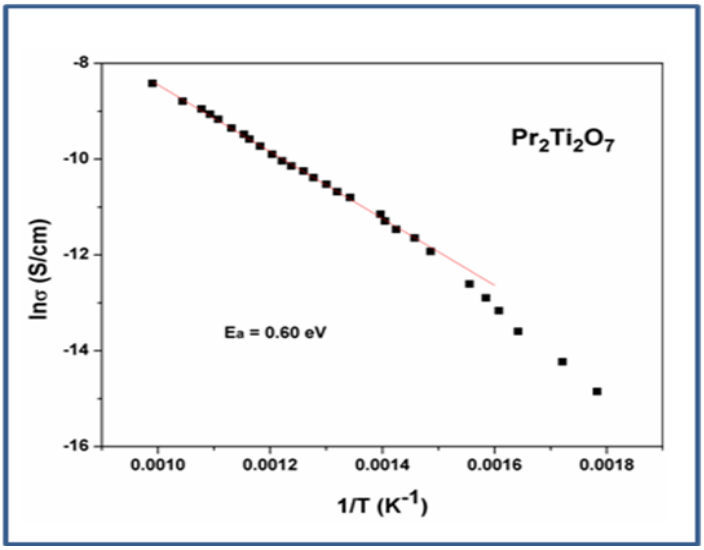

Fig.4.19: Variation of total conductivity of $Pr_2Ti_2O_7$ with temperature at high temperature (Arrhenius fits are shown as solid line).

The dielectric behaviour is similar to any of the ferroelectric materials while at higher temperature the migration of ions, in particular anions and electrons due to valency fluctuation of Pr^{3+} may occur. As explained earlier, the monoclinic phase of $Ln_2Ti_2O_7$ has a layered perovskite structure which is formed by stacking of slabs of four layers of highly distorted TiO_6 octahedra with rare-earth as interstitials in the perovskite

frame and in between the slabs of octahedral frame. The anionic defects can be easily formed in the perovskite sublattice, either during the preparation or due to slight deviation in the composition. Since the ferroelectric properties are related to the metal ion shift and distortion of the octahedral TiO_6, a feeble deviation in oxygen may not alter the polar character drastically, but at higher temperature they appear as loss contribution due to ion or electron movement.

4.7. Conclusion

The structural and electrical properties investigated on two types of $A_2B_2O_7$ compositions, namely $Pr_2Zr_2O_7$ and $Pr_2Ti_2O_7$ show different behaviors due to differences in their structures. The former has pyrochlore-type structure which was retained on substitution of Ca^{2+} at the Pr^{3+} sites. The maximum solubility of Ca^{2+} ion in $Pr_2Zr_2O_7$ is 10 %. A monoclinic perovskite-type structure with symmetry $P2_1$ was established for $Pr_2Ti_2O_7$. Both the structures show stability at higher temperature. Weight gain due to oxidation of $Pr_2Zr_2O_7$ system was attributed to incorporation of oxygen in the lattice. No significant oxidation was observed in $Pr_2Ti_2O_7$. $Pr_2Zr_2O_7$ and its substituted compositions show appreciable conductivity at lower temperature compared to $Pr_2Ti_2O_7$. At 765 K, the maximum electrical conductivity of about 1.72×10^{-2} S/cm was observed for the un-substituted composition $Pr_2Zr_2O_7$. $Pr_2Ti_2O_7$ is mainly a dielectric material and shows ferroelectric amenable structure. The dielectric constant about 30-40 is observed in a wider range temperature and frequency. In both the studied system, existence of electronic conductivites was inferred from the low activation energy for conduction. In addition $Pr_2Ti_2O_7$ shows two types of dielectric relaxation, one at lower frequency due to thermally activated polarization process at the grain boundaries and other at higher frequency due to dipolar reorientation.

CHAPTER 5

TUNABLE MAGNETIC AND DIELECTRIC PROPERTIES OF Ln_2MnMO_6 (Ln = Eu AND Y, M = Co AND Ni)

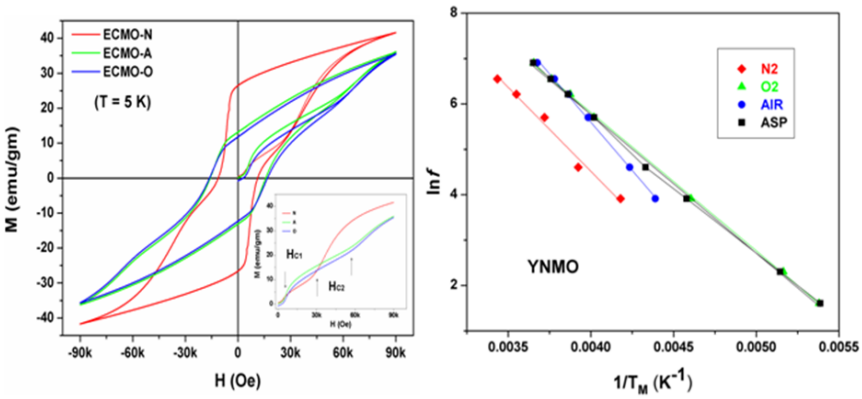

1. Effect of annealing environment on low temperature magnetic and dielectric properties of $EuCo_{0.5}Mn_{0.5}O_3$
   K.Vasundhara, S. N. Achary, S. K. Deshpande, P. D. Babu, H. G. Salunke, N. Gupta and A. K. Tyagi
   J. Phys. Chem. C. 118 (2014) 17900-17913.

2. Magnetic and dielectric properties of Y_2MMnO_6 (M = Co, Ni): effect of annealing environment
   K. Vasundhara, P. D. Babu, S. K. Mishra, R. Mittal, S. N. Achary, S. K. Deshpande and A. K. Tyagi
   J. Appl. Phys **(Communicated)**

5.1. Introduction

In the recent time, transition metal containing perovskite type materials have attracted significant attention due to their magnetoelectric and multiferroic properties [147]. In particular, the perovskite AMO_3 type (A = rare-earth, Bi^{3+}; M = transition metal ions like Fe, Mn, Cr etc.) and $A_2MM'O_6$ (A = rare-earth or alkaline earth ions; M and M′ = *3d* transition metal ions) compounds exhibit wide varieties of magnetic properties like ferro, ferri and antiferromagnetic as well as dielectric properties like colossal magneto capacitance, relaxor behavior and ferroelectricity [147d,147e,148]. Magnetic properties of perovskite AMO_3 type (Ln = rare-earth ions; M = transition metal ions) and related compositions with heterovalent cation substitution on either A or M sites have been extensively investigated. It has been reported that $La_2M^1M^{11}O_6$ (M^1 and M^{11} = transition metal ions) compositions show cation ordered or disordered structures depending on the relative ionic radii and oxidation states of the transition metal ions and often they exhibit ferromagnetism with high Curie temperature (T_C) due to the 180° super exchange of the M^1 and M^{11} transition metal ions [149]. It has been observed that the sample preparation conditions of such transition metal ion containing rare-earth perovskites significantly affect the cation distributions at the octahedral sites and hence their dielectric and magnetic properties [149]. The studies on La_2NiMnO_6 composition often show coexisting monoclinic and rhombohedral phases and the fractions of these two phases depend strongly on the sample preparation temperature and atmosphere [150]. In addition, the fractions of these phases vary with the post annealing conditions, like oxygen partial pressure (P_{O2}) of the annealing atmosphere and temperature. Because of such structural changes as well as induced defects in post annealing conditions, variations in their magnetic and

dielectric properties are observed [149b,150-151]. From the earlier literature it has been observed that double perovskites, like La_2MgMnO_6, La_2NiMnO_6 partially decompose on annealing in inert or low oxygen partial pressure atmosphere [150a,150c]. The studies on Eu_2CoMnO_6 and La_2CoMnO_6 indicated that the former shows partial decomposition. While the later retained the structure on annealing in inert atmosphere [150c,152].

La_2MMnO_6 (M = Ni, Co and Mg) samples show relaxor-like dielectric and magneto dielectric properties [150a,150c,151a,151c,151d,153]. In case of La_2NiMnO_6 and La_2CoMnO_6 samples the relaxor-like dielectric properties vary with the annealing atmosphere. Structural studies of Booth et al. [154] on a series of double perovskite type Ln_2NiMnO_6 (Ln = La to Y) compounds indicated cation ordered structures for all of them. Also this study indicated normal dielectric like behavior with dielectric constants in between 15-25 for all the Ln_2NiMnO_6 samples [154]. Studies on Y_2MMnO_6 (M = Co and Ni) revealed that the cation distribution at the octahedral sites affect their ferromagnetic transition temperature [155]. Kumar et al. [156] have predicted that the ferroelectric properties are due to $P2_1/n$ to $P2_1$ structural transition. Maiti et al. have reported ferromagnetic transition and ferroelectricity even in nano-structured Y_2NiMnO_6 [157]. The dielectric studies on Y_2NiMnO_6 and Y_2CoMnO_6 indicated a deviation near the magnetic transition which has been related to the coupling of the magnetic and dielectric properties. Compared to Y_2NiMnO_6, the magnetic properties of Y_2CoMnO_6 indicated diversified behavior, like ferromagnetic, spin glass and metamagnetic [158]. In order to understand effect of sample preparation condition and oxygen partial pressure on magnetic and relaxor-like dielectric behavior of perovskite as well as to study the role of rare-earth ions,

Eu_2CoMnO_6, Y_2NiMnO_6 and Y_2CoMnO_6 were synthesized and they are explained in this chapter.

5.2. Experimental method

The Eu_2CoMnO_6 (ECMO) and Y_2MMnO_6 (M = Co and Ni) (Y_2NiMnO_6 = YNMO and Y_2CoMnO_6 = YCMO) samples were prepared by gel combustion method by using Eu_2O_3, Y_2O_3 $CoCO_3$ and $MnCO_3$ as initial reactants. Stoichiometric amounts of reactants were dissolved in 1:1 nitric acid to get corresponding nitrate solutions. To this solution, calculated amount of glycine (for oxidant to fuel ratio 3.5:1) was added and then heated to approximately 373 K. The mixed solution was allowed for chelation and then to remove the excess amount of the water at this temperature. After removal of excess water the solution transformed to highly viscous gel. On further heating the gel undergoes auto-ignition and turned to black coloured powder. The amorphous powder thus obtained was calcined at 973 K for 3h. The calcined powder was pressed into pellets and heated at 1173 K for 42h. The obtained product was rehomogenized and sintered at 1523 K for 24h in pellet form. These sintered pellets (ECMO-ASP) were annealed at 1123 K for 10h under static air (ECMO-A, YCMO-A, YNMO-A), flowing oxygen (ECMO-O, YCMO-O, YNMO-O) and argon (ECMO-N, YCMO-N, YNMO-N) atmosphere.

The studies on phase purities and the structure of the synthesized samples were carried by powder X-ray diffractometer (Rigaku, Japan) equipped with a rotating anode using monochromatic CuKα radiation. For structural studies, powder diffraction data were collected in the two theta range of 10-100°, with a step width and time 0.02° and 3s, respectively. The observed XRD patterns were analyzed by Rietveld method using Fullprof-2K software package.

The magnetic properties of the samples were investigated (between 5 to 300K) using SQUID magnetometer and 9T PPMS based Vibrating Sample Magnetometer (VSM) (both Quantum Design) in both zero field cooled (ZFC) and field cooled (FC) conditions. The hysteresis loops (M vs. H) of the samples were also recorded at temperatures between 5 and 300 K.

The dielectric properties of ECMO and YNMO samples were investigated in metal-dielectric-metal configuration using sintered cylindrical pellets painted with silver paste. Novo control Alpha impedance analyzer (Novo control Technologies, Germany) was used for dielectric measurements. Quarto liquid nitrogen gas cryosystem was used for studying ECMO samples while a CCR based cryostat was used for studying YCMO samples. All the measurements were done over wide range of frequencies while cooling from 293 to 128 K for ECMO samples and to 5 K for YCMO and YNMO samples.

5.3. Results and discussion of Eu_2CoMnO_6 (ECMO)

5.3.1. XRD studies

The XRD patterns of the ECMO samples processed under different conditions, viz. sintered at 1523 K followed by annealing at 1123 K under different atmospheres like air, oxygen and argon is shown in **Fig.5.1**. The XRD patterns of the samples indicate the crystalline perovskite type phase for all of them. Since cation ordering depends on the preparation conditions, like annealing temperature and atmosphere as well as heating and cooling protocols, the Rietveld refinement of the observed powder XRD data were carried out by considering both cation ordered ($P2_1/n$) and disordered (Pnma) structural models. All the observed reflections in the XRD pattern could be accounted by the cation disordered (Pnma) model. Thus, a cation disordered

orthorhombic structure with composition as $EuCo_{0.5}Mn_{0.5}O_3$ is assigned for the studied sample and here onwards the terminology ECMO will be used for this composition. The observed XRD patterns of the studied ECMO samples were analyzed by Rietveld method using refined structural models and results are shown in the **Table 5.1**. A comparison of the XRD results of the samples annealed in air (pO_2 ~ 0.2 atm.), oxygen (pO_2 ~ 1 atm.) and N_2 revealed that the structure of the original orthorhombic structure is retained in all.

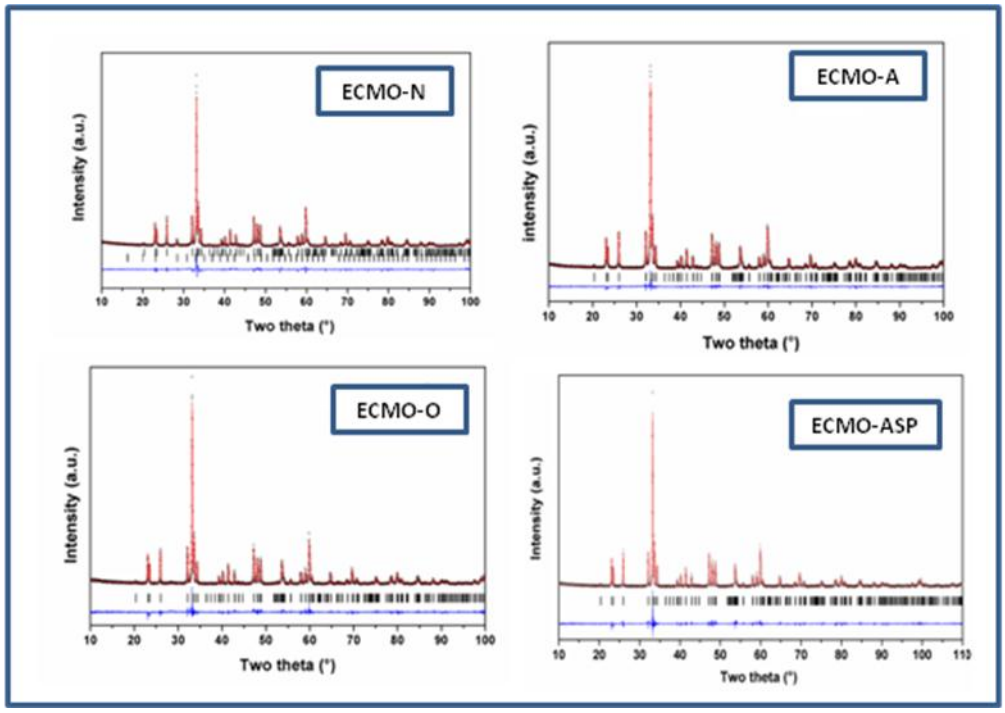

Fig.5.1: Rietveld refinement plots of powder XRD data of Eu_2CoMnO_6 sintered sample and annealed under different atmospheres.

However, the sample annealed in N_2 atmosphere shows a partial separation of Eu^{3+} ion from the lattice, leading to the formation of a cation deficient perovskite phase like $Eu_{1-x}Co_{0.5}Mn_{0.5}O_3$ and small amounts of Eu_2O_3. The structural refinement of the observed XRD pattern of ECMO-N sample revealed the composition to be as $Eu_{0.94}Co_{0.5}Mn_{0.5}O_3$, which is in accordance with the separated Eu_2O_3 phase (~ 3 wt %). Despite Eu^{3+} deficiency, the ECMO-N sample also does not show any deviation in

oxygen occupancies, which suggest that the oxygen stoichiometry is maintained and charge is balanced by partial oxidation of Co^{2+} or Mn^{3+} present in the lattice. Analyses of the structural parameters of the samples revealed that 1:1 stoichiometry of Co:Mn is retained in all the investigated ECMO samples. Sazonov et al. [159] have investigated magnetic properties of partially cation ordered Nd_2CoMnO_{6+x}, i.e. $Nd_{2-y}CoMnO_6$, perovskite with varying concentration of oxygen stoichiometry and concluded that the existence of Co^{2+} and Mn^{4+} is favored with x = 0.0 [159]. However, the exact oxidation state of the Co and Mn in the samples can be Co^{2+}, Co^{3+}, Mn^{4+} and Mn^{3+}. Such variable oxidation states have also been observed in earlier studied systems, like La_2CoMnO_6 and La_2NiMnO_6 [149b,150a,150b,153]. In particular, they are more prominent in the Co-Mn systems due to marginal difference in the redox potentials between Co^{2+}-Mn^{4+} and Co^{3+}-Mn^{3+} couples (electrochemical potential differences between Co^{2+}-Co^{3+} = 1.8 eV and Mn^{3+}-Mn^{4+} = 1.6 eV [149b]. Thus, the coexistence of variable oxidation states of these transition metal ions is common in such perovskites. The presence of such multiple oxidation states was confirmed by X-ray photoelectron spectroscopic (XPS) studies.

5.3.2. XPS studies

The XPS spectra for the annealed samples show broad peak around 640 eV attributable to Mn2P photoelectrons. Typical XPS spectra in the region of Mn2p3/2 are shown in the **Fig.5.2.** From the variation of shape of Mn2p peak and deconvolution of the peaks, it could be inferred that the relative proportion of Mn^{3+} and Mn^{4+} varies with the annealing conditions, viz. $Mn^{3+} > Mn^{4+}$ (in ECMO-A), $Mn^{3+} \sim Mn^{4+}$ (ECMO-O) and $M^{3+} < Mn^{4+}$ (ECMO-N). Thus, it is likely that Mn^{4+} and Co^{2+} are favoured on annealing in atmospheres with low oxygen partial pressure. The

qualitative information for the existence of Mn^{3+} and Mn^{4+} could also be verified by XANES study (not included in the thesis). Thus in the thesis the relative variation are only emphasized and hence could not be quantitatively correlated to the properties.

	ECMO-A	**ECMO-A**	**ECMO-N ***
Annealing atmosphere	O_2	Air	Argon
Space Group	Pnma	Pnma	Pnma
Unitcell parameters(Å)	5.5647(1) 7.5690(2) 5.3251(1)	5.5660(10 7.5692(1) 5.3256(1)	5.5770(1) 7.5802(1) 5.3295(1)
Volume $(Å)^3$	224.291(7)	224.369(5)	225.306(5)
Eu *(4c: x,1/4,z)* U ($Å^2$) x 100	0.0612(2) 0.25 -0.0146(3) 0.63(5)	0.062(1) 0.25 0.015(1) 1.2(2)	0.0616(2)* 0.25 0.0145(2) 1.49(3)
Co/Mn *(4b: 0,0,1/2)* U ($Å^2$) x 100	0 0 0.5 0.29(9)	0 0 0.5 0.742(040)	0 0 0.5 1.53(6)
O1 *(4c: x,1/4,z)* U ($Å^2$) x 100	0.480(1) 0.25 0.088(2) 1.8(4)	0.476(1) 0.25 0.091(10 2.6(2)	0.471(1) 0.25 0.094(2) 2.7(4)
O2 *(8d: x,y,z)* U ($Å^2$) x 100	0.298(2) 0.046(1) 0.699(2) 0.8(3)	0.296(1) 0.046(10 0.700(10 2.2(20	0.302(1) 0.049(1) 0.698(1) 2.9(3)
Rwp,Rp,χ^2,R_{F2}	0.1606 0.1162, 1.513, 0.0558	0.0877 0.0665, 1.683, 0.0301	0.1090 0.0869, 3.267, 0.0613

Table 5.1: Refined structural parameters of $EuCo_{0.5}Mn_{0.5}O_3$ samples annealed in different atmosphere.

* Seconary phase Eu_2O_3 (Cubic: Ia-3). a = 10.866(1) Å, V = 1283.1(4) $Å^3$

Wt. Fraction of Eu_2O_3 phase. 3.1(7) % $ 0.958 (occ)

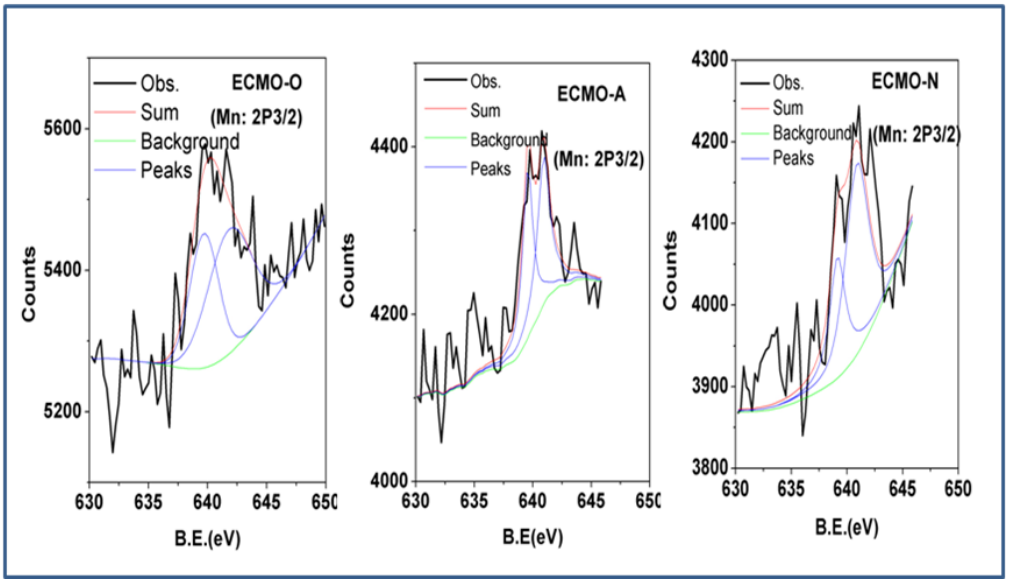

Fig.5.2: X-ray photoelectron spectra and typical fits of Mn $2P_{3/2}$ peaks.

5.3.3. Magnetic properties

The temperature dependences of zero-field-cooled (ZFC) and field-cooled (FC) magnetizations are shown in **Fig.5.3.** The transition temperature observed in the studied samples are little higher than that reported earlier for ECMO (124 K) [158b, 160]. Besides, the observed transition temperature in ECMO-N (136 K) is higher than those observed for ECMO-A and ECMO-O (132 K). FC data of ECMO-A and O samples exhibit a gradually increasing trend but without any indication to saturate down to 5 K, while the magnetization of the sample annealed in N_2 atmosphere tends to saturate at lower temperature. From the FC and ZFC curves, it is observed that ECMO-O and -A samples show multiple magnetic transitions, while a single magnetic transition is observed in the ECMO-N sample. In both ECMO-O and -A samples, the second magnetic transition is observed at around 115 K. The multiple magnetic ferromagnetic transitions with a considerably different T_C due to different magnetically coupled ion pairs have been earlier reported in La_2CoMnO_6 and

La_2NiMnO_6 [149b,150a,150b,151a]. The lower transition temperature for the ECMO-A and ECMO-O sample is due to the presence of larger fraction of Co^{3+} and Mn^{3+} ions. Below the transition temperature, divergence of ZFC and FC magnetization curves is observed, but they are almost similar above the transition temperature.

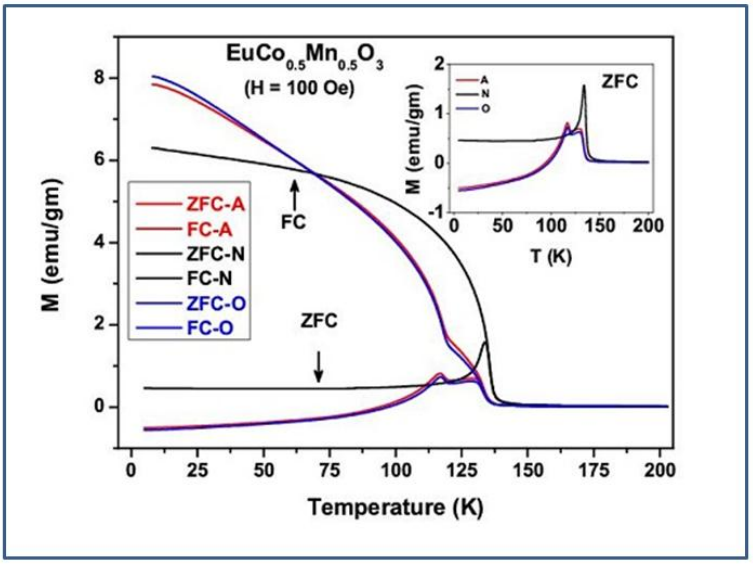

Fig.5.3: Temperature dependent magnetic susceptibility (FC and ZFC) of ECMO-A, ECMO-O and ECMO-N measured at applied field of 100 Oe.

All the ZFC magnetization curves show peak at the transition temperature. The peak-like features in ZFC magnetizations at the transition temperatures are quite similar to antiferromagnetic or spin glass systems. In addition, the ZFC traces of ECMO-A and -O samples gradually decrease and even showed a negative traces. However, the same for ECMO-N remains positive down to 5 K. The decreasing magnetization or even negative magnetization in ZFC in such double perovskites and other related spinel type ferrimagnetic systems have been reported in literature [150a,150b,158b,159-160]. The origin of such decreasing magnetization and negative magnetization has been attributed to several factors, namely the contribution of antiferromagnetically coupled rare-earth magnetic moments, dominating antifferomagnetic clusters of transition

metal ion pairs at low temperature, as well as residual trapped magnetic field superconducting solenoids of the magnetometer [160-161].

To understand the magnetization behavior, the FC magnetization of the ECMO samples were measured at different fields and they are shown in **Fig.5.4.**

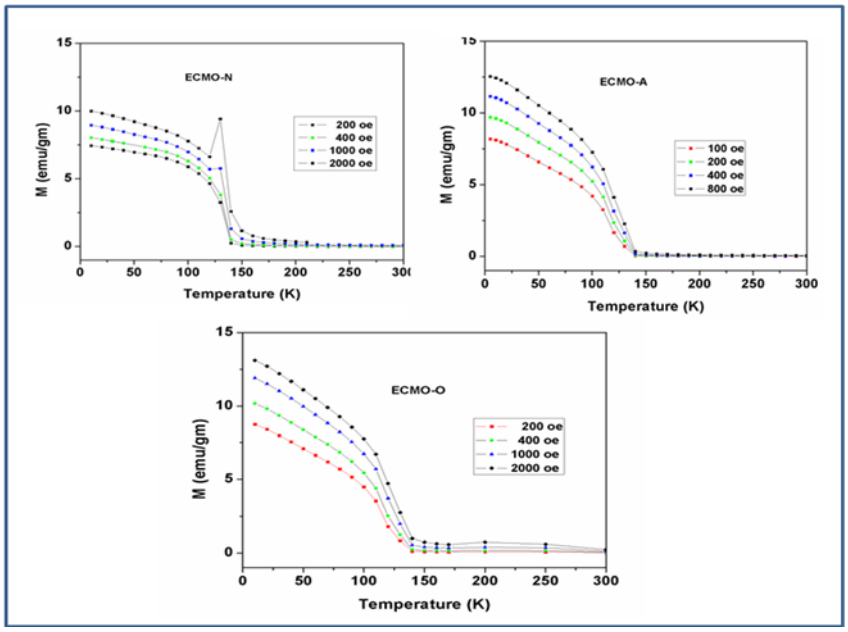

Fig.5.4: Temperature dependent FC magnetic magnetization of ECMO-A, ECMO-O and ECMO-N samples measured at different field.

The net magnetization gradually increases with the increase in the applied field for measurement which indicates that the antiferromagnetically coupled magnetic ion pairs contribute to the ZFC magnetization behavior of all at lower temperatures. In such coexisting antiferromagnetically and ferromagnetically coupled system, the ZFC magnetization depends on the applied field strength, strength of antiferromagnetic interaction and magnetic anisotropy energy of the domains. In general, the ZFC magnetization is directly proportional to the applied field strength and inversely to the magnetic anisotropy energy. In ZFC condition, the temperature induced randomness decreases, which favor a particular type of ordering. Thus, the measurement under the applied field favors the magnetic ordering and hence the ZFC magnetization provides

information on the cluster, spin glass, frustrated etc. type magnetization. The lower magnetic anisotropy in ECMO samples is expected as they show metamagnetic behavior with smaller critical fields. Further as the nature of magnetic interactions are altered by the annealing conditions, the ZFC and FC magnetization show differences. It can be noticed that the ZFC behavior of ECMO-O, ECMO-A samples are drastically different below T_{C2} compared to T_{C1}. This might be due to the presence of larger proportion of antiferromagnetically coupled ion pairs in these compared to ECMO-N.

The variations of magnetic susceptibility with temperature (M/H vs T) of all the three samples measured at different applied field are shown in **Fig.5.5.**

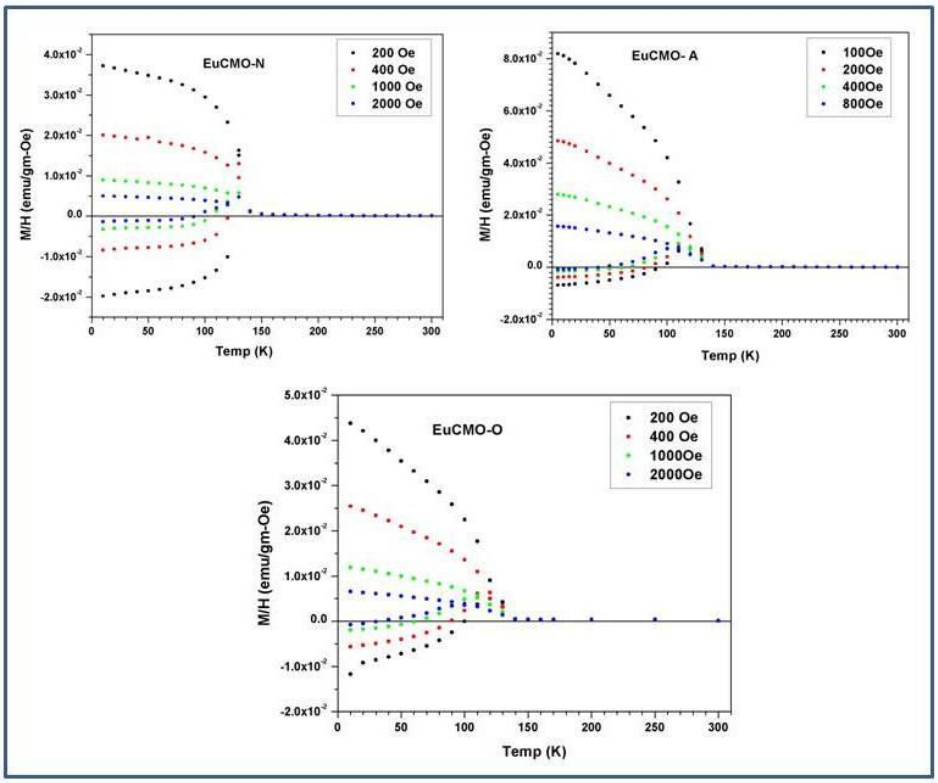

Fig.5.5: Variation of magnetic susceptibility of ECMO samples measured at different applied field.

A decreasing trend with the increasing field and tendency to saturate at higher field, at lower temperature are observed only ECMO-N. Such behaviors of magnetic

interaction in all these samples indicate that they are sensitive to the applied magnetic field. Considering the observed negative magnetization in ZFC, the crossover temperature for negative to positive magnetization is found to decrease with the increase in the applied field. Thus, it can be suggested that metamagnetic nature of the sample has a significant role in the negative ZFC magnetization. Thus, contributing antiferromagnetic and metamagnetic behavior can be inferred in the ECMO samples. Further evidences for these have been obtained from the magnetic hysteresis loops recorded at different temperatures.

The magnetic hysteresis (MH) loops for ECMO samples recorded at several temperatures between 5 and 150 K are shown in **Fig 5.6**.

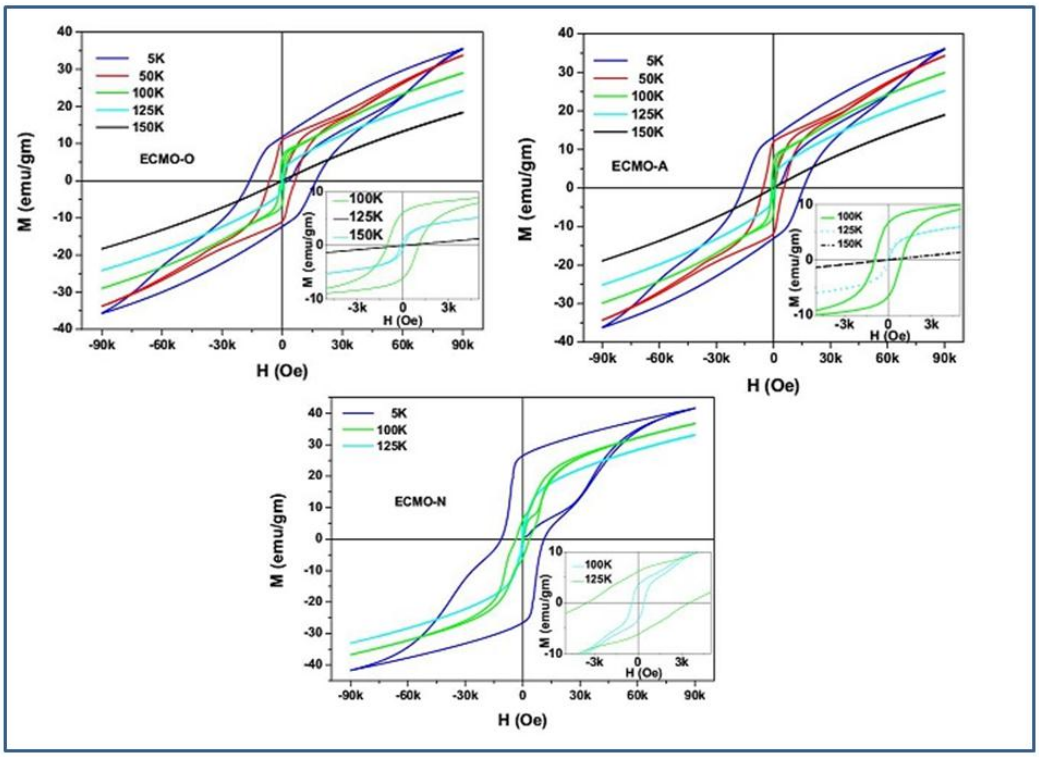

Fig.5.6: Magnetic hysteresis loops of ECMO samples measured at some representative temperature.

All the samples show ferromagnetic like hysteresis loops below 150 K confirming their ferromagnetic natures. However, the magnetizations of all the ECMO samples do

not show any saturation up to an applied field of about 9 Tesla. This can be due to the existence of antiferromagnetic ordering and their contribution is reduced with the increasing applied external field. It can be noticed from the hysteresis loop of the ECMO-N at 5 K (**Fig.5.7**), magnetization increases like a step at around 30kOe similar to metamagnetic materials. Similar metamagnetic like hysteresis loops have been observed by Vasiliev et al. [160] in $EuCo_{0.5}Mn_{0.5}O_3$. A comparison of the hysteresis loops of ECMO samples at 5K indicates that the critical field increases on annealing in the oxygen containing atmosphere.

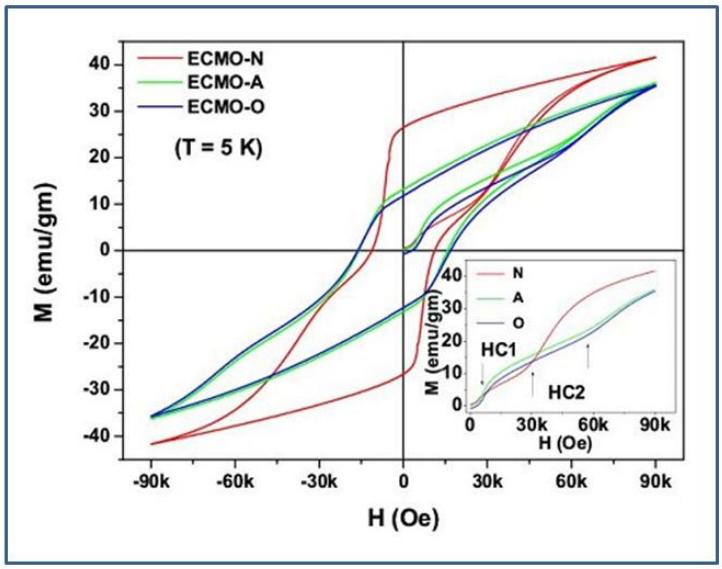

Fig.5.7: Magnetic hysteresis loops of ECMO-A,O and N samples at 5 K.

All the samples show two critical magnetic fields (H_{C1} and H_{C2}) (inset in **Fig 5.7**) in the first cycle magnetization in the positive field, and they are reproduced in the successive cycles. A comparison of the M vs. H loops of the three samples indicate that the H_{C1} remains almost similar while the H_{C2} shifts to lower field on annealing in ECMO-N. This suggests that the antiferromagnetic interactions are weakened by annealing in lower oxygen partial pressure. The magnetic phase diagram for $EuCo_{0.5}Mn_{0.5}O_3$ reported by Troyanchuk et al. suggests ferrimagnetic structure with

oppositely aligned spins of Co^{2+} and Mn^{4+} ions, which transforms to ferromagnetic state with increasing field [158b]. The observed magnetic behaviors indicate field dependent switching of the magnetic interactions in the ECMO which can be further tuned by simple annealing conditions.

Variations of inverse magnetic susceptibility of ECMO samples with temperature are shown in the **Fig.5.8**. The paramagnetic region of the temperature dependent inverse susceptibility of ECMO samples were fitted with Curie-Weiss ($\chi = \frac{C}{T-\theta}$) relation, where C= Curie constant defined as $C = \frac{N\mu_{eff}^2}{3k}$ and θ = Weiss constant. The effective magnetic moment (μ_{eff}/F.U.) observed for the ECMO-O and ECMO-A samples are 4.94 and 4.96μ_B, respectively, while ECMO-N shows larger value (6.63 μ_B). However, the Weiss constant (θ) for all the samples are closely similar, viz. 100.6, 103.4, 102.5 K, for ECMO-O, ECMO-A and ECMO-N, respectively. The positive values of θ indicate ferromagnetic interaction of the transition metal ions in all of these samples. In all the cases, the observed θ is lower than the T_C due to the contributions of antiferromagnetic interactions in the system. The effective magnetic moments comparable to that expected in such Co containing compounds (as: $\mu_{eff} = 0.5\mu_B^2[g_{Mn}^2 S_{Mn}(S_{Mn}+1) + g_{Co}^2 S_{Co}(S_{Co}+1)]$; with S_{Co2+} (HS) and S_{Mn4+} are 3/2, g_{Co2+} = 3.00, g_{Mn4+} = 2.00, the μ_{eff} = 4.94 μ_B). It is known that low spin configuration Co^{2+} ($3d^7$) ($t_{2g}^6 e_g^1$; S=1/2) only shows nearly isotropic g ($g_\perp$~ 2.2 > g_{II} = 2.02-2.01) at room temperature due to sufficiently long spin lattice relaxation time, while the high spin configuration ($t_{2g}^5 e_g^2$; S=3/2), Co^{2+} can exhibit large anisotropic g ($g_\perp$= 4.5 > g_{II} = 2.02-2.04) due to shorter spin lattice relaxation time. The EPR studies on La_2CoMnO_6 indicate a larger g value (g ~ 2.98) for the high spin Co^{2+} (S=3/2)

[150c]. From the magnetic measurements of $EuCo_{0.5}Mn_{0.5}O_3$, Vasiliev et al. have reported g ~ 3.1 for high spin Co^{2+} ions [160]. It can be mentioned here that the $EuCo_{0.5}Mn_{0.5}O_3$ sample studied by Vasiliev et al. [160] has about 8 % Co^{3+} ($3d^6$) in low spin $t_{2g}^6 e_g^0$ state. The observed effective moment for the ECMO-N indicates a g-value of 4.4 for Co^{2+} ion. However, the exact spin state and oxidation states of the Co and Mn cannot be concluded in such strongly interacting systems. Thus, it can only be suggested that the effective spin state of Co and distortion around the Co ions vary appreciably on annealing in inert atmosphere.

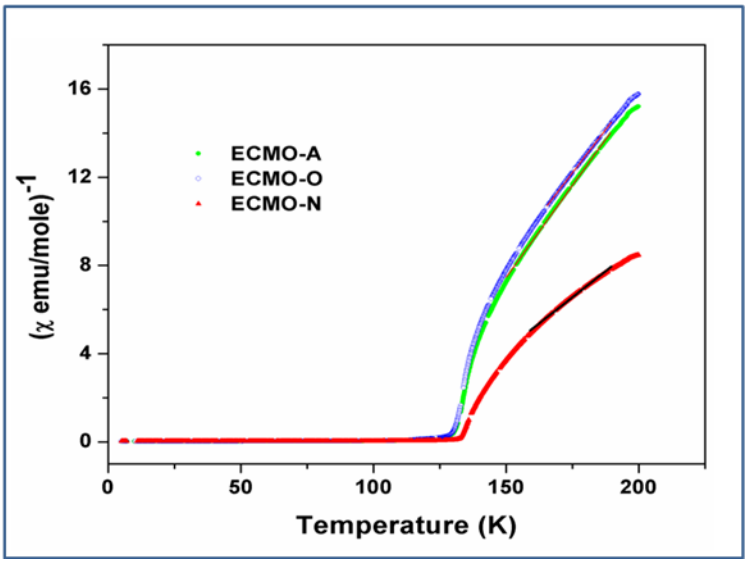

Fig.5.8: Variations of inverse magnetic susceptibility of ECMO samples with temperature.

The magnetic behaviors of the Co-Mn containing rare-earth double perovskites show diversified magnetic properties, like ferromagnetic, antiferromagnetic to spin glass or metamagnetic behavior [149b,150a,158b,159-160]. The magnetic phase diagram investigated in such system revealed the presence of different magnetically coupled transition metal pairs which govern their magnetic properties. It has been reported that the ferromagnetic transition in the cation ordered Co-Mn containing double perovskites originates from the Co^{2+}-O-Mn^{4+} super exchange interactions

[149a,149c,150a,150b,151a,151b,153]. The different ferromagnetic interactions due to different magnetically coupled pairs have been observed in La_2CoMnO_6 [149b,150b,151c]. As mentioned earlier, the Co and Mn containing double perovskite can retain Co^{2+}, Co^{3+}, Mn^{3+} and Mn^{4+} ions in structure, a number of possible interactions of magnetic ions can be expected. In such perovskites, the ferromagnetic interactions are mainly arising from the Mn^{3+}-O-Mn^{4+}, Co^{2+}-O-Co^{3+} (LS), Co^{2+}-O-Mn^{4+} and vibronically coupled Co^{3+}-O-Mn^{3+}, while all other interactions of magnetic ions are of antiferromagnetic nature [149b,150b,161b,162]. Even, in the cation ordered rare-earth double perovskite structures, the antisite defects cause an appreciable contribution of antiferromagnetic interactions [149b,150a,150b,151,153, 163]. Besides, the spin states of Co^{2+}, and Co^{3+} are also strongly dependent on the temperature and composition of the samples [162b,164]. Thus, wider range of effective paramagnetic moments for such materials is expected. Since the coexistence of Co^{2+}, Co^{3+}, Mn^{3+} and Mn^{4+} is evident in the present studied ECMO samples, a number of possible magnetic interactions between these transition metal ions are likely to exist. The ferromagnetism in the ECMO samples is mainly arising from the Co^{2+}-O-Mn^{4+}, Co^{3+}-O-Mn^{3+} clusters as all the other interactions have negative super-exchange interaction [155,162b,164b,165]. Besides, the presence of all the magnetic interacting pair in a disordered system as is the present case may lead to spin glass type behavior. Investigation of magnetic structure of partially cation disordered monoclinic (~ 35 % disordering) systems, like La_2CoMnO_6, Tb_2CoMnO_6, Y_2CoMnO_6 etc. revealed ferromagnetic ordering in the transition metal ions but with a significant contribution from the spin glass or paramagnetic phases [150b,155,162b, 164b,165-166]. This appears to be reason for the observation of significantly lower effective

magnetic moment compared to the spin only value. Metamagnetic transitions with field induced ferromagnetic phase having significantly lower magnetic moment in double perovskites-type compositions are reported with Ln = Gd, Tb, Dy, Nd, Eu, Y etc. [149b,158b,160,166-167]. But later studies on Tb_2CoMnO_6 suggest the reorientation of antiparallel Tb^{3+} moments is the origin of the metamagnetic transition [168]. However, this reason cannot be generalized as similar metamagnetic behavior has also been observed in perovskites with diamagnetic ions as well as ions with low magnetic contribution as A-site cation [158b]. Thus, the clusters of different magnetically coupled ion pairs and their reorientation with the magnetic field might be the origin of the metamagnetic transition.

5.3.4. Dielectric properties

The dielectric properties of the samples prepared under different annealing conditions were investigated and they are explained in this section. The variations of real part of relative permittivity (ε′) with frequency as well as with temperature are shown in **Fig 5.9 and 5.10**, respectively. Both the temperature and frequency dependent permittivities of all the samples show two step-like relaxations with large dispersion. The ECMO-A sample shows a large dielectric constant of about 800 at 273K at frequencies around 2 kHz. Since, the dielectric measurements could not be measured up to the magnetic transition temperature, the behavior of the samples at magnetic transition temperature is not delineated. Above the magnetic transition temperature, all the studied samples show two relaxations, one weaker towards the lower frequency and the main relaxation at higher frequency. The permittivity in ECMO-A for the main relaxation varies around 250-650 in the entire temperature range. However, at lower frequency, the permittivity of about 150 is observed at low

temperature and that increases with the increase in temperature. Similar behaviors are observed in ECMO-O sample also, but the permittivity increases to about 2000 at 273 K, which remains almost unchanged in the range 10^2Hz-10^5Hz. However, the ECMO-N sample shows a reduced permittivity both at low and high frequency regions.

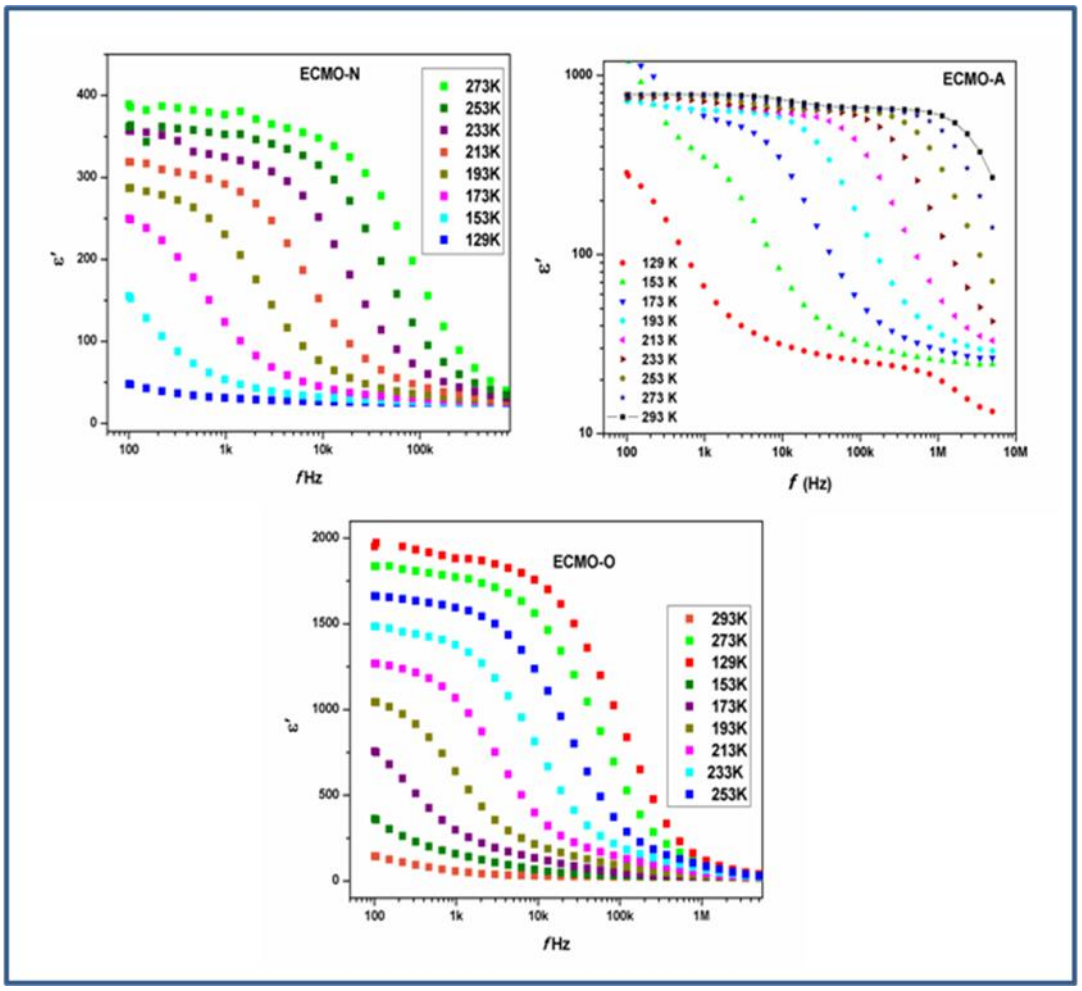

Fig.5.9: Frequency dependent real part of relative permittivity of ECMO samples measured at different temperatures.

The variation of loss tangent tanδ (= $\varepsilon''/\varepsilon'$) with temperature at different frequencies of different samples are shown in **Fig. 5.11**. The ECMO-O sample shows two distinct relaxation peak while others shows only the one main relaxation process in the *tanδ* vs. T plots. Both the temperature dependence of dielectric permittivity or tanδ revealed presence of the dielectric relaxations in all, but the features of relaxation

peaks are different for different samples. It can also be observed that the ECMO-A sample shows peak with strong frequency dispersion in tanδ compared to others. In addition, a large increase in the loss tangent in ECMO-O sample is observed at higher temperature. In the ECMO-N sample, the relaxation peaks are hardly distinguishable, especially at higher frequencies but the permittivities increases sharply at higher temperatures. This suggests that the annealing conditions play crucial role in tailoring the dielectric response of ECMO samples, and the permittivity can be enhanced by almost an order of magnitude with oxygen annealing.

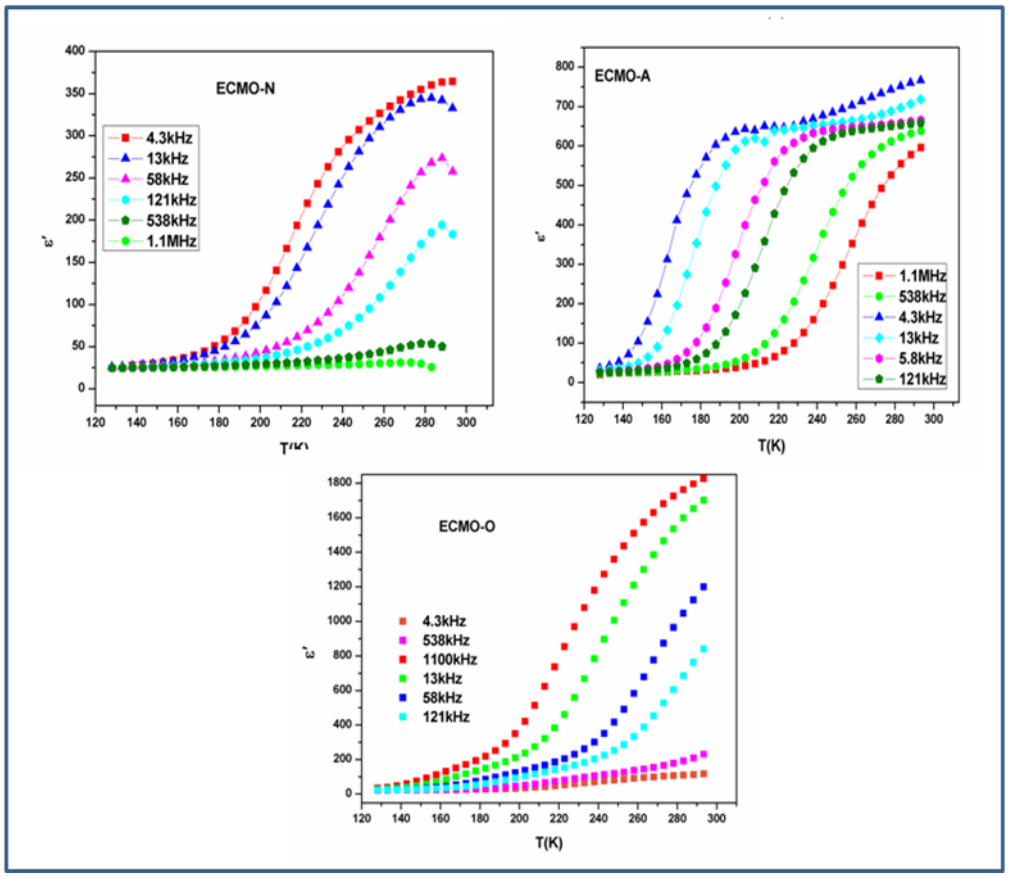

Fig.5.10: Temperature dependent real part of relative permittivity of ECMO samples measured at different frequencies.

The dielectric relaxation observed in the samples can have two types of origins, viz. conduction or dipolar origins. The large increase in loss tangent in both ECMO-O and

N at higher temperature suggests enhanced electrical conductivities in them. In all the samples the peak relaxation temperature shifts towards higher temperature with the increase in frequency. In case of ECMO-N, no distinct peak could be observed due to dominating conducting contributions. However the changes in slope, i.e. the shoulder of the traces, were used as the peaks (Tmax). In case of ECMO-O, the first peak is only considered and thus the period of the 1st relaxation only deciphered in all of the three studied samples. The relation between the relaxation frequency and temperature T_m of the tanδ peaks was found to follow the Arrhenius relation of Eq (5.3), as shown in **Fig.5.12.**

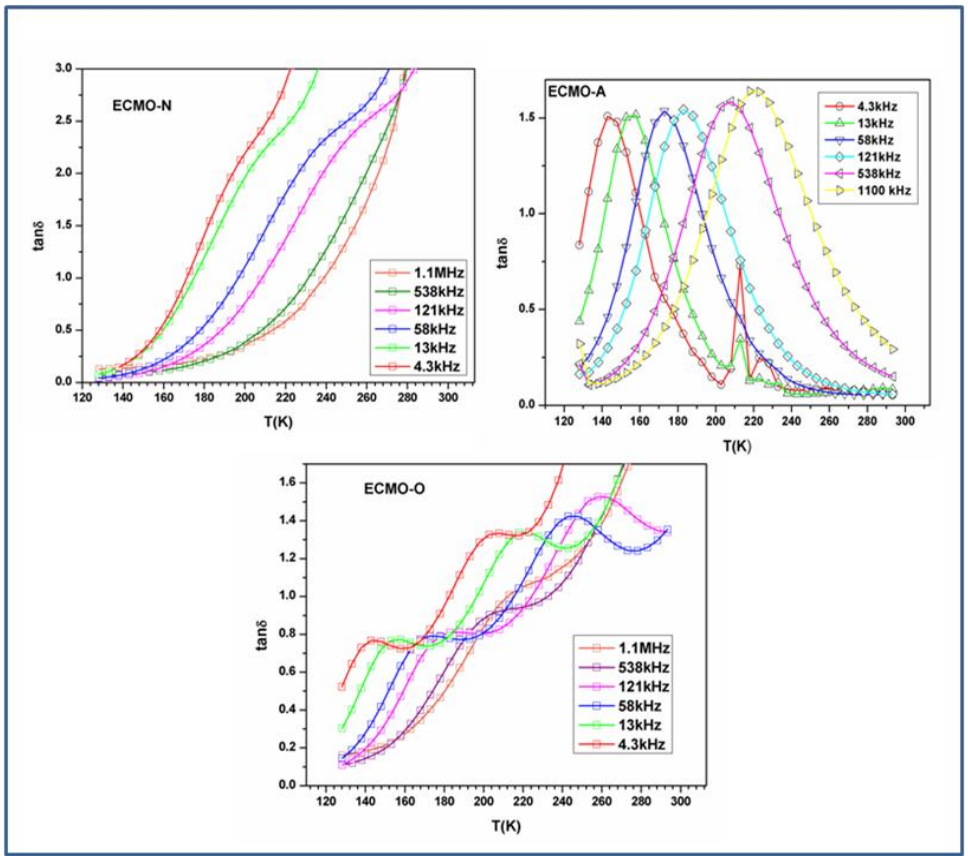

Fig.5.11: Variation of loss tangent of ECMO samples with temperature.

The values of activation energy for the main relaxation as obtained from the Arrhenius relation are: 0.20eV, 0.20eV and 0.22eV for ECMO-A, ECMO-O and ECMO-N

samples, respectively. In all the cases the activation energies are more or less similar which suggests an identical conduction mechanism in these samples. Further, the values of the activation energies suggest conduction of the polarons associated with the defects. Although, no detectable anion vacancies are observed in any of the system under study, a feeble concentration of point defects cannot be ruled out in any system containing transition metal ions having variable oxidation states. The oxygen vacancies, ($O^{2-} = V_{02-} + 2e^{-} + 1/2O_2$) can be expected in such systems. Also, the Eu^{3+} vacancies observed in ECMO-N samples also likely to form holes ($Eu^{3+} = V_{Eu3+} + 3h^{+}$). Thus, these holes may be balanced by equivalent increase in valence states of Co^{2+} or Mn^{3+} to Co^{3+} or Mn^{4+} in the lattice or can associate with the anions forming a localized bound state polaron. However, the presence of extra polarons in ECMO-N sample might be a reason for the higher loss in it compared to others.

Further to differentiate the relaxation due to the conduction or dipolar fluctuations from the interfacial or electrode polarization at low frequency ends, the temperature and frequency dependent dielectric data were analyzed in electric modulus representation. In general the modulus representations of frequency dispersion data suppress the electrode/grain boundary effects and clearly delineate the hopping conduction and dipolar relaxations. The modulus data were extracted from the permittivity data using the following relation.

$$M^*(\omega) = M'(\omega) + iM''(\omega) = 1/\varepsilon^*(\omega) \qquad [5.1]$$

Where, $M^*(\omega) = M'(\omega) - i\,M''(\omega)$ and $\varepsilon^*(\omega) = \varepsilon'(\omega) - i\,\varepsilon''(\omega)$ are complex modulus, permittivity, respectively and $\omega = 2\pi f$ is the angular frequency of the applied electric field.

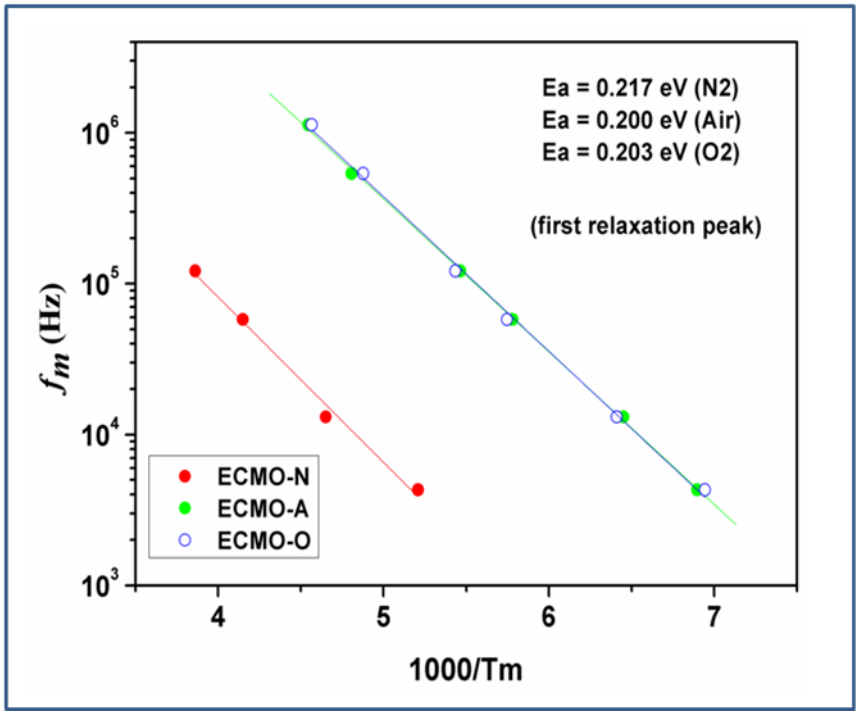

Fig.5.12: Arrhenius fit of the peak relaxation frequency (tanδ) for ECMO samples.

The modulus data can also provide more information to differentiate the hopping conduction or dipolar relaxation. The variations of M″ with frequency as well as with temperature are shown in **Fig 5.13 and 5.14**, respectively. In general, the conduction induced relaxation process is observed as peak in the *M″ vs f* but not in the *ε″ vs f* plots. However, for the dielectric relaxation due to localized dipolar relaxation and long range hopping conductivity are observed as peak in both *M″* as well as ε″ plots .

In the modulus representation, the relaxation time $\tau_M = 1/f_m$, where f_m is the position of relaxation peaks in *M″*(*f*), and is related to the dielectric relaxation time $\tau_D=1/f_D$ in the Debye model as [39]

$$f_m = 1/\tau_M = (\varepsilon_s/\varepsilon_\infty)(f_D) \qquad [5.2]$$

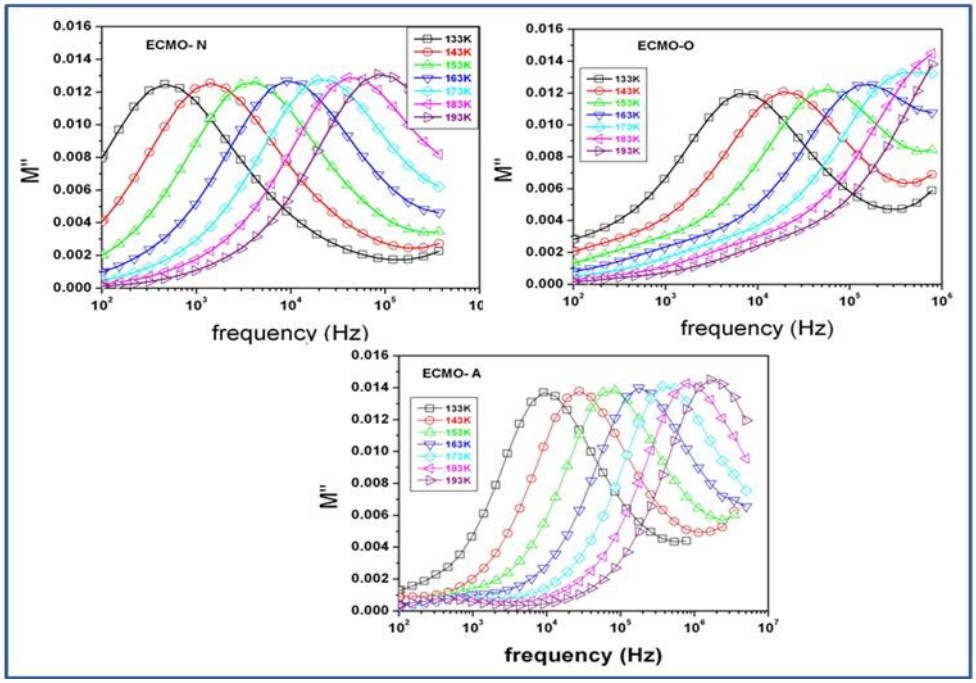

Fig.5.13: Variation of imaginary part of Modulus (M") of ECMO samples with frequency.

The variations of imaginary parts of the modulus (M″ *vs f*) of all the three samples show clear peaks which are similar to that observed in tanδ vs. *f* plots. In the frequency region below the peak maximum (M''_{max}), the carriers are mobile at longer distances while in the frequency region above peak the carriers are confined and have shorter range mobility. The extended dipole formed in the anion defective lattices may favor for a longer relaxation process and hence larger dielectric permittivity as well as loss. Such features are also likely to exist in the ECMO-O and -A samples. However, in the ECMO-N sample the presence of Eu^{3+} ion vacancies might be resulting into holes at the Eu^{3+} site and the hole and electron may be forming a trapped polaron. But the polaron migration is favored at higher temperature. Thus, the dielectric permittivities are significantly reduced with the concurrent increase in loss. A comparison of the loss peaks in M″ *vs f* of the ECMO samples indicates a systematic

shift towards higher frequency with the increase in temperature. Thus, the frequency region for the long range conductivity increases with the increasing temperature.

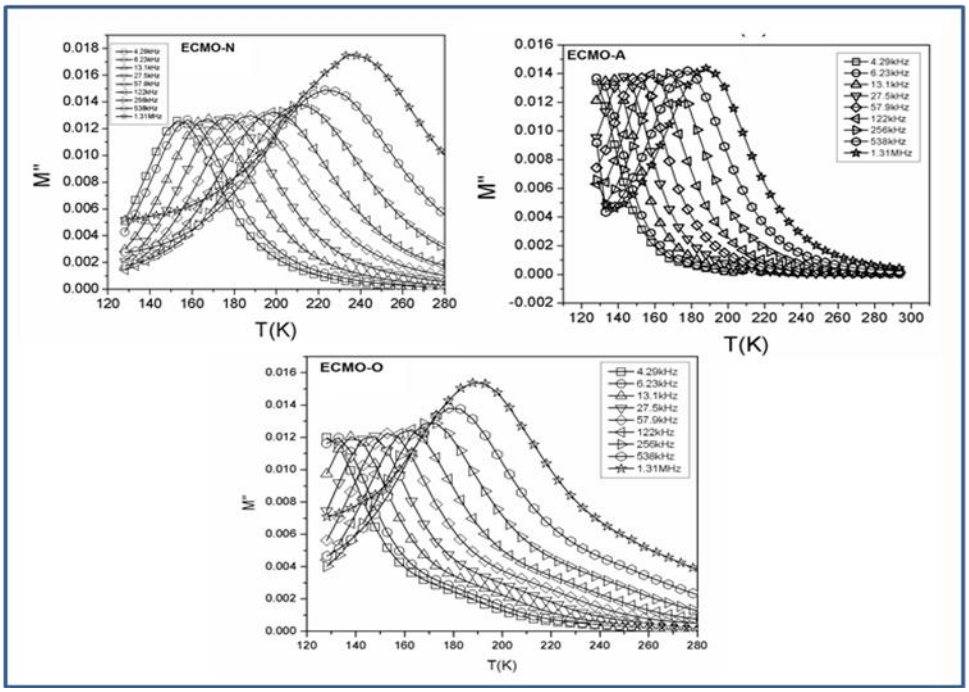

Fig.5.14: Variation of imaginary part of Modulus (M") of ECMO samples with temperature.

The temperature dependence of the relaxation frequency has been obtained from the positions of the maxima (f_m) in the frequency dependent M″ plots and they are shown in **Fig. 5.15.** Typical Arrhenius type (Eqn. 5.3) behavior is observed for all of them.

$$f_m = f_0 \exp(-E/(k_B T)) \qquad [5.3]$$

Where f_o is a pre exponential factor, k_B is the Boltzmann constant, T is the temperature and E is the activation energy.

The values of activation energy are 0.19eV, 0.20eV, and 0.19eV for ECMO-A, O and N samples, respectively. Similar Arrhenius type behaviors are observed for the relaxation frequency f_m and peak temperature (T_m) of M'' (**Fig 5.16**).

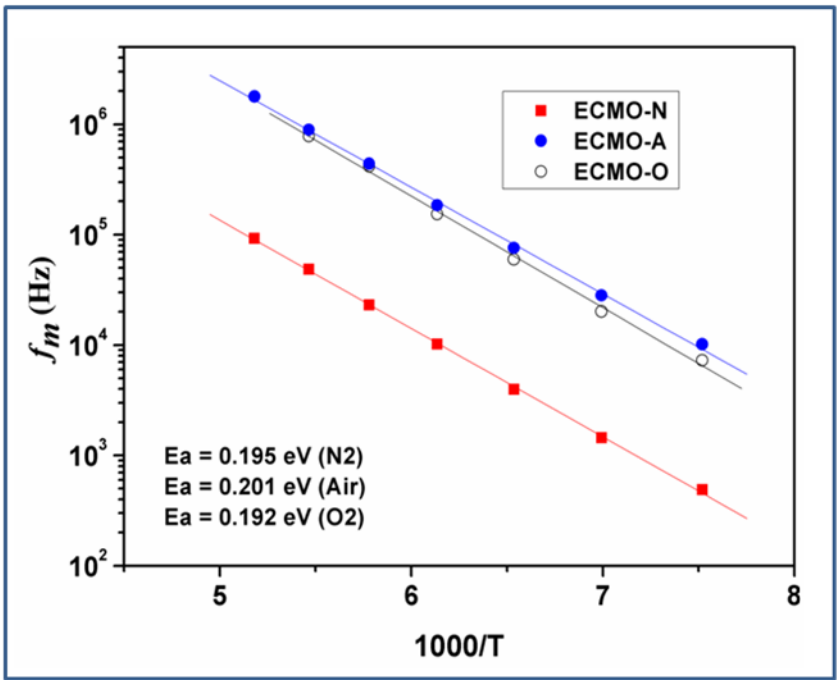

Fig.5.15: Arrhenius plots of relaxation peak frequency (M") of ECMO samples.

These values are close to the activation energy in the charge-ordered magnetodielectric La_2CoMnO_6 exhibiting polaronic conduction [153]. It is notable that, according to electrochemical data, the energy required to transfer an electron from the Co^{2+} to Mn^{4+} in La_2CoMnO_6 requires 0.20eV [150a,153]. It is therefore presumed that the observed low temperature dielectric relaxations in $EuCo_{0.5}Mn_{0.5}O_3$ are polaronic in nature, and they are dependent upon the annealing conditions. From the above observations, it is clear that the dielectric relaxations of the samples, though qualitatively different based on sample treatment conditions, most likely originate from polaron hopping. For charge ordered double perovskites like La_2MMnO_6 (M=Co, Ni), the ordering of M^{2+} and Mn^{4+} induces a strong local polarization leading to high dielectric constants and polaronic hopping at low temperatures [149b,153,168].

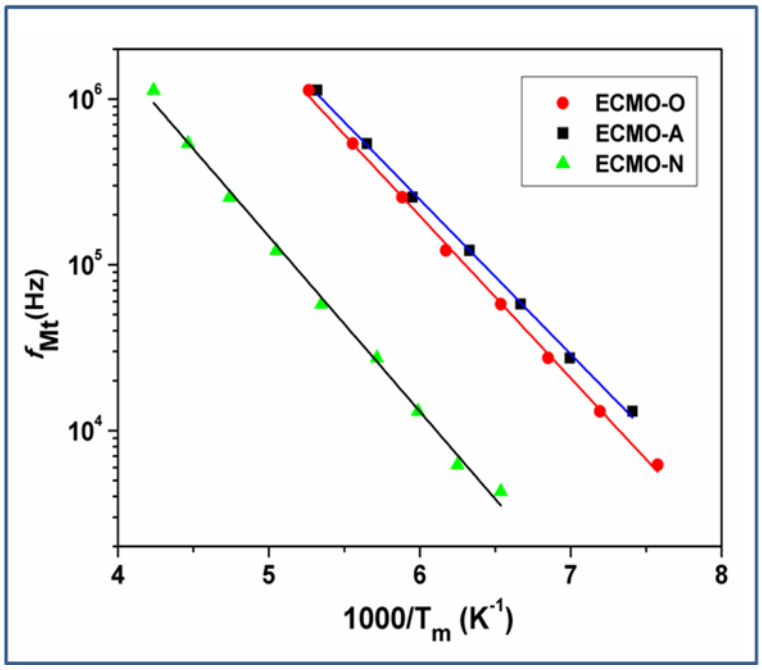

Fig.5.16: Arrhenius fit of the peak relaxation frequency of ECMO samples as observed from M″ vs f plots.

It is worth noting that while the Mott variable range hopping (VRH) behaviour was seen in La_2CoMnO_6 [153], where the behavior deviated from Arrhenius law (Eq.(5.3)), it is observed that ECMO data could be very well fitted to Eq.(5.3), suggesting a simple thermally activated hopping of the polarons to nearest neighbours in $EuCo_{0.5}Mn_{0.5}O_6$ structure. Such behavior has also been observed in La_2MgMnO_6 [168], where co-existence of Mn^{3+} and Mn^{4+} mediate the polaronic conduction. It is therefore likely that both the ordering of Co^{2+} and Mn^{4+} as well as mixed valence states of Mn lead to the dielectric relaxations of the ECMO samples. The significant differences in the dielectric relaxations in the three samples suggest that the syntheses conditions play a significant role in the polaron dynamics. It is also evident that the dielectric constant can be tuned by altering the annealing conditions.

In order to study the effect of structural features and ionic radius of A site cation on the magnetic and dielectric properties, an additional system with yttrium at

the A- site has been investigated. Both Y_2NiMnO_6 and Y_2CoMnO_6 are expected to form cation ordered peroskite structure, contrast to Eu_2CoMnO_6 which has cation disordered lattice. A comparative study of these systems revealed the effect of structure and ionic radii on these properties, which are explained subsequentialy.

5.4. Result and discussion of Y_2CoMnO_6 (YCMO) and Y_2NiMnO_6 (YNMO)

5.4.1. XRD Studies

The sintered samples of both YCMO and YNMO obtained after 1250°C were characterized by the Rietveld refinement of the powder XRD data. It can be mentioned here that the $Ln_2MM'O_6$ (M and M' = transition metal ions) double perovskites can exist in cation disordered orthorhombic structure or cation ordered monoclinic structure. The feeble distortion arising from the cation ordering in the octahedral sites are reflected in the β angle of the monoclinic unit cell marginally deviated from 90°. The values of β depend on the ionic radii of rare-earth ions and for larger Ln^{3+} ions it remains more close to 90°. In the cases of Y_2CoMnO_6 or Y_2NiMnO_6 the deviations are little higher compared to analogous Eu or La compounds [150a,150c].

All the observed reflections of the YNMO and YCMO could be accounted by orthorhombic lattice and thus both orthorhombic (Pnma) and monoclinic ($P2_1/n$) structure models have considered for the Rietveld refinement, however no significant differences are observed in the residuals of refinements due to closer x-ray scattering factors of Co, Mn and Ni. However, earlier neutron diffraction studies indicated clear cation ordering in them [158a,169]. A partial cation disorder in the range of 12 to 33 % depending on the preparation temperature and time has been reported for such perovskites. Shrama et al. [158a] have indicated fully cation ordered monoclinic

structure while Mouallem-Bahouta et al. [169] indicated a partial disorder in Y_2CoMnO_6. The present observed magnetic properties and transition temperatures of YCMO and YNMO samples are more comparable to the cation ordered samples reported earlier in literature [157-158]. Thus, the monoclinic cation ordered structure is inferred for both the samples. Pseudo-Voigt profile function and fifth order polynomial function respectively were used for modeling the peak shape and background of the powder XRD data of as-prepared samples of YCMO and YNMO. The progress and goodness of the refinements were monitored by the residuals of refinement and difference plots. In both the samples weak peaks attributable to C-type cubic phase of Y_2O_3 were observed and the structural parameters of C-type phases were included in the refinement. The positional parameters and overall thermal parameters were also refined subsequently. The individual isotropic thermal parameters of cations and anions were refined in the final cycles of refinements. The XRD patterns of the samples annealed in different atmospheres were refined in similar procedures by using the refined structural parameters of their respective *asp*- samples. The powder XRD patterns as well as refined structural parameters of air or O_2 annealed samples of both YCMO and YNMO were almost similar. In the powder XRD pattern of YCMO sample annealed in N_2 atmosphere show weak additional reflections. These weak reflections could be assigned to the spinel type $(Co,Mn)_3O_4$ phase similar to that observed for Fe_3O_4. Refined structural parameters for all the investigated samples are given in **Table 5.2 and 5.3** and their corresponding Rietveld refinement plots are shown in **Fig.5.17. (a,b).**

(a)

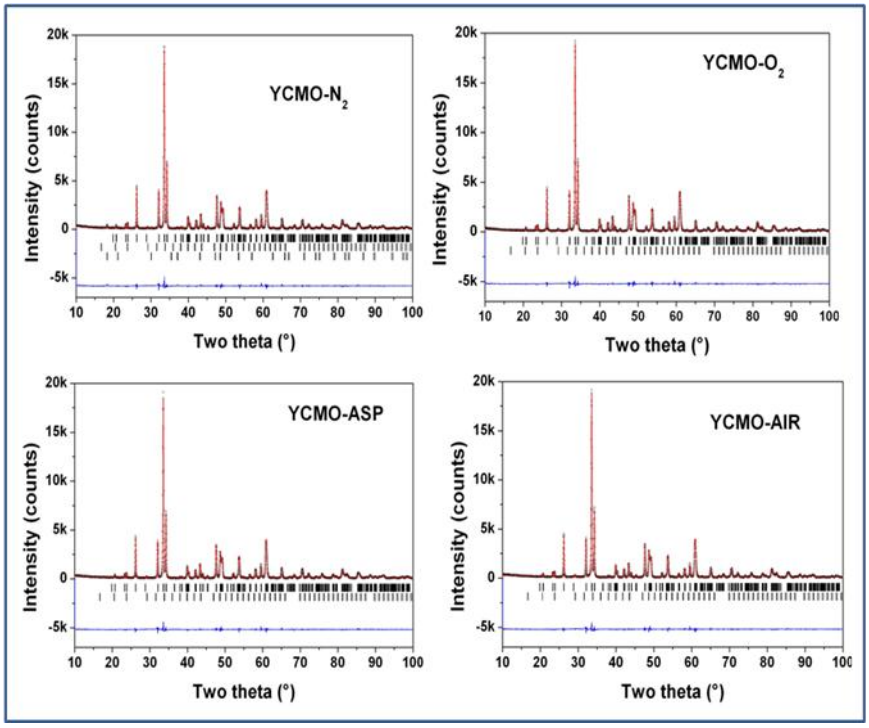

(b)

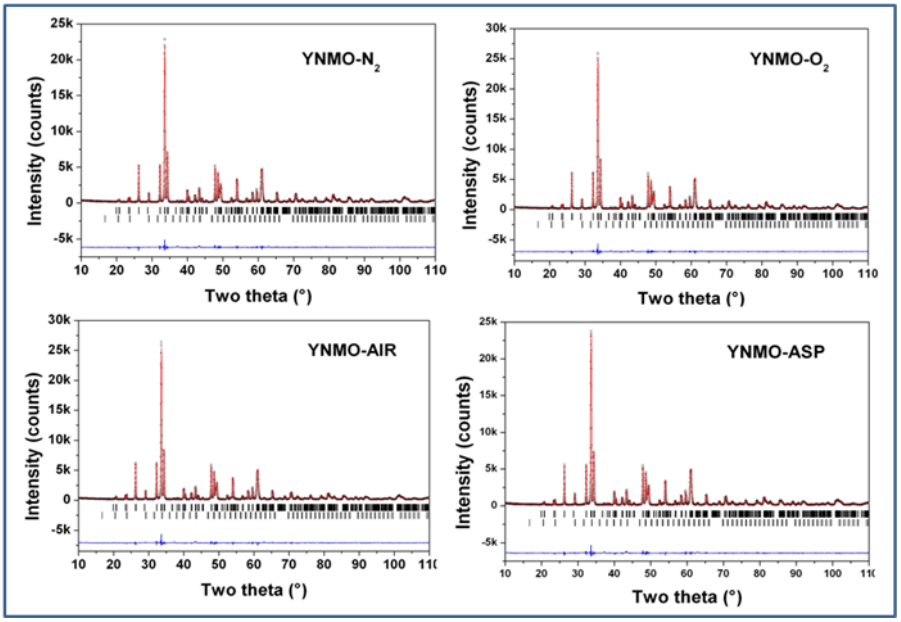

Fig.5.17: Rietveld refinement plots of powder XRD data of (a) Y_2CoMnO_6 sample annealed different atmosphere. (b) Y_2NiMnO_6 sample annealed in different atmospheres.(nitrogen, oxygen, air and asprepared) (Bragg positions of perovskite and Y_2O_3 phases are indicated by top to bottom vertical ticks).

	YCMO-O	**YCMO-A**	**YCMO-N ***	**YCMO-ASP**
Annealing atmosphere	O_2	Air	N_2	
Source	RA, CuKα	RA, CuKα	RA, CuKα	RA, CuKα
Wavelength (Å)	1.5406, 1.5444	1.5406, 1.5444	1.5406, 1.5444	1.5406, 1.5444
2-theta range (°)	10-100	10-100	10-100	10-100
Space Group	$P2_1/n$	$P2_1/n$	$P2_1/n$	$P2_1/n$
Unit cell parameters(Å)	5.2310(1) 5.5766(1) 7.4699(1) 89.836(3)	5.2313(1) 5.5754(1) 7.4706(1) 89.834(3)	5.2315(1) 5.5745(1) 7.4715(1) 89.836(3)	5.2314(1) 5.5747(1) 7.4709(1) 89.843(3)
Volume ($Å^3$)	217.906(7)	217.890(7)	217.890(7)	217.878(6)
Y *(4c: x,1/4,z)* B ($Å^2$)	-0.0193(2) 0.0721(1) 0.2494(4) 0.41(1)	-0.0191(2) 0.0721(1) 0.2499(4) 0.47(1)	-0.0191(2) 0.0723(1) 0.2497(4) 0.32(1)	-0.0189(2) 0.0721(1) 0.2496(4) 0.26(1)
Mn/Co *(4b: 0,0,1/2)* B ($Å^2$)	0.5 0 0 0.17(2) 0.37(6):0.13(6)	0.5 0 0 0.23(1) 0.43(6):0.07(6)	0.5 0 0 0.09(2) 0.43(6):0.07(6)	0.5 0 0 0.01(1) 0.43(6): 0.07(6)
Co/Mn *(4b: 0,0,1/2)* B ($Å^2$)	0.5 0 0.5 0.17(2) 0.37(6):0.13(6)	0.5 0 0.5 0.23(1) 0.43(6)	0.5 0 0.5 0.09(2) 0.43(6):0.07(6)	0.5 0 0.5 0.01(1) 0.43(6): 0.07(6)
O1 *(4c: x,1/4,z)* B ($Å^2$)	0.1074(4) 0.4664(4) 0.2559(11) 1.06(4)	0.1079(4) 0.4663(4) 0.2560(10) 1.07(4)	0.1073(4) 0.4666(4) 0.2588(10) 0.74(4)	0.1075(4) 0.4665(4) 0.2590(9) 0.61(3)
O2 *(8d: x,y,z)* B ($Å^2$)	0.6804(10) 0.2942(9) 0.0595(6) 1.06(4)	0.6792(9) 0.2936(9) 0.0564(6) 1.07(4)	0.6793(10) 0.2920(9) 0.0550(7) 0.74(4)	0.6803(9) 0.2953(9) 0.0573(6) 0.61(3)
O3 *(8d: x,y,z)* B ($Å^2$)	0.7032(9) 0.3140(9) 0.4540(6) 1.06(4)	0.7048(8) 0.3153(9) 0.4517(6) 1.07(4)	0.7032(9) 0.3153(9) 0.4494(7) 0.74(4)	0.7034(9) 0.3116(9) 0.4514(6) 0.61(3)
Rwp,Rp, χ^2 R_B, R_F	5.76, 7.91, 2.21 2.05, 1.60	5.53, 7.63, 2.03 2.15, 1.57		5.61, 7.70, 1.97 2.10, 1.55

Table 5.2: Refined structural parameters of Y_2CoMnO_6 samples annealed in different atmosphere.

	YNMO-O	**YNMO-A**	**YNMO-N***	**YNMO ASP**
Annealing atmosphere	O_2	Air	N_2	
Source	RA, CuKα	RA, CuKα	RA, CuKα	RA, CuKα
Wavelength (Å)	1.5406, 1.5444	1.5406, 1.5444	1.5406, 1.5444	1.5406, 1.5444
2-theta range (°)	10-100	10-100	10-100	10-100
Space Group	$P2_1/n$	$P2_1/n$	$P2_1/n$	$P2_1/n$
Unit cell parameters(Å)	5.2193(1) 5.5443(1) 7.4777(1) 89.761(1)	5.2196(1) 5.5442(1) 7.4782(1) 89.761(1)	5.2211(1) 5.5419(1) 7.4801(1) 89.765(1)	5.2211(1) 5.5415(1) 7.4797(1) 89.765(1)
Volume ($Å^3$)	216.382(5)	216.401(5)	216.435(4)	216.406(4)
Y *(4c: x,1/4,z)* B ($Å^2$)	-0.0186(2) 0.0714(1) 0.2502(3) 0.404(6)	-0.0185(1) 0.0712(1) 0.2500(3) 0.669(6)	-0.0184(1) 0.0711(1) 0.2501(3) 0.190(6)	-0.0188(1) 0.0712(1) 0.2502(3) 0.192(6)
Mn/Co *(4b: 0,0,1/2)* B ($Å^2$)	0.5 0 0 0.25(1) 0.271(3):	0.5 0 0 0.51(1) 0.239(2):	0.5 0 0 0.06(1) 0.23(4)	0.5 0 0 0.08(1) 0.26(4)
Co/Mn *(4b: 0,0,1/2)* B ($Å^2$)	0.5 0 0.5 0.25(1) 0.271(3)	0.5 0 0.5 0.51(1) 0.239(2)	0.5 0 0.5 0.06(1) 0.27(4):	0.5 0 0.5 0.08(1) 0.26(4)
O1 *(4c: x,1/4,z)* B ($Å^2$)	0.1041(4) 0.4656(3) 0.2505(6) 0.76(5)	0.1048(3) 0.4646(3) 0.2507(6) 1.08(5)	0.1055(3) 0.4649(3) 0.2498(7) 0.33(5)	0.1053(3) 0.4637(3) 0.2511(7) 0.38(10)
O2 *(8d: x,y,z)* B ($Å^2$)	0.6860(6) 0.2934(8) 0.0519(5) 0.85(10)	0.6875(6) 0.2919(6) 0.0522(4) 0.87(10)	0.6858(6) 0.2928(8) 0.0504(4) 0.09(9)	0.6840(7) 0.2884(7) 0.0518(4) 0.52(10)
O3 *(8d: x,y,z)* B ($Å^2$)	0.6972(6) 0.3117(8) 0.4457(4) 0.55(10)	0.6954(6) 0.3146(6) 0.4441(4) 1.42(10)	0.6953(7) 0.3128(8) 0.4432(4) 0.58(10)	0.6975(6) 0.3157(7) 0.4441(4) 0.32(10)
Rwp,Rp, χ^2 R_B, R_F	5.00, 7.17, 2.61 2.43, 1.77	4.91, 6.94, 2.40 2.45, 1.80	5.00, 7.08, 2.27 2.58, 1.90	4.98, 7.19, 2.41 2.30, 1.61

Table 5.3: Refined structural parameters of Y_2NiMnO_6 samples annealed in different atmosphere.

Studies on similar Ln_2MMnO_6 (Ln = La and Eu; M = Co and Ni) samples indicate phase separation on annealing in inert atmosphere. Most often they form cation deficient perovskite phases. However similar phase separations have not been observed in La_2CoMnO_6 [150c] or Y_2NiMnO_6 of present study. In the case of Eu_2CoMnO_6, separation of Eu_2O_3 leading to $Eu_{1-x}Co_{0.5}Mn_{0.5}O_{3-y}$, with x ~ 0.03 and y ~ 0.02 type perovskite phase and on prolonged annealing under similar atmosphere an additional CoO-MnO sold solution phase has been observed [152]. Though the phase separation does not cause appreciable deficiency in the oxygen stoichiometry, which is retained by the valence fluctuation, there are ample reflections in the magnetic and dielectric properties of such materials. Sazonov et al. have investigated several partially cation disordered $Nd_{2-x}CoMnO_{6-\delta}$ samples and concluded that the oxygen nonstoichiometry is within $0.00 \leq \delta \leq 0.05$ and the oxygen stoichiometry is maintained by the variations of oxidation states of transition metals [159]. Similar feeble oxygen deficiency has been also been observed in La_2MMnO_6 [149a,149b] and cation disordered Eu_2CoMnO_6 mentioned earlier [152]. But they are appeared as shifts in ferromagnetic transition temperatures (T_c). Further insights on such variable oxidation state ion pairs and oxygen defects were inferred from the magnetic and dielectric studies as explained below.

5.4.2. Magnetic properties

In order to understand the magnetic properties of YCMO and YNMO, the temperature dependent magnetizations plots (M vs T) in both field cooled (FC) and zero field cooled (ZFC) conditions were measured and they are shown in **Fig.5.18**. From the FC magnetization, it is observed that both the samples show paramagnetic to ferromagnetic transition below around 80 K. The observed T_c s are in agreement with

those reported earlier for YCMO and YNMO samples [157-158]. A closer look on the magnetization data indicated the *asp*-YCMO sample lower T_c (79 K) compared to all other YCMO samples (~ 83 K). Besides, the T_c's of all other YCMO samples are nearly similar which suggests that the temperature of preparation of YCMO sample has more important bearing than the annealing atmosphere. Further it is observed that the T_c's of all the YNMO samples are similar (88.5 K) irrespective of preparation conditions.

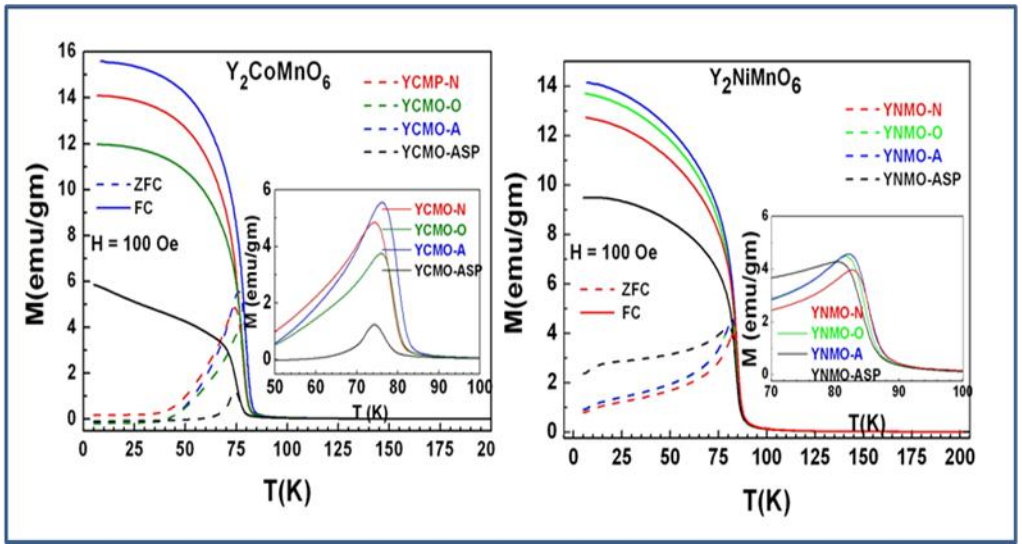

Fig.5.18: Temperature dependent magnetic susceptibility (FC and ZFC) of YCMO samples measured at applied field of 100 Oe.

A comparison of the FC magnetization of the YCMO and YNMO samples indicates that the T_c of *asp*-YCMO is higher compared to that observed for the annealed samples. In addition both YCMO and YNMO samples show only a single magnetization down to 5 K. Contrary to La_2NiMnO_6 and La_2CoMnO_6 , no multiple magnetic transitions have been reported for YNMO or YCMO samples. The multiple ferromagnetic transitions with a larger difference in T_C in La_2CoMnO_6 and La_2NiMnO_6 have been assigned to different magnetically coupled transition metal ion pairs, which arise due to the coexistence of significantly larger fraction of variable

oxidation states of these transition metal ions and appreciable cation disorder in octahedral sites of the structures [149a, 149b,150,170] Sazonov et al. [159] have suggested that a partial involvement of low spin Co^{3+} can also lead to a lower T_c. However, the observed effective magnetic moments of YCMO of the present study, explained later in the chapter, as well as that reported by Sharma et al. [158a] indicate no significant contribution from low spin Co^{3+} ions. Similar comparison of the magnetization behavior of YNMO samples with that reported in literature indicates that the T_c is mainly arising from the ferromagnetic super-exchange interaction between Ni^{2+} and Mn^{4+} [157]. The insignificant effect of annealing conditions on the T_c of YNMO samples compared to YCMO samples suggests the variation of oxidation states has an important role compared to cation distribution. As observed from the diffractions studies, the disordering of cations in octahedral sites of YNMO samples is more compared to that in the YCMO samples. Thus, the effect of cation disorder is likely to have minimal role on the observed magnetic properties. Further, it can be mentioned here the cation distribution is likely to remain unchanged on annealing in lower temperature compared to the sintering temperature. This has been confirmed by powder neutron diffraction study of La_2NiMnO_6 [150a]. Thus, the noticeable variation of T_c of YCMO samples can be attributed to the presence of high spin Co^{3+} and Mn^{3+} ions. This can be expected from the smaller differences in the reduction potentials of Co^{2+}-Co^{3+} and Mn^{3+}-Mn^{4+} couples compared to the Ni^{2+}-Ni^{3+} and Mn^{3+}-Mn^{4+} couples [150a,150c,151a]. It has been observed that the fractions of the ferromagnetically coupled ion pairs are altered by annealing in different oxygen partial pressures at relatively lower temperature than the preparation conditions. Further it is observed that the maximum magnetization of as-prepared YCMO or

YNMO samples show lower values compared to their corresponding annealed samples. This suggests that the annealing redistribute the valences states or possibly reduce distortions induced by strain. However, to confirm this further studies are desired on the samples.

The variation of inverse susceptibility with temperature for both YCMO and YNMO samples **Fig.5.19** could be fitted with Curie-Weiss relation, $(\chi = \frac{C}{T-\theta})$ where C= Curie constant defined as $C = \frac{N\mu_{eff}^2}{3k}$ and θ = Weiss constant.

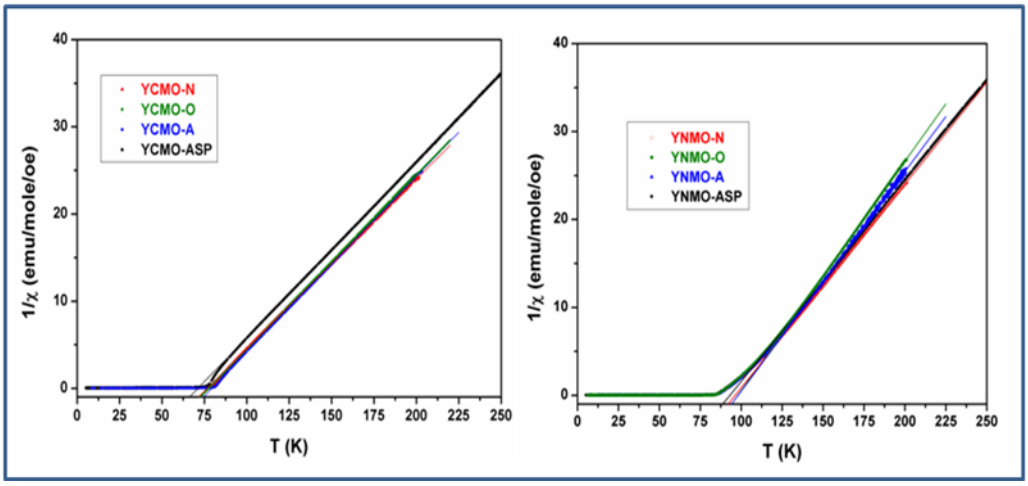

Fig.5.19: Variations of inverse magnetic susceptibilities of YCMO and YNMO samples with temperature.

The observed values of effective magnetic moment (μ_{eff}/F.U.) and Weiss constants are given in **Table 5.4**. In all the cases the positive values of θ indicate ferromagnetic interaction of the transition metal ions and also they are closely similar with those reported in literature [157-158]. The values of μ_{eff}/FU indicate the high spin Co^{2+} and Mn^{4+}or Co^{3+} and Mn^{3+} ion pairs in YCMO samples [158a] and Ni^{2+} and Mn^{4+} in YNMO samples [150a,171]. Similar to the FC magnetization, the ZFC magnetizations of all the samples **(Fig.5.18)** indicate closely similar behavior in YNMO samples while noticeable differences are observed in the YCMO samples. In both the cases,

the ZFC and FC magnetizations show separation below T_c. All the ZFC magnetization curves show peak at the transition temperature which gradually decreases with decreasing temperature

Sample	μ_{eff} (μ_B)	θ (K)
YCMO-ASP	**6.30**	**71.2**
YCMO-Air	**6.29**	**79.5**
YCMO-N_2	**6.41**	**76.6**
YCMO-O_2	**6.32**	**77.6**
YNMO-ASP	**6.21**	**102.7**
YNMO-Air	**5.66**	**98.1**
YNMO-N_2	**5.87**	**96.4**
YNMO-O_2	**5.54**	**98.0**

Table 5.4: Summary of magnetic properties of YCMO and YNMO samples annealed in different atmospheres.

The possible reason for decreasing magnetization in ZFC has been mentioned earlier in this chapter. In addition to the earlier mentioned reasons, the metamagnetic natures of Ln_2CoMnO_6 (Ln = Nd, Y, Eu) [152,158b,160] may also be reflected as a decreasing magnetization in the ZFC traces. From the field dependent magnetization, metamagnetic nature of the YCMO samples has been inferred. The origin of such decreasing magnetization might be arising from the antiferomagnetic clusters of transition metal ion pairs at low temperature. In addition, the peak shapes of ZFC magnetization of YCMO and YNMO samples are also almost similar and no diffusiveness, as observed in the Eu_2CoMnO_6 or La_2CoMnO_6, is noticed [150c,152]. The peak-like features in ZFC magnetizations at the transition temperatures are quite similar to ferri- or antiferromagnetic as well as metamagnetic or spin glass like systems. The differences in the ZFC and FC behavior of YCMO or YNMO samples

indicate the antiferromagnetic interactions are weak and thus on applied field conditions, the spins rotate along the field direction.

The magnetic hysteresis (MH) loops for ECMO samples recorded at some representative temperatures in paramagnetic and ferromagnetic regions are shown in **Fig.5.20 and 5.21,** respectively.

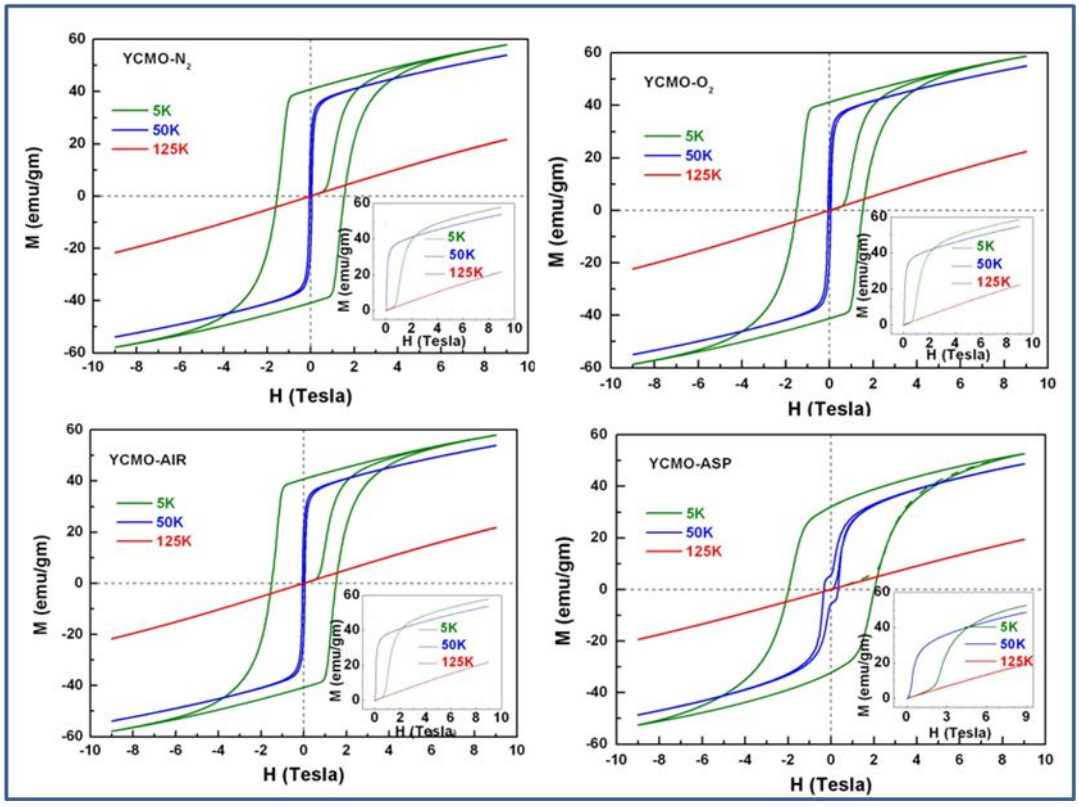

Fig.5.20: Magnetic hysteresis loops of YCMO samples measured at some representative temperatures.

Ferromagnetic like hysteresis loops are observed in all the samples below transition temperature, which further confirm their ferromagnetic nature. However, the YCMO samples show increasing magnetization with increasing field and do not tend to saturate even up to a field of 9 Tesla. Similar behavior has also been observed earlier explained $EuCo_{0.5}Mn_{0.5}O_3$ and reported La_2MgMnO_6 [150c]. The lack of tendency to saturate suggests the presence of an appreciable contribution from antiferromagnetic

interactions in the YCMO sample. However, in all the YNMO samples the magnetization saturates at much lower field, *viz.*1 to 1.5 Tesla. The difference in the YCMO and YNMO might be related to the larger valance fluctuations in the former compared to the later. Being the Ni^{2+} has more stability compared to Co^{2+}, the Ni^{2+}-Mn^{4+} interaction is dominating interaction in the YNMO. In the case of YCMO, the contributions from the antiferromagnetically interacting pairs are reduced with the increasing applied magnetic field. Also MH loops of the YCMO samples indicate step like hysteresis loops which are similar to the magnetization of metamagnetic materials. Similar to the $EuCo_{0.5}Mn_{0.5}O_3$ sample [152,158b,160], the YCMO samples also show field and preparation dependent switching of the magnetic interactions. A comparison of the MH loops of the YCMO samples recorded at 5 K shows (**Fig.5.22**) shift of the critical field to lower side compared to the as prepared one (critical fields: *asp*-YCMO: 2.1 T and other YCMO samples: 0.6 T, marked in (**Fig.5.22**). This also suggests the annealing atmosphere has lower role in the sample compared to the temperature of preparation. Thus it can be concluded that oxidation state of transition metal ions in the high temperature prepared sample were equilibrated to stable configuration on annealing at lower temperature. Similar effects were also observed in YNMO sample, but without any signature of metamagnetic nature. The ferrimagnetic like spin arrangement of the YCMO [157,158b,160] is expected to flip to ferromagnetic state with increasing field as is observed in other related perovskite-type materials [152, 158b]. However the exact magnetic structure at different applied field on this sample is yet to be studied.

It may be mentioned here ferromagnetic transition in the cation ordered Co-Mn containing double perovskites originates from the Co^{2+}-O-Mn^{4+} or vibronically

coupled Co^{3+}-O-Mn^{3+} super exchange interactions [149b,150c,152]. However, the possible existence of multiple valence state as well as partial cation disorder can lead to a number of different magnetically coupled pairs. Such coupled pairs are either reflected at a different ferromagnetic transition temperature as in the case of La_2CoMnO_6 or spin glass or metamagnetic transition as in Y_2NiMnO_6 or Eu_2CoMnO_6 [152,158b,160]. Among the possible magnetic interactions only the Mn^{3+}-O-Mn^{4+}, Co^{2+}-O-Co^{3+} (LS), Co^{2+}-O-Mn^{4+} and vibronically coupled Co^{3+}-O-Mn^{3+} interactions are of ferromagnetic nature while others are of antiferromagnetic types. Thus, the presence of such interactions due to both charge or antisite cation disorder as well as spin state of Co^{2+} and Co^{3+} can lead to an appreciable contribution of antiferromagnetic interactions.

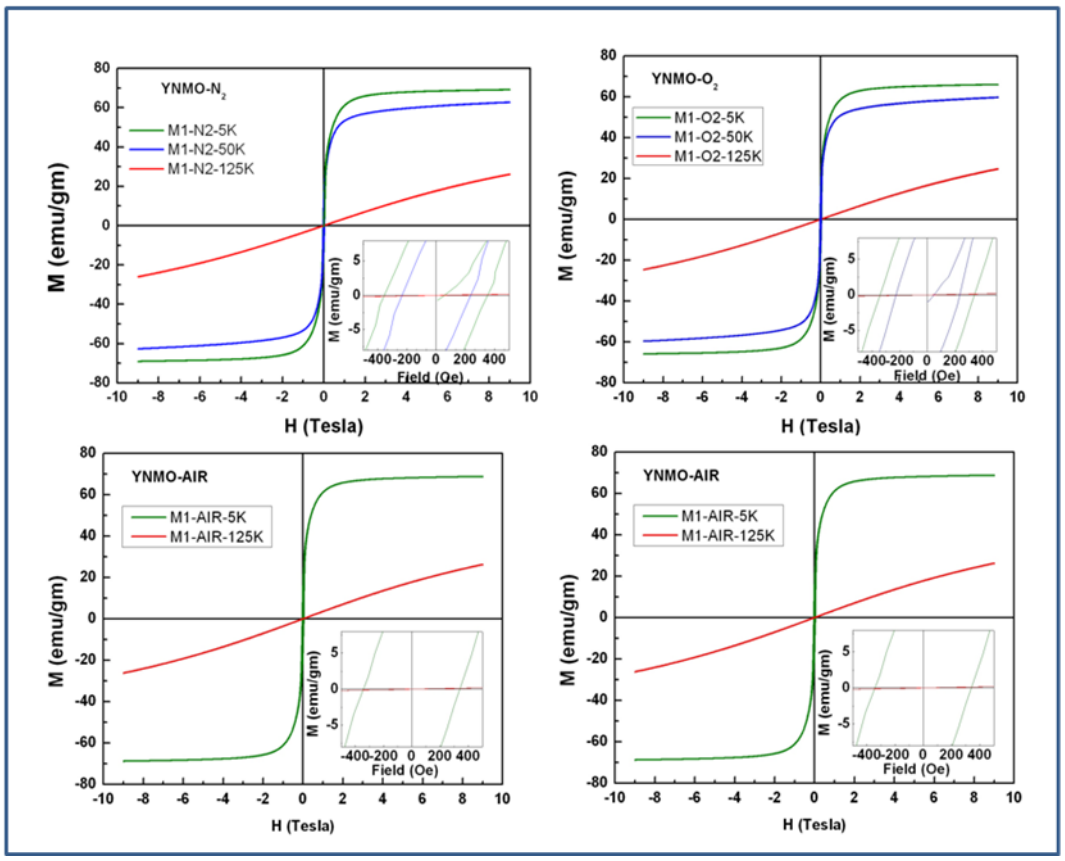

Fig.5.21: Magnetic hysteresis loops of YNMO samples measured at some representative temperatures.

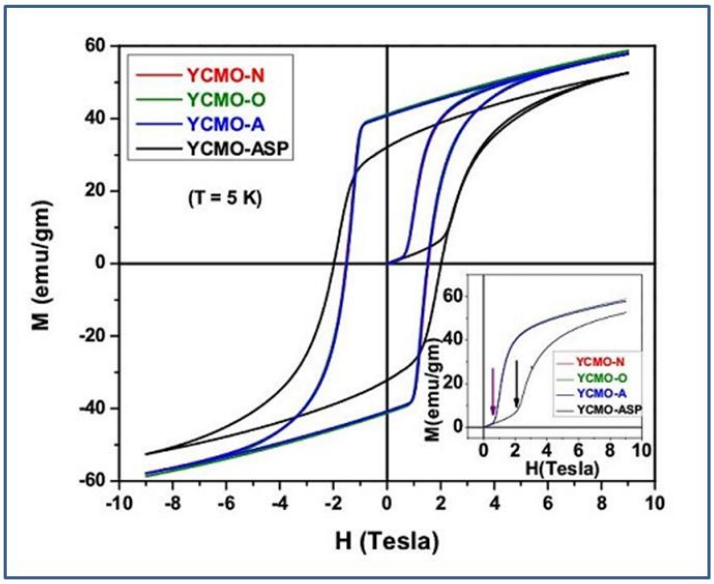

Fig.5.22: Magnetic hysteresis loops of YCMO samples measured at 5 K. Inset shows the virgin magnetization feature of different samples.

5.4.3. Dielectric properties

Similar to the magnetic properties, the preparation does have significant influence on their electrical properties, and thus the dielectric measurements in between ambient to 5 K were carried out on all the samples. The variation of real part of permittivity with temperature for the YCMO and YNMO samples are shown in **Fig. 5.23 and 5.24**. In all the samples, the temperature dependent permittivity show step like rise above 100K. Further it can be seen that the step like rise of the permittivity is clearly observed for the *asp*-YCMO sample while they are gradually smeared in air or O_2 annealed samples. However, no anomaly in temperature dependent permittivities near the magnetic transition temperature has been observed in any of the YCMO or YNMO samples. A comparison of permittivity of the LCMO samples indicates that the maximum permittivity of asp-YCMO is significantly lower compared to others. In the O_2 or air-annealed samples of YCMO show appreciably

larger values of permittivities (~ 10^4) near the ambient temperature, which gradually decrease with decreasing temperature and increasing frequency. All the samples show typical Debye-type dielectric behavior, where a rapid increases in permittivity with decreasing frequency is observed. The larger dielectric permittivity at lower frequency can be attributed to the interfacial polarization due to the ionic migration. This is substantiated from the analyses of the loss tangent of the samples, explained subsequently in this article. In all the cases the permittivity observed at higher frequency are in the range of 15 to 40, which is generally expected from the ionic polarization. Similar to the YCMO samples, all the YNMO samples show frequency dispersion of permittivity.

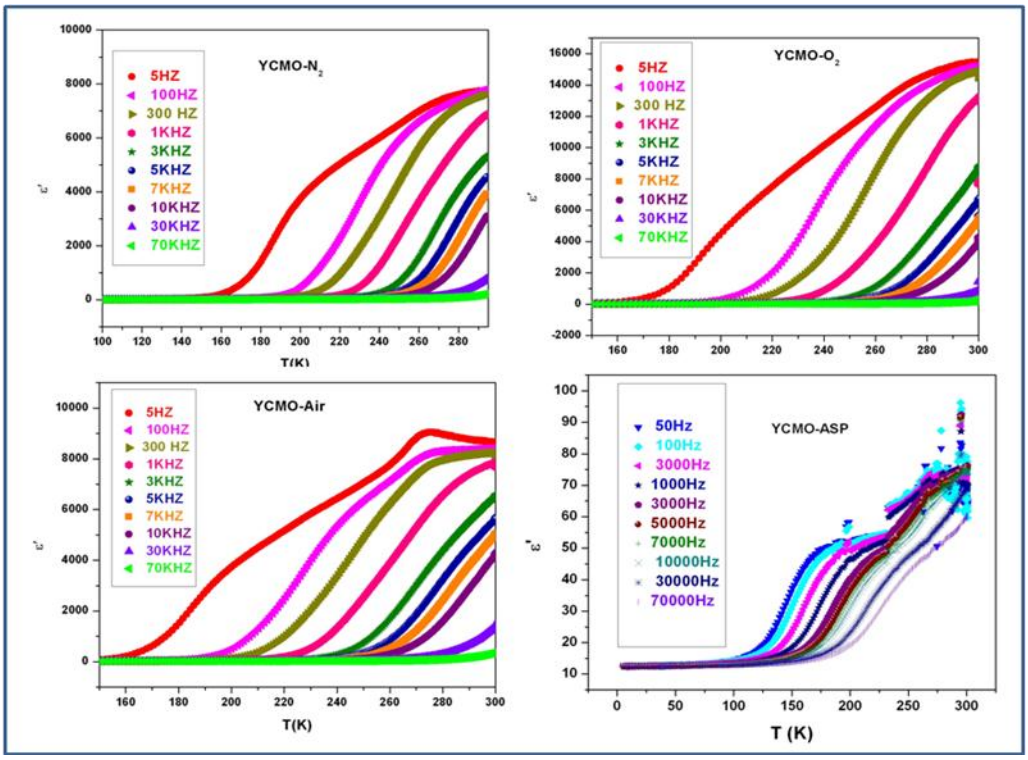

Fig.5.23: Temperature dependent real part of relative permittivity (ε′) of YCMO samples measured at different frequency.

However, in the YNMO samples two relaxations, one weak relaxation, at lower temperature (~ 100K) and another strong one at above 175 K are observed. However,

both the relaxations of YNMO samples are smeared at higher temperature. Compared to the YCMO, the relative permittivities of YNMO samples do not show any appreciable variation and the maximum permittivities are within 2000 to 5000 at lower frequency near ambient temperature, while they are in the range of 8-15 in high frequency (1 MHz) region. The larger variation of permittivity in YCMO compared to the YNMO samples with preparation conditions can be related to the defects and valence fluctuations. The lower permittivity of the as-prepared and N_2 annealed samples may be due to appreciable conductivity contributions arising from the oxygen defects. These defects are expected to annihilate on annealing in air or O_2 atmosphere. As mentioned earlier, the YCMO sample annealed in N_2 atmosphere has small amount of phase separated spinel type phase contrary to the N_2 annealed YNMO sample. Thus the oxygen stoichiometry though insignificant but are effective to control their dielectric properties. Further conclusions on these aspects were obtained from the analyses of the loss behavior of the samples.

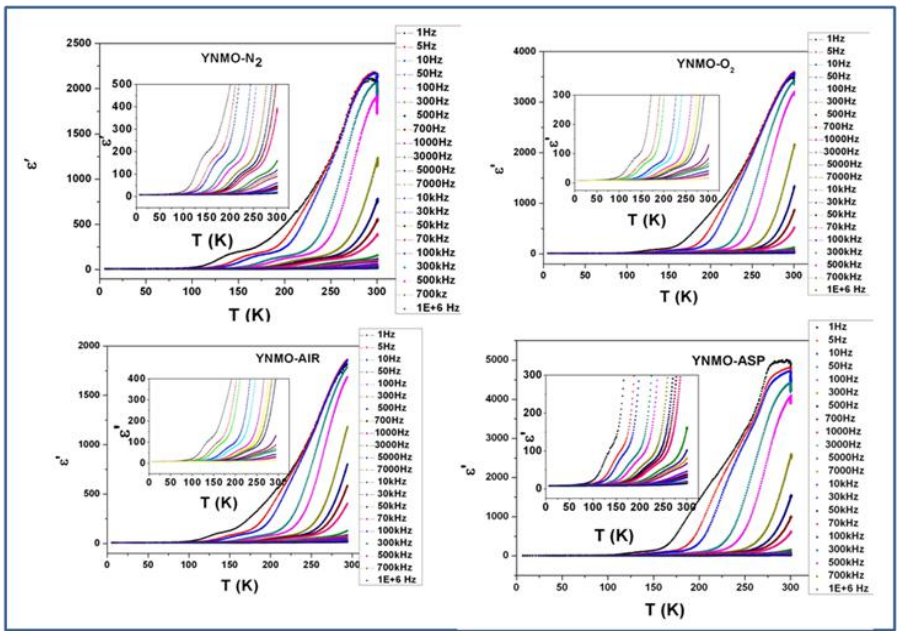

Fig.5.24: Temperature dependent real part of relative permittivity (ε′) of YNMO samples measured at different frequencies.

The variation of loss tangent tanδ (= $\varepsilon''/\varepsilon'$) with temperature of all the YCMO and YNMO samples are shown in **Fig. 5.25 and 5.26.**

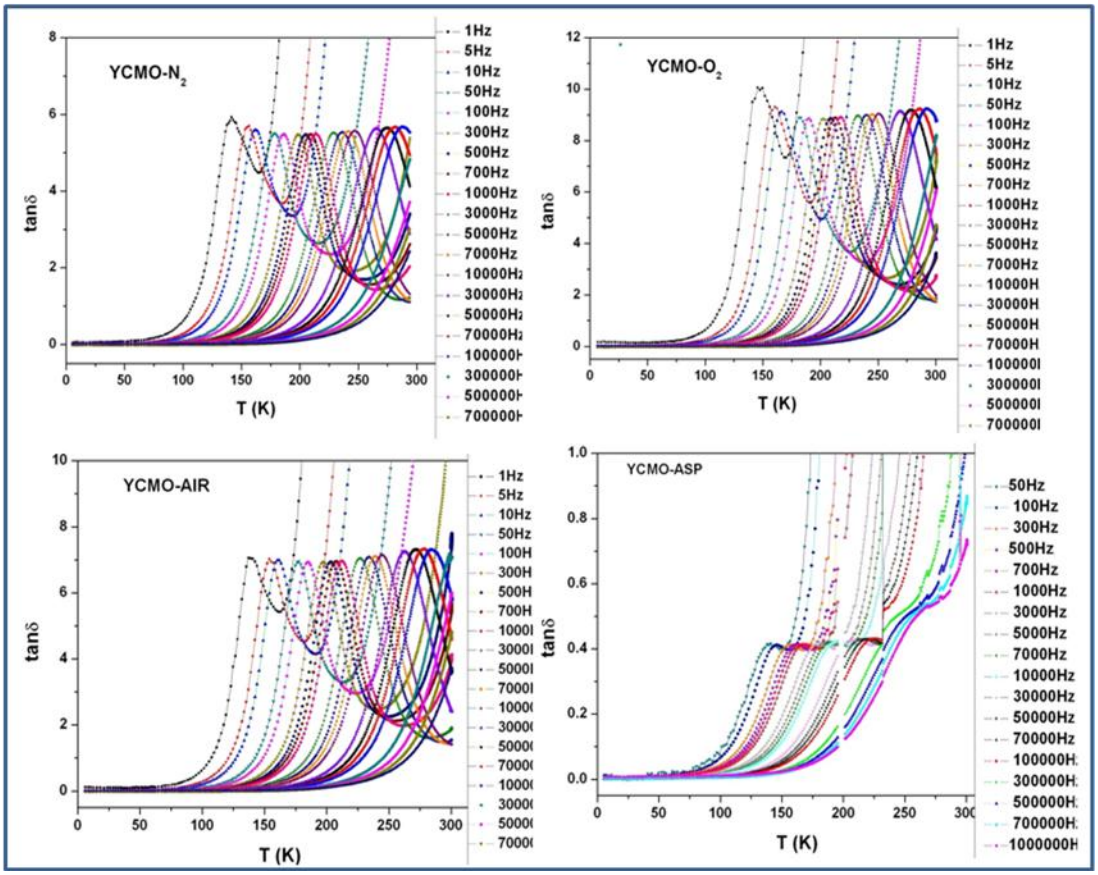

Fig.5.25: Variation of loss tangent (tanδ) of YCMO samples with temperature.

A comparison of the loss tangents of the YCMO and YNMO samples indicates the almost similar trend with temperature. Typical loss values are lower than 15 and clear frequency dispersion of loss tangent are observed in these plots. Similar to the temperature dependent permittivity, the variation of tanδ with temperature show two relaxation features in YNMO samples. However, the low temperature relaxation appeared as smeared peak or step, while clear relaxation peaks are observed at high temperature. The peak (maxima of loss) shows a gradual shift towards higher temperature with increasing frequency. YCMO sample shows larger frequency dispersion compared YNMO, which can be due to larger valence fluctuations of Co-

Mn pair compared to Ni-Mn pair. It can be mentioned here that the earlier studies on fully cation ordered La_2MgMnO_6 with feeble oxygen defects and multiple oxidation states of Mn do not show any relaxation features. However, analogous La_2NiMnO_6 shows relaxor like dielectric properties which are due to the multiple valence and partial cation disorder in the structure [150a]. In both the YCMO and YNMO of present study, the loss does not show much variation with temperature, but the loss of YCMO samples varies appreciably with the conditions of preparation.

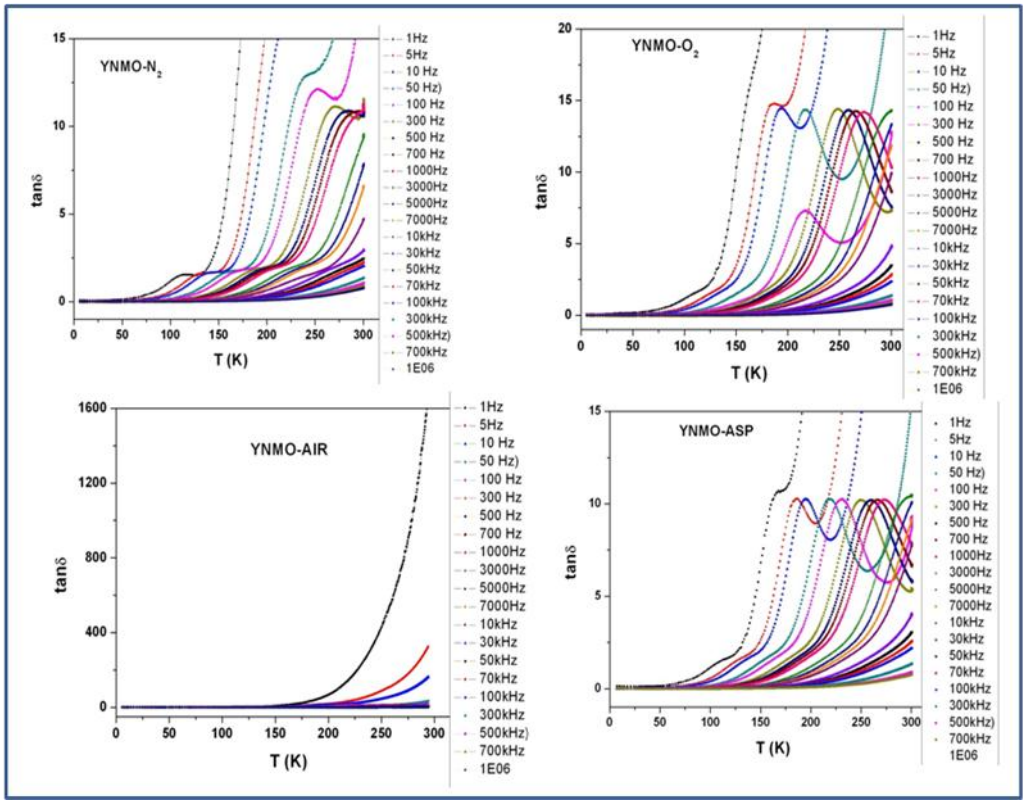

Fig.5.26: Variation of loss tangent (tanδ) of YNMO samples with temperature.

A comparison of our earlier studies on transition metal ion containing rare-earth perovskites suggests the Co-Mn combination has a larger $f = f_0 \exp(-E_1 / k_B T_m)$ tunability of dielectric constants compared to others. This might be attributed to the easier control on the multiple oxidation states of the Co ions. The variations of the

peak temperature of tanδ for all the YCMO or YNMO samples with relaxation frequency (*f*) show Arrhenius like behavior and they are shown in **Fig.5.27**. The f_0 is a pre-exponential fitting parameter of the YCMO samples about 10^{10} Hz.

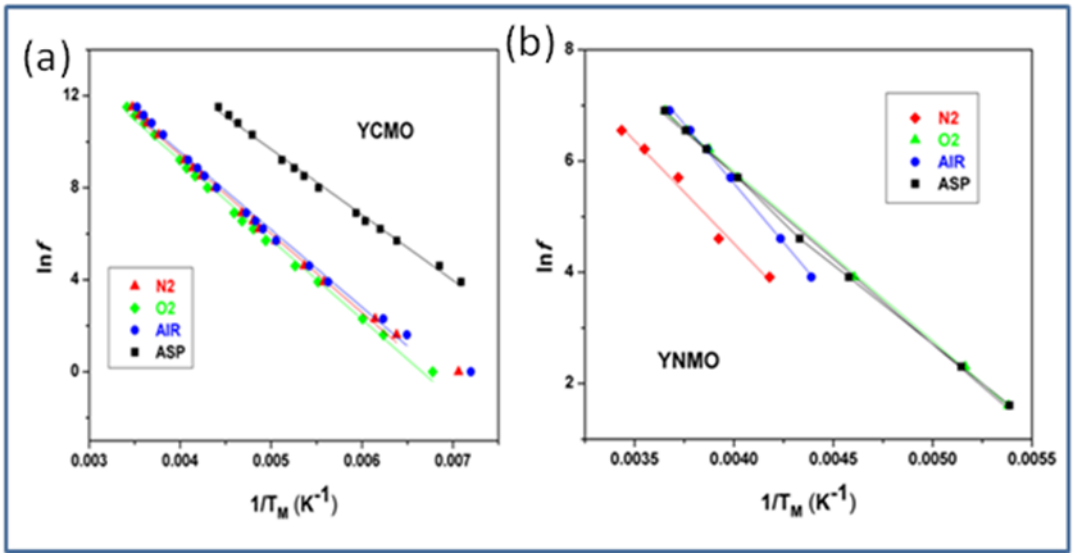

Fig.5.27: Arrhenius fit of the peak relaxation frequency for (a) YCMO (b) YNMO samples at different atmosphere (nitrogen, oxygen, air, as-prepred).

The activation energies (E_1) for relaxations of the YCMO samples are almost similar for annealed samples compared to as-prepared sample (0.25 eV for asp-YCMO, 0.29 eV for YCMO-Air, 0.29 eV for ECMO-N_2 and 0.30 eV for YCMO-O_2). Similar analyses of the relaxation peak of the YNMO samples revealed the value f_0 *are* in between 10^7 to 10^9 and activation energies are in between 0.26 to 0.37 eV. The present observed activation energies are little higher than those observed in La_2CoMnO_6 or Eu_2CoMnO_6 samples [150c,152]. In all such compositions the polaron hopping is common reason for their dielectric relaxation.

The dielectric relaxation of YCMO and YNMO samples can arise from conduction or dipolar origins as commonly observed in various perovskite-type

materials [150a,151a,172]. The larger dielectric constant in low frequency suggests a possible ionic movement and they are expected only in N_2 or ASP sample compared to O_2 or Air annealed samples. Since the oxygen or air annealed YCMO samples show larger permittivity, the defect contribution appears to be minimal compared to local dipolar origins. It has been reported in literature that the magnetic transition of the Y_2CoMnO_6 disrupts the inversion symmetry of the lattice leading to the ferroelectric character in the sample [156,158a]. Thus, it is easy to expect that a small deviation in the oxidation state and/or oxygen defect can lead to polar clusters in YCMO sample. Thus a large permittivity, as observed in the present studied YCMO or YNMO samples, can be expected from the local polar clusters. These observations are also similar to earlier studies on the rare-earth manganites [150a,150c,151a,152-153,173]. Hence, it is expected that the local distortion arising from the variable oxidation states and cation distribution are likely to be important factor to control their dielectric as well as magnetic properties. Thus, it can be suggested that the multifferoic or magnetodielectric character of the YCMO or YNMO samples can be easily tuned by annealing conditions.

5.5. Conclusion

Cation ordered monoclinic Y_2CoMnO_6, Y_2NiMnO_6 and cation disordered $EuCo_{0.5}Mn_{0.5}O_3$ were prepared and subsequently annealed under different atmospheres. Y_2NiMnO_6 retains the monoclinic structure under all the annealing conditions while the Y_2CoMnO_6 shows a feeble separation of spinel type phase on annealing in inert atmosphere. Powder XRD patterns of the $EuCo_{0.5}Mn_{0.5}O_3$ revealed that samples annealed in air or oxygen environment were found to have cation disordered orthorhombic structure (Pnma) structure, the sample annealed in inert

atmosphere have Eu^{3+} deficient perovskite-type structure. The transition temperature, critical field and temperature dependent magnetization indicates that the variation of oxygen partial pressure not only varies the relative concentration of various ions but also affects the spin state transition of the Co^{2+} ions. The ferromagnetic T_c of Y_2CoMnO_6 samples is found to be affected by preparation conditions, while no effect of preparation condition is observed in Y_2NiMnO_6. Metamagnetic behavior is observed in all the Y_2CoMnO_6 and $EuCo_{0.5}Mn_{0.5}O_3$ samples. However, no such behavior is observed in Y_2NiMnO_6. The Dielectric properties of the $EuCo_{0.5}Mn_{0.5}O_3$ show larger permittivity ($\geq$ 2000) on annealing in oxygen containing atmosphere than that in inert atmosphere (~ 400). Similar variations in dielectric properties are also observed in Y_2NiMnO_6 and Y_2CoMnO_6 samples.

CHAPTER 6

MAGNETIC AND DIELECTRIC PROPERTIES OF M: PVDF FERROELECTRIC COMPOSITE FILMS (M = Co AND Ni)

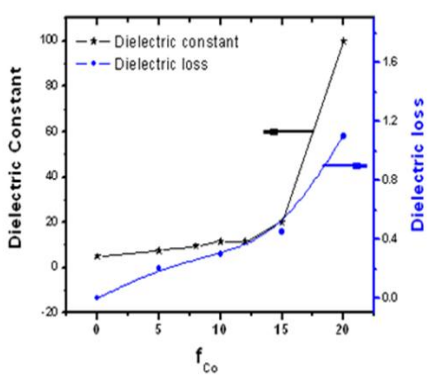

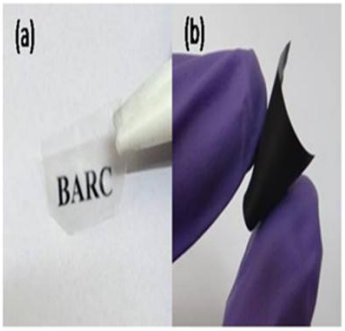

1. Improvement of magnetodielectric coupling by surface modification of nickel nanoparticle in Ni and PVDF (polyvinylidene fluoride) nano-hybrids
B. P. Mandal, **K. Vasundhara**, E. Abdelhamid, G. Lawes, H. G. Salunke and A. K. Tyagi
J. Phys. Chem. C 118 (2014) 20819-20825.

2. Enhancement of dielectric permittivity and ferroelectricity of modified cobalt nanoparticle and Polyvinylidene fluoride based composite
K. Vasundhara, B. P. Mandal and A. K. Tyagi
RSC. Adv. 5 (2015) 8591-8597.

6.1. Introduction

The electric energy density of dielectric materials related to both effective dielectric permittivity and breakdown strength of materials. Generally polymer dielectric materials have high breakdown field strength. Some of the polymers used for capacitor manufacture are polyvinylidene fluoride (PVDF), polyester (PET), polypropylene (PP), polyphenylenesulfide (PPS), and polyethylene naphlate (PEN). Among them bioxially orientated polypropylene (BOPP) has the highest breakdown field strength (600 MV/m) [68,174]. Compared with the conventional ceramic dielectric materials, polymers have the low dielectric constant. For example polyvinylidene fluoride (PVDF) has dielectric constant of about 12 at kHz and 25^{o}C [68]. In the present studies the PVDF polymer was chosen due to its comparable high dielectric constant than other polymers, low cost, chemical resistance, electrical resistance and easy processability. PVDF is a semi crystalline polymer which exhibits at least five polymorphs including α, β, γ, δ and ε. Among them, α-phase is the most common thermodynamically stable and easily obtainable phase, which has Trans-gauche (TGTG) conformation. It has orthorhombic symmetry with unit cell dimension as a=4.96 Å, b=9.64 Å and c=4.62 Å, and does not show net polarization due to its opposite arrangement of neighboring chains. Therefore, α-phase of the PVDF is non polar phase. The δ-phase is formed by applying the electric field on α-phase. β-phase is the polar phase of the PVDF in which molecule being configured in all trans (TTTT) in Zig-Zag configuration. In this configuration all C-F dipoles are aligned in the same direction resulting in the highest possible dipole density among all four polymorph [175]. The γ-phase consists of TTTGTTTG conformation **[175a-c,176].**

Among all polymorphs of PVDF, β-phase has the great importance due to its technological importance. Hence main aim in this thesis is to increase the β-phase content as well as increase the dielectric constant of PVDF.

One straight way of increasing dielectric constant and β phase of the PVDF polymer is by adding ceramic oxide [$BaTiO_3$, $Pb(Zr,Ti)O_3$, $CaCu_3Ti_4O_{12}$ (CCTO)], etc. filler into the PVDF matrix to form particulate type (0-3) composites [177]. In this method large amounts of ceramic fillers are required to obtain high dielectric constant. In this process, at very high concentration of ceramics, lot of pores, voids, and imperfections are developed in the matrix which results in lowering of the breakdown voltage. In addition, the ceramic particle loaded polymer loses its mechanical flexibility and often poor quality composite films are obtained. Few materials with high dielectric constant contain Pb which is highly undesirable due to its chemical toxicity. In view of this lead free materials with high dielectric constant have been getting increasing interest [178].

To overcome the limitations of ferroelectric ceramics loaded polymer composites, some efforts have been made by different researchers, where a small fraction of conductive filler was mixed with the polymer matrix to attain a high dielectric constant, without compromising the mechanical flexibility of the polymer [178-179]. Saidi *et al*. fabricated PANI (polyaniline)/PVDF (polyvinyledene flouride) composite which exhibits excellent improvement in dielectric constant with 5% PANI in the PVDF matrix [180]. In CNT/PVDF composite, the dielectric constant reaches 600 at 10^3 Hz with the composite sample of 8 vol% of CNT [181]. In case of Ni-MWNT/PVDF composite the dielectric constant increases to 300 near percolation threshold of the filler [182]. Panda et al. have reported that in case of Ni/PVDF

composite, a high effective dielectric constant was observed near the percolation threshold of 27 vol% of Ni [183].

In percolative composites, the dielectric loss increases abruptly near the percolation threshold of the filler. Furthermore, filler particles agglomerate due to high surface energy and strong cohesion which leads to highly inhomogeneous films. This problem can be reduced by avoiding the direct contact among the conductive particles. The core-shell structure with conductive filler as core and insulating materials as shell were found to be ideal for the polymer nano-composite materials. Surface modified nanoparticles not only prevent the agglomeration but also increase the boundary area and interfacial interaction between the nanoparticles and the polymer matrix. Since dielectric constant in nanocomposite is dependent on interfacial polarization and space charge polarization, therefore, it is highly probable that surface modified nanoparticle exhibit high dielectric constant with low dielectric loss.

6. 2. Experimental method

6.2.1. Synthesis of Co/Ni nanoparticles

Cobalt acetate was dissolved in 30 ml of ethylene glycol and then required amount of sodium borohydride ($NaBH_4$) was added to this solution under stirring condition. The solution was kept for heating at 140^{o}C until the solution turned to black. The obtained black cobalt nanoparticle precipitate was separated using a strong magnet. These cobalt nanoparticles were washed several times with distilled water and finally with methanol. The precipitate was dried at room temperature for overnight. Similar procedure followed for the Ni nanoparticle from nickel acetate by using hydrazine hydrate as reducing agent.

6.2.2. Surface modification of Ni nanoparticles

200mg of Ni nanoparticles obtained from above method was dispersed in 100 ml of H_2O_2 and refluxed at 100^oC for 4h. The precipitate was then filtered from the H_2O_2 solution and washed several times with deionised water and finally washed with methanol. The obtained particles were dried at room temperature for overnight.

6.2.3. Preparation of Co/Ni-PVDF nano-composites

Nano-composite films with different concentration of Co/Ni nanoparticle in PVDF were prepared. Required amount of as-prepared Co/Ni nanoparticle was dispersed in 10 ml DMF, sonicated for 15 min. Stoichiometric amount of PVDF was added to the above solution and sonicated again for 30 min till a well dispersed solution was obtained. The solution was then poured on to clean glass slide and kept for drying at ~70°C. Earlier reports indicate that drying at ~70°C is most suitable for getting higher amount of β-phase. Schematic representation of preparation of composite films and interaction of cobalt nanoparticles with PVDF is shown in the **Fig. 6.1**. In case of PVDF-Ni composite samples with following compositions have been prepared PVDF, PVDF-10 wt% Ni, PVDF-20 wt% Ni, and PVDF-40 wt% Ni. The samples have been denoted as PNi1, PNi2, PNi4 for the compositions PVDF-10 wt% Ni, PVDF-20 wt% Ni, PVDF-40 wt% Ni, respectively. The surface modified nickel nanoparticles were also dispersed in PVDF with same manner. These samples have been denoted as PNim1, PNim2, PNim4 for the surface modified nickel-PVDF samples PVDF-10 wt% Ni (modified), PVDF-20 wt% Ni (modified), and PVDF-40 wt% Ni (modified) respectively.

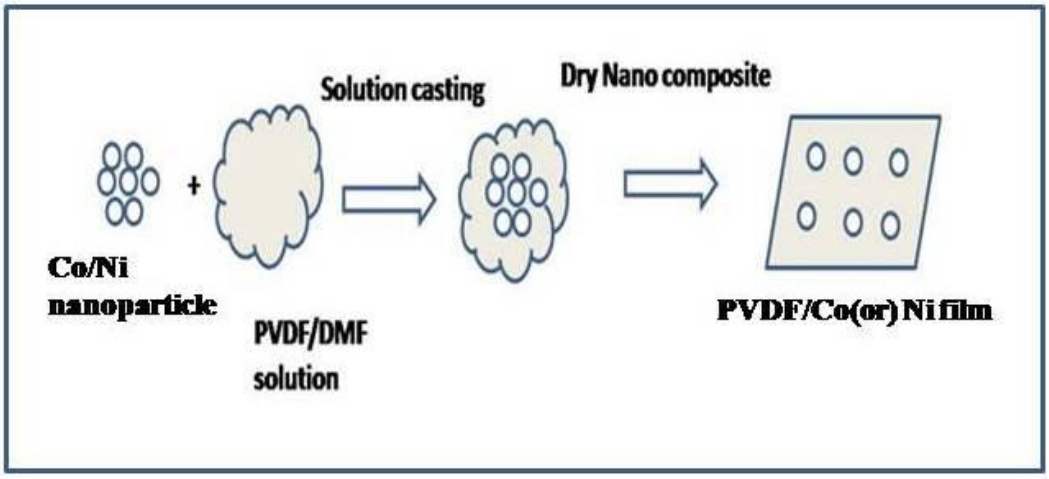

Fig.6.1: Schematic representation of preparation of PVDF/Co (or) Ni composite films.

The phase purity of the all the samples were characterized by XRD using a Philips PW1820-X-ray diffractometer coupled with a PW 1729 generator operated at 30 kV and 20mA. A graphite crystal monochromator was used for generating monochromatic Cu-Kα radiation. FTIR spectra of composite films were recorded using a Bomem MB102FTIR (model 610) equipped with DTGS detector.

Both the sides of the thick films were painted with Electrolube's conductive silver paint and dried at room temperature. The permittivity, dielectric loss and conductivity were measured using Novocontorl's Alpha-A High Performance Frequency Analyzer. The electrical polarization and leakage current of the films has been measured using aixACCT's TF analyzer 2000. All the hysteresis polarization measurements were carried out at 100 Hz under the field of 50kV/cm at room temperature**.**

In case of Ni, the room temperature magnetization measurements were carried out using Quantum Design Physical Property Measurement System unit (PPMS). The zero-field-cooled (ZFC) measurements were performed by cooling the sample in zero

field up to 5K and then the magnetization is measured while warming in a field of 100 Oe. In field-cooled (FC) measurements, the sample is cooled in a field of 100 Oe up to 5 K, and the moment is evaluated while warming up to ~300K.

A thin layer of Ag paint was applied to the top and bottom of the films separately to which Au wires were attached to make parallel plate capacitor. An Agilent 4284A LCR meter was used to measure the dielectric signal at a frequency of 30 kHz under a 100 mV excitation, while PPMS was used to provide the magnetic field. Background correction was made to extract the magneto-dielectric data.

6.3. Results and Discussion of Co/PVDF composites

6.3.1. XRD studies

The diffraction patterns of PVDF and its nano-composites with different loading of cobalt nanoparticles are shown in **Fig.6.2.** The peaks at 18.0±0.2°, 26.5±0.1° corresponds to (020) planes of α form of PVDF, whereas the peaks observed at 20.2 ±0.2^{o} corresponds to the (110) plane of the β-phase of PVDF [184]. In the inset XRD pattern of cobalt nanoparticle has been shown. The position of PVDF peaks remains unaltered after addition of metal nanoparticle indicating addition of cobalt does not affect the structure of the PVDF. The XRD peaks of cobalt are very much dominant in comparison of that of PVDF due to its high crystallinity and higher scattering cross section of cobalt nanoparticles compared to PVDF. The amount of the α-phase is found to be decreased by addition of cobalt nanoparticles. Interestingly, cobalt nanoparticles promote the formation of β-phase of the PVDF. This observation has been corroborated by FTIR study also. It is worthwhile to mention that XRD

pattern of the pure cobalt nanoparticle does not show any impurity phase such as cobalt oxide.

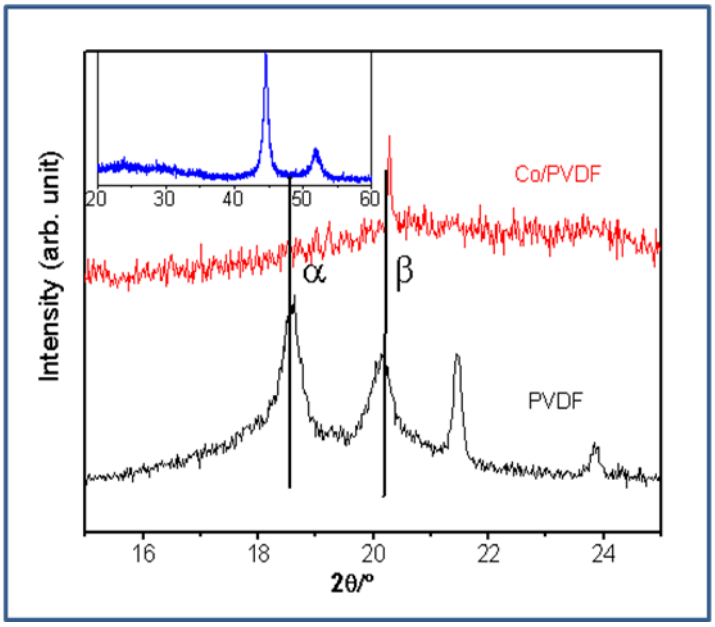

Fig.6.2: XRD patterns of pristine PVDF, cobalt nanoparticle and cobalt loaded PVDF.

6.3.2. FTIR studies

FTIR is a suitable technique to determine the different phases of PVDF. The infrared spectra of PVDF and 5 vol% of cobalt loaded PVDF are shown in **Fig. 6.3.** The FTIR spectrum of PVDF exhibits the presence of α, β and γ forms of PVDF. The IR bands of the composites have been assigned as follows. The characteristic bands observed at 485, 612, 760, 796, 853 and 975 cm^{-1} correspond to α-phase of PVDF. The bands at 612 and 760 cm^{-1} are the bending and wagging vibration of CF_2 groups and rocking vibration in the PVDF chain, respectively [185]. The IR bands at 511, 840 and 878 cm^{-1} are assigned to β-phase of PVDF. The absorbance band at 878 cm^{-1} was assigned to the CH_2 and CF_2 groups of β-phase of PVDF originated due to CH_2 rocking and CF_2 stretching, whereas the bands at 1171 and 1232 cm^{-1} were assigned to

the wagging and rocking of CH_2 group. The bending of C–C–C moiety appeared at 1070 cm^{-1}.

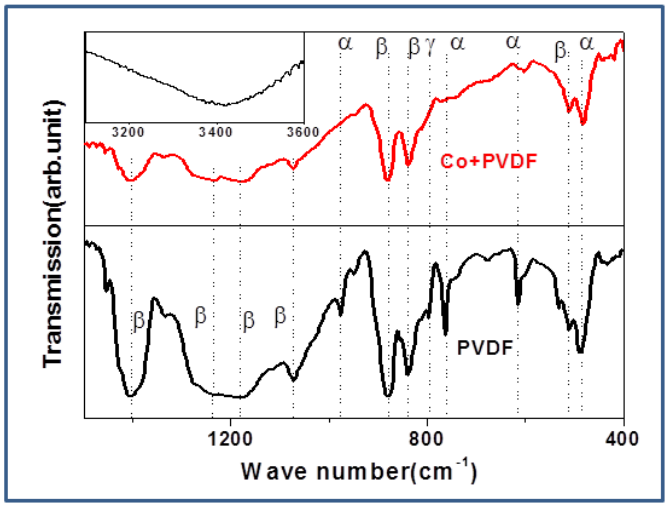

Fig.6.3: FTIR spectra of pristine PVDF and cobalt loaded PVDF. Inset of upper panel shows the FTIR spectra of surface functionalized cobalt nanoparticles.

The band at 801cm^{-1} has been assigned to γ form of PVDF and its relative intensity decreases upon successive cobalt loading. The polar β-phase of PVDF is the most desirable form because of its high permittivity. The relative amount of β and α-phases of PVDF in both the samples have been calculated by determining the relative ratio of the intensity of the characteristic peaks of α (760 cm^{-1}) and β-phase (840cm^{-1}). In case of pristine PVDF, the ratio is found to be 1.9 which increases to 12.76 in the 5 vol% cobalt loaded PVDF sample. The presence of cobalt nanoparticles aids in nucleating the polar β form of PVDF. IR spectra of the highly cobalt loaded samples could not be recorded due to black colour of the samples. It is important to mention that the presence of –OH groups on cobalt nanoparticles can be observed in FTIR spectra. The broad band in the range 3200-3600cm^{-1} (inset of **Fig. 6.3**) corresponds to the hydroxyl groups which are attached to the cobalt nanoparticles.

6.3.3. Dielectric properties

The dielectric constant and loss of Co/PVDF samples were investigated and have been shown in the **Fig.6.4 (a,b).**

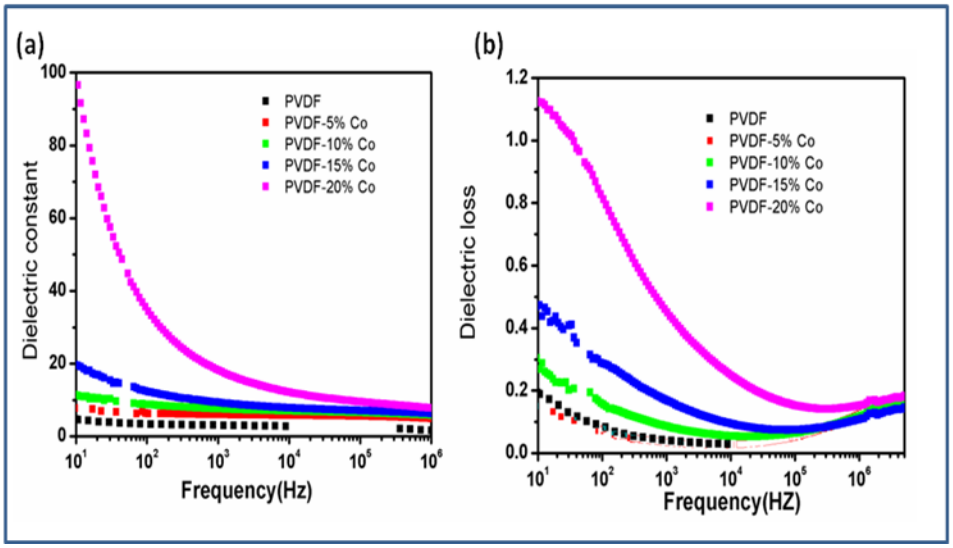

Fig.6.4: Variation of (a) real part of relative permittivity and (b) tan δ (dielectric loss) with frequency.

The dielectric constant of the composite films is high at lower frequency due to higher polarization time, compared to high frequency region. The dielectric constant of the sample with low concentration of filler i.e. 5 vol% Co-PVDF is 8 at 10 Hz and it remains almost constant till the frequency 1 MHz. In case of composites of 10 and 15 vol% cobalt-PVDF, the dielectric constant was found to be 11 and 20, respectively at 10 Hz which slowly decreases with increase in applied frequency. The dielectric constant of 20 vol% cobalt-PVDF soars to reasonably high value i.e. 100 at 10 Hz which also decreases with increase in frequency. It implies that introduction of the conductive filler into PVDF is responsible for enhancement of dielectric constant of these composites. The high dielectric constant at low frequency is due to the entrapment of the free charges at the interface of cobalt nanoparticles and PVDF

polymer matrix which is related to the Maxwell–Wagner–Sillar (MWS) effect. According to MWS effect, when current flows across the interface of two materials with different electrical conductivities, charges can accumulate at the interface of the dielectric materials. This interfacial polarization increases with the concentration of cobalt and it results in higher permittivity at higher concentration of cobalt nanoparticle. The plot of dielectric constant with filler concentration shows that dielectric constant increases by about 15 times as compared to pristine PVDF **(Fig.6.5).** This sudden increase in dielectric constant of Co-PVDF composite can be explained by micro-capacitor model which has been discussed subsequent section.

Dielectric constant is the ability of a material to be polarized under the applied electric field. Charges can accumulate at the interface of two dielectric materials with different relaxation times when the current flows across these two materials. Therefore, it is expected that large charge accumulation takes place at the interface of PVDF and cobalt nanoparticles near the percolation threshold.

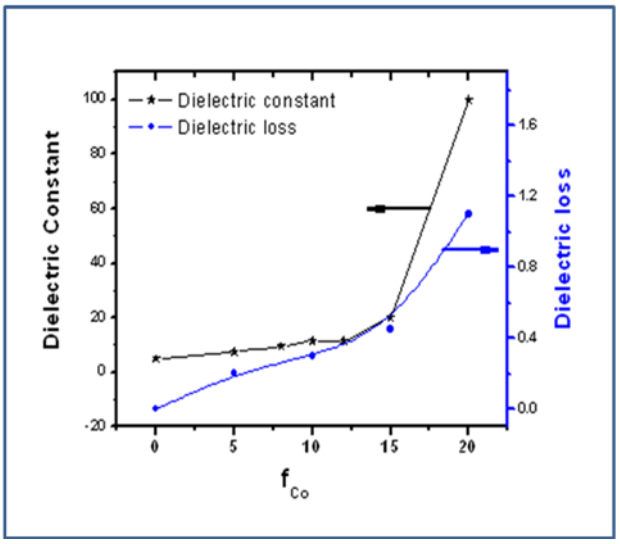

Fig.6.5: Effective dielectric constant and dielectric loss of Co/PVDF composites at 10 Hz at room temperature as a function of cobalt volume fraction.

The adjacent cobalt nanoparticles can be considered as parallel electrodes whereas thin layer of PVDF as dielectric material placed in between electrodes giving rise to several micro capacitors. With increase in cobalt content in PVDF matrix, not only the number of micro-capacitors increases but also the thickness of the dielectric layer decreases which lead to high dielectric constant [182]. The observed dielectric loss in these composites remain relatively low (≤0.4) at lower concentration of cobalt. However, the compositions above percolation threshold i.e. 20 vol% Co-PVDF exhibits slightly higher dielectric loss (0.8). Generally dielectric loss in nano-composite originates from the several sources including interfacial polarization contribution, direct current conduction or transport related loss and from the movement of the molecular dipoles. In the present case, lower dielectric loss may be due to several-OH groups on the surface of cobalt nano particles, which act as insulating moieties. A schematic illustration of the surface modification treatment has been shown in **Fig.6.6.** These hydroxyl groups inhibit the direct contact among the cobalt nanoparticles and also prevent the Co nano-fillers from the aggregation, which lead to superior properties**.**

The increasing trend in dielectric loss with increase in cobalt concentration, as shown in **Fig.6.5** (right-Y axis), could be due to decrease in the thickness of the insulation PVDF layer. The conduction is the primary loss mechanism near the percolation threshold, so the dielectric loss increases as the content of cobalt increases. It is to be noted that the characteristic dielectric relaxation of PVDF at ~2 MHz is related to glass transition relaxation. Previous researchers mentioned that this relaxation is associated to the micro-Brownian cooperative motions of the main chain of PVDF [186].

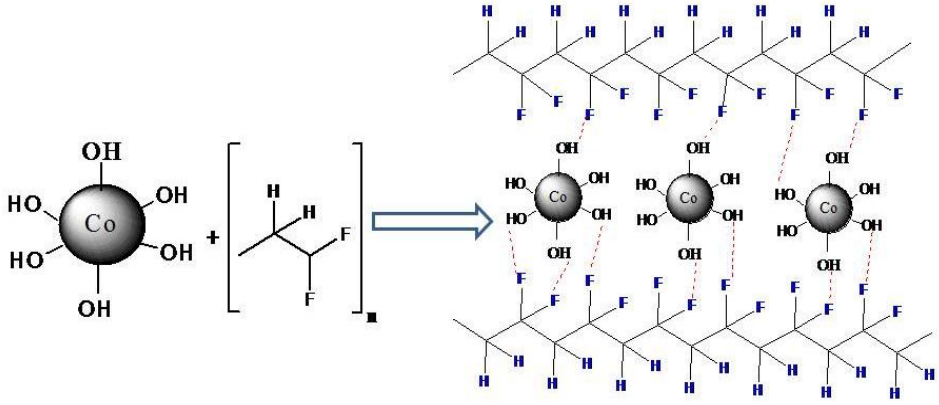

Fig.6.6: Schematic description of surface functionalization of cobalt nanoparticles and PVDF–matrix interaction.

From **Fig.6.7,** it can be observed that electrical conductivity increases with increase in the volume fraction of cobalt nanoparticle. This is typical characteristic of the conductor-insulator percolative system. In this kind of conductor-insulator percolative system, the dc conductivity increases with increase in conductor fraction indicating the formation of percolation network in PVDF matrix [187]. Another important observation is that at the higher frequency region conductivity is independent of the concentration of the inorganic moiety. The electrical conductivity of the Co/PVDF composites is in the range of 10^{-11} to 10^{-9} Scm^{-1}. Since the samples have been synthesized in polyol medium, therefore, these polyols remain as capping agent on the Co nano particle. Xie *et al.* also observed the low ac electrical conductivity in $BaTiO_3$-PMMA nanocomposites due to capping of the $BaTiO_3$ by the insulating polymer shell [188]. Percolation theory describes the conductivity near the percolation threshold of metal-insulator transition as $\sigma \alpha (f_c - f_{Co})^{-s}$ for $f_c > f_{Co}$ where f_c is percolation threshold and s is critical exponent in insulating region. The experimental data have been fitted using the above equation and f_c and s were found to be 0.19±0.1 and 1.8±0.07, respectively **(Fig.6. 8).**

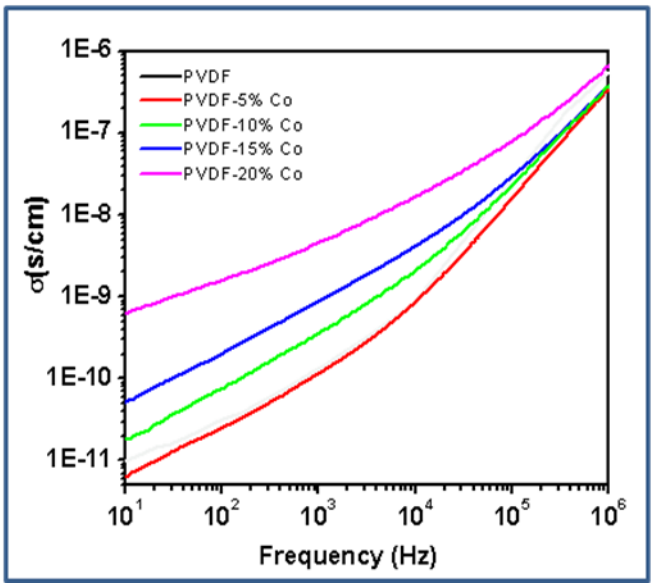

Fig.6.7: Frequency dependent electrical conductivity (σ) of pure PVDF and cobalt loaded PVDF samples at room temperature.

The percolation threshold commonly obtained in two phase media is 0.16, however, in this system slightly higher threshold value has been obtained. The higher percolation threshold (f_c) might be due to the coulomb repulsion between the surface functionalized cobalt nanoparticles. Therefore, it is difficult to form percolative network at relatively lower concentration of conductive filler. Similarly Wang *et al.* found increase in percolation threshold in oleic acid coated Fe_3O_4/PVDF system [189]. Panda *et al.* also found higher percolation threshold (27 vol%) in the Ni-PVDF composite [183]. The critical exponent (s) has also found to be higher than universal one ($s_{universal}$ = 0.8-1). This kind of higher exponent has been reported in many other systems and can be well explained by inverse Swiss-cheese model [190]. The inverse Swiss-cheese model, which is based on conducting medium embedded in insulating medium, can be applied in this system where conduction process is governed by inter-particle tunnelling [178].

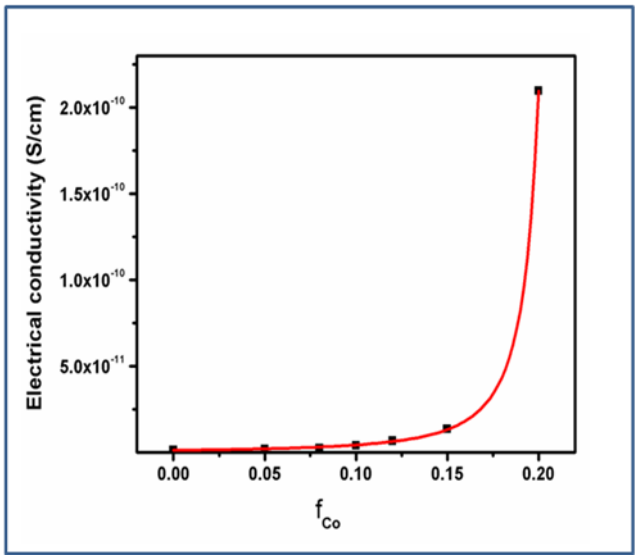

Fig.6.8: Variation of electrical conductivity with different volume fraction of cobalt in PVDF at room temperature. The solid line is the fitting.

6.3.4. Electric field polarization studies

Electric field dependent polarization behavior of the samples with different concentration of cobalt in the polymer matrix is shown in **Fig.6.9**.

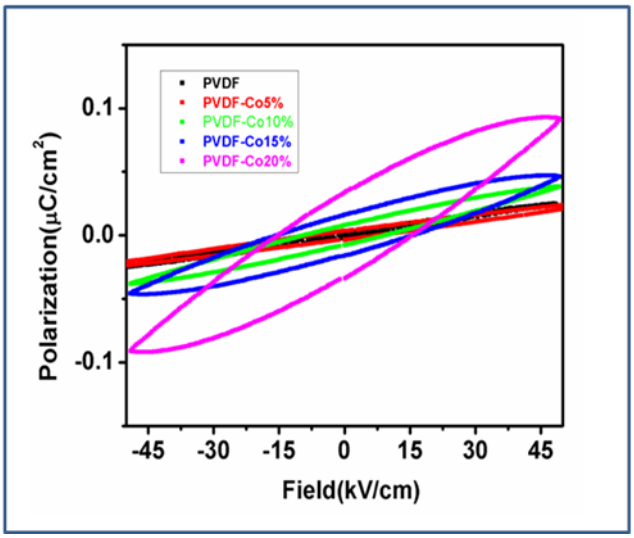

Fig.6.9: Electrical field dependent polarization at 100 Hz at room temperature.

The films were little stretched to remove the center of symmetry of spherulitic structure [191]. All the samples were polarized under the field of 50kV/cm at 100 Hz at room temperature for direct comparison. β-PVDF is capable of showing

ferroelectric property due to its intrinsic dipole moment which favors the polarization of the electric dipoles in the direction of the applied electric field. The ferroelectric properties of the nano-composite films improve with increase in cobalt loading in PVDF. The saturation polarization increased from 0.026 μC/cm^2 for pristine PVDF to 0.05μC/cm^2 for 15 vol% Cobalt loaded PVDF. In case of 20 vol% Co-PVDF composite, the polarization was found to be 0.09μC/cm^2, however, this polarization might be infested by leakage current because the composition (20 vol% of cobalt) is above percolation threshold (19 vol%).The remanent polarization also increases with cobalt which is due to increase in the amount of β-phase as it has been established by IR spectroscopy. The polymeric chains are in opposite direction (TGTG', T= trans, G= gauche) in α-phase of PVDF which results in zero polarization whereas in β-phase the dipoles can align (TTTT) in the direction of the electric field and gives rise to definite polarization. The saturation polarization increases with the concentration of cobalt nanoparticle due to higher β content of cobalt loaded PVDF.

6.4. Results and Discussion of Ni/PVDF composites

The transparent, free-standing and flexible nature of PVDF has been shown in photographs **Fig.6.10.**

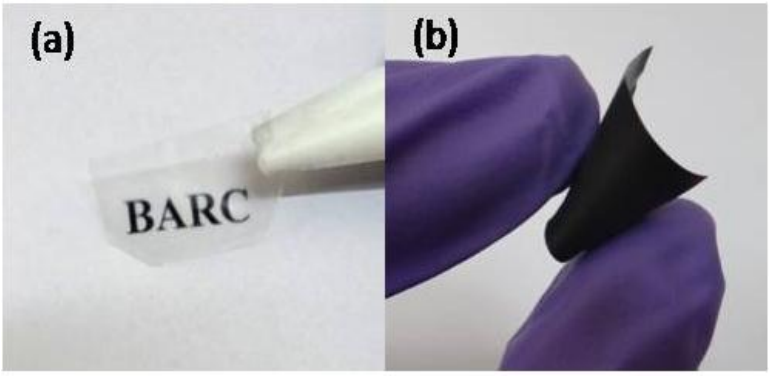

Fig.6.10: Flexibility and free-standing nature of PVDF and PVDF- Ni films.

After loading of ferromagnetic nickel nanoparticles on PVDF, the color of the thick films turns to black without compromising its flexibility and freestanding nature which are very important criteria for fabrication of new devices.

6.4.1. XRD studies

The XRD patterns of pure PVDF and Ni/PVDF composites are shown in **Fig.6.11.** The peaks corresponding to any possible impurity phases were not observed in any of these XRD patterns. The XRD pattern of pristine PVDF is shown in **Figure 6.11a**. PVDF is known to crystallize in α, β and γ forms at room temperature. The most intense peak at 20.3° is the summation of (110) and (200) peaks and the minor peak at 21.5° is characteristic of γ phase of PVDF [184].

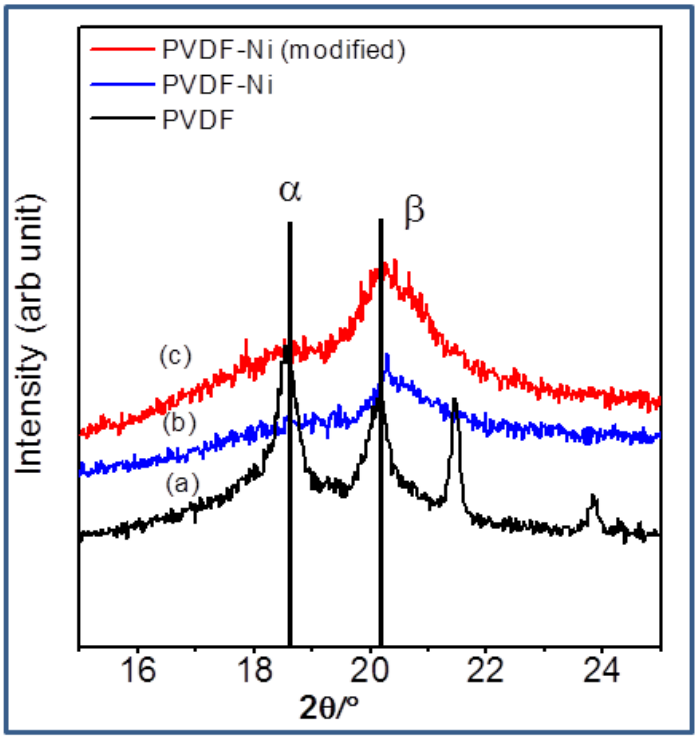

Fig.6.11: Typical XRD pattern of (a) PVDF (b) PNi1 (c) PNim1 composite

The XRD peaks at 2Θ = 18.4°, 20.3° corresponding to α and phase β of PVDF. Hence PVDF used in this experiment is mixture of nonpolar α phase and polar β

phase. The ratio of intensity of peaks at 20.3 and 18.4 ratio ($I_{20.3}/I_{18.4}$) gives the idea of α and β phase content in the mixture. In pure PVDF, the it is found to be 0.7 which increases to 3.4 in PNi1. It suggests that β content of PVDF increases with nickel loading. The content of β phase further increases on using surface modified nickel nanoparticles as the ratio ($I_{20.3}/I_{18.4}$) becomes 5.9 for 10% modified Ni loaded PVDF (PNim1) sample. Similar kind observation has been found in FTIR studies also

6.4.2. FTIR studies

Fourier Transform infra red (FTIR) study has been performed on surface modified nickel, pristine PVDF and modified nickel loaded PVDF samples **Fig.6.12.**

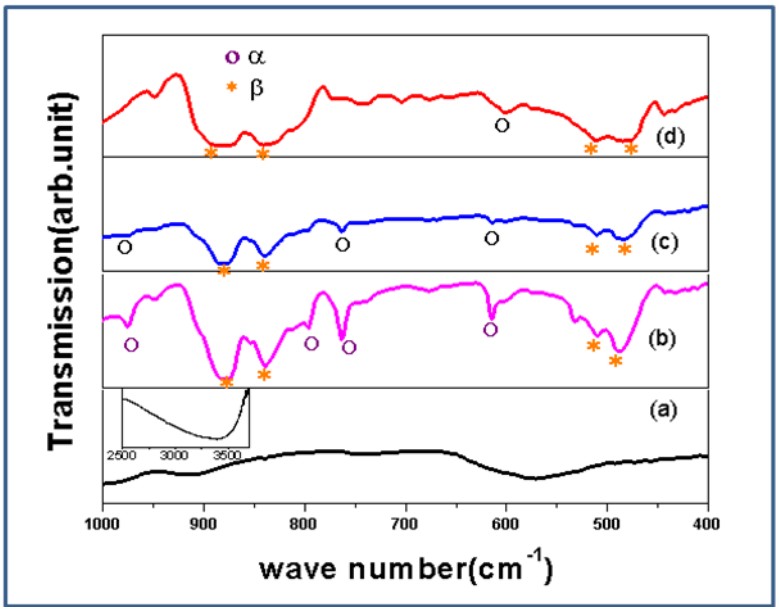

Fig.6.12: FTIR spectra of (a) hydroxylated Ni (b) pristine PVDF (c) PNi1(PVDF-10 wt% Ni) (d) PNim1 (PVDF-10 wt% Ni-OH). Inset in (a) shows the presence of hydroxyl group on nickel nanoparticle.

The band in the range 3200-3600cm^{-1} (inset of **Fig.6.12a**) corresponds to the hydroxyl groups which are attached to the nickel nanoparticle [192]. The absorption at ~570cm^{-1} also corresponds to the Ni-OH bond [193]. These observations confirm the

formation of hydroxyl group on the surface of nickel nanoparticles. The FTIR spectrum of PVDF exhibited the presence of α and β forms of PVDF **Fig.6.12b.** The infra-red bands have been assigned following the previous work on PVDF [194]. The characteristic bands observed at 487, 612, 760, 796, 853 and 975 cm^{-1} correspond to α-phase of PVDF whereas the bands at 840, 511, 878 and 472 cm^{-1} indicate the presence of β-phase of PVDF [195]. The relative amount of β and α-phase of PVDF in different samples have been estimated by calculating the relative ratio of the intensity of the characteristic peaks of α (760 cm^{-1}) and β-phase (840cm^{-1}). The ratio I_{840}/I_{760} for virgin PVDF and 10 wt% Ni loaded PVDF (PNi1) are found to be 1.9, 3.9 respectively, suggesting the amount of polar β-phase increases with nickel loading, as also observed in case of Co/PVDF The content of β-phase further increases on using surface modified nickel nanoparticles as the ratio I_{840}/I_{760} becomes 8.7 for 10 wt% modified Ni loaded PVDF (PNim1) sample.

6.4.3. Dielectric properties

To investigate the effect of Ni nanoparticle on dielectric properties of composites different amounts of Ni nanoparticle mixed with the PVDF polymer matrix and the films were made as described earlier in case of Co/PVDF composites. For comparison of the dielectric properties of the composite films experiment carried out at room temperature and results are shown in the **Fig.6.13**.The dielectric constant of the composite films decrease with increasing frequency due to decrease in the dipolar contribution at the high frequency. When loading of Ni 10 wt% the relative permittivity is around 25, as compared to permittivity of pure PVDF sample at 100 Hz frequency. The dielectric constant of 19 was observed at 1 kHz for 30 wt% of TiO_2 in

the PVDF-TrFE polymer matrix which is due to Maxwell Wagner sillar (MWS) relaxation [196].

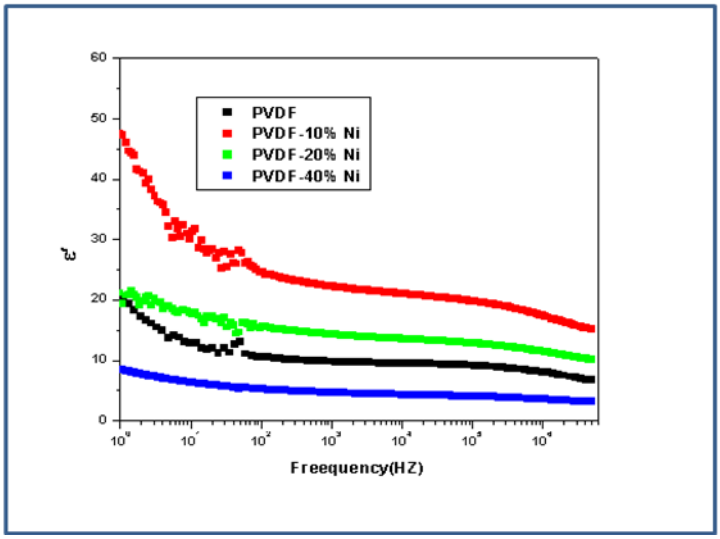

Fig.6.13: Variation of relative permittivity of PVDF and PVDF-Ni composite with frequency at RT.

With further increase in the concentration of the Ni the dielectric constant was found to be decreased. This indicates that the introduction of the Ni nanoparticle in the polymer matrix could enhance the dielectric constant of pure PVDF up to certain concentration of Ni. The increase in the dielectric constant with Ni is due to the interfacial polarization. Due to difference in electrical properties of components in composite materials the entrapment of charges are possible at the interface between the PVDF and Ni nanoparticle by the application of electrical field. The decrease in the dielectric constant at higher concentration of Ni is due to non-uniform distribution of Ni in the polymer matrix. Similar results observed with the surface unmodified $BaTiO_3$ show lower dielectric constant than the unmodified $BaTiO_3$ due to non-uniform dispersion caused by high concentration of ceramic filler [197].

The decrease in the dielectric constant beyond 10^3 Hz is due to dielectric relaxation which also evidenced by the dielectric loss peak in the **Fig.6.14.**

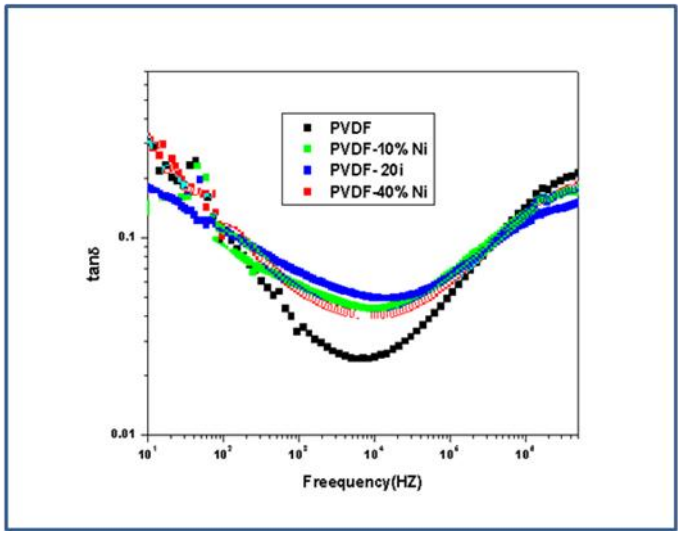

Fig.6.14: Variation of dielectric loss of PVDF and PVDF-Ni composite with frequency at RT.

The dielectric loss of the composite films is almost equal to the pure PVDF and not higher than the 0.06 in the frequency of around $5X10^3$ Hz. Even the samples, in present investigations exhibits interfacial polarization, the low dielectric loss can be explained as, since these samples are prepared in the polyol medium, ethylene glycol groups are coated on the surface of the Ni nanoparticle which can be act as a barrier between the Ni nanoparticles to prevent the direct contact between the nanoparticle and in turn results in the lower dielectric loss. Xiwen Kuang et al. also observe the low dielectric loss in the Ag@C/PVDF composites due to carbon layer acts as a insulation layer to avoid the leakage current [198].

6.4.4. Electric field polarization studies

The characterization of ferroelectric materials from polarization vs electric field (P-E) loop is very important; however, often it can lead to misleading conclusions. For true ferroelectrics, the electrical polarization saturates at certain field and exhibit concave nature in the polarization-electric field curves. In the present samples, PVDF is the ferroelectric backbone which shows saturation in polarization

curve. In the nickel loaded PVDF samples too, the saturation polarization and concave region could be observed like true ferroelectrics. The polarization of the pristine PVDF film increases from 0.060μC/cm^2 to 0.087μC/cm^2 upon 10 wt% nickel loading (PNi1). The increase in polarization in PNi1 could be due to formation of higher amount of polar beta phase of PVDF in presence of nickel nano particles. The increase in beta phase was established by FTIR study also. However, high electrical field could not be applied on highly nickel loaded samples i.e. 20 wt% Ni-PVDF (PNi2) and 40 wt% Ni-PVDF (PNi4) as shown in the **Fig.6.15.** The breakdown voltages of these highly loaded Ni-PVDF films might be low due to higher amount of metallic component present in these samples. The increased polarizations in both the samples are due to contribution from leakage current in the system discussed in next section.

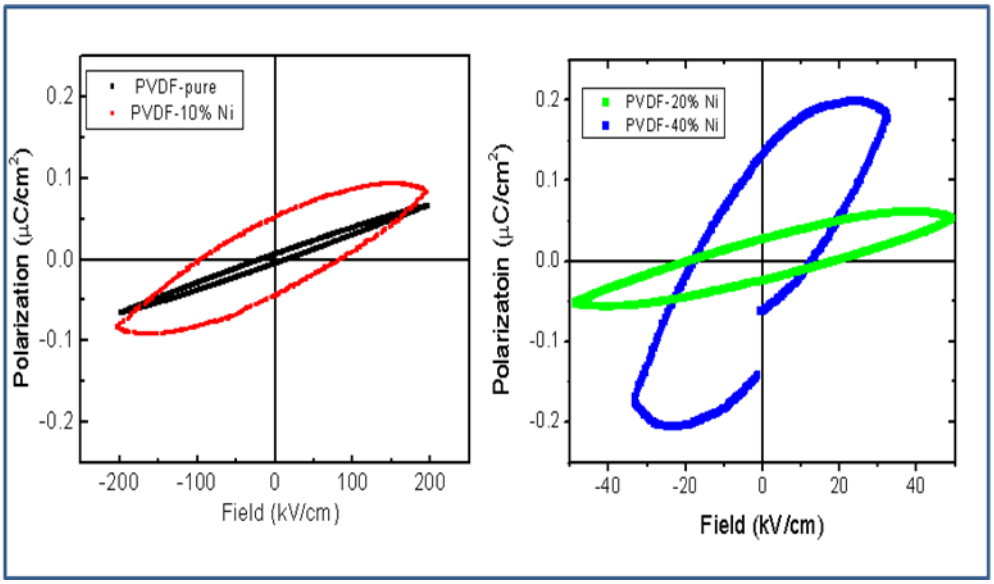

Fig.6.15: Electrical field dependent polarization of Ni-PVDF composites.

The ferroelectric or multiferroic materials with lower leakage current are desirable for possible applications in devices. The leakage current of thick film of pure PVDF is found to be 0.01μA/cm^2 at 100kV/cm which shows a sudden increase upon Ni loading as shown in the **Fig.6.16**.

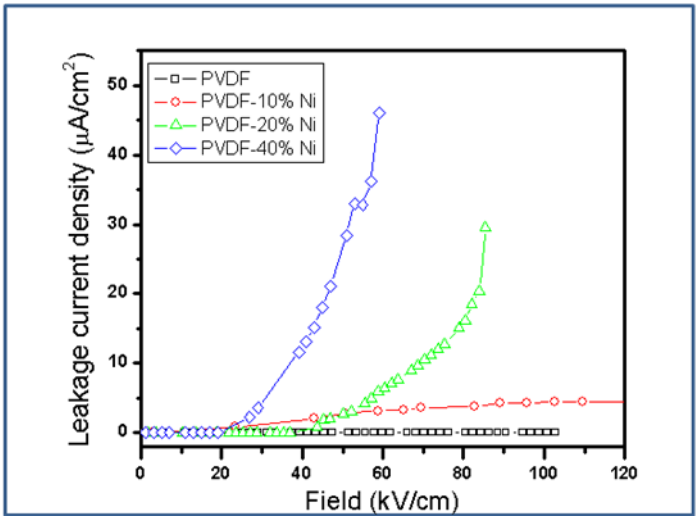

Fig.6.16: Comparison of leakage current of different composites.

The leakage current for PNi1 increases to 4.332μA/cm^2 whereas PNi2 sample exhibits an abrupt increase in leakage current above field 50kV/cm. The sudden rise in leakage current for PNi4 starts even at lower field i.e. 20kV/cm onwards. Since with increase in nickel amount in the composites, the proximity of the conducting nickel nano-particles increase which led to decrease in resistivity, therefore the ferroelectric samples become more and more leaky. Among the samples, the polarization of 10 wt% Ni-PVDF composite exhibit highest polarization, however, its moderately high leakage current is a point of concern for practical application. In order to achieve higher polarization without compromising the leakage current, the surface of the nickel nanoparticles was modified and 10 wt% modified nickel nanoparticles was dispersed in PVDF matrix. Since other samples showed relatively less polarization and more leaky poor electrical behavior, therefore, the data corresponding to only 10 wt% nickel-PVDF sample have been discussed here.

A remarkable improvement in polarization to 0.109 μC/cm^2 has been observed in the surface modified nickel (10 wt%)-PVDF composite (PNim1) as shown in **Fig.6.17.**

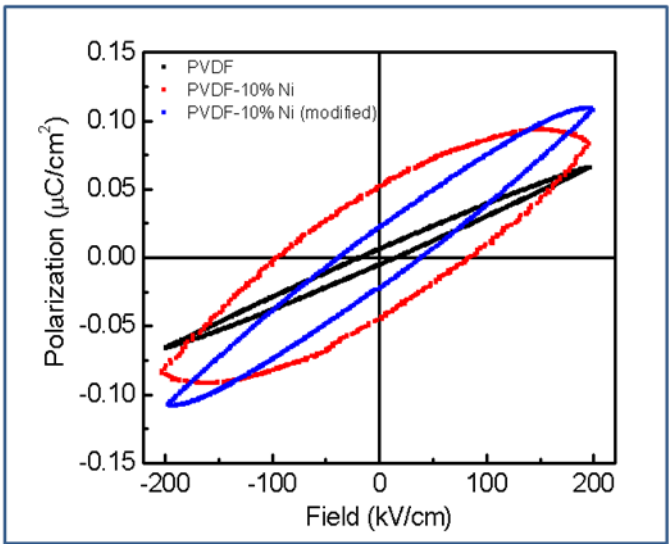

Fig.6.17: Electrical field dependent polarization of hydroxylated Ni-PVDF composite.

The leakage current of the surface modified nickel-PVDF has been measured and presented in the **Fig.6.18**. Strikingly, the leakage current of the composite having surface modified Ni decreases markedly compared to the unmodified one. The reduction of the leakage current and improvement in polarization in hybrid films containing functionalized Ni is attributed to the improved interface between ferromagnetic and ferroelectric phases. A schematic has been shown in **Fig.6.19** to illustrate the interaction between the surface modified nickel nanoparticles and PVDF. The -OH groups on nickel nanoparticles can support strong dipole interaction between the fluorine atoms of PVDF which results in the better dispersion of the nanoparticles in the polymer matrix. In addition, the charge trapping by surface hydroxyl groups minimizes possible charge conduction pathways in the film resulting in considerable reduction in the leakage currents. Similar kind of observation was found in dielectric study of hydroxylated $BaTiO_3$ [199].

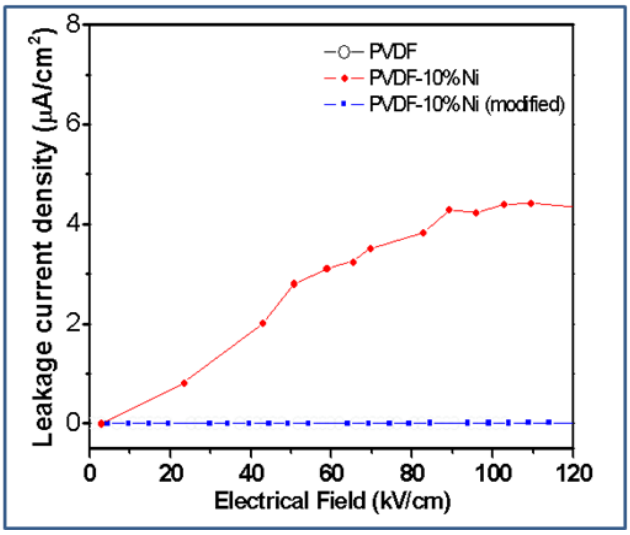

Fig.6.18: Comparison of leakage current of different composites.

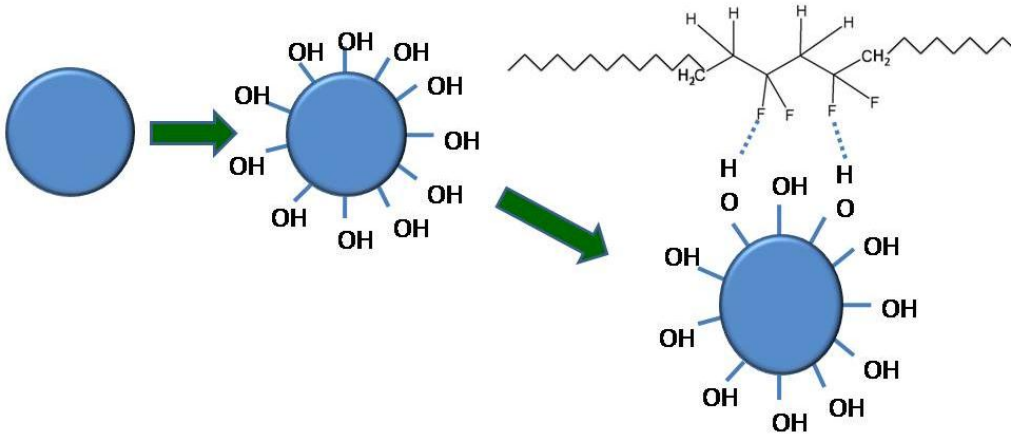

Fig.6.19: Schematic diagram of hydroxylated Ni-PVDF composite.

6.4.5. Magnetic properties

The magnetic field dependent magnetization data for hydroxylated nickel nanoparticles at 5 K and 300 K are shown in the inset of **Fig.6.20**, indicating ferromagnetic nature of the sample. The coercivity of hydroxylated nickel nanoparticles was found to be 275Oe and 160Oe whereas saturation magnetization was 20emu/g and 18.8emu/g at 5K and 300K, respectively

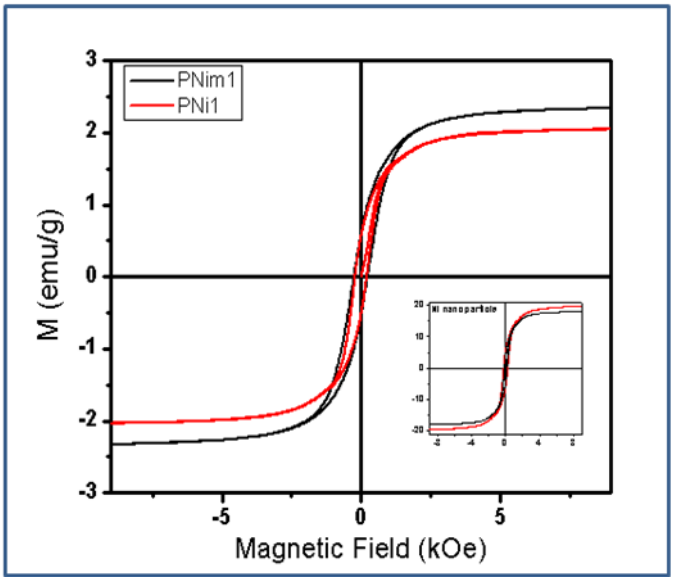

Fig.6.20: Magnetization of Ni-PVDF (PNi1) and functionalized Ni-PVDF (PNim1) composite. Inset shows the magnetization of functionalized nickel nanoparticle.

.Nickel is well studied ferromagnetic material with saturation magnetization of 58 emu/g for bulk sample [200]. However, the sample used in this experiment shows lower magnetic moment. The plausible reason could be that the particles were in nano-regime and some hydroxyl groups were attached to these nanoparticles. It has been reported earlier that with decrease in particle size, the saturation magnetization decreases [201]. Additionally, it has been reported a decrease in magnetization of metal nanoparticles when the nanoparticles are functionalized with different ligands which support our findings [202].

The magnetic field dependent magnetization of PNim1 and PNi1 i.e. 10 wt% modified Ni and unmodified Ni dispersed in PVDF matrix are shown in **Fig.6.21**. The saturation magnetic moments were found to be 2.1 and 2.0 emu/g for PNim1 and PNi1, respectively. The decrease in moment of the composite is obviously due to presence of diamagnetic PVDF phase which reduces the fraction of magnetic constituent. On the other hand the little decrease in magnetic moment of the modified sample (PNim1) in

comparison with unmodified one is attributed to the extra hydroxyl groups present on the nickel nanoparticles.

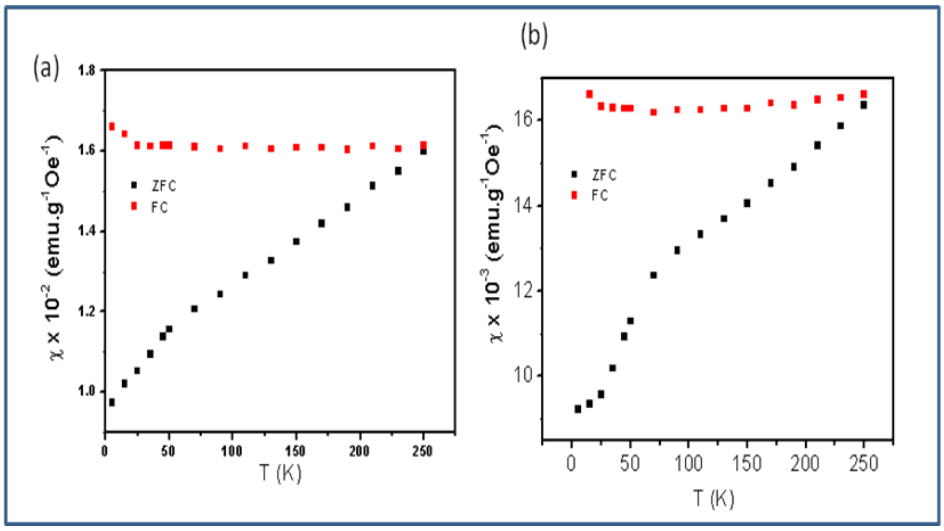

Fig.6.21: Variation of magnetic susceptibility with temperature of modified (a) nickel nanoparticle (b) 10 wt% modified Ni-PVDF (PNIm1).

Temperature dependent magnetization study has been done on these samples. The ZFC curves for functionalized nickel show that, the magnetic susceptibility decreases with decreasing temperature, whereas FC curve shows nearly constant magnetic susceptibility. The sample PNim1 composite also shows similar trend (As shown in **Fig.6.21**). These curves also indicate that there is no secondary phase in the system.

6.4.6. Magneto-dielectric studies

The coexistence of ferromagnetic and ferroelectric order in these multiferroic composites is not enough for the proposed applications as transducer, multistate data storage devices or magnetically tunable electronics devices. The composite materials need to show appreciable coupling between these physical properties. The coupling between magnetic electric polarizations can be measured by observing the change in dielectric constant under magnetic field. The change in dielectric constant with applied magnetic field is characterized by the magneto-dielectric constant defined as

$\frac{\varepsilon_H - \varepsilon_0}{\varepsilon_0}$ X 100% where ε_H and ε_o are the dielectric constants with and without applying magnetic field, respectively. PVDF-modified Ni 10 wt% (PNim1) sample showed highest polarization along with lowest leakage current among the samples, therefore, it has been chosen for magnetocapcitive measurement. In order to compare, the composite samples without surface modification with 10 wt% Ni loading (PNi1) was also tested under similar condition as shown in the **Fig.6.22**. Both the samples showed a linear drift in dielectric constant as a function of magnetic field. The dielectric constants were adjusted by subtracting the linear background. The obtained curve could be fitted well in parabolic equation as $(\varepsilon_H - \varepsilon_0)/\varepsilon_0 = \gamma H^2$, originating from the lowest order coupling terms polarization P and magnetization H in the free energy term, as described in previous literature [203].

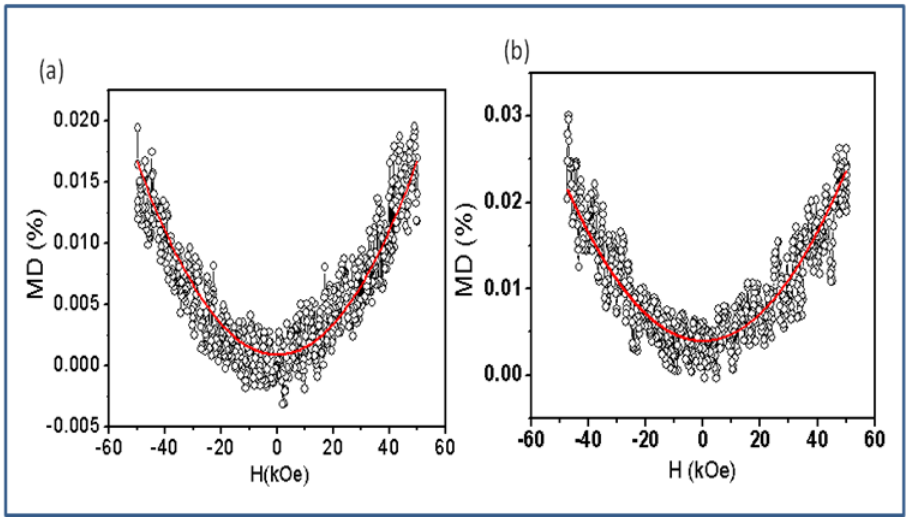

Fig.6.22: Magnetodielectric (MD = ($\varepsilon_H - \varepsilon_0$)/ ε_0 × 100%) coupling of the (a) Ni-PVDF and (b) hydroxylated Ni-PVDF sample.

The value of γ in unmodified samples was found to be 6.1 x 10^{-12} whereas for modified sample 7.9x10^{-12}. The slightly higher value of γ suggests that the surface modified Ni-PVDF composite has higher magnetodielectric coupling than the unmodified analogue. Magnetodielectric term arises from the free energy term. The

free energy (F), given in terms of the sample magnetization (M) and the polarization (P) and the external electric field (E) is $F= (1/2\varepsilon_o) P^2-PE-\alpha PM+\beta PM^2+\gamma P^2M^2$ where ε_0 is the dielectric susceptibility and α, β, and γ are coupling constants. In this expression, the αPM term produces linear magnetoelectric coupling. Since P is a polar vector and M is an axial vector terms linear in both P and M will typically not yield a scalar and hence vanish from the free energy expansion. The term βPM^2 is also forbidden by symmetry in many cases. Since the effective dielectric constant is determined by taking the second derivative of the free energy with respect to the polarization, using the above stated equation we see that this value will depend on both the bare dielectric constant, ε_0, and the magnetodielectric correction, which is proportional to γM^2. Now M^2 is proportional to H^2 (field), therefore, MD is proportional to H^2 . In these samples, the magneto-dielectric showed quadratic dependence on magnetization, which is observed in many magnetoelectric multiferroic materials [204]. It has been mentioned above that the magneto-dielectric coupling arises in the composites as a result of the product of the magnetostrictive effect of the magnetic phase and the piezoelectric effect of the ferroelectric phase [190]. The coupling of electric and magnetic phenomena takes place through elastic interaction between these two phases. Hence, the magnetoelectric effect in these composite systems is extrinsic in nature, which depends on the composite microstructure and coupling interaction across the magnetic and ferroelectric interfaces [205]. In these multiferroic hybrids, the applied magnetic field probably modifies the magnetic alignment of nickel nanoparticles, which generates a stress on adjoining ferroelectric PVDF phase via magnetostriction and it eventually leads to some surface charges by the piezoelectric effect [206]. The hydroxyl groups on nickel nanoparticles cause better bonding with the ferroelectric

PVDF phase, therefore, the strain arising due to magnetostriction of nickel nanoparticles could easily be transferred to the ferroelectric PVDF phase. Therefore, the magneto-dielectric coupling of the functionalized Ni-PVDF composite found to be higher in magnitude.

6.5. Conclusion

The flexible and free-standing films of PVDF loaded with Co/Ni could be fabricated successfully. The amount of polar β phase of PVDF increases upon loading of Co/Ni nanoparticles in PVDF. The dielectric constant increases to about 100 without much compromise in dielectric loss at percolation threshold (19 vol%) of cobalt nanoparticle in PVDF matrix. Higher relative permittivity around 25 is observed at the 10 wt%. loading of Ni. The electrical conductivity of ~10^{-11}-10^{-9} S/cm has been observed for all the composites which increases with increase in frequency. The high dielectric permittivity and low electrical conductivity of the composite with 20 vol% Co-PVDF are due to charge accumulation at interfacial layers between PVDF chains and cobalt nanoparticles dispersed in the composites, and the formation of several microcapacitor structures. The surface fuctionalization of nickel could substantially improve the polarization and also reduces the leakage current significantly. In case of Ni/PVDF composites magnetoelectric coupling was also studied by magneto capacitance measurements which show that the surface functionalized Ni-PVDF composite exhibit higher magneto-dielectric coupling than the unmodified one.

CHAPTER 7

PREPARATION, STRUCTURE AND PHYSICAL PROPERTIES OF SOME TRANSITION METAL BASED COMPLEX OXIDES

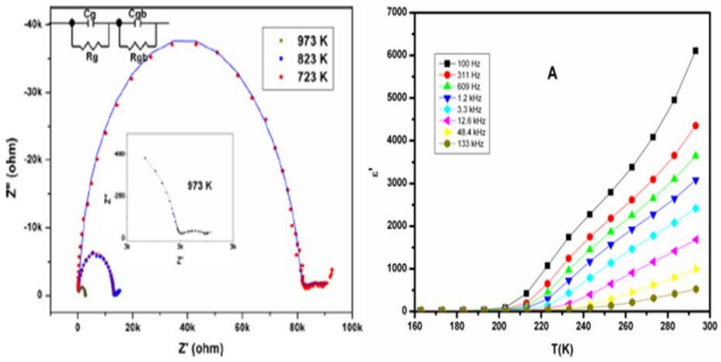

1. Size dependent magnetic and dielectric properties of nano $CoFe_2O_4$ prepared by a salt assisted gel-combustion method
K. Vasundhara, S. N. Achary, S. K. Deshpande, P. D. Babu, S. S. Meena and A. K Tyagi
J. Appl. Phys.113 (2013) 194101-194107.

2. High temperature structural dielectric and ion conduction properties of orthorhombic $InVO_4$
K. Vasundhara, S. J. Patwe, S. N. Achary and A. K. Tyagi
J. Am. Ceram. Soc. 96 (2013) 166-173.

7.1. Introduction

Transition metals are the elements with incomplete d sub-shells, which govern the range of physical and chemical properties. These elements can exhibit multiple oxidant states depending on the number of d-electrons, and thus, they commonly exist in divalent to tetravalent oxidation states. The simple transition metal monoxides have NaCl type structures, where the 180^o cation-oxygen-cation interactions govern their magnetic properties. If the monoxides have cation-cation separation higher than the critical value, it leads to insulating behaviour, viz. TiO. Dioxides of transition metals have the rutile-type structures. In such structures, two types of interaction occurs viz.135^0 cation-oxygen-cation interactions between corner-shared octahedra and 90° cation-anion-cation interaction between edge-shared octahedra. These oxides can be metallic through cation-cation or cation-oxygen-cation interactions. For example, CrO_2 is a metallic ferromagnet where one of the d-electrons forms an n* bond through cation-anion-cation interaction. Oxides of the first row of the transition metal in trivalent state form corundum type structures. The corundum type transition metal oxides, like Ti_2O_3 and V_2O_3 show temperature induced metal-insulator transitions. The 180^o cation–oxygen-cation interactions are observed in the ABO_3 perovskite, where cation–cation interactions are remote, due to the large distance associated with the cube-face diagonal. The type of magnetism observed in transition metal oxides can be explained by the exchange interaction between the neighboring magnetic ions will force the individual moments into parallel (ferromagnetic) or antiparallel (antiferromagnetic) alignment with the neighboring cations. In the case materials with magnetic ions separated by a non-magnetic, the magnetic properties are governed by two types of exchange interactions, (a). double exchange and (b). super exchange.

Similar to magnetic properties, electrical properties of complex metal oxides attract significant attention to develop better materials for wide varieties of applications, viz. photovoltaic cell for solar cell, catalyst for water splitting, solid electrolyte or electrode for SOFC and battery, active material for gas sensors etc. The material characteristics for such applications have been defined in term of their response to the electric field or light or surrounding atmosphere. In these aspects a continuous research is being carried out on various metal oxides having controlled chemical composition, size as well as morphology.

In this chapter, preparation and properties of two transition metal containing complex materials, namely $InVO_4$ and $CoFe_2O_4$ are presented. In case of $InVO_4$, the V^{5+} (d^0) state does not lead to any magnetic order but exhibit semiconducting behavior. $CoFe_2O_4$, shows magnetic interaction due to the interactions of the partially filled d-electrons of the transition metal ions and semiconducting behavior. The details of the studies carried out on these systems are explained sequentially explained in this chapter.

7.2. InVO4

Among the transition metal based ABO_4 type vanadates, $FeVO_4$ and $CrVO_4$ have drawn significant attention due to the unpaired electrons of the transition metal ions [207], which facilitate interesting electronic and magnetic properties. Studies of electrical properties of such transition metal (Fe and Cr) containing vanadates indicate an n-type semiconducting behaviour [207a-d]. The thermal hopping of electron due to the variable valence states or oxygen ion vacancies due to non-stoichiometry in composition has been attributed to their electrical conduction [208]. Also literatures indicate polaron hopping conduction mechanism in $FeVO_4$ even without any

fluctuation in valency of Fe or V ions [207d-f]. Typical values of activation energies 0.13, 1.7 and 2.7 eV are reported for $FeVO_4$, $CrVO_4$ and $AlVO_4$, respectively [207d]. This suggests that thermal activation of carriers depend on the electronic structure of the A^{3+} ion. Impedance spectroscopic studies on nano-crystalline $FeVO_4$ also show similar low activation energy (0.28 eV) and an increasing trend of permittivity with decreasing frequency as well as with increasing temperature [207f]. The changes in oxidation states of Fe and V with concurrent ion movement are assigned to such high permittivity at lower frequencies. As the temperature increases, the ion/dipole orientations are favoured and they contribute to conductivities and dielectric properties of orthovanadates like $CaThV_2O_8$ [209], $LnVO_4$ (Ln = Rare-earth ions) [210] etc. As not many reports in literature are available on the high-temperature electrical properties on $CrVO_4$ type orthovanadates with cations having filled electronic configuration, no general conclusion can be drawn for the transition metal containing orthovanadates. Due to significant amounts of empty spaces and highly distorted polyhedral units in lattice of $CrVO_4$ type structures, the dielectric and conduction process may have independent effect other than the involvement of electrons due to valence fluctuation. To investigate such type of contributions detailed study on $InVO_4$ has been undertaken.

$InVO_4$ belongs to a large family of orthovanadates and exists as a line compound in In_2O_3-V_2O_5 system [211]. It is well established that $InVO_4$ can exist in different polymorphic forms, viz. monoclinic, orthorhombic and tetragonal and an unknown structure type depending the preparation conditions [212]. The orthorhombic form is most stable phase of $InVO_4$, which is iso-structural to orthorhombic $CrVO_4$. Although $InVO_4$ has attracted significant interest for several practical applications as

well as in understanding fundamental crystallography and phase transitions, very little details are available on its intrinsic properties responsible for such applications and properties under non-ambient temperatures [213].

From the ambient temperature optical absorption and impedance spectroscopic studies, an indirect bandgap of 3.2 eV with a pronounced sub-bandgap near 2.5 eV and dielectric constant of ~50 were reported for $InVO_4$ [213c]. The poor photo response of $InVO_4$ has been attributed to the high density of deep donors [213c]. Plotkin et al. have reported the dielectric nature of $InVO_4$ [214]. Literature also indicates a narrower band gap of 1.9-2.2 eV for $InVO_4$ [215]. Both, the stable orthorhombic and metastable monoclinic modifications of $InVO_4$, have octahedral InO_6 and tetrahedral VO_4 units as building blocks of crystal structure. Also, both the structures have significant open spaces to facilitate intercalation of cations like lithium [216] and to create intrinsic defect structures with cation or anion interstitials [208].

As $InVO_4$ has significant importance in applied sciences and is a suitable candidate to understand the high-temperature conduction process of $CrVO_4$ structure-related materials, its high-temperature structural and electrical properties have been investigated and the results are presented in this chapter.

7.2.1. Synthesis and characterisation of $InVO_4$

$InVO_4$ was synthesized from appropriate amounts of In_2O_3 (99.9 %, Aldrich) and V_2O_5 (99.5 %, Riedel-de Haen). Pellets of homogeneous mixture of the reactants were heated at 973 K for about 8 h followed by re-homogenization and reheating at 1123 K. Further, the product was re-ground pressed into pellets and sintered at 1173 K for 12 h.

The product obtained after this heat treatment was characterized by powder XRD patterns, recorded on a Panalytical Powder X-ray diffractometer (X'Pert-Pro) using monochromatic Cu Kα radiation. For structural studies, powder diffraction data were collected in the two theta range of 10-100°, with step width and step time of 0.02 and 3 sec. The *in situ* high temperature XRD patterns of the sample were recorded in static air on a Panalytical X'Pert-Pro diffractometer equipped with Anton Parr high temperature attachment. The HT-XRD patterns were recorded in the two-theta range of 10-80° with step width and step time as 0.02° and 1.5 seconds, respectively. The sample was heated to a desired temperature at a rate of 20 K/min and held for 5 minutes for equilibration and then XRD data were collected. The Rietveld refinements of the powder diffraction data were carried out using GSAS software package [220]. For impedance measurements, a cylindrical pellet of about 88 % of theoretical density coated with platinum paste was used. The impedance measurements were carried in the frequency range of 0.1 Hz to 10 MHz using a Solartron impedance analyzer (Model 1290). The impedance data were collected while cooling the pellet from 973 K.

7.3. Results and discussion of $InVO_4$

7.3.1. XRD studies

All the reflections of the XRD pattern of the sample obtained after final heat treatment could be assigned to orthorhombic $InVO_4$. Further characterization was carried out by the Rietveld refinement of the XRD data. The Rietveld refinement was carried out by using the earlier reported structural data for orthorhombic $InVO_4$ (In: *(4a: 0, 0, 0),* V: (*4c: 0,y,1/4),* O1: (*8g: x,y,1/4)* and O2: (*8f: 0,y,z),* Z = 4 with Space group: Cmcm, No. 63). The profile was fitted with pseudo-Voigt profile function and

the background was fitted with cosine Fourier series. Initially the unit cell parameters, half width, asymmetry and low and high angle broadening parameters were refined along with the scale factor. No preferred orientation correction was required to match the intensities of the Bragg peaks. Later, the position coordinates and isotropic thermal parameters of various atoms were included in the refinement. Finally the thermal parameter of In atom was refined anisotropically. An appreciably good refinement was observed from the residuals of refinement (R_p = 7.81, R_{wp} = 10.16, R_F^2 =4.97 and $\chi 2$ = 3.78) and difference between the observed and calculated diffraction patterns. The refined unit cell parameters for $InVO_4$ are: a = 5.75194(5), b = 8.52148(8) and c = 6.58426(6) Å and V = 322.728(4) $Å^3$, which are in agreement with the earlier reported values [217]. The Rietveld refinement plot of the final cycle is shown in **Figure 7.1**.

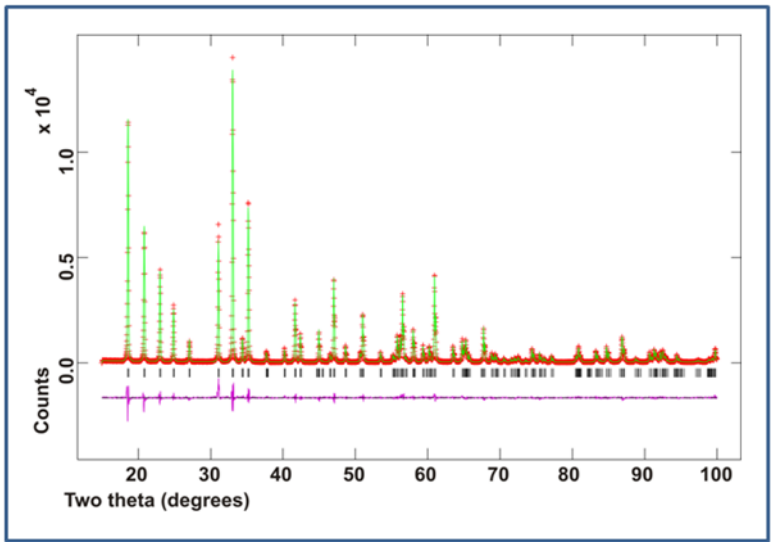

Fig.7.1: Rietveld refinement plot of XRD data observed at ambient temperature radiation (Cu Kα Radiation; λ = 1.5406 and 1.5444 Å).

The analysis of the structural parameters observed at ambient temperature shows that the In atoms are octahedrally coordinated (four equatorial O1 and two apical O2) and V atoms are tetrahedrally coordinated (two of O1 and two of O2) with oxygen atoms. The typical inter-atomic distances for In-O1 and In-O2 are 2.162(3) and 2.200(4) Å,

respectively. The InO_6 octahedra are linked to other octahedral units by sharing two opposite edges of the equatorial planes to form an infinite chain propagating along the *c*-axis. These chains are linked together in *a*- and *b*- directions by sharing the vertices of octahedral InO_6 units with tetrahedral VO_4. The typical crystal structure of $InVO_4$ indicating the InO_6 octahedra and VO_4 tetrahedra is shown in **Fig.7.2**.

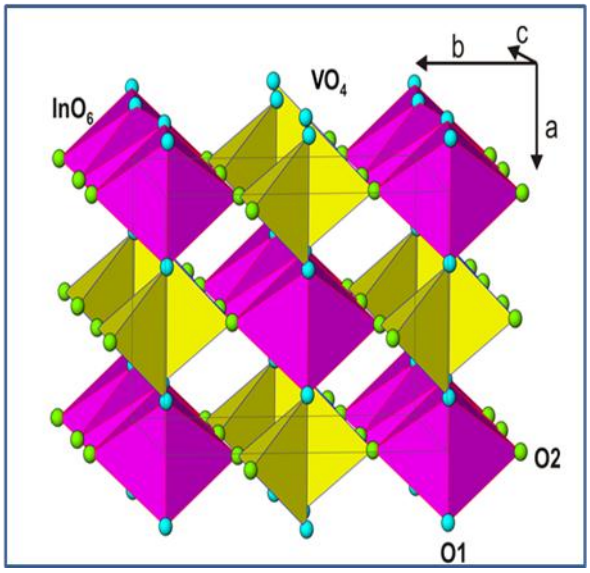

Fig.7.2: Typical crystal structure of $InVO_4$ (InO_6 octahedra and VO_4 tetrahedra are shown).

Both the InO_6 octahedra and VO_4 tetrahedra are distorted as observed from the significant differences in In-O and V-O bond lengths. Also the distortion in the VO_4 tetrahedra is more compared to the InO_6 octahedra (Polyhedral distortion in VO_4 and InO_6 are 32.3×10^{-4} and 0.67×10^{-4}, respectively). A comparison of the refined structural parameters with those reported earlier for tetrahedral VO_4 units of $InVO_4$ and other related structures indicates that an appreciable variation in V-O bond lengths is a common feature. However, the O-V-O angles in all cases remain close to the normal tetrahedral angles. Such distortions often destabilize the lattice and thus the structure has a tendency to transform to different structure-types under temperature or pressure, as well as to form significant amount of intrinsic point defects in the lattice

[208, 218]. In order to further understand further on these aspects and their correlation with the electrical properties, *in situ* high temperature XRD and high temperature *ac*-impedance studies were carried out and results are explained subsequently.

The high temperature structural parameters of $InVO_4$ were obtained from the analyses of *in situ* high temperature powder XRD patterns. The powder XRD patterns recorded up to 1023 K are closely similar to that observed at ambient temperature. Since, the reflections due to the platinum (Pt) strip used as sample holder-cum-heater are also observed in the *in situ* high temperature XRD patterns, the diffraction data have been analyzed by considering both the orthorhombic $InVO_4$ (Sp. Gr. Cmcm) and cubic Pt (Sp. Gr. Fm3m) simultaneously. All the diffraction patterns observed at higher temperature were refined by Rietveld method in a similar fashion as in ambient temperature study. The refined position coordinates and unit cell parameters observed at ambient temperature are used as the initial parameters. The analyses of the refined structural parameters indicate no significant changes in their structural parameters but show a smooth increase in the unit cell parameters with temperature. The temperature evolutions of unit cell parameters of $InVO_4$ are shown in **Fig.7.3.** The polynomial fit functions of the temperature evolutions of unit cell parameter are given below.

$$a\ (Å) = 8.507(1) + 4.2(3) \times 10^{-5}\ [T] + 2.1(2) \times 10^{-8}\ [T]^2$$

$$b\ (Å) = 6.472(1) + 3.6(2) \times 10^{-5}\ [T] + 1.6(2) \times 10^{-8}\ [T]^2$$

$$c\ (Å) = 5.745(1) + 2.0(2) \times 10^{-5}\ [T] + 5.8(2) \times 10^{-9}\ [T]^2$$

$$V\ (Å)^3 = 321.2(1) + 4.4(3) \times 10^{-3}\ [T] + 2.0(3) \times 10^{-6}\ [T]^2$$

Where T = Temperature in K

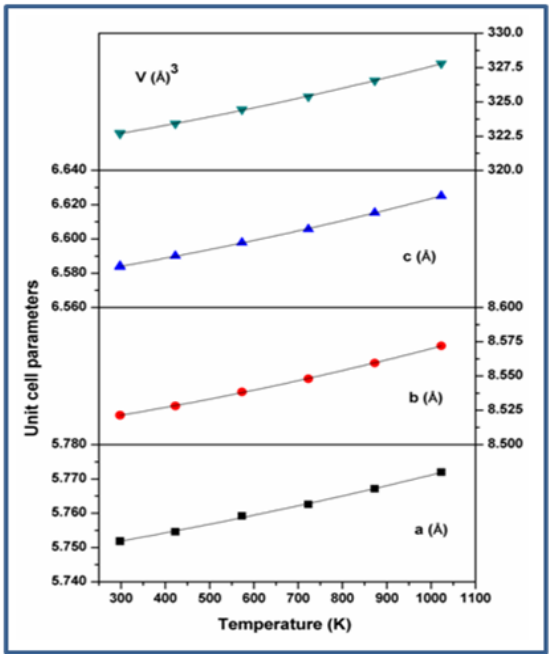

Fig.7.3: Variation of unit cell parameters of $InVO_4$ with temperature. Continuous lines indicate the polynomial fit values.

From the high temperature structural studies, it is observed that the distortions around In as well as V remain similar as those at ambient temperature. The In-O bonds show a large increasing trend with temperature compared to the V-O bonds. It is observed that the amplitude of thermal vibration of all atoms in particular O1 and O2 increase appreciably with the increase in temperature. Since anisotropic refinements of thermal parameters were not successful from the observed data, further conclusion on the directional displacement of ions could not be obtained. However, in general it can be mentioned here that the larger U values can act as a possible origin of ionic conductivity of $InVO_4$ and in particular at higher temperature which has been explained subsequently.

7.3.2. Electrical properties

The high temperature electrical properties of $InVO_4$ were studied over a frequency range of 0.1 Hz to 10 MHz and temperature range between ambient (300 K)

to 1023 K. Such measurements are often useful to differentiate electrical properties of grain and grain boundary of electroceramics. The impedance spectra obtained at ambient temperatures show an arc of a large semicircle at the high frequency side. The analysis of high frequency data using an equivalent circuit element consisting of one resistance and one capacitor in parallel (RC-circuit) configuration could give the resistance and capacitance of the bulk material. At ambient temperature $InVO_4$ shows highly resistive behavior (resistance 6.3 MΩ and $C = 1.5 \times 10^{-11}$ F) as reported earlier in literature [213c]. However, no reliable signal at low frequency could be observed at ambient temperature. Reliable data for real and imaginary part of impedance displaying a proper semicircle is observed only above 673 K. Also, above this temperature a clear contribution from grain, grain boundary and electrode effects could be observed. Thus the electrical properties are determined from the spectra recorded in between 673 to 973 K. Typical Cole-Cole plots indicating the real and imaginary part of the impedances at some representative temperatures are shown in **Fig.7.4**.

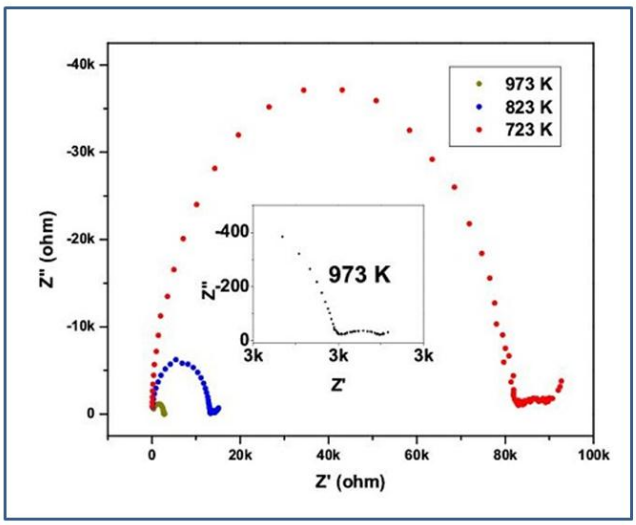

Fig.7.4: Typical Cole-Cole plots of $InVO_4$ at selected temperatures (insets shows expanded data observed at 973 K.

The impedance data shows a large semicircle in Cole-Cole plot at high frequency end while a small semicircle and an inclined spike are observed at low frequency end. The semicircle observed at high frequency can be attributed to the conductivity of grains and the semicircle and spike observed at low frequency ends can be attributed to the grain boundary and electrode polarization related phenomena. Assuming two RC circuit elements in series, the resistance and capacitance of the grain as well as grain boundaries were extracted from the temperature 673 to 973 K. It is observed that the resistances of the grains as well as grain boundaries decrease with the increase in the temperature, which suggests thermally activated conduction phenomena in $InVO_4$. Also, it is seen from the impedance data **(Fig.7.4)** that the resistance offered inside the grains is appreciably higher than that in grain boundaries. Typical values of resistances of grains at 698 K and 973 K are 1.7×10^6 Ω and 2.5×10^3 Ω, respectively. The conductivities of both, grains (σ_b) and grain boundaries (σ_{gb}) were extracted from the resistance data at various temperatures and they are shown in **Fig.7.5**.

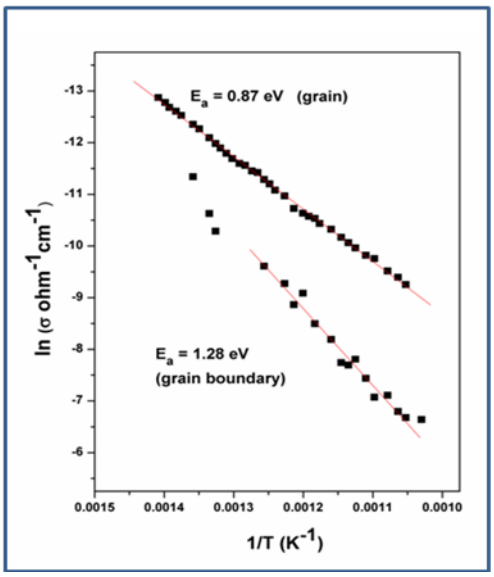

Fig.7.5: Variation of grain and grain boundary conductivities with temperature. Continuous lines are fitted by Arrhenius equation.

The variation of conductivities of both grain and grain boundaries with temperature were fitted by the Arrhenius expression.

$\ln\sigma = \ln\sigma_0 - E_a/kT$, where σ_0 = pre exponential factor E_a = activation energy k = Boltzmann's constant. The activation energies for conductivities in grain and grain boundaries are obtained from the slope and they are 0.87 and 1.28 eV, respectively. The observed bulk conductivity is lower compared to the grain boundary while the activation energy is higher for the grain boundary. Compared to $FeVO_4$ [207f], the activation energy for conductivity is higher in $InVO_4$. This difference may be attributed to the ease of formation of free electron carriers in $FeVO_4$ due to variable valence states of Fe. However, the observed activation energy of $InVO_4$ is lower compared to isostructural materials, like $CrVO_4$ and $AlVO_4$ [207d] as well as several other orthovanadates. The behavior of temperature dependent conductivity is closely comparable to that of $CrVO_4$ and $AlVO_4$ [207d]. In general the low conductivity and higher activation energy have been observed for several orthovanadate with filled electronic configuration cations compared to analogous materials with partially filled cations. Such differences were assigned to the additional contribution from the electronic conductivity in partially filled cation containing materials [209, 219]. From the dc- conductivity data Gron et al [207d] suggested that the thermally activated hole or electrons govern the electrical properties of AVO_4 (A = Fe, Cr and Al). Thus, the origin of conductivity in such materials arises from the electronic as well as ion mobilities. Recent studies of van de Krol et al. [208] in the context of the photocatalytic properties of $InVO_4$ revealed a deep electron donor state due to the formation of In interstitial ($In_{In}^{\bullet\bullet\bullet}$) and the corresponding amount of vacancies at V ($V_V^{''''}$) and oxygen ($V_O^{\bullet\bullet}$) sites

An insignificant deviation from stoichiometry of In to V can also give rise appreciable concentration of oxygen vacancies in the lattice. In literature, the presence of such oxygen vacancies has been confirmed by photoluminescence studies [208]. In addition, the structure of $InVO_4$ can be explained as distorted cubic close packed oxygen lattice with partially occupied octahedral and tetrahedral sites. The distorted close packed layer can lead to intrinsic oxygen vacancies in $InVO_4$. The intrinsic vacancies and poor packing of lattice of $InVO_4$ can favor the ion movement in the lattice, which can be observed as ionic conduction at higher temperature. Distorted local coordination sphere around the In and V and increasing thermal parameters of anions with the increase in temperature as explained earlier are also likely to facilitate the ion movement in addition to the electronic contribution to the conductivities.

In order to further understand the conductivity process the dielectric parameters were derived from the impedance spectra recorded at different temperatures using the following relation.

$$\varepsilon^*(\omega) = \varepsilon' - i\,\varepsilon'' = 1/\,[G\, i\, \omega\, \varepsilon_0\, Z^*(\omega)] \qquad [7.1]$$

Where G = geometrical factor defined as A/l

A = Area and l = thickness of specimen

$i = \sqrt{-1}$

ω = angular frequency = $2\pi f$

ε_0 = permittivity of free space = 8.85×10^{-14} F/cm

$Z^*(\omega)$ = complex impedance = $Z' - iZ''$

The variations of real part of relative permittivity (ε') with frequency at selected temperatures are shown in **Fig.7.6 (a-c).** It is observed that ε' increases with

decreasing frequency as commonly observed in the normal dielectric materials[220]. However, in the frequency domain of 10 kHz to 1 MHz, the observed values of relative permittivity (ε′) is about 35 and they are almost independent of frequency and very feebly dependent on temperature (see insets in **Fig.7.6.a and b**). The higher values of relative permittivity observed at lower frequency can be attributed to the presence of different types of polarizations, namely, electronic, ionic, dipolar and space charge polarizations. However, as the frequency increases the contribution of only electronic polarization becomes effective and thus ε′ gradually decreases. The higher frequency dependency of the ε′ at the low frequency region is known as the low frequency dispersion (LFD) behavior, which is in general attributed to electrode polarization effects [129-130]. The low frequency end, frequency dependent ε′ can be explained as follows:

$\varepsilon' = A\ (\omega)^{-(1-p)}$ where A = pre exponential constant p is an exponent in the range of 0.1 to 0.2

Using the above relation, the frequency dependencies of ε′ at various temperatures were analyzed and are shown in **Fig.7.6.c**. The values of p are in the range of 0.2 to 0.3. The observed values are similar to the values expected for the ionic and dipole orientations. It is also observed that the values of p increase with the increase in temperature. Thus, it can be suggested that the ions migrate towards the electrode which in turn polarize the electrode and hence block the further movement of ions. This effect can cause a decreasing trend in conductivity with frequency. Such phenomena can be better observed from the deviation from the plateau region in *ac* conductivity data explained in latter section.

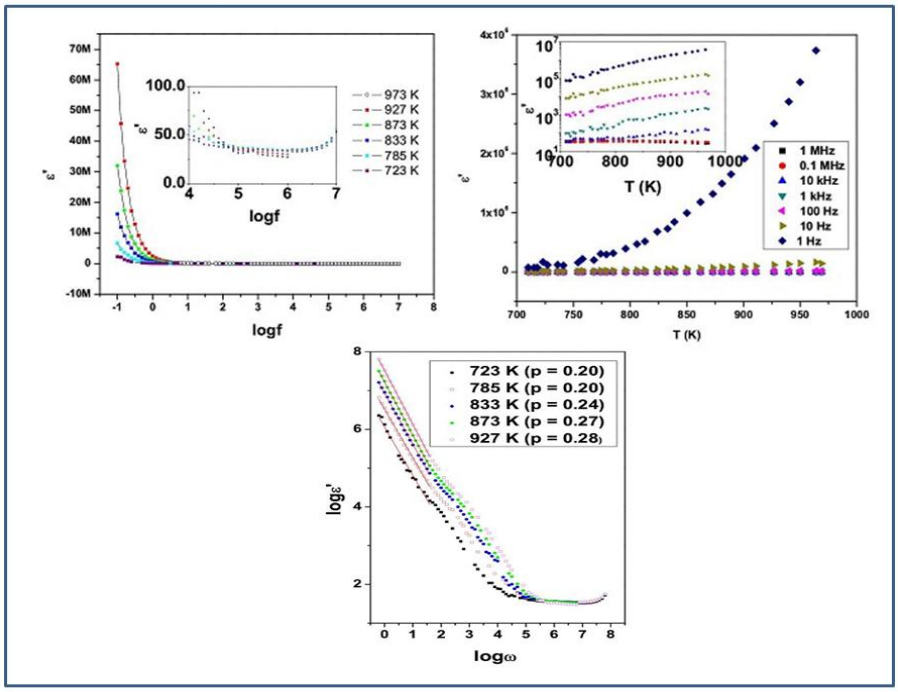

Fig.7.6: Variation of real part of relative permittivity with frequency (a), with temperature (b), the variation of logε′ with logω (c) (solid lines indicate the LFD behavior).

Further conclusions on the conduction behavior were obtained from the analyses of frequency and temperature dependent imaginary part of permittivity (ε″) data. The variation of ε″ with frequency and also with temperature are shown in **Fig.7.7(a and b)**. Similar to the variation of ε′, the ε″ also increases with the decreases in frequency which indicate higher loss at lower frequency. Besides, a rapid increasing trend of ε″ is observed at lower frequency and higher temperature. However, all curves in ε″ versus frequency are almost similar at all temperatures at the high frequency end. The loss at lower frequency can be assigned to both migration of ions and orientation of dipoles in the materials. However, the significant role of the temperature on the frequency dependent ε″ suggests an appreciable contribution from the translational motion of ions to the loss factor. Also the ε″ vs. frequency data indicate two humps in between the 100 Hz to 1 MHz due to the frequency dependent relaxation processes.

These features are clearly observed as two clear peaks in the variations of tanδ vs frequency (See inset in **Fig 7.7.a**). The peak frequency of the two relaxation process shifts towards the higher frequency side with the increase in temperature. By comparing with the real and imaginary impedance data of Cole-Cole plots, these two relaxation peaks (peak in tanδ) can be assigned to the grain and grain boundary phenomena. The increase in the relaxation peak (tanδ) with the increase in temperature further supports the ion migration process in $InVO_4$, which could be further supported from the analysis of *ac*- conductivity data.

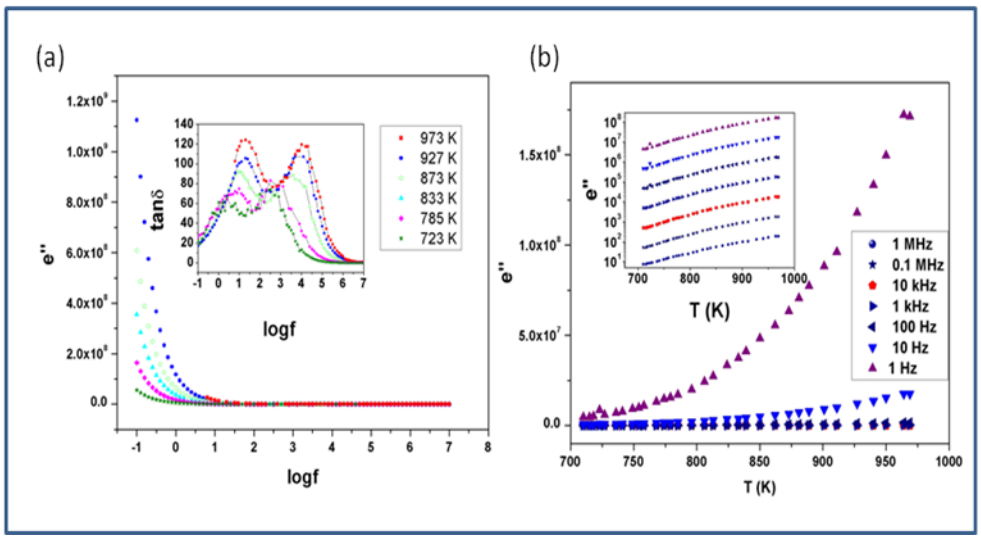

Fig.7.7: Variation of imaginary part of relative permittivities (ε″) with frequency (a) and with temperature (b). (Inset in (a) shows variation of tanδ with frequency).

The *ac* conductivity (σ^*_{ac}) data for $InVO_4$ were obtained from the complex permittivity (as $\sigma^*_{ac} = -i\ \omega\ \varepsilon^*$). The variations of σ′ with frequency at selected temperatures are shown in **Fig.7.8**. The *ac* conductivity (σ′) data of $InVO_4$ indicate a feebly frequency dependent plateau region in low frequency side which can be attributed to the *dc* contribution (σ_{dc}) to the conductivity, a deviation at the very low frequency due to the LFD phenomena and a non-linear deviation at high frequency

end as an universal dielectric behavior **(Fig. 7.8).** Also, it is observed that σ'_{ac} increases with the increase in temperature in a similar manner as the σ_{dc} shown in **Fig. 7.5.**

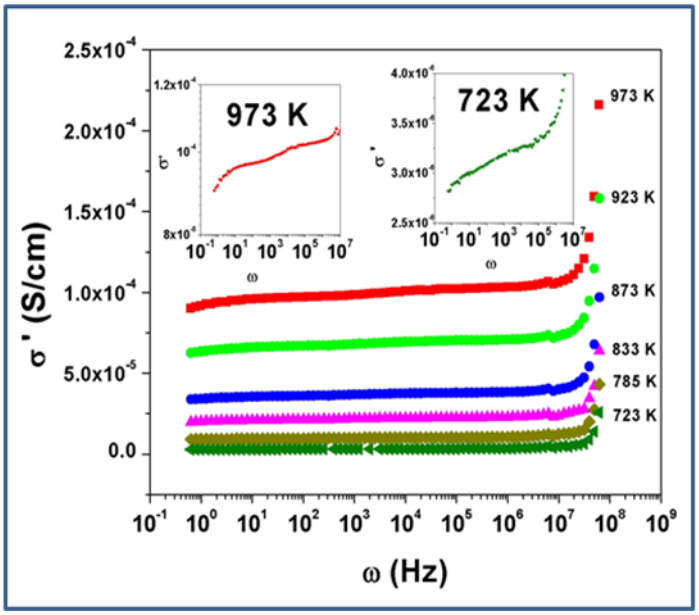

Fig.7.8: Variation of real part of ac- conductivities (σ′) with frequency at selected temperatures (expanded views indicating linear frequency dispersion (LFD) are shown as inset).

However, the onset of high frequency dispersion of σ′ remains almost similar in the temperature range of present study, which appears to have some resonating phenomena. The strong frequency dependency of σ'_{ac} at high frequency side is known as the universal dielectric dispersion of crystalline and amorphous ionic conductors and such behavior can be explained by Jonscher power law as

$$\sigma'_{ac} = \sigma_{dc} + A\,(\omega)^n \qquad [7.2]$$

Where σ_{dc} is frequency independent net conductivity (or dc conductivity) A is a constant n is a coefficient which governs the mode of conduction process. The constant A and n are in general representative of the frequency dependency of the conductivity and they are used as an indicator for the conductive mechanism. Usually the values of A are often small, in the order 10^{-10} or so in most of the cases.

Using the above relation and observed σ'_{ac} in between the frequency 10^5 to 10^6 Hz, the values of σ_{dc}, A and n were calculated for selected temperatures. The typical values of σ_{dc}, A and n are: 3.4×10^{-6} S/cm, 5.8×10^{-16} S/cm, 1.38 (at 723 K), 3.8×10^{-5} S/cm, 3.6×10^{-14} S/cm, 1.15 (at 873 K) and 1.1×10^{-4} S/cm, 4.2×10^{-10} S/cm, 0.59 (at 973 K). In general the values of n remain within 0.5 to 1.0, where the end values indicate disordered diffusion and ideal long range path of diffusion modes of conduction [221]. Thus, from the observed values of n it can be suggested the long range ideal diffusion process tends towards disordered hopping process with increase in temperature. The sharp divergence at higher frequency end region could not be explained by the above universal power law with the expected range of n values. In this high frequency end the values of n are observed to be in between 2.5 to 2.9, which are significantly larger than the expected values. Thus, the analyses of σ'_{ac} were restricted within 1 MHz.

7.4. Conclusions of the studies on $InVO_4$

Detailed structural analysis of orthorhombic-$InVO_4$ at ambient and high temperature revealed structural stability up to 1023 K, the maximum temperature of the present study. A smooth increasing trend in unit cell parameters and large increase in thermal parameters of various atoms are observed with increasing temperature. At ambient temperature $InVO_4$ shows significantly high resistance which decreases with the increase in temperature, and an appreciable conductivity is observed above 723 K. The detailed analysis of *ac* conductivity and complex dielectric properties with frequency and temperature revealed appreciable contribution of ion migration towards the conductivity at high temperature. Activation energy of about 0.87 eV is observed in bulk the $InVO_4$. The relative permittivity of about 35 is observed over a wider range

of frequencies and temperatures. The frequency dispersion studies indicate thermally activated hopping process in electrical and dielectric properties.

7.5. $CoFe_2O_4$ system

In order to study the effect of particle size and preparation dependent properties, a typical spinel type transition metal oxide, namely $CoFe_2O_4$ was considered for investigation. In general spinel-type oxides have been of known for their tunable electronic properties. The ferrite nanoparticles often exhibit moderate magnetization and high coercive field as well as higher chemical and structural stabilities. However, the magnetic and dielectric properties of ferrites are highly sensitive to their preparation conditions, sintering temperature and compositions. Spinel-type ferrites are considered as important materials relevant for modern electronic industry [222]. The selected example, meant to delineate the effect on both magnetic and electrical properties.

The cubic spinel-type $CoFe_2O_4$ has drawn significant attention for its remarkable magnetic properties at nano and bulk scale [222b]. $CoFe_2O_4$ crystallizes in an inverse spinel structure where the oxygen O^{-2} ions form FCC lattice and metal ions are distributed in tetrahedral and octahedral interstitial sites. It has been reported that nanocrystalline $CoFe_2O_4$ has a blocking temperature (T_B) 100 K higher and coercivity 50 times larger than those of similar sized Fe_3O_4 [223]. In addition, the saturation (M_s) and remanent magnetization (M_r) of $CoFe_2O_4$ also depend on the size, viz. both M_s and M_r increase with the size up to about 12 nm and then remain as almost constant. However, the coercive field (H_c) shows an increasing trend up to 12 nm and then it decreases due to surface anisotropy contribution. Maaz et al. [224] have prepared $CoFe_2O_4$ of different sizes by varying the annealing temperature and time and reported

large coercivity for smaller particles, viz. 12.5 kOe (for 28 nm), 14.5 kOe (for 3.8 nm). The maximum coercivity for 3.8 nm sized $CoFe_2O_4$ has been attributed to the increasing surface anisotropy and formation of partially inverted spinel structure.

Similar to magnetic properties, the electrical properties of $CoFe_2O_4$ also depend on the size, shape as well as preparation conditions. A number of reports explaining the electrical conductivity of nano- and bulk $CoFe_2O_4$ are available in literature [225]. Jonker [225a] has reported the electrical conductivity of bulk $CoFe_2O_4$ at higher temperature and suggested that the hopping of holes from Co^{2+} to Co^{3+} and electron from Fe^{2+} to Fe^{3+} contributes to their electrical properties. As the preparation methods drastically alter the morphology and structure of the materials, they are very likely to affect the dielectric properties of such materials. The size dependent dielectric properties reported by Sivakumar et al. [226] indicate two regions of electrical conduction for $CoFe_2O_4$, viz. low temperature region due to hole hopping in Co^{2+}-Co^{3+} and high temperature region due to electron hopping in Fe^{2+}-Fe^{3+} pairs.

Due to such interesting fundamental properties and technological relevancies, properties of crystalline cobalt ferrites prepared by a number of synthetic methods, like sol-gel, micro-emulsion, combustion, chemical co-precipitation, hydrothermal and forced hydrolysis, etc. has been investigated in several literatures. In this chapter the size dependent dielectric and magnetic properties of nano $CoFe_2O_4$ at lower temperature is presented.

7.6. Experimental of $CoFe_2O_4$

The $CoFe_2O_4$ sample was prepared by the salt assisted combustion synthesis method in a procedure similar to that reported by Zhang et al. [227]. $CoCO_3$ (Alfa, 99 %), $Fe(NO_3)_3.9H_2O$ (Alfa, 99 %), KCl (Alfa, 99 %) and glycine were used as the

starting materials for preparation. Initially, 0.01 mol of $CoCO_3$ and 0.02 mol of $FeCl_3$ were dissolved in 50 ml of 1:1 HNO_3:H_2O solution. To this solution 0.02 mol of KCl and 0.02 mol of glycine were added and then heated on a hot plate till the formation of a viscous gel. On further heating the gel auto-ignited and finally produced black powder. The product was boiled in de-ionized water, filtered, washed with de-ionized water and ethanol. The product was then dried at 333 K for 2h (Sample A). A part of the product was pressed into pellet and heated at 1173 K (Sample B). Both the samples were characterized by XRD, SEM, FTIR, dielectric spectroscopy, Mössbauer spectroscopy and SQUID magnetometry.

The powder XRD data of the samples were recorded in the two theta range of 10-80° on an X-pert Pro Powder X-ray diffractometer (Panalytical) using monochromatized Cu-Kα X-ray. Fourier Transform Infrared Spectra (FTIR) samples were recorded by using a Bomem FTIR spectrometer. Small amounts of sample was mixed with KBr and pressed to thin transparent pellets for IR spectroscopic studies. The temperature and field dependent magnetic properties of the samples were investigated by using SQUID magnetometer (Quantum Design, USA) in both field cooled (FC) and zero field cooled (ZFC) conditions. Mössbauer spectra (MS) at room temperature were recorded with a conventional spectrometer (Nucleonix Systems Pvt. Ltd., Hyderabad, India) operated in constant acceleration mode in transmission geometry with Co^{57} source in Rh matrix of 50 mCi. The calibration of the velocity scale was done by using an enriched ^{57}Fe metal foil. The isomer shift values are measured with respect to Fe metal foil (= 0.0 mm/s). For dielectric properties green pellets of nano powder and pellets sintered at 1173 K were used. The dielectric properties of the samples were studied at several frequencies using a Novocontrol

Alpha AN impedance analyzer and Quatro nitrogen cryosystem in the temperature range of 130 to 293 K. The surfaces of cylindrical pellets of the samples were coated with silver paste for better contact, and the pellets were sandwiched between two gold coated electrodes.

7.7. Results and discussions of $CoFe_2O_4$

7.7.1. XRD studies

The XRD patterns of both samples of $CoFe_2O_4$ are shown in **Fig.7.9.** The observed reflections of both samples are in agreement with the earlier reported data (JCPDF-22-1086). Single phasic nature of the samples were inferred from the absence of any additional unaccounted reflections in the XRD patterns. The average crystalline sizes of samples were calculated from the broadening of the intense (311) reflection by using Scherrer equation: $d = 0.9\ \lambda/(B\cos\theta)$, where λ = wavelength of x-rays, θ = Bragg angle and B = peak width at half-maximum. The average sizes of the as-prepared (A) and sintered (B) samples are 6 and 50 nm, respectively. The unit cell parameters as observed from the XRD data of A and B are 8.177(1) and 8.379(1) Å, respectively. The observed unit cell parameter for the sample B is close to that reported for bulk crystalline $CoFe_2O_4$, while that of A is appreciably lower than that expected. Earlier, Ferrera et Al. [228] have reported such lower values of unit cell parameters for Co rich cobalt ferrites. Thus a possibility of distributed spinel structure is expected for the sample A, which is further confirmed by FTIR and Mössbauer spectroscopy explained later in this chapter. Besides, a compressed structure with smaller unit cell parameters can also be a consequence of the smaller particle size and excessive contribution from strain as observed from the asymmetry of the XRD peaks

[229]. The SEM micrographs of the samples are shown in **Fig.7.10.** Appreciable sintering and grain growth is observed in the sintered sample

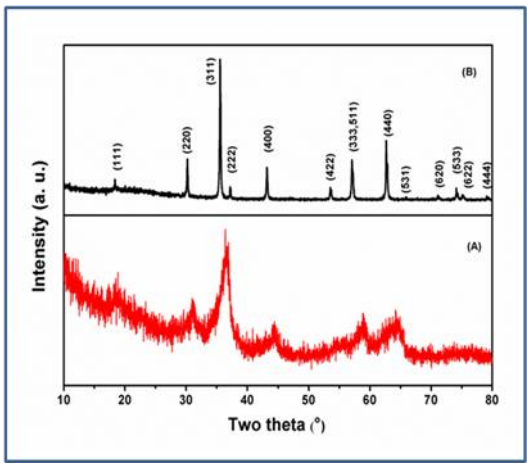

Fig.7.9: XRD pattern of $CoFe_2O_4$ samples (A) as-prepared and (B) sintered at 1173 K.

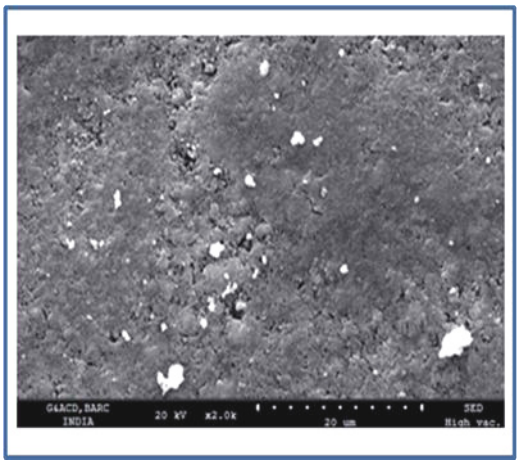

Fig.7.10: SEM micrographs of the sintered $CoFe_2O_4$.

7.7.2. IR studies

The characteristic IR absorption peaks of octahedral and tetrahedral groups of spinel lattice are often useful to characterize structure and cation distributions [230]. The tetrahedral and octahedral metal-oxygen groups are observed as two distinct stretching frequencies, namely at 650 cm^{-1} for tetrahedral group and 400 cm^{-1} for octahedral group [230]. Thus, the FTIR studies can give substantial information on the

nature of the tetrahedral and octahedral group cations. In the present experimental range no clear band for octahedral group is observed, due to experimental limitation of frequency range and thus the band due to the tetrahedral group is focused. Typical FTIR spectra recorded for both samples **(Fig.7.11.)** show distinct and clear absorption band around 600 cm^{-1} attributable to stretching vibration for the tetrahedral group. Incidentally the sample B show a clear single band at around 593 cm^{-1}, while the nano sample (A) it appeared as split band (580 cm^{-1} and 650 cm^{-1}). By comparison of these absorption bands it can be suggested the tetrahedral group in sample A is an admixture of Co^{2+} and Fe^{3+} in tetrahedral site. Due to the differences in force constants of Co^{2+}-O^{2-} and Fe^{3+}-O^{2-} bonds they appeared as two distinct bands.

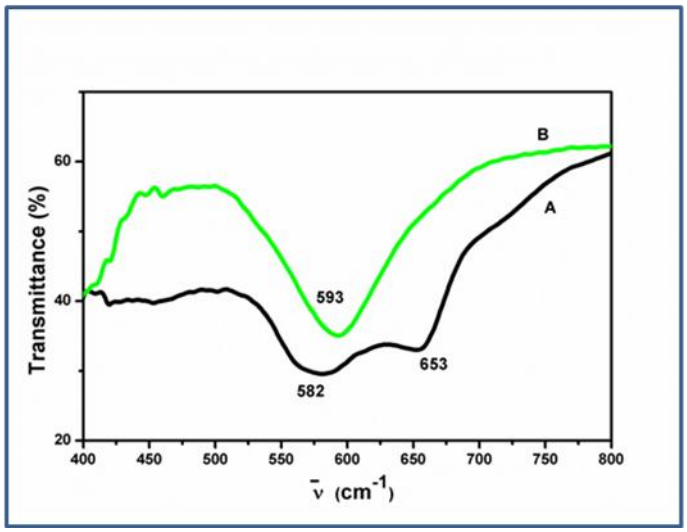

Fig.7.11: FTIR spectra of $CoFe_2O_4$ samples (A) as-prepared and (B) sintered at 1173 K.

7.7.3. Magnetic properties

In order to observe the effect of structural features on magnetic properties, the ZFC and FC magnetization are recorded and they are shown in **Fig. 7.12**. It can be seen from the figure that the FC magnetization of sintered sample (B) remains almost independent of temperature over a wider range of temperature while the ZFC trace

shows a decreasing trend with the decrease in temperature. The decreasing trend of ZFC can be explained by the variation of canting angle of the spins of tetrahedral and octahedral site which favor anti-parallel alignment of the ferrimagnetic $CoFe_2O_4$. Earlier studies on the $CoFe_2O_4$ sample indicate that the canting angle depends on the annealing temperature of the sample [231]. The sample annealed at significantly higher temperature leads to the perfect ferrimagnetic lattice, while the sample annealed at lower temperature shows a significant amount of canted structure contribution. Such effects will be more dominating in the measurements at lower applied field as in the present case (50 Oe). The FC and ZFC magnetizations of as-prepared sample-A are drastically different from that of the sample-B **(Fig.7.12).**

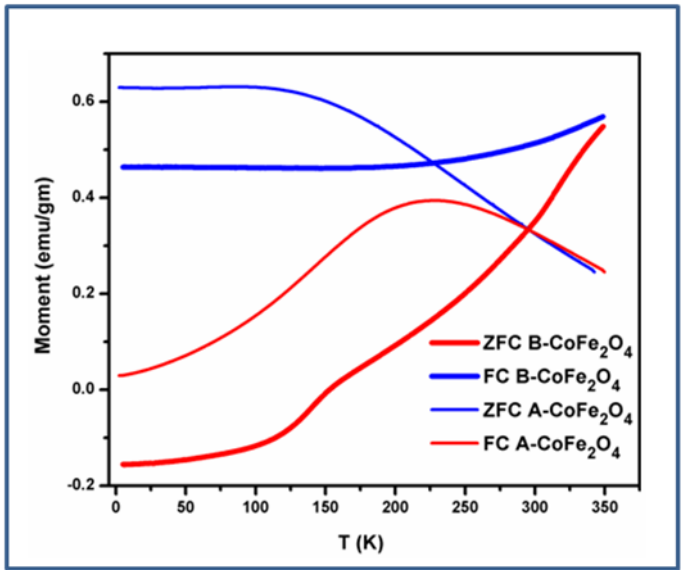

Fig.7.12: Temperature dependent ZFC and FC magnetization traces for $CoFe_2O_4$ samples. (A: as-prepared and B : sintered) (Applied field = 50 Oe).

The ZFC and FC magnetizations of sample-A appear to separate from 350 K onwards as in the case of sample-B. However, a broad maximum in ZFC magnetization around 225 K and continuously increasing trend in FC magnetization are observed in sample-A. Around 100 K, the FC magnetization of sample-A tends to saturate. However, the distribution of cations in the octahedral sites might result in the canted spin structure

and partial spin disorder structure. The variation of ordering of the spins with temperature is reflected in the ZFC behavior. In the magnetic nanoparticles the peak in ZFC varies with size which is an indication of the magnetic alignment. In addition, the trapped magnetic filed in solenoids are also effective in the ZFC magnetization behavior. In the present study size of sintered nanoparticle is 60 nm which is above the critical size. The decreasing magnetization at lower temperature is due to spin canting. However, this system needs more attention at higher temperature for more inferences. The differences in the magnetic behavior of the sample-A and B are further reflected in their M-H (hysteresis) loops recorded at different temperatures **(Fig.7.13**).

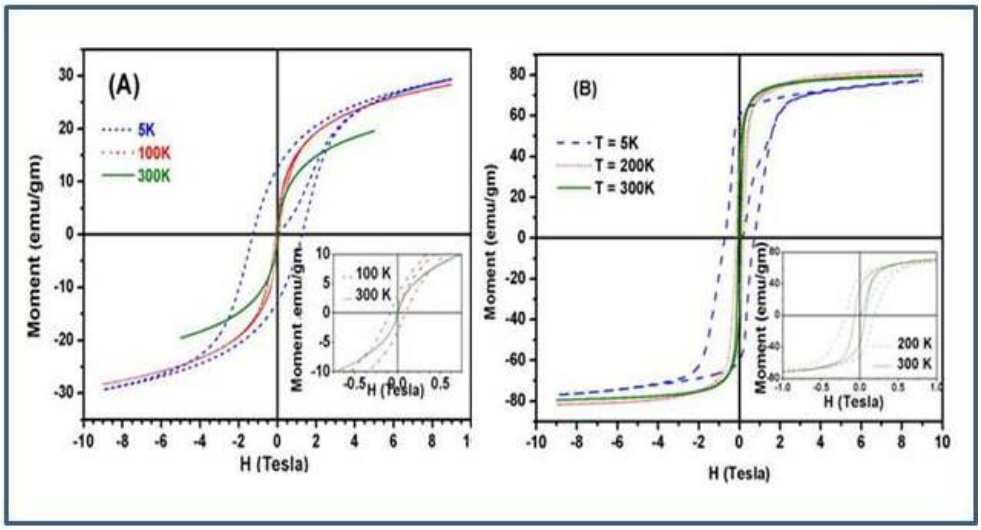

Fig.7.13: Magnetic hysteresis loops for $CoFe_2O_4$ samples at selected temperature. (A : as-prepared and B : sintered).

The M vs H data measured at 300 K shows no coercive field (H_c) and remanence magnetization (M_r) for sample-A, as in the case of a typical of super-paramagnetic materials. At 100 and 5 K, the observed H_c for sample-A are 88 and 1275 Oe, respectively. However, the observation of clear hysteresis loops at 300, 200 and 5 K suggest ferrimagnetic nature of the sample-B. At 300, 200 and 5 K, the observed

values of H_c are 66, 188 and 745 Oe, respectively. It can also be seen from the hysteresis loops that the magnetization of sample-A does not saturate completely even up to applied field of 8T. This suggests that an appreciable contribution from the canting of spins in the tetrahedral and octahedral cations or paramagnetic phase fraction towards magnetization of the as-prepared sample.However, the tendency towards saturation in the FC magnetization as well as the increasing trend of coercivity and remanence with decreasing temperature suggest the predominant effect of the spin canting than the paramagnetic phase fraction. It is important to note here that coercive field observed at 5 K for as prepared sample (A) is much higher than that observed for sintered sample. Since, the as-prepared sample has higher surface to volume ratio, they exhibit higher spin canting on the surface than that in core of the particles. The increasing role of surface anisotropy with the decrease in size of particles is reflected in higher coercive field. However, the saturation magnetization of sample–B (77emu/g) at 5 K is higher than that of the sample-A (30 emu/g). Similarly, the remanent magnetization of the sample B is 60 emu/g which is be higher than that of the sample A (13 emu/g). The reduced values of saturation and remanent magnetizations of sample-A are the consequence of higher canted spin contribution in it. In addition, higher surface area and surface energy of nano-samples can alter the cationic site preferences and exhibit higher degree of anti site defects, which in turn may render lower magnetization.

7.7.4. Mössbauer spectroscopic studies

Further the cationic structure and magnetic properties have been investigated by Mössbauer spectroscopy. Room temperature Mössbauer spectra of both A and B samples are shown in **Fig.7.14**. The Mössbauer spectrum of sample-A, is recorded at

two different velocities (higher velocity ± 11.0 and lower velocity ± 4.0 mm/s). No magnetic contribution is observed in sample-A (see higher velocity Mössbauer spectrum shown as inset of **Fig.7.14**, while clear magnetic interaction is observed in the sample-B. The Mössbauer spectrum for sample-A, recorded at low velocity scale is fitted with two symmetric paramagnetic doublets, whereas the Mössbauer spectrum of the sample-B is fitted with two magnetic sextets (Zeeman splitting) and one paramagnetic symmetric doublet. The analysis results of Mössbauer parameters like hyperfine magnetic field (H_{hf}), isomer shift (δ), quadrupole splitting (Δ), line width (Γ) and relative areas (R_A) in percentage of tetrahedral and octahedral sites of Fe ions are summarized in **Table7.1.**

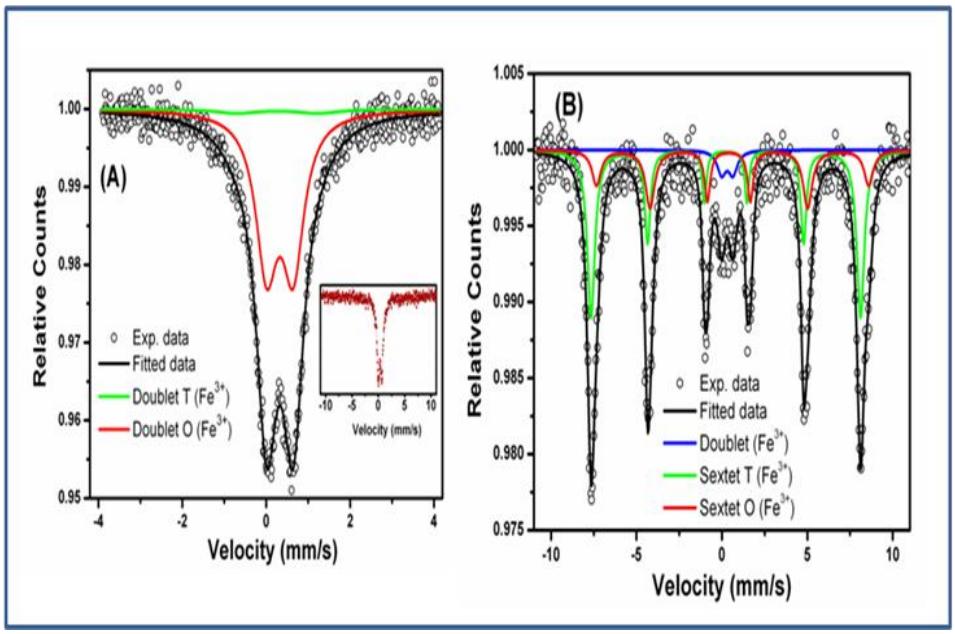

Fig.7.14: Ambient temperature Mossbauer spectra of $CoFe_2O_4$ samples. (A : as-prepared and B: Sintered).

$CoFe_2O_4$	Size	Unit cell parameter (Å)	Iron Sites	Hyperfine field (H_{hf}) (Tesla)	Isomer shift (δ) (mm/s)	Quadrupole splitting (Δ) (mm/s)	Line width (Γ) (mm/s)	Area R_A (%)
A	6 nm	8.177(1)	Doublet (tet.)	--	0.258 ±0.070	1.943 ±0.342	1.177 ±0.409	8.6
			Doublet B (oct.)	--	0.326 ±0.003	0.635 ±0.007	0.625 ±0.015	91.4
B	50 nm	8.379(1)	Doublet	--	0.314 ±0.021	0.664 ±0.035	0.621 ±0.072	5.5
			Sextet A (tet.)	48.90 ±0.02	0.222 ±0.009	0.012 ±0.016	0.304 ±0.059	54.2
			Sextet B (oct.)	49.39 ±0.09	0.515 ±0.023	0.218 ±0.042	0.405 ±0.053	40.3

Table 7.1: Summary of the results of structure and Mössbauer spectroscopic study of $CoFe_2O_4$ samples.

The two doublets with isomer shift (δ) values (relative iron metal foil) of 0.258 ±0.070 mm/s and 0.326 ±0.003 mm/s observed in the Mössbauer spectrum of sample-A are consistent with the high spin Fe^{3+} charge state [85b]. These values also support for the absence of Fe^{2+} ion in the sample as the Fe^{2+} ions show much higher δ value [232]. From the values of the observed isomer shifts, the smaller (0.258 mm/s) and larger (0.326 cm/s) δ can be assigned to tetrahedral (T) and octahedral (O) site Fe^{3+}, respectively. The values of quadrupole splitting ($\Delta E_Q = e^2qQ/4$) of the doublets corresponding to T and O sites are 1.943 ±0.342 mm/s and 0.635 ±0.007 mm/s, respectively. The line widths (Γ) of doublets A and doublet B are found to be ~ 1.177 ±0.409 and ~ 0.625 ±0.015 mm/s, respectively.

The relatively sharp lines of the doublet of sample-B at lower relative velocity indicate a positive EFG (electric field gradient) parameter. The values of ΔE_Q are often used as a measure of distortion and defects in local coordination around Fe [233]. The higher quadrupole splitting of the doublets corresponding to tetrahedral site of sample-A indicates distorted tetrahedra and larger crystal defects around Fe^{3+} ions. Further from the relative area (R_A) of doublet T (~ 8.6 %) and doublet O (~ 91.4%) it can be inferred that the structure of sample-A largely deviated from the expected inverse spinel structure of $CoFe_2O_4$. From the relative areas of two doublets the composition of nano sample can be written $(Co_{0.83}Fe_{0.17})_{tet}[Co_{0.17}Fe_{1.83}]_{oct}O_4$, which is close to a normal spinel structure, with a partial disorder.

The Mössbauer spectrum of sample-B (**Fig.7.14**) exhibits a superposition of two Zeeman sextets and a paramagnetic doublet. The two sextets (Zeeman patterns), corresponding to tetrahedral and octahedral sites indicate inverse spinel structure and ambient temperature ferrimagnetic nature of $CoFe_2O_4$. The isomer shift (δ) values (relative iron metal foil) of two sextets (T and O) are (δ_A) 0.222 ±0.009 mm/s and (δ_B) 0.515 ±0.023 mm/s, respectively. The corresponding values of hyperfine magnetic field (H_{hf}) for two sextets are 48.90 ±0.02 and 49.39 ±0.09 Tesla. From the values of δ and H_{hf}, the two sextets can be assigned to tetrahedral (T) and octahedral (O) Fe^{3+} ions. Also the presence Fe^{2+} in the sample B is ruled out from the observed δ values. The values of quadrupole splitting $\{\Delta(M) = (\Delta_{12}-\Delta_{56})/4\}$ and line width (Γ) for both tetrahedral (T) site and octahedral (O) site magnetic sextets are Δ_{tet}: 0.012 ±0.016, Γ_{tet}: 0.304 ±0.059 and Δ_{oct}: 0.218 ±0.042, Γ_{oct}: 0.405 ±0.053 mm/s, respectively. For the paramagnetic doublet, the quadrupole splitting $\Delta E_Q = e^2qQ/4$ (separation between two resonance lines), quadrupole splitting for magnetic sextet $\Delta(M) = (\Delta_{12}-\Delta_{56})/4$,

hyperfine magnetic field (H_{hf}), isomer shift (δ), line width (Γ) and relative areas (R_A) of tetrahedral and octahedral sites of Fe^{3+} ions. These values indicate that the tetrahedral site is having cubic symmetry whereas the octahedral site is having distortion. Apart from the sextets, Mössbauer spectrum of crystalline (sintered) sample shows a paramagnetic doublet with δ, ΔE_Q, Γ and R_A values are to be 0.314 ±0.021 mm/s, 0.664 ±0.035 mm/s, 0.621 ± 0.072 mm/s and 5.5%, respectively. The relative percentage of sextet to doublet patterns is found to be 94.5:5.5. These values indicate that the Fe^{3+} ions in high spin state are situated in distorted local lattice environments. The quadrupole splitting of the doublet is larger than that of the sextets. Thus, it can be suggested smaller fraction of the sample exist with incomplete magnetic structure. The analyses of the relative area (R_A) of the two sextets corresponding to the tetrahedral and octahedral sites and paramagnetic doublet (54.2, 40.3, and 5.5%) of the sample-B indicate the relative fractions of Fe^{3+} in tetrahedral and octahedral sites are ~54.2% and ~45.8%. (The δ value (0.314 ±0.021) of the doublet can be assigned to octahedral Fe^{3+}). Thus, the composition of sample-B can be written as $(Co_{0.00}Fe_{1.08})_{tet}[Co_{1.08}Fe_{0.92}]_{oct}O_4$, which is close to a complete inverse spinel structure.

7.7.5. Dielectric properties

In order to understand the differences in the dielectric and conductivity behavior of the sample-A and B, the complex dielectric properties were studied. Similar to the magnetic properties, the dielectric properties also show different behaviors in the sample-A and B. The variations of real part of relative permittivity (ε′) of both sample-A and B with temperature at selected frequencies are shown in **Fig. 7.15.** At all the frequencies, the relative permittivities of both samples show an increasing trend with the increase in temperature. A very weak peak like feature is

observed in the variation of ε′ vs. temperature for both sample-A and B, which moves towards higher temperatures with increasing frequency. However, in the sample-A such features could not be observed due to the large increase in ε′ at higher temperatures and larger conductivity. At 100 Hz, the observed relative permittivity for the sample-B is about 20 at 163K and increases to about 300 at 293 K. However, the relative permittivity of sample-A, increases drastically with the increase in temperature (ε′ = 20 at 163K and 6000 at 293K). Thus, the dielectric permittivity increases by an order with the decrease in crystallite size. This is probably due to the increase in the interfacial polarization caused by larger grain boundary between the much smaller grains as compared to the bulk sample. The frequency dependent relative permittivities of both the samples indicate a decreasing trend of permittivity of with the increase in frequency which is expected for a normal dielectric material

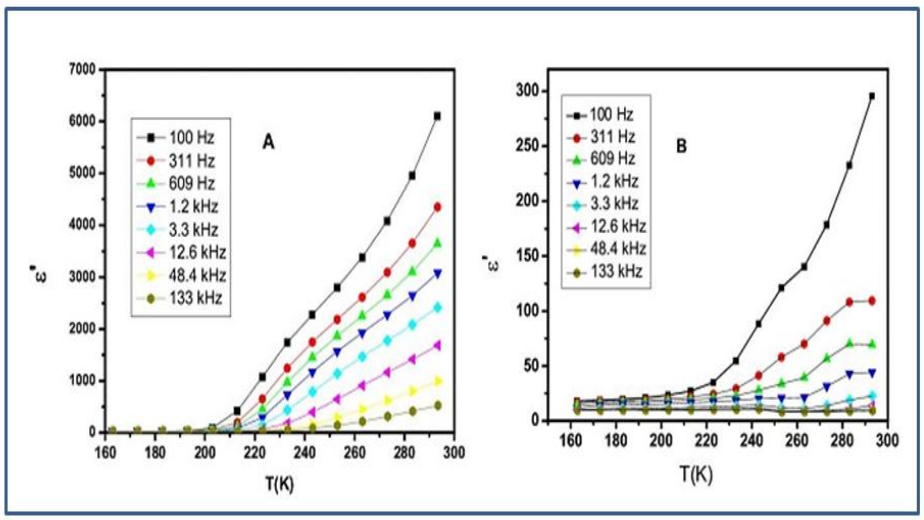

Fig.7.15: Variation of real part of relative permittivity with temperature in $CoFe_2O_4$ samples (A : as-prepared and B : sintered).

The *dc* conductivities for both the samples were extracted from the experimentally observed *ac*-conductivity at several temperatures and they are shown in **Fig. 7.16**. A sharp frequency-dependent increase in conductivity in the low frequency region can

be attributed to the contributions from the grain-boundaries. This is more clearly seen at the lower temperatures in the **Fig. 7.16**.

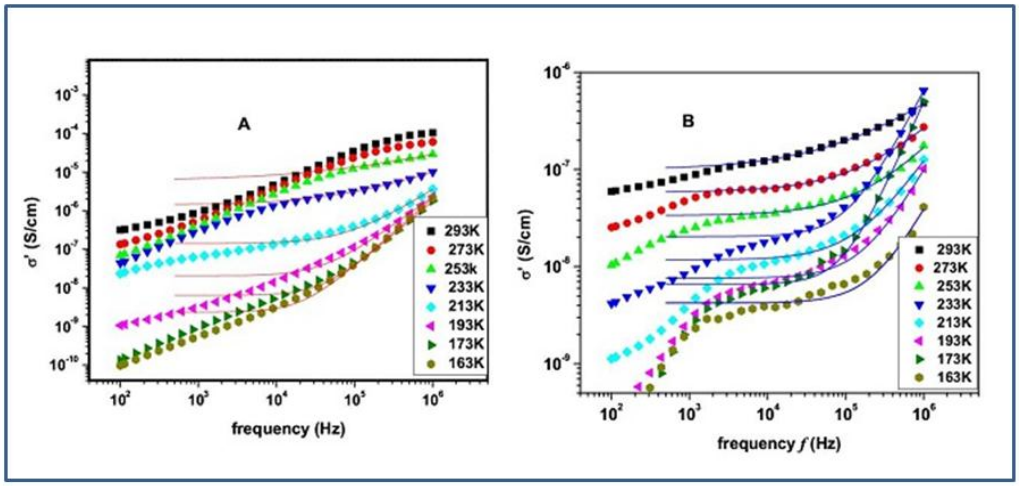

Fig.7.16: Conductivity spectra for $CoFe_2O_4$ samples. The solid lines are fit data according to the UDR model (A : as-prepared and B : sintered).

In the high frequency region, the *dc* conductivities are due to the bulk contribution and they are known to follow the universal dielectric response (UDR).

$$\sigma = \sigma_{dc} + \sigma_0^{UDR} f^s \qquad [7.3]$$

Where, σ_{dc}: bulk dc conductivity, σ_0^{UDR}: a constant, *f*: frequency and *s:* an exponent smaller than 1.

(Eq 7.3) is a common feature of all amorphous semiconductors and many materials exhibiting structural disorder [234].

The values σ_{dc}, σ_0 and *s* at different temperatures were extracted by fitting the *dc*-conductivities of high frequency end with (Eq. 7.3). The temperature dependence of σ_{dc} thus obtained was analyzed by fitting the data to the Arrhenius relation.

$$\sigma_{dc} = \sigma_1 \exp(-E_a / k_B T) \qquad [7.4]$$

Where σ_1, is a pre-exponential factor and E_a is the activation energy for hopping conduction. However, a much better fit was obtained using the Mott variable-range

hopping (VRH) behavior (Eq. 7.5) and they are shown in **Fig.7.17.**

$$\sigma_{dc} = \sigma_0 \exp[-(T_1/T)^{1/4}] \quad [7.5]$$

Where σ_0 and T_1 are constants.

In Eq.(7.5), T_1 is given by

$$T_1 = 24/[\pi k_B N(E_F)\xi^3] \quad [7.6]$$

where $N(E_F)$ is the density of localized states at the Fermi level, and ξ is the decay length of the localized wave function. The value of T_1 was 3.18×10^6 K for sample-B and 4.58×10^8 K for sample-A. The activation energy W at a particular temperature T is given by

$$W = 0.25 k_B T_1^{1/4} T^{3/4} \quad [7.7]$$

and the hopping range of polarons (R) is given by

$$R = \xi^{1/4}/[8\pi k_B N(E_F)T]^{1/4} \quad [7.8]$$

Using the values of T_1 obtained through fitting, the value of activation energy W for sample-A and B were calculated. The calculated values of W at 293 K are 0.22 eV and 0.06 eV for sample-A and B, respectively. The corresponding values of W at 130 K are 0.12 and 0.04 eV for sample-A and B, respectively.

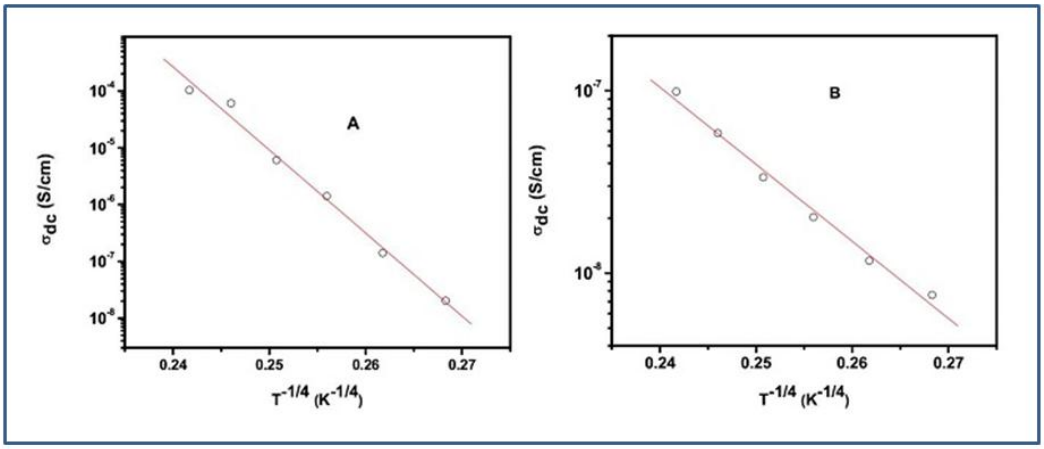

Fig.7.17: Temperature dependent dc conductivities of $CoFe_2O_4$ samples. Solid lines are fit to the data according to the Mott VRH relationship (A : as-prepared and B : sintered).

Assuming the value of ξ to be equal to the cation-cation distance for the octahedral sites in $CoFe_2O_4$, which is about 3 Å, the values of $N(E_F)$ for both compounds were calculated by using Eq.(7.6). The values of $N(E_F)$ were found to be 7.17×10^{18} eV/cm^3 for sample-A, and 1.03×10^{21}eV/cm^3 for sample-B. From (Eq. 7.8), the decay lengths R (at 293K) were found to be 28.5 Å for sample-A and 8.23 Å for sample-B.

It has been reported in literature that the low temperatures conductivity mainly arises from thermally assisted tunneling of polarons between localized states and they usually follow Mott variable range hopping (VRH) model [235]. In particular, the frequency dependent electrical conductivity of spinel type ferrites, has a direct correlation with hopping of carriers or polarons [236]. From the observed low temperature electrical properties of $CoFe_2O_4$, Mott VRH type polaronic conduction is concluded. The polarization and dielectric behavior of spinel type ferrites have been investigated in a number of studies [225a,234,236-237]. The dielectric polarization in ferrites has been in general attributed to the mechanism of conduction in them. The coexistence of Fe^{2+} and Fe^{3+} ions in the octahedral sites of spinel lattice can act as a source of polarization due to the local displacement of electrons [237]. Such displacement of electron cloud arises due to the hopping of electron from Fe^{2+} to Fe^{3+} ions and lead to their loss behavior and conductions process. The magnetic and Mössbauer spectroscopic studies of both the investigated $CoFe_2O_4$ systems of the present study indicate the absence of Fe^{2+} in the lattice. However, the distributions of the Fe^{3+} ions in the tetrahedral and octahedral sites are different in these two samples. As mentioned earlier the cation distribution in the samples-A and B are as: $(Co_{0.83}Fe_{0.17})_{tet}[Co_{0.17}Fe_{1.83}]_{oct}O_4$ and $(Co_{0.00}Fe_{1.08})_{tet}[Co_{1.08}Fe_{0.92}]_{oct}O_4$, respectively. The variation of cationic distribution acts as a local compositional inhomogeneity

which leads to local polar clusters. Thus, the presence of Co^{2+} and Fe^{3+} in the octahehedral sites are expected to form polarons in the lattice and they follow hopping conduction according to the VRH behavior. In the studied temperature range, the observed dc conductivity in sample-A is much larger than that in sample-B. This suggests formation of polaron is much easier in the nanocrystalline phase. Thus, it appears that the dc conductivity has a significant size dependency in such materials.

7.8. Conclusion of the studies on $CoFe_2O_4$

From the structural studies a nearly normal spinel type $CoFe_2O_4$ is observed for the as-prepared (6 nm) sample. The normal spinel structure transforms to complete inverse spinel structure on heating at high temperature. The temperature and field dependent magnetization studies revealed super paramagnetic nature of the for normal spinel type nano $CoFe_2O_4$ (6 nm), while ferrimagnetic with partial spin canting structure for sintered sample (50 nm). From the low temperature dielectric measurements, it is observed that both the samples show dielectric constant of about 20 in a wider temperature and frequency. Further, it is also observed that the dielectric constant increases with the decrease in particle size. The dielectric constants of both samples smoothly increase with the increase in temperature. The ac conductivity measurements suggest a polaron hopping process in both the studied samples.

CHAPTER 8
SUMMARY AND FUTURE SCOPE

8.1 Summary of the present thesis

The present thesis demonstrated the facile synthesis, characterization and property measurements of ion conducting and dielectric materials with fluorite and perovskite based oxides.

At first an introduction of basis of the research work carried on ionic and dielectric materials was briefly provided. Origin of importance of these materials for different applications is explained.

In the aim of fluorite based oxide ion conducting materials, a series of compositions $Ln_{1-x}Bi_xO_{1.5}$ ($0.0 \leq x \leq 0.5$), Ln= Dy and Yb were prepared by solid state reaction method. The products were characterized by XRD, SEM and Raman spectroscopy. $Dy_{1-x}Bi_xO_{1.5}$ system had three different phases, namely fluorite-type phase, a fluorite related rhombohedral and a feebly Bi doped rare-earth oxide phase. In $Yb_{1-x}Bi_xO_{1.5}$ system, all the compositions except x = 0.00, exist as composites of fluorite-type $Bi_{1-y}Yb_yO_{1.50}$ with y ~ 0.35 and feebly Bi^{3+} doped Yb_2O_3 compositions. In both the systems, conductivity increased with the Bi^{3+} concentration. Observed high ionic conductivity in $Dy_{0.5}Bi_{0.5}O_{1.5}$ was due to coexistence of fluorite-type phase of δ-Bi_2O_3 phase. In case of $Bi_{1-y}Yb_yO_{1.50}$ ($0.0 \leq x \leq 0.5$), an appreciably higher conductivity at relatively lower temperature with about 20 % of $BiO_{1.5}$ is observed in $YbO_{1.5}$. The enhancement of conductivity in such composites with lower concentration of Bi^{3+} is attributed to the easy diffusion of ions at the interface. The higher conductivity of the higher Bi^{3+} containing compositions is attributed to the increasing contribution of the F-type phase.

$A_2B_2O_7$ type compositions have been of great importance due to their interesting crystal chemistry and several technological applications. Two different

types of structures with $A_2B_2O_7$ compositions, viz. $Pr_2Zr_2O_7$ with pyrochlore-type structure and another $Pr_2Ti_2O_7$ with layered perovskite-type structure have been prepared and characterized in detail. The electrical properties of these materials have been investigated. Similar studies have also been carried out on Ca^{2+} substituted $Pr_2Zr_2O_7$. The maximum solubility of Ca^{2+} ions in $Pr_2Zr_2O_7$ is found to be about 5 at % at Pr^{+3} site. It is concluded that with increasing the Ca^{2+} content the activation energy for conduction increases and in turn the conductivity decreases. From the *dc*-conductivity measurements, an increasing electronic conductivity with increasing Ca^{2+} content is observed in Ca^{2+} doped $Pr_2Zr_2O_7$ system. A monoclinic perovskite-type structure with symmetry $P2_1$ is established for $Pr_2Ti_2O_7$. A partial decomposition at 1673 K is noticed in $Pr_2Ti_2O_7$. This material is found to be a ferroelectric with dielectric constant of 30-40 at ambient temperature. At higher temperature it also shows an increasing electronic conductivity.

Magnetism and dielectric properties in double perovskite-type complex oxides of rare-earth and transition metal oxides, namely Y_2CoMnO_6 (YCMO), Y_2NiMnO_6 (YNMO) and Eu_2CoMnO_6 (ECMO) were studied. The properties like magnetic transition temperature, magnetization as well as dielectric constants were found to depend on the valence state and oxygen defects in the structure. The magnetic transition temperatures of YCMO samples were found to depend on the preparation conditions while the Tc remains almost unchanged in YNMO samples. Contrast to the YNMO samples, the YCMO and ECMO samples showed the meta-magnetic like behavior. All samples showed the higher dielectric permittivity on annealing in air or oxygen atmosphere.

In order to get the larger electric energy density, hybrid organic-inorganic composites have also been studied. In this aspect, the M-PVDF (M=Co and Ni) were prepared. In both the composites remarkable increase in the amount of polar β phase of PVDF has been observed upon dispersion of metal nanoparticles in the PVDF matrix. In case of Ni-PVDF multiferroic materials coupling effect has been observed between the ferroelectric PVDF and magnetic cobalt. The drastic reduction of leakage current has been attributed to the presence of hydroxyl groups on the metal nanoparticle. The dielectric constant of the Co-PVDF composite increased significantly near the percolation threshold of filler metal nanoparticle in PVDF matrix, which has been explained by space charge polarization at the interfaces between metal nanoparticle and PVDF. In present thesis, magnetic and dielectric properties with respect to particle size were studied in spinel type $CoFe_2O_4$. Ferromagnetic behavior has been observed in larger size of crystallites and super paramagnetic behavior is observed in smaller size materials. Variable range polaron hopping conduction is observed in both samples. Electrical properties of orthorhombic $InVO_4$ have also been studied.

8.2. Future scope of the present thesis

Though the above interesting conclusions have been obtained in the present study, certain aspects need more exploration to further understand the subject matter of this study. The scope for the extension of this thesis work can be based on the two aspects, like ionic conducting and dielectric materials.

- In ionic conducing materials Bi_2O_3 doped rare earth oxide [M_2O_3 (M=Dy and Yb)] composites were studied. These materials should be studied for their

thermal stability in reducing atmosphere. The potential of these materials in IT-SOFC should be explored.

- To qualify the presodynum based pyrochlore compounds as electrode material for SOFC, new experiments on compatibility with anode and cathode materials need to be investigated. Also, sintering behavior, effect of grain size on the ionic conductivity can be studied.
- There is a need to control grain size and composition of the dielectric materials in ordered to maximize the dielectric properties. Therefore alternate preparation methods for synthesis of these materials should be attempted.
- Practical application of dielectric materials, which are synthesized in this thesis for capacitors, resonators and high energy density capacitor applications need to be explored.
- Attempts should be made to improve performance of the nanocomposites using several nanofillers.

1. (a) S. P. S. Badwal; F. T. Ciacchi; D. Milosevic, *Solid State Ionics* **2000,** *91*, 136; (b) V. V. Kharton; F. M. B. Marques; A. Atkinson, *Solid State Ionics* **2004,** *174*, 135.

2. (a) S. P. S. Badwal, *Solid State Ionics* **1992,** *52*, 23; (b) J. A. Kilner, *Solid State Ionics* **2000,** *129*, 1.

3. T. Takahashi; H. Iwahara; T. Arao, *J. Appl. Electrochem.***1975,** *5*, 187.

4. P. Shuk; H. D. Wiemhferb; U. Guth; W. Gijpeld; M. Greenblatt, *Solid State Ionics* **1996** *89*, 179.

5. (a) M. A. Subramanian; G. Aravamudan; G. V. S Rao, *Prog. Solid State. Chem.* **1983,** *15*, 55; (b) R. E. Williford; W. J. Weber; R. Devanathan; J. D. Gale, *J. Electro. Ceram.* **1999,** *3*, 409.

6. J. W. Schwank; M. Dibattista, *Mater. Res. Bull.* **1999**, 24, 44.

7. (a) A. F. Wells, *Structural Inorganic Chemistry*. 3rd edn OxfordPress;1962; (b) U. Muller, *inorganic structural chemistry* willey & sons ltd: 1993.

8. A. M. Glazer, *Acta Crystallogr. B* **1972,** *28*, 3384.

9. L. Malavasi; C. A. J. Fisher; M. S. Islam, *Chem. Soc. Rev.* **2010,** *39*, 4370.

10. R. Ramamoorthy; P. K. Dutta; S. A. Akbar, *J. Mater. Sci* **2003,** *38*, 4271.

11. (a) D. Yuan; F. A. Kroger, *J. Electrochem. Soc* **1969,** *116*, 594; (b) Y. K. Agarwal; D. W. Short; R. Gruenke; R. A. Rapp, *ibid* **1974,** *121*, 354.

12. K. E. Oberg; L. M. Friedman; W. M. Boorstein; R. A. Rapp, *Met. Trans.* **1973,** *4*, 75.

13. H. G. Scott, *J. Mater. Sci.* **1975** *10* 1527.

14. A. Lashtabeg; S. J. Skinner, *J. Mater. Chem.* **2006,** *16*, 3161.

15. (a) R. Devanathan; S. Thevuthasan; J. D. Gale, *Phys. Chem. Chem. Phys.* **2009,** *11*, 5506; (b) N. Sammes; A. Smirnova, *J. Power Sources* **2006,** *160*, 892.

16. S. C. Singhal; K. Kendall, *High Temperature Solid Oxide FuelCells: Fundmentals, Design, and Applications*. Elsevier Advanced Technology, Oxford,: UK,, 2003.

17. (a) H. Inaba; H. Tagawa, *Solid State Ionics* **1996,** *83*, 1; (b) M. Mogensen; N. M. Sammes; G. A. Tompsett, *Solid State Ionics* **2000,** *129*, 63; (c) N. M. Sammes; G. A. Tompsett; H. Nafe; F. Aldinger, *J. Eur. Ceram. Soc.* **1999,** *19*, 1801.

18. V. V. Kharton; E. N. Naumovich; A. A. Vecher, *J. Solid State Electrochem.* **1999,** *3*, 61.

19. J. Drennan; G. Auchterlonie, *Solid State Ionics* **2000,** *134*, 75.

20. M. Gaudon; E. Djurado; N. H. Menzler, *Ceram. Int.* **2004,** *30*, 2295.

21. (a) R. Doshi; L. Von Richards; J. D. Carter; X. Wang; M. J. Krumpelt, *Electrochem. Soc.* **1999,** *146*, 1273; (b) B. C. H.Steele, *Eur. Fuel Cell News* **2000,** *7*, 16.

22. V. V. Kharton; F. M. Figueiredo; L. Navarro; E. N. Naumovich; A. V. Kovalevsky; A. A. Yaremchenko; A. P. Viskup; A. Carniero; F. M. B. Marques; J. R. Frade, *J. Mater. Sci* **2001,** *36*, 1105.

23. S. Omar; E. D. Wachsman; J. C. Nino, *Solid State Ionics* **2008,** *178*, 1890.

24. (a) C. Kleinlogel; L. J. Gauckler, *Solid State Ionics* **2000,** *135*, 567; (b) T. Suzuki; I. Kosacki; H. U. Anderson, *Solid State Ionics* **2002,** *151*, 111.

25. (a) E. P. Murray; S. A. Barnett, *Solid State Ionics* **2001,** *143*, 265; (b) J. Zhang; Y. Ji; H. Gao; T. He; J. Liu, *J. Alloy. Compd.* **2005,** *395*, 1; (c) S. P. Jiang; W. Wang, *Solid State Ionics* **2005,** *176*, 1351.

26. J. M. Ralph; J. T. Vaughey; M. Krumpelt, *Electrochemical Society Proceedings, 2001-16, SOFC VII*, **2001**, 466.

27. (a) M. J. Verkerk; A. J. Burggraaf, *J. Electrochem. Soc.* **1981,** *128*, 75; (b) V. V. Kharton; E. V. Naumovich; A. A. Yaremchenko; F. M. B. Marques, *J. Solid State. Electrochem.* **2001,** *5*, 160.

28. (a) T. Takahashi; H. Iwahara; T. Esaka *J. Electrochem. Soc.* **1977,** *124*, 1563; (b) T. Takahashi ; H. Iwahara, *J. Appl. Electrochem.* **1973,** *3*, 65.

29. K. Fung; H. D. Back; A. Virkar, *Solid State Ionics* **1992,** *52*, 199.

30. (a) J. Y. Park; H. Yoon; E. D. Wachsman, *J. Am. Ceram. Soc.* **2005,** *88* 2402; (b) Y. J. Leng; S. H. Chan; K. A. Khor, *Electrochemical Society Proceedings, 2005-07, SOFC IX*, **2005**, 1110; (c) J.-Y. Park; E. D. Wachsman, *Electrochemical Society Proceedings, 2003-07, SOFC VII* **2003**, 289.

31. (a) H. M. T. Ishihara; Y. Takita, *J. Am. Chem. Soc.* **1994,** *116*, 3801; (b) T. Ishihara; Y. Hiei; Y. Takita, *Solid State Ionics* **1995,** *79*, 371.

32. J. W. Fergus, *J. Power Sources* **2006,** *162*, 30.

33. M. Yashima; K. Nomura; H. Kageyama; Y. Miyazaki; N. Chitose; K. Adach, *Chem. Phys. Lett.* **2003,** *380*, 391.

34. T. Ishihara; T. Shibayama; S. Ishikawa; K. Hosoi; H. Nishiguchi ; Y. Takita, *J. Eur. Ceram. Soc.* **2004,** *24*, 1329.

35. K. Huang; M. Feng; J. B. Goodenough; C. Milliken, *J. Electrochem. Soc.* **1997,** *144*, 3620.

36. J. B. Goodenough; J. E. Ruiz-Diaz; Y. S. Zhen, *Solid State Ionics* **1990,** *44*, 21.

37. K. Kakinuma; S. Machida; T. Arisaka; H. Yamamura; T. Atake, *Solid State Ionics* **2005,** *176* 2405.

38. K. Kakinuma; T. Arisaka; H. Yamamura; T. Atake, *Solid State Ionics* **2004,** *175*, 139.

39. G. A. Samara, *Phys. Rev.* **1976,** *13*, 4529.

40. (a) A. J. Bosman; E. E. Havinga, *Phys.Rev.* **1963,** *129*, 1593; (b) J. Fontenella; C. W. Andeen; D. Schuele, *Phys. Rev. B* **1972,** *6*, 582.

41. (a) C. Ramasastry; S. B. S. Sastry, *Solid state Physics Symposium, N.P.L.* **1965**; (b) C. Ramasastry; Y. V. G. S. Murthi, *J. Phys. chem. Solids* **1963,** *24*, 384; (c) G. A. Samara, *J. Phys. Chem. Solids* **1979,** *40* 509.

42. M. J. M. Rao. Kakatiya University 1977. Ph.D thesis, P154

43. L. W. Barr; A. B. Lidiard, *Defects in ionic crystals' in volume 10 of Physical chemistry , An advanced treatise* Academic Press.1968

44. X. Shan,. Auburn University 2009 Ph.D thesis.

45. M. M. Vijatovic; J. D. Bovic; B. D. Stojanovic, *Sci. Sinter.* 2008, *40*, 155

46. (a) A. Sasaki; T. Chiba; Y. Mamiya; E. Otsuki, *Jpn. J. Appl. Phys. Part* **1999,** *1(38)*, 5564; (b) T. Takenaka; K. I. Maruyama; K. Sakata, *Jpn. J. Appl. Phys. Part* **1991,** *1*, 2236.

47. (a) U. Bianchi; J. Dec; W. Kleemann; J. G. Bednorz, *Phys. Rev. B:Condens. Matter.* **1995,** *51*, 8737; (b) C. Ménoret; J. M. Kim; M. Dunlop; H. Dammark; O. Hernandez, *Phys. Rev. B:Condens. Matter.* **2002,** *65*, 224104; (c) R. Wang; Y. Inaguma; M. Itoh, *Mater. Res. Bull.* **2001,** *36*, 1693; (d) V. V. Lemanov; E.

P. Smirnova; P. P. Syrnikov; E. A. Tarakanov, *Phys. Rev. B: Condens. Matter.* **1996,** *52*, 3151.

48. A. Durán; E. Martínez; J. A. Díaz; J .M. Siqueiros, *J. Appl. Phys.* **2005,** *97*, 104109.

49. A. Tkach; M. P. Vilarinho; A. L. Kholkin, *Acta. Mater.* **2005,** *53*, 5061.

50. J. J. Zhang; J. W. Zhai; X. J. Chou; J. Shao ; X. Lu; X. Yao, *Acta. Mater.* (2009), 57, 4491

51. P. K. Panda, *J. Mater. Sci.* **2009,** *44*, 5049.

52. J. H. Koh; S. I. Khartsev; A. Grishin, *Appl. Phys. Lett.* **2000,** *77*, 4416.

53. H. Y. Park; J. Y. Choi; M. K. Choi; K. H. Cho; S. Nahm, *J. Am. Ceram. Soc.* **2008,** *91*, 2374.

54. (a) G. Goodman, *J. Am. Ceram. Soc.* **1953,** *36*, 368; (b) M. H. Francombe; B. Lewis; *Acta. Crystallogr.* **1958,** *11*, 696.

55. W. Kleemann; J. Dec; P. Lehnen; R. Blinc; B. Zalar; R. Pankrath, *Eur. phys. Lett.* **2002,** *57*, 14.

56. (a) E. Cavelli; G. Calestani; A. Belletti; E. Bovero, *J. Alloy. Compd.* **2008,** *451*, 143; (b) M. Bouziane; A. Benabad; J. C. Niepce; B. Elouadi, *Phys. Chem. News* **2008,** *44*, 133.

57. (a) T. Ukasiewicz; M. A. Swirkow icz; J. Dec; W. Hofman; W. Szyrski, *J. Cryst. Growth* **2008,** *310*; (b) W. H. Huang; D. Viehland; R. R. Neurgaonkar, *J. Appl. Phys.* **1994,** *76*.

58. S. P. Gaikwad; V. Samuelb; R. Pasrichac; V. Ravia, *Mater. Lett.* 2004, *58*, 3700

59. B. Aurivillius, *Ark. Kemi.* **1949,** *1*, 463

60. (a) B. H. Park; B. S. Kang; S. D. Bu; T. W. Noh; J. Lee; W. Jo, *Nature* **1999,** *401*, 682; (b) U. Chon; H. M. Jang; M. G. Kim; C. H. Chang, *Phys. Rev. Lett.* **2002,** *89*.

61. Z. Li; L. A. Fredin; P. Tewari; S. A. DiBenedetto; M. T. Lanagan; M. A. Ratner; T. J. Marks, *Chem. Mater.* **2010,** *22*, 10.

62. M. Arbatti; X. B. Shan; Z. Y. Cheng, *Adv. Mater.* **2007,** *19*, 1369.

63. Y. Bai; Z. Y. Cheng; V. Bharti; H. S. Xu; Q. M. Zhang, *Appl. Phys. Lett.* **2000,** *76*, 3804.

64. J. Yao; C. Xiong; L. Dong; C. Chen; Y. Lei; L. Chen; R. Li; Q. Zhu; X. Liu, *J. Mater. Chem.* **2009,** *19*, 2817.

65. H. X. Tang; Y. R. Lin; C. Andrews; H. A. Sodano, *Nanotechnology* **2011,** *22*, 015702.

66. J. W. Xu; C. P. Wong, *Appl. Phys. Lett.* **2005,** *87*, 082907.

67. (a) D. Bhadra; A. Biswas; S. Sarkar; B. K. Chaudhuri; K. F. Tseng; H. D. Yang, *J. Appl. Phys.* **2010,** *107*, 124115;(b) L. L. Sun; B. Li; Y. Zhao; G. Mitchell; W. H. Zhong, *Nanotechnology* **2010,** *21*, 305702; (c) M. N. Tchoul; S. P. Fillery; H. Koerner; L. F. Drummy; F. T. Oyerokun; P. A. Mirau; M. F. Durstock; R. A. Vaia, *Chem. Mater.* **2010,** *22*, 1749; (d) Y. Shen; Y. H. Lin; C. W. Nan, *Adv. Funct. Mater* **2007,** *17*, 2405; (e) Y. Shen; Y. H. Lin; M. Li, C. W. Nan, *Adv. Mater* **2007,** *19*, 1418.

68. G. Picci; M. Rabuffi, *IEEE Trans. Plas Sci.* **2002,** *30*, 1939.

69. G. A. Samara; E. L. Venturini, *Phase Transition* **2006,** *79*, 21.

70. G. A. Smolenskii, *J . Phys. Soc. Japan* **1970,** *28*, 26.

71. L. E. Cross, *Ferroelectrics* **1987,** *76*, 241.

72. D. Viehland; S. J. Jang; L. E. Cross, *J. Appl. Phys* **1990,** *68*, 2916

73. (a) D. L. Segal; Ed. R. J. Brook; *Materials Science and Technology: A Comprehensive Treatment Processing of Ceramics*. VCH Publishers: Weigheim 1996; (b) W. D. Kingery; H. K. Bowen; D. R. Uhlmann, *Introduction to Ceramics*. Wiley: New York 1976.

74. L. A. Chick; L. R. Pederson; G. D. Maupin; J. L. Bates; L. E. Thomas; G. J. Exarhos, *Mater. Lett.* **1990,** *10*, 6.

75. K. V. Damodaran; U. Selvaraj; K. J. Rao, *Mater. Res. Bull.* **1988,** *23*, 151.

76. S. R. Jain; K. C. Adiga; V. R. PaiVerneker, *Combust. Flame* **1981,** *40*, 71.

77. (a) B. D. Cullity, *Elements of X-ray diffraction*. Addison-Wilson Publishing Comp.Inc: U.S.A, **1959;** (b) H. P. Klug; L. E. Alexander, *X-ray diffraction procedures*. Wiley-Interscience Publication: New York 1974**.**

78. (a) P. W. Atkins, *Physical Chemistry*. Oxford University Press: London 1990; (b) T. Allen, *Particle Size Measurement,*. Chapman and Hall: London 1992.

79. (a) https://wiki.utep.edu/pages/viewpage.action?pageId=39195028(b)G. Vlaic; L.olivi,*Croat.Chem.Acta*2004**,***77*,427(c)https://www.bnl.gov/ps/nsls/industry/techniques/files/Spectroscopy_EXAFS.pdf

80. A. Vincent, *Molecular Symmetry and Group Theory*. 2nd Edn ed.; Wiley: UK, 2001.

81. D. R.Vij *Handbook of Applied Solid State Spectroscopy*. Springer: U.S.A 2006.

82. (a) D. A. Long, *The Raman Effect: A Unified Treatment of the Theory of Raman Scattering by Molecules* John Willey & Sons Ltd: 2002; (b) B. Schrader Ed, *Infrared and Raman Spectroscopy-Methods and Applications*

VCH VerlagsgesellschaftmbH, Weinheim (Germany) and VCH PublishersInc: NewYork, USA 1995; (c) G. Herzberg, *Molecular Spectra and Molecular Structure-II Infrared and Raman Spectra of Polyatomic Molecules*. D. Van Nostrand Company: USA, 1945.

83. (a) C. Duval, *Inorganic Thermogravimetric Analysis*. Elsevier: 1953; (b) P. D. Garn, *Thermoanalytical Methods of Investigations*. Academic Press: 1965.

84. M. D. Graef, *Introduction to Conventional Transmission Electron Microscopy*. Cambridge University Press:Cambridge, UK 2000.
(b)http://cnx.org/contents/ba27839d-5042-4a40-afcf-c0e6e39fb454@20.8:110

85. (a) G. K. Wertheim; *Mossbauer effect, principles and applications*. academic press: NewYork 1964; (b) N. N. Greenwood; T. C. Gibbs, *Mossbauer spectroscopy*. Chapman and hall: London 1971; (c) V. G. Bhide, *Mossbauer effect and its application.* Tata Mcgraw Hill new Delhi 1973. (d) M. D. Dyar, D. G. Agresti, M. W. Schaefer, C. A. Grant, and E. C. Sklute, *Annu. Rev. Earth. Planet. Sci.*, **2006**, 34, 83.

86. http://www.physics.utoronto.ca/~phy326/mos/mos.pdf.

87. L. G. Silen, *ARk. Kemi Mineral. Geol* **1937,** *12A*, 1.

88. G. Gattow; H. Schroder, *Z. Anorg. Allg. Chem.* **1962,** *318*, 176.

89. B. T. M. Willis, *Acta Crystallogr. B* **1965,** *18* 75.

90. P. D. Battle; C. R. A. Catlow; J. Drennan; A. D. Murray, *J. Phys.* **1983,** *C16*, L561.

91. H. A. Harwig, *Z. Anorg. Allg. Chem.* **1978,** *444*, 151.

92. S. Hull; S. T. Norberg; M. G. Tucker; S. G. Eriksson; C. E. Mohn; S. Stølen, *Dalton Trans.* **2009**, 8737.

93. T. Takahashi; T. Esaka; H. Iwahara, *J. Appl. Electrochem.* **1977,** *7*, 299.

94. I. Abrahams; A. J. Bush; S. C. M. Chan; F. Krok; W. Wrobel, *J. Mater. Chem.* **2001,** *11*, 1715.

95. P. P. Fedorov; M. V. Nazarkin; R. M. Zakalyukin, *Crystallogra. Rep.* **2002,** *47*, 281.

96. F. J. Manjón; D. Errandonea, *Phys. Status Solidi (B)* **2009,** *246*, 9.

97. A. L. J. Pereira; L. Gracia; D. Santamaría-Pérez; R. Vilaplana; F. J. Manjón; D. Errandonea; M. Nalin; A. Beltrán, *Phys. Rev. B* **2012,** *85*, 174108.

98. A. Watanabe, *J. Solid State Chem.* **1995,** *120*, 30.

99. (a) Y. Jinling; L. Jingkui; T. Weihua; S. Ying; C. Xiaolong; R. Guanghui, *J. Alloy. Compd.* **1997,** *252*, 143; (b) X. L. Chen; F. F. Zhang; Y. M. Shen; J. K. Liang; W. H. Tang; Q. Y. Tu, *J. Solid State Chem.* **1998,** *139*, 398; (c) M. Drache; S. Obbade; J. P. Wignacourt; P. Conflant, *J. Solid State Chem.* **1999,** *142*, 349.

100. M. Drache; P. Roussel; J. P. Wignacourt, *Chem. Rev.* **2007,** *107*, 80.

101. (a) S. Obbade; M. Drache; P. Conflant; E. Suard, *J. Solid State Chem.* **2001,** *162*, 10; (b) S. Obbade; M. Huve; E. Suard; M. Drache; P. Conflant, *J. Solid State Chem.* **2002,** *168*, 91; (c) X. L. Chen; W. Eysel; J. Q. Li, *J. Solid State Chem.* **1996,** *124*, 300; (d) R. Horyń; M. Wołcyrz; A. Wojakowski, *J. Solid State Chem.* **1995,** *116*, 68.

102. (a) C. Michel; V. Caignaert; B. Raveau, *J. Solid State Chem.* **1991,** *90*, 296; (b) Y. Li; T. P. Hutchinson; X. Kuang; P. R. Slater; M. R. Johnson; I. R. Evans, *Chem. Mater.* **2009,** *21*, 4661.

103. M. Wołcyrz; L. Kepiński; R. Horyń, *J. Solid State Chem.* **1995,** *116*, 72.

104. A. Watanabe, *Solid State Ionics* **1996,** *86-88*, 1427.

105. M. Drache; P. Roussel; P. Conflant; J. P. Wignacourt, *Solid State Sci.* **2005,** *7*, 269.

106. (a) H. T. Cahen; T. G. M. Van Den Belt; J. H. W. De Wit; G. H. J. Broers, *Solid State Ionics* 1980, *1*, 411; (b) P. D. Battle; C. R. A. Catlow; L. M. Moroney, *J. Solid State Chem.* 1987, *67*, 42.

107. M. Wołcyrz; R. Horyń; F. Bourée, *J. Phys. Condens. Matter* **1999,** *11*, 5757.

108. (a) N. Dilawar; S. Mehrotra; D. Varandani; B. V. Kumaraswamy; S. K. Haldar; A. K. Bandyopadhyay, *Mater. Charact.* **2008,** *59*, 462; (b) B. P. Mandal; V. Grover; M. Roy; A. K. Tyagi, *J. Am. Ceram. Soc.* **2007,** *90*, 2961.

109. F. D. Hardcastle; I. E. Wachs, *J. Solid State Chem.* **1992,** *97*, 319.

110. (a) A. Ubaldini; M. M. Carnasciali, *J. Alloy. Compd.* **2008,** *454*, 374; (b) Y. Repelin; C. Proust; E. Husson; J. M. Beny, *J. Solid State Chem.* **1995,** *118*, 163.

111. A. Rubbens; M. Drache; P. Roussel; J. P. Wignacourt, *Mater. Res. Bull.* **2007,** *42*, 1683.

112. (a) S. Venugopalan; A. K. Ramdas, *Phys. Rev. B* **1972,** *5*, 4065; (b) A. J. Salazar-Pérez; M. A. Camacho-López; R. A. Morales-Luckie; V. Sánchez-Mendieta; F. Ureña-Núñez; J. Arenas-Alatorre, *Superficiesy Vacío* **2005,** *18*, 4.

113. M. Drache; P. Roussel; J. P. Wignacourt; P. Conflant, *Mat. Res. Bull.* **2004,** *39*, 1393.

114. G. V. S. Rao; S. Ramdas; P. N. Mehrotra; C. N. R. Rao, *J. Solid State Chem.* **1970,** *2*, 377.

115. I. Kosacki; T. Suzuki; V. Petrovsky; H. U. Anderson, *Solid State Ionics* **2000,** *136-137*, 1225.

116. G. Y. Meng; Q. X. Fu; S. W. Zha; C. R. Xia; X. Q. Liu; D. K. Peng, *Solid State Ionics* **2002,** *148*, 533.

117. P. Gopalan; S. Saha; S. Bobade; A. Kulkarni, *J. Solid State Chem.* **2000,** *155*, 154.

118. H. L. Tuller, *Solid State Ionics* **2000,** *131*, 143.

119. L. G. Shcherbakova; L. G. Mamsurova; G. E. Sukhanova, *Russ. Chem. Rev.* **1979,** *48*, 228.

120. (a) H. Yan; H. Ning; Y. Kan; P. Wang; M. Reece, *J. Am. Ceram. Soc.* **2009,** *92*, 2270; (b) T. M. Pan; M. D. Huang; C. W. Lin; M. H. Wu, *Sensor and Actuat. B* **2010,** *144*, 139; (c) S. Nanamatsu; M. Kimura; K. Doi; S. Matsushita; N. Yamada, *Ferroelectrics* **1974,** *8*, 511; (d) Z. P. Gao; H. X. Yan; H. P. Ning; M. J. Reece, *Adv. Applied Ceramics* **2013,** *112*, 69; (e) N. A. Zakharov; V. S. Krikorov; E. F. Kustov; S. Y. Stefanovich, *Phys. Status Solidi A* **1978,** *50*, K13; (f) N. A. Zakharov; S. Y. Stefanovich; E. F. Kustov; Y. N. Venevtsev, *Krist. Tech* **1980,** *15*, 29; (g) D. W. Hwang; J. S. Lee; W. Li; S. H. Oh, *J. Phys. Chem .B* **2003,** *107*, 4963.

121. (a) Z. Hui; G. Nicolas; V. Francoise; P. Michele, *Solid State Ionics* **2003,** *160*, 317; (b) Q. A. Islam; S. Nag; R. N. Basu; *Mater. Res. Bull* **2013,** *48*, 3103; (c) S. N. Achary; S. K. Sali; N. K. Kulkarni; P. S. R. Krishna; A. B. Shinde; A. K. Tyagi, *Chem. Mater.* **2009,** *21*, 5848; (d) B. P. Mandal; R. Shukla; S. N. Achary; A. K. Tyagi, *Inorg. Chem.* **2010,** *49*, 10415; (e) H. Taguchi; R. Chiba; T. Komatsu; H. Orui; K. Watanabe; K. Hayashi *J. Power Sources* **2013,** *241*,

768; (f) M. Boaro; A. Trovarelli; J. H. Hwang; T. O. Mason, *Solid State Ionics* **2002,** *147* 85; (g) F. Esch; S. Fabris; L. Zhou; T. Montini; C. Africh; P. Fornasiero; G. Comelli; R. Rosei, *Science* **2005,** *309* 752; (h) Z. H. Xu; L. M. He; X. H. Zhong; J. F. Zhang; X. L. Chen; H. M. Ma; X. Q. Cao, *J. Alloy. Compd.* **2009,** *480* 220.

122. A. Doménech; N. Montoya; J. Alarcón, *J. Solid State Electrochem.* **2012,** *16*, 963.

123. (a) J. K. Gill; O. P. Pandey; K. Singh *Int. J. Hydrogen En.* **2012,** *37*, 3857; (b) B. J. Wuensch; K. W. Eberman; C. Heremans; E. M. Ku; P. Onnerud; E. M. E. Yeo; S. M. Haile; J. K. Stalick; J. D. Jorgensen, *Solid State Ionics* **2000,** *129* 111; (c) F. N. Sayed; D. Jain; B. P. Mandal; C. G. S. Pillai; A. K. Tyagi, *RSC. Adv.* **2012,** *2*, 8341.

124. (a) P. Holtappels; F. W. Poulsen; M. Mogensen, *Solid State Ionics* **2000,** *135*, 675; (b) X. L. Xia; J. H. Ouyang; Z. G. Liu, *J. Power Sources* **2009,** *189* 888.

125. (a) N. A. Dhas; K. C. Patil, *J. Mater. Chem.* **1993,** *3*, 1289; (b) F. Fu-kang; A. K. Kuznetsov; K. Keler; I. V. Grebenshchikov, *Izv. Akad. Nauk SSSR, Ser. Khim.* **1965,** *4* 585.

126. (a) M. Glerup; O. F. Nielsen; F. W. Poulsen, *J. Solid State Chem.* **2001,** *160*, 25; (b) M. T. Vandenborre; E. Husson; J. P. Chatry, *J. Raman Spect.* **1983,** *14* 63.

127. (a) J. Nair; P. Nair; G. B. M. Doesburg; J. G. Van Ommen; J. R. H. Ross; A. J. Burggraaf; F. Mizukam, *J. Am. Ceram. Soc.* **1999,** *82*, 2066; (b) D. Errandonea; R. S. Kumar; S. N. Achary; O. Gomis; F. J. Manjon; R. Shukla; A. K. Tyagi, *J. Appl. Phys.* **2012,** *111* 053519.

128. S. Kramer; M. Spears; H. L. Tuller, *Solid State Ionics* **1994,** *72* 59.

129. A. K. Jonscher, *J. Phys. D: Appl. Phys.* **1999,** *32*, R57.

130. S. R. Elliott, *Solid State Ionics* **1988,** *27* 131.

131. L. Sun; L. Ju; H. Qin; M. Zhao; W. Su; Hu, *J. Physica B* **2013,** *431*, 49.

132. (a) P. A. Kozmin; N. A. Zakharov; M. D. Surazhskaya, *Inorg. Mater.* **1997,** *33*, 850; (b) N. Ishizawa; F. Maruo; S. Iwai; M. Kimura; T. Kawamura, *Acta Crvst. B* **1980,** *36*, 763.

133. (a) K. Scheunemann; H. Mueller-Buschbaum, *J. Inorg. Nucl. Chem.* **1975,** *37*, 1879; (b) K. Scheunemann; H. Mueller-Buschbaum, *J. lnorg. Nucl. Chem.* **1974,** *36*, 1965.

134. E. J. Harvey; S. E. Ashbrook; G. R. Lumpkin; S. A. T. Redfern, *J. Mater. Chem.* **2006,** *16*, 4665.

135. N. Ishizawa; F. Marumo; S. I. Iwai, *Acta Cryst. B* **1982,** *38*, 368.

136. N. Ishizawa; K. Ninomiya; T. Sakakura; J. Wang, *Acta. Cryst. E* **2013,** *69*, i19.

137. J. M. Pruneda; E. Artacho, *Phys. Rev. B* **2005,** *72*, 085107.

138. Z. L. Zhang; H. Y. Xiao; X. T. Zu; F. Gao; W. J. Weber, *J. Mater. Res.* **2009,** *24*, 1335.

139. H. Y. Xiao; L. M. Wang; X. T. Zu; J. Lian; R. C. Ewing, *J. Phys.: Condens. Matter.* **2007,** *19*, 346203.

140. E. Bruyer; A. Sayede, *J. Appl. Phys.* **2010,** *108*, 053705.

141. G. Herreraa; J. Jiménez-Mierc; E. Chavira, *Mater. Charact.* **2014,** *89*, 13.

142. V. V. Atuchin; T. A. Gavrilova; J. C. Grivel; V. G. Kesler; I. B. Troitskaia, *J. Solid State Chem.* **2012,** *195*, 125.

143. S. Saha; S. Prusty; S. Singh; R. Suryanarayanan; A. Revcolevschi; A. K. Sood, *J. Solid State Chem.* **2011,** *184*, 2204.

144. A. Schönhals; F. Kremer, *Broadband Dielectric Spectroscopy*. Springer Verlag Berlin, 2003

145. C. C. Wang; H. B. Lu; K. J. Jin; G. Z. Yang, *Phys. Lett. B* **2008,** *22*, 1297.

146. J. Zhang; W. Peng; Z. Chen; H. Chen; L. Han, *J. Phys. Chem. C* **2012,** *116*, 19182.

147. (a) M. Fiebig; T. Lottermoser; D. Fröhlich; A. V. Goltsev; R. V. Pisarev, *Nature* **2002,** *419*, 818; (b) S. W. Cheong; M. Mostovoy, *Nat. Mater.* **2007,** *6*, 13; (c) T. Kimura; T. Goto; H. Shintani; K. Ishizaka; T. Arima; Y. Tokura, *Nature* **2003,** *426*, 55; (d) R. Ramesh; N. A. Spaldin, *Nat. Mater.* **2007,** *6*, 21; (e) W. Prellier; M. P. Singh; P. Murugavel, *J. Phys.: Condens. Matter.* **2005,** *17*, R803.

148. (a) N. S. Rogado; J. Li; A. W. Sleight; M. A. Subramanian, *Adv. Mater.* **2005,** *17*, 2225; (b) J. F. Scott, *Ferroelectr. Rev.* **1998,** *1*, 1.

149. (a) R. I. Dass; J. -Q.Yan; J. B. Goodenogh, *Phys. Rev. B* **2003,** *68*, 064415; (b) R. I. Dass; J. B. Goodenough, *Phys. Rev. B* **2003,** *67*, 014401; (c) G. Blasse, *J. Phys Chem Solids* **1965,** *26*, 1969.

150. (a) F. N. Sayed; S. N. Achary; O. D. Jayakumar; S. K. Deshpande; P. S. R. Krishna; S. Chatterjee; P. Ayyub; A. K. Tyagi, *J. Mater. Res.* **2011,** *26*, 567; (b) P. A. Joy; Y. B. Khollam; S. K. Date, *Phys. Rev. B* **2000,** *62*, 8608; (c) F. N. Sayed; S. N. Achary; S. K. Deshpande; B. Rajeswari; R. M. Kadam; S. Dwebedi; A. K. Nigam; A. K. Tyagi, *Z. Anorg. Allg. Chim.* 2014, *640*, 1907.

151. (a) M. P. Singh; C. Grygiel; W. C. Sheets; Ph. Boullay; M. Hervieu; W. Prellier; B Mercey; Ch. Simon; B. Raveau, *Appl. Phys. Lett.* **2007,** *91*, 012503; (b) S. N. Barilo; V. I. Gatal'Skaya; S. V. Shiryaev; L. A. Kurochkin; R. Shimchak; M. Baran, *Low Temp. Phys.* **2002,** *28*, 853; (c) A. J. Bańon-Gonzźalez; C. Frontera; J. L. Garćıa-Mũnoz; B. Rivas-Murias; J. Blasco, *J. Phys.: Condens. Matter.* **2011,** *23*, 496003; (d) S. Yáñez-Vilar; M. Sánchez-Andújar; J. Rivas; M. A. Señarís-Rodríguez, *J. Alloy Compd.* **2009,** *485*, 82.

152. I. O. Troyanchuk; N. V. Samsonenko; A. Nabiaiek; H.Szymczak, *J. Magn. Magn. Mater.* **1997,** *168***,** 309.

153. Y. Q. Lin; X. M. Chen, *J. Am. Ceram. Soc.* **2011,** *94*, 782.

154. R. J. Booth; R. Fillman; H. Whitaker; A. Nag; R. M. Tiwari; K. V. Ramanujachary; J. Gopalakrishnan; S. ELofland, *Mater. Res. Bull.* **2009,** *44*, 1559.

155. I. O. Troyanchuk; N. V. Samsonenko; N. V. Kasper; H. Szymczak; A. Nabialek, *J. Phys.: Condens. Matter.* **1997,** *9*, 8287.

156. S. Kumar; G. Giovannetti; J. Van den Brink; S. Picozzi, *Phys. Rev. B* **2010,** *82*, 134429.

157. R. P. Maiti; S. Dutta; M. Mukherjee; M. K. Mitra; D. Chakravorty, *J. Appl. Phys.* **2012,** *112*, 044311.

158. (a) G. Sharma; J. Saha; S. D. Kaushik; V. Siruguri; S. Patnaik, *Appl. Phys. Lett.* **2013,** *103*, 012903; (b) I. O. Troyanchuk; D. D. Khalyavin; J. W. Lynn; R. W. Erwin; Q. Huang; H. Szymczak; R. Szymczak; M. Baran, *J. Appl. Phys.* **2000,** *88*, 360; (c) J. KrishnaMurthy; K. Devi Chandrasekhar; H. C. Wu; H. D. Yang; J. Y. Lin; A Venimadhav, *arxiv: Cond-Mat.*, 1407.8276.

159. A. P. Sazonov; I. O. Troyanchuk; V. V. Sikolenko; H. Szymczak; K. Bärner, *Phys. Stat. Sol. B* **2007,** *244*, 3367.

160. A. N. Vasiliev; O. S. Volkova; L. S. Lobanovskii; I. O. Troyanchuk; Z. Hu; L. H. Tjeng; D. I. Khomskii; H. -J. Lin; C. T. Chen; N. Tristan; F. Kretzschmar; R. Klingeler; B. Büchner, *Phys. Rev. B* **2008,** *77*, 104442.

161. (a) N. Kumar; A. Sundaresan, *Solid State Commun.* **2010,** *150*, 1162; (b) Y. Ren; T. T. M. Palstra; D. I. Khomskii; A. A. Nugroho; A. A. Menovsky; G. A. Sawatzky, *Phy. Rev. B* **2000,** *62*, 6577.

162. (a) J. Baier; S. Jodlauk; M. Kriener; A. Reichl; C. Zobel; H. Kierspel; A. Freimuth; T. Lorenz, *Phy. Rev. B* **2005,** *71*, 014443; (b) M. A. Korotin; S. Y. Ezhov; I. V. Solovyev; V. I. Anisimov; D. I. Khomskii; G. A. Sawatzky, *Phys. Rev. B: Condens. Matter Mater. Phys* **1996,** *54*, 5309.

163. M. P. Singh; K. D. Truong; S. Jandl; P. Fournier, *J. Appl. Phys* **2010,** *107*, 09D917.

164. (a) H. Z. Guo; A. Gupta; J. Zhang; M. Varela; S. J. Pennycook, *Appl. Phys. Lett.* **2007,** *91*, 202509; (b) M. R. Ibarra; R. Mahendiran; C. Marquina; B. García-Landa; J. Blasco, *Phys. Rev. B: Condens. Matter Mater. Phys.* **1998,** *57*, R3217.

165. V. A. Khomchenko; I. O. Troyanchuk; A. P. Sazonov; V. V. Sikolenko; H. Szymczak; R. Szymczak, *J. Phys.: Condens. Matter.* **2006,** *18*, 9541.

166. A. Kichizo; F. Kouji; N. Nobuhiko; S. Yasumasa; K. Yoshihiko; M. Moriji, *J. Phys. Soc. Jpn.* **1998,** *67*, 4218.

167. I. M. Hodge; M. D. Ingram; A. R. West, *J. Electroanal. Chem.* **1976,** *74*, 125.

168. Y. Q. Lin; X. M. Chen, *Appl. Phys. Lett.* **2010,** *96*, 142902.

169. M. Mouallem-Bahouta; T. Roisnela; G. Andreb; C. Mourec; O. Penaa, *J. Solid State Chem.* **2007,** *180*, 1737.

170. S. S. Yánez-Vilar; M. Sánchez-Andújar; J. Rivas; M. A. Se˜narís-Rodríguez *J. Alloy. Compd.* **2009,** *485*, 82.

171. M. E. Fleet, *J. Solid State Chem.* **1986,** *62*, 75.

172. J. B. Goodenough; A. Wold; R. J. Arnott ; N. Menyuk, *Phys. Rev. B* **1961,** *124*, 373.

173. (a) W. Z. Yang; X. Q. Liu; H. J. Zhao; Y. Q. Lin; X. M. Chen, *J. Appl. Phys.* **2012,** *112*, 064104; (b) Y. Guo; L. Shi; S. Zhou; J. Zhao; W. Liu, *Phys. Lett.* **2013,** *102*, 222401.

174. W. J. Sarjeant; J. Zirnheld; F. W. MacDougall, *IEEE Trans.* **1998,** *26*, 1368.

175. (a) J. B. Lando; H. G. Olf; A. J. Peterlin, *Polym. Sci., Part A-1* **1966,** *4*, 941; (b) K. Tashiro; H. Tadokoro; M. Kobayashi, *Ferroelectrics* **1981,** *32*, 167; (c) M. Kobayashi; K. Tashiro; H. Tadokoro, *Macromolecules* **1975,** *8*, 158; (d) S. L. Hsu; F. J. Lu; D. A.Waldman; M. Muthukumar, *Macromolecules* **1985,** *18*, 2583.

176. M. A. Bachmann; W. L. Gordon; J. L. Koenig; J. B. Lando, *J. Appl. Phys. Lett.* **1979,** *50*, 6106.

177. (a) P. Kim; N. M. Doss; J. P. Tillotson; P. J. Hotchkiss; M. -J. Pan; S. R. Marder; J. Li, J. P. C.; J. W. Perry, *ACS Nano* **2009,** *3*, 2581; (b) J. Yao; C .Xiong; L. Dong; C. Chen; Y. Lei; L. Chen; R. Li; Q. Zhu; X. Liu, *J. Mater. Chem.* **2009,** *19*, 2817; (c) L. J. Romasanta; P. Leret; L. Casaban; M. Hernandez; M. A. De la Rubia; J. F. Fernandez; J. M. Kenny; M. A. Lopez-Manchado; R. Verdejo, *J. Mater. Chem.* **2012,** *22*, 24705.

178. Z. M. Dang; Y. H. Lin; C. W. Nan, *Adv. Mater.* **2003,** *15*, 1625.

179. (a) Q. Huang; M. Su. Zhang, *J. Appl. Phys. Lett.* **2003,** *82*, 3502; (b) X. Huang; P. Jiang; L.Xie, *Appl. Phys. Lett.* **2009,** *95*, 242901; (c) S. Ricardo; S. Jaime; V. Richard; S. Vitor; C. Pedro; G. Joao; L. M. Senentxu, *Nanotechnology* **2009,** *20*, 035703; (d) F. He; S. Lau; H. L. Chan Fan, *J. Adv. Mater.* **2009,** *21*, 710.

180. S. Saidi; B. Mouna; M. Aymen; G. Fethi; D. Hassen; M. Abdellatif, *J. Phys. D: Appl. Phys.* **2013,** *46*, 355101.

181. Z. M. Dang; L. Wang; Y. Yin; Q. Zhang; Q. Lei, *Adv. Mater.* **2007,** *19*, 852.

182. D. Yang; H. Xu; J. Wang; Y. Wu, *J. Appl. Polym. Sci.* **2013**, DOI: 10.1002/APP.39645

183. M. Panda; V. Srinivas; A. K. Thakur, *Appl. Phys. Lett.* **2011,** *99*, 042905.

184. S. Ansari; E. P. Giannelis, *J. Polym. Sci. Part B: Polym. Phys.* **2009,** *47*, 888.

185. (a) A. K. Zak; W. C. Gan; W. H. A. Majid; M. Darroudi; T. S. Velayutham, *Ceram. Int.* **2011,** *37*, 1653; (b) L. Yu; P. Cebe, *Polymer* **2009,** *50*, 2133.

186. (a) A. Bello; E. Laredo; M. Grimau, *Phy. Rev. B* **1999,** *60*, 12764; (b) K. P. Pramoda; A. Mohamed; I. Y. Phang; T. Liu, *Polym. Int.* **2005,** *54*, 226.

187. H. P. Xu; Z. M. Dang; N. C. Bing; Y. H. Wu; D. D. Yang, *J. Appl. Phys.* **2010,** *107*, 034105.

188. X. Liyan; H. Xingyi; W. Chao; J. Pingkai, *J. Mater. Chem.* **2011,** *21*, 5897.

189. W. Tingting; L. Weiping; L. Laihui; Z. Yuejin, *Appl. Phys. Lett.* **2013,** *102*, 092904.

190. C. W. Nan, *Phys. Rev. B* **1994,** *50*, 6082.

191. H. Kawai, *Jpn. J. Appl. Phys.* **1969,** *8*, 975.

192. A. Hiroki; J. A. LaVerne, *J. Phys. Chem. B* **2005,** *109*, 3364.

193. Z. Hengbin; L. Hansan; C. Xuejing; L. Shujia; S. Chiachung, *Mater. Chem. and Phys.* **2003,** *79*, 37.

194. S. Lanceros-Mendez; J. F. Mano; A. M. Costa; V. H. Schmidt, *J. Macromolecule. Phys, B* **2001,** *40*, 517.

195. (a) P. Martins; C. Caparros; R. Gonçalves; P. M. Martins; M. Benelmekki; G. Botelho; S. Lanceros-Mendez, *J. Phys. Chem. C* **2012,** *26*, 15790; (b) P. Martins; A. C. Lopesa; S. Lanceros-Mendeza, *Prog. Polym. Sci.* **2014,** *39*, 683.

196. X. Kuang; Q. Gao; H. Zhu, *J. Appl. Polym. Sci.* **2013**, DOI: 10.1002/APP.38729.

197. M. F. Lin; V. K. Thakur; E. J. Tan; P. S. Lee, *RSC. Adv.* **2011,** *1*, 576.

198. X. Kuang; Z. Liu; H. Zhu, *J. Appl. Poly. Sci.* **2013,** *129*, 3411.

199. (a) M. N. Almadhoun; U. S. Bhansali; H. NAlshareef, *J. Mater. Chem.* **2012,** *22*, 11196; (b) T. Zhou; J. -W. Zha; R. -Y. Cui; B. -H. Fan; J. -K. Yuan; Z. -M. Dang, *ACS Appl. Mater. Interfaces* **2011,** *3*, 2184.

200. (a) H. Danan; A. Herr; A. J. P. Meyer, *J. Appl. Phys.* **1986,** *39*, 669; (b) M. Feygenson; A. Kou; L. E. Kreno; A. L. Tiano; J. M. Patete; F. Zhang; M. S. Kim; V. Solovyov; S. S. Wong; M. C. Aronson, *Phy. Rev. B* **2010,** *81*, 014420.

201. (a) X. He; W. Zhong; C. Au; Y. Du, *Nanoscale Res. Lett.* **2013,** *8*, 446; (b) D. A. Van Leeuwen; J. M. Van Ruitenbeek; L. J. DeJongh; A. Ceriotti; G. Pacchioni; O. D. Häberlen; N. Rösch, *Phys. Rev. Lett.* **1994,** *73*, 1432.

202. (a) P. M. Paulus; H. Bönnemann; A. M. Van der Kraan; F. Luis; J. Sinzig; L. J. de Jongh, *Eur. Phys. J. D* **1999,** *9*, 501; (b) O. D. Jayakumar; B. P. Mandal; J. Majeed; G. Lawes; R. Naik; A. K. Tyagi, *J. Mater. Chem. C* **2013,** *1*, 3710.

203. D. P. Dutta; B. P. Mandal; R. Naik; G. Lawes; A. K. Tyagi, *J. Phys. Chem. C* **2013,** *117*, 2382.

204. (a) G. Lawes; T. Kimura; C. M. Varma; M. A. Subramanian; N. Rogado; R. J. Cava; A. P. Ramirez, *Prog. Solid State Chem.* **2009,** *37*, 40; (b) G. Lawes; A. P. Ramirez; C. M. Varma; M. A. Subramanian, *Phys. Rev. Lett.* **2003,** *91*, 257208.

205. J. Ma; J. Hu; Z. Li; C. W. Nan, *Adv. Mater.* **2011,** *23*, 1062.

206. C. A. F.Vaz; J. Hoffman; C. H.Ahn; R. Ramesh, *Adv. Mater.* **2010,** *22*, 2900.

207. (a) N. S. Rao; O. G. Palanna, *Bull. Mater. Sci.* **1995,** *18*, 229; (b) P. I. Cowin; R. Lan; L. Zhang; C. T. G. Petit; A. Kraft; S. Tao, *Mater. Chem. Phys.* **2011,** *126*, 614; (c) T. Groń; J. Krok-Kowalski; M. Kurzawa; J. Walczak, *J. Magn. Magn. Mater.* **1991,** *101*, 148; (d) T. Groń; H. Duda; J. Krok-Kowalski; J. Walczak; E. Filipek; P. Tabero; A. Wyrostek; K. Bärner, *Radiat. Eff. Defects Solids* **1995,** *133*, 341; (e) A. Dixit; P. Chen; G. Lawes; J. L. Musfeldt, *Appl. Phys. Lett.* **2011,** *99*, 141908; (f) V. D. Nithya; R. Kalai Selvan, *Phys. B* **2011,** *406*, 24.

208. R.Van De Krol; J. Ségalini; C. S. Enache, *J. Photonics Energy* **2011,** *1*, 016001.

209. S. J. Patwe; S. N. Achary; A. K. Tyagi, *J. Mater.Res.* **2009,** *24*, 3551.

210. K. Gaur; H. B. Lal, *J. Mater. Sci.* **1986,** *21*, 2289.

211. M. Touboul; A. Popot, *J. Therm. Anal.* **1986,** *31*, 117.

212. (a) M. Touboul; K. Melghit; P. Bénard; D. Louër, *J. Solid State Chem.* **1995,** *118*, 93; (b) M. Touboul; D. Ingrain, *J. Less Common Metal* **1980,** *71*, 55; (c)

D. I. Roncaglia; I. L. Botto; E. J. Baran, *J. Solid State Chem.* **1986,** *62*, 11; (d) T. Tojo; Q. Zhang; F. Saito, *J. Solid State Chem.* **2006,** *179*, 433.

213. (a) L. Zhang; H. Fu; C. Zhang; Y. Zhu, *J. Solid State Chem.* **2006,** *179*, 804; (b) M. Oshikiri; M. Boero; J. Ye; F. Aryasetiawan; G. Kido, *Thin Solid Films* **2003,** *445*, 168; (c) C. S. Enache; D. Lloyd; M. R. Damen; J. Schoonman; R. Van De Krol, *J. Phys. Chem. C* **2009,** *113*, 19351.

214. S. S. Plotkin; V. E. Plushchev; J. A. Rozdin; V. P. Romanov, *Izv. Akad Nauk SSSR Neorg Mater* **1975,** *11*, 1529.

215. J. Ye; Z. Zou; H. Arakawa; M. Oshikiri; M. Shimoda; A. Matsushita; T. Shishido, *J. Photochem. Photobio. A: Chem.* **2002,** *148*, 79.

216. (a) S. Denis; E. Baudrin; M. Touboul; J. M. Tarascon, *J. Electrochem. Soc.* **1997,** *144*, 4099; (b) B. Orel; A. Šurca Vuk; U. Opara Krašovec; G. Dražič, *Electrochim. Acta.* **2001,** *46*, 2059; (c) B. Li; Y. Wang, *Mate. Res. Bull.* **2010,** *45*, 1903.

217. M. P. Touboul; P. Toledano, *Acta Crystallogr. B* **1980,** *36*, 240.

218. E. V. Tsipis; V. V. Kharton; N. P. Vyshatko; A. L. Shaula; J. R. Frade, *J. Solid State Chem.* **2003,** *176*, 47.

219. D. Errandonea; F. J. Manjón, *Prog. Mater. Sci.* **2008,** *53*, 711.

220. A. C. Larson; R. B.Vandreele, GSAS: General Structure Analysis System Report LA-UR 86-748, Los Alamos National Laboratory, Los Alamos, NM2000.

221. (a) J. C. Maxwell, Oxford Univ Press: London, 1973; (b) A. K. Jonscher, Chelsea Dielectric Press: London 1983.

222. (a) Y. Suzuki; R. B. Van Dover; E. M. Gyorgy; J. M. Phillips; V. Korenivski; D. J. Werder; C. H. Chen; R. J. Cava; J. J. Krajewski; W. F. Peck Jr; K. B. Do, *Appl. Phys. Lett.* **1996,** *68*, 714; (b) W. F. J. Fontijn; P. J. Van Der Zaag; L. F. Feiner; R. Metselaar; M. A. C. Devillers, *J. Appl. Phys.* **1999,** *85*, 5100.

223. Q. Song; Z. John Zhang, *J. Phys. Chem. B* **2006,** *110*, 11205

224. K. Maaz; A. Mumtaz; S. K. Hasanain; A. Ceylan, *J. Magn. Magn. Mater.* **2007,** *308*, 289.

225. (a) G. H. Jonker, *J. Phys.Chem. Solids* **1959,** *9*, 165; (b) J. G. Na; M. C. Kim; T. D. Lee; S. J. Park, *IEEE Trans. Magn.* **1993,** *29*, 3520.

226. N. Sivakumar; A. Narayanasamy; K. Shinoda; C. N. Chinnasamy; B. Jeyadevan; J. M. Greneche, *J. Appl. Phys.* **2007,** *102*, 013916.

227. X. Zhang; W. Jiang; D. Song; H. Sun; Z. Sun; F. Li, *J. Alloys Compd* **2009,** *475*, L34.

228. T. A. S. Ferreira; J. C. Waerenborgh; M. H. R. M. Mendonça; M. R. Nunes; F. M. Costa, *Solid State Sci.* **2003,** *5*, 383.

229. G. Li; J. Boerio-Goates; B. F. Woodfield; L. Li, *Appl. Phys. Lett.* **2004,** *85*, 2059.

230. (a) R.D. Waldron, *Phys. Rev.* **1955,** *99*, 1727; (b) W. B. White; B. A. DeAngelis, *Spectrochim. Acta, Part A* **1967,** *23*, 985.

231. D. Peddis; N. Yaacoub; M. Ferretti; A. Martinelli; G. Piccaluga; A. Musinu; C. Cannas; G. Navarra; J. M. Greneche, *J. Phys. Condens. Matter* **2011,** *23*, 426004.

232. (a) K. Sharma; S. Singh; C. L. Prajapat; S. Bhattacharya; Jagannath; M. R.Singh; S. M. Yusuf; G. P. Kothiyal, *J. Magn. Magn. Mater.* **2009,** *321*,

3821; (b) M. Darbandi; Stromberg; F. Landers, J. N. Reckers; B. Sanyal; W. Keune; H. Wende, *J. Phys. D: Appl. Phys.* **2012,** *45*, 195001.

233. K. Sharma; S. S. Meena; S. Saxena; S. M. Yusuf; A. Srinivasan; G. P. Kothiyal, *Mater. Chem. Phys.* **2012,** *133*, 144.

234. S. R. Elliott, *Adv. Phys.* **1987,** *36*, 135.

235. N. F. Mott; E. A. Davis, *Electronic Processes in Non-Crystalline Materials*. Oxford: Clarendon, 1979.

236. I. G. Austin; N. F. Mott, *Adv. Phys.* **2001,** *50*, 757.

237. C. N. Chinnasamy; B. Jeyadevan; K. Shinoda; K. Tohji; D. J. Djayaprawira; M. Takahashi; R. Justin Joseyphus; A. Narayanasamy, *Appl. Phys. Lett.* **2003,** *83*, 2862.

.